Towards the development of advanced hierarchical CHAbazite core-shell catalysts for reduction of NOx

Brenda Silveira de Araujo

THESE de DOCTORAT DE
L'UNIVERSITE CLAUDE BERNARD LYON 1

Ecole Doctorale N° 206
Ecole Doctorale de Chimie de Lyon

Discipline : Catalyse

Soutenue publiquement le 12/12/2022, par :
Brenda Roberta Silveira De Araujo

Towards the development of advanced hierarchical CHAbazite core-shell catalysts for reduction of NO_x

---

Devant le jury composé de :

Galvez-Parruca, Maria Elena	Maître de Conférences, Sorbonne Université	Rapporteuse
Can, Fabien	Maître de Conférences, Université de Poitiers	Rapporteur
Viricelle, Jean-Paul	Directeur de Recherche, Ecoles des Mines de Saint-Etienne	Examinateur
Afanasiev, Pavel	Directeur de Recherche, CNRS IRCELYON	Examinateur
Giroir-Fendler, Anne	Professeure Universités, Université de Lyon 1	Présidente
Gil Villarino, Sonia	Maître de Conférences, Université de Lyon 1	Directrice de thèse
Caravaca, Angel	Chargé de recherche, CNRS IRCELYON	Invitée

Université Claude Bernard – LYON 1

Président de l'Université	M. Frédéric FLEURY
Président du Conseil Académique	M. Hamda BEN HADID
Vice-Président du Conseil d'Administration	M. Didier REVEL
Vice-Président du Conseil des Etudes et de la Vie Universitaire	M. Philippe CHEVALLIER
Vice-Président de la Commission de Recherche	M. Petru MIRONESCU
Directeur Général des Services	M. Pierre ROLLAND

COMPOSANTES SANTE

Département de Formation et Centre de Recherche en Biologie Humaine	Directrice : Mme Anne-Marie SCHOTT
Faculté d'Odontologie	Doyenne : Mme Dominique SEUX
Faculté de Médecine et Maïeutique Lyon Sud - Charles Mérieux	Doyenne : Mme Carole BURILLON
Faculté de Médecine Lyon-Est	Doyen : M. Gilles RODE
Institut des Sciences et Techniques de la Réadaptation (ISTR)	Directeur : M. Xavier PERROT
Institut des Sciences Pharmaceutiques et Biologiques (ISBP)	Directrice : Mme Christine VINCIGUERRA

COMPOSANTES & DEPARTEMENTS DE SCIENCES & TECHNOLOGIE

Département Génie Electrique et des Procédés (GEP)	Directrice : Mme Rosaria FERRIGNO
Département Informatique	Directeur : M. Behzad SHARIAT
Département Mécanique	Directeur M. Marc BUFFAT
Ecole Supérieure de Chimie, Physique, Electronique (CPE Lyon)	Directeur : Gérard PIGNAULT
Institut de Science Financière et d'Assurances (ISFA)	Directeur : M. Nicolas LEBOISNE
Institut National du Professorat et de l'Education	Administrateur Provisoire : M. Pierre CHAREYRON
Institut Universitaire de Technologie de Lyon 1	Directeur : M. Christophe VITON
Observatoire de Lyon	Directrice : Mme Isabelle DANIEL
Polytechnique Lyon	Directeur : Emmanuel PERRIN
UFR Biosciences	Administratrice provisoire : Mme Kathrin GIESELER
UFR des Sciences et Techniques des Activités Physiques et Sportives (STAPS)	Directeur : M. Yannick VANPOULLE
UFR Faculté des Sciences	Directeur : M. Bruno ANDRIOLETTI

Acknowledgment/Remerciements

First, I would like to thank “l'Agence Nationale de la Recherche (ANR)” and the “Centre National de la Recherche Scientifique (CNRS)” for sponsoring the JCJC CHARO project presented in this thesis and also the partners of the “Universidad del País Vasco” and the “Universidad Politécnica de Madrid” for their advice, analysis, and contributions to the work improvement.

Thank you very much to my two thesis directors, Sonia GIL and Angel CARAVACA, who are two young incredibly dedicated researchers that love the science. Thank you so much for all the instructions, assistance, and time spent together. You provided me innumerous lessons.

Many thanks Maria Elena GALVEZ-PARRUCA and Fabien CAN, for agreeing to be the rapporteurs of this these. In the same manner, I am also glad with accepting of Jean-Paul VIRICELLE, Pavel AFANASIEV, and Anne GIROIR-FENDLER on my jury, Thanks.

I would like also to express my appreciation to the entire CARE team for the academic/scientific experience and the members of the technical and administrative services of IRCELYON thanks for their kindness to assist. Thanks all of my lab colleagues for their company over these years, especially Guillermo PEDROSA, Weidong ZHANG, Feng PAN, Jie YU, Elizabeth VERA, and Jesus GONZALEZ-COBOS.

To my entire family, thank you very much for their support and belief in me, especially my mother Marluci Almeida and my brother and sister Marlon Bruno and Barbara Maria for sending me so much love and strength at this time. Being away from you, the weekend video calls were essential.

I cannot forget those who supported the beginning of my PhD, but are no longer with us. Thank you my grandparents Raimunda and Constancio, as well as my dear father Afonso Murilo, who left me an example of his constant desire to learn. Thanks!

D'abord, je tiens à remercier l'Agence Nationale de la Recherche (ANR) et le Centre National de la Recherche Scientifique (CNRS) pour le financement du projet JCJC CHARO associé à cette thèse. Par ailleurs, je souhaite remercier aussi aux collègues de la “Universidad del País Vasco” et la “Universidad Politécnica de Madrid” pour leurs conseils, analyses et contributions à l'amélioration du travail.

Un grand merci à mes deux directeurs de thèse, Sonia GIL et Angel CARAVACA, qui sont deux jeunes chercheurs incroyablement passionnés par la science. Merci beaucoup pour toutes les instructions, l'aide et le temps passé ensemble. Vous m'avez donné d'innombrables leçons.

Merci beaucoup à Maria Elena GALVEZ-PARRUCA et Fabien CAN, d'avoir accepté d'être les rapporteurs de ma thèse. De la même manière, je tiens à remercier Prof. Jean-Paul VIRICELLE, Dr. Pavel AFANASIEV et Prof. Anne GIROIR-FENDLER d'avoir accepté de participer à mon jury de thèse en tant qu’examinateurs. Merci.

Je tiens à remercier toute l'équipe de CARE pour l'expérience académique et scientifique ainsi que tous les membres des services techniques et administratifs de l’IRCELYON pour leur gentillesse. Je tiens à remercier tous mes collègues de laboratoire pour leur compagnie au cours de ces années, en particulier Guillermo PEDROSA, Weidong ZHANG, Feng PAN, Jie YU, Elizabeth VERA et Jesus GONZALEZ-COBOS.

A ma famille, un grand merci pour leur soutien et la confiance qu’ils m’ont accordé au fil des ans. Un merci spécial à ma mère Marluci Almeida et mon frère et sœur Marlon Bruno et Barbara Maria pour m'avoir envoyé tant d'amour et de force en ce moment. Étant loin de vous, les appels vidéo du week-end étaient essentiels.

Je ne peux pas oublier ceux qui ont soutenu le début de mon doctorat, mais qui ne sont plus parmi nous. Merci à mes grands-parents Raimunda et Constancio, ainsi que de mon cher père Afonso Murilo, qui m'a laissé un exemple de son désir incessant d'apprendre. Merci!

CONTENTS

Abstract

The reduction of atmospheric pollution from stationary sources and mobile engines, especially NO_x and N_2O emissions, is a serious challenge associated with stringent environmental regulations. In this respect, revisiting after-treatment systems under the prism of disruptive concepts may significantly improve their eco- and health-friendliness. This is the standpoint of this PhD project, which ambitions to develop novel catalysts combining several functionalities in extended ranges of operating conditions. For this purpose, porous zeolites called chabazites (CHA), known to be highly efficient and hydrothermally stable molecular sieves, will be used. However, these materials allow only limited gas diffusion in operation conditions typical of modern engine exhaust systems. To reach high performance, selectivity and stability, the project targets hierarchical materials allowing efficient gas diffusion though mesopores, and further aims at combining the activity of copper and iron sites in core-shell structures.

First of all, novel CHA-based (SAPO-34) materials with a hierarchical architecture (mesopores connected to micropores) were developed, optimized and thoroughly characterized. The hierarchical zeolites with the best physico-chemical features, were used as a support for the development of hierarchical Cu/SAPO-34 catalysts, which were characterized by several techniques and tested for the NH_3-SCR reaction, and compared with the conventional microporous Cu/CHA catalyst. In addition, their hydrothermal stability, a feature of paramount importance in view of its further practical implementation, was studied. The results obtained highlighted the potential of the hierarchical catalysts, mainly based on their improved activity at low reaction temperatures, which was even better after the hydrothermal treatment. Finally, this project aims to develop a novel all-zeolite core-shell catalyst, where the core is the optimized hierarchical Cu/SAPO-34 catalyst, and the shell is a microporous Fe/SAPO-34 material (with slightly bigger pores than conventional CHA materials). Different approaches were studied, showing that the use of positive surfactants (such as CTAB, to modify the surface charge of the core) and the calcination of intermediate synthesis materials, among other factors, seemed to enhance the interaction between core and shell. This latter study allowed therefore to identify the main direction to follow towards the development of the desired core-shell materials.

Keywords: Selective Catalytic Reduction with NH_3, NO_x reduction, hierarchical SAPO-34 zeolites, all-zeolite core-shell materials.

Résumé

La réduction de la pollution issue des moteurs mobiles et stationnaires, notamment les émissions de NO_x et de N_2O, est un enjeu majeur assorti des normes environnementales contraignantes. Des ruptures technologiques pourraient rendre les systèmes de post-traitement significativement plus propres. Avec ce parti pris, le projet développera des catalyseurs orignaux performants, sélectifs et stables, combinant plusieurs fonctionnalités dans des conditions de fonctionnement étendues. Des zéolites appelées chabazites (CHA), connues pour être des tamis moléculaires efficaces et stables hydrothermiquement, seront utilisées. Ces chabazites ne permettent cependant habituellement qu'une diffusion limitée des gaz en condition d'utilisation des systèmes d'échappement des moteurs modernes. Des matériaux hiérarchiques permettant une diffusion gazeuse efficace à travers des mésopores pallieront cette difficulté ; des structures cœur-coquille exploiteront les effets synergiques de sites de fer et de cuivre.

Tout d'abord, de nouveaux matériaux type CHA (SAPO-34) à architecture hiérarchisée (mésopores et micropores reliés entre eux) ont été développés, optimisés et parfaitement caractérisés. Les zéolithes à porosité hiérarchisée présentant les meilleures propriétés physico-chimiques ont alors été utilisées en tant que support pour le développement de catalyseurs à porosité hiérarchisée de type Cu/SAPO-34. Ces derniers ont à leur tour été caractérisés via différentes techniques analytiques et leurs performances dans le cadre de la réaction de réduction des NO_x par l'ammoniac (NH_3-SCR) ont été évaluées. Une comparaison a ainsi pu être menée avec les performances obtenues avec le catalyseur conventionnel et de référence, à savoir le catalyseur microporeux de type Cu/CHA. Par ailleurs, en vue d'une éventuelle utilisation pratique et en tant que paramètre clé, la stabilité du catalyseur Cu/SAPO-34 dans des conditions hydrothermales typiques a été étudiée. Les résultats obtenus mettent en évidence que l'utilisation de catalyseurs à porosité hiérarchisée peut se révéler objectivement prometteur. En effet, ceux-ci présentent des activités catalytiques à basse température largement améliorées, en particulier après leur traitement hydrothermal. Enfin, ce projet avait également pour but de développer un nouveau catalyseur cœur-coquille 100% zéolithes avec pour cœur le catalyseur à porosité hiérarchisée précédemment optimisé Cu/SAPO-34, et pour coquille un matériau microporeux type Fe/SAPO-34 aux pores légèrement plus gros que ceux du matériau CHA conventionnel. Pour ce faire, différentes approches ont été menées et ont montré, entre autres, que l'utilisation de surfactants (ou tensioactifs) cationiques tel que le CTAB ou encore la calcination des matériaux synthétisés lors des étapes intermédiaires de la synthèse permettaient

de décupler les interactions cœur-coquille. Cette dernière étude a ainsi permis d'identifier la stratégie adéquate à mener dans le cadre du développement de matériaux type cœur-coquille.

Mots clés : Réduction Catalytique Sélective par l'ammoniac, réduction des NO_x, zéolithes SAPO-34 à porosité hiérarchisée, matériaux type cœur-coquille 100% zéolithes.

TABLES, SCHEMES AND FIGURES CAPTION

LIST OF ABREVIATIONS

4-MR: 4-Member Rings

6-MR: 6-Member Rings

8-MR: 8-Member Rings

BEA: Beta

BJH: Barrett-Joyner-Halenda

CHA: Chabazite

CAA: Clean Air Act

CRT: Continuously Regenerating Trap

CTAB: Cetyltrimethylammonium bromide

DIPEA: N,N-diisopropylethylamine

DOC: Diesel Oxidation Catalyst

DPF: Diesel Particulate Filter

DRIFTS: Diffuse Reflectance Infrared Fourier Transform Spectroscopy

E-TEM: Environmental Transmission Electron Microscopy

EU: European Union

EGR: Exhaust Gas Recirculation

EFM: Exhaust mass Flow Meter

FER: Ferrierite

FTIR: Fourier Transform Infrared

GPS: Global Positioning System

GHG: GreenHouse Gas

HA: Hexadecylamine

HK: Horvath-Kawazoe

HT: High Temperature

HT: Hydrothermal Treatment

H_2-TPR: Hydrogen Temperature Programmed Reduction

ICP-OES: Inductively Coupled Plasma Optical Emission Spectroscopy

IZA: International Zeolite Association

LNT: Lean NO_x Traps

LT: Low Temperature

MOR: Mordenite

MAS NMR: Magic Angle Spinning Nuclear Magnetic Resonance

MT: Medium Temperature

NEPA: National Environmental Protection Act

NEDC: New European Driving Cycle

NH_3-SCR: Selective Catalytic Reduction via ammonia

NH_3-TPD: Ammonia Temperature-Programmed Desorption

OSDA: Organic Structure Direct Agent

PEMS: Portable Emissions Measurement System

PGM: Platinum Group Metals

PSA: Peugeot Société Anonymes

RDE: Real Driving Emissions

STEM: Scanning Transmission Electron Microscopy

sbus: Secondary building units

SOF: Soluble Organic Fraction

TEOS: Tetraethyl orthosilicate

TGA: ThermoGravimetric Analyses

TEAOH: Tetraethylammonium hydroxide

TPAOH: Tetrapropylammonium hydroxide

TEM: Transmission Electron Microscopy

WHO: World Health Organization

XRD: X-ray Diffraction

General Introduction

The increasing concerns about global warming on account of the rising CO_2 emissions are leading the current research efforts towards the use of renewable energies and carbon-free energy carriers (mainly H_2 [1,2]). These environmentally-friendly technologies aim to substitute the traditional combustion of fossil-fuels (e.g. natural gas), and fossil fuels-derivatives (e.g., gasoline or diesel). Even though the world is in the right path to this transition, regarding the automotive technologies, internal combustion engines will likely be around for at least the next several decades, and fuel efficiency is supposed to be gradually improved [3]. Among other pollutants produced by vehicles (including CO, unburnt hydrocarbons and particulate matter), nitrogen oxides (NO_x) are known to cause alarming environmental issues, such as acid rain and photochemical smog [4,5]. In this sense, the NO_x emissions regulations are becoming increasingly more stringent, stimulating the continuous improvement of high-performance catalytic systems.

Efficient technologies and catalytic systems have been developed in the last decades for the reduction of NO_x under lean-burn conditions [6]. Selective Catalytic Reduction with ammonia as reducing agent (NH_3-SCR) is one of the most promising NO_x abatement technologies, where ammonia is obtained by the thermal decomposition of urea (thermolysis). In this sense, Cu-based zeolite catalysts were reported to exhibit high activity for the NH_3-SCR reaction. In particular, small-pore Cu-exchanged Chabazite (Cu-CHA) catalysts, such as Cu-SAPO-34 and Cu-SSZ-13, were discovered and commercialized by researchers from BASF and Johnson Matthey, and are now widely applied to control vehicle exhausts emissions [7]. One of the most interesting attributes of these catalysts is their high hydrothermal stability at temperatures over 700 ^oC. This feature is of paramount importance in view of the further implementation and commercialization of novel catalytic systems for the NH_3-SCR technology, since: i) water (steam) is one of the main products emitted from internal combustion engines, and ii) the exhaust temperature can reach over 700 ^oC on account of the regeneration of the diesel particulate filter [8].

Considering the expected gradual fuel efficiency enhancement [3], together with the progress and further implementation of upgraded engine technologies, the engine-exhaust temperatures are expected to drop sharply [6]. In addition, under “cold-start” operating conditions, the exhaust temperature is much lower compared to that “on-road”. However, in

such low temperature window, the above described Cu-CHA catalysts do not seem to exhibit sufficient activity to efficiently reduce NO_x [6]. Among other reasons, this could be attributed to the small pore size of CHA-zeolite, which strongly hinders the access of reactants to the catalytically active sites. It leads to significant intra-crystalline diffusion limitations, mainly at low temperatures [9,10]. The development of hierarchical zeolites with structured and ordered micropores and mesopores could be a promising solution to overcome such issue.

In this sense, first objective of ANR JCJC project CHARO (*Hierarchical CHAbazite core-shell catalysts for Reduction of NO_x and N_2O*) and the present PhD was to develop, and optimise, hierarchical CHA-based (SAPO-34) materials (**Chapter III**), which were synthetized by soft-templating method (never used before for small-pore zeolites) using different amounts of cetyltrimethylammonium bromide (CTAB) as a mesoporous template. Both microporous and soft mesoporous templates where introduced at the same time and at different stages of the synthesis procedure. The physico-chemical, structural and acid properties of developed materials were evaluated by several characterisation techniques in order to verify the incorporation of mesopores into the solely microporous chabazite framework. Two hierarchical zeolite materials were further selected on account of their enhanced physico-chemical properties [11] and used as a catalytic support for Cu ions. Cu-exchanged hierarchical catalysts were then synthetized, carefully characterized and tested for NO_x reduction by the NH_3-SCR reaction (**Chapter IV**). However, one may think that the creation of mesopores could eventually weaken the zeolite structure, decreasing therefore its hydrothermal stability. This is indeed expected if aggressive post-treatment methods (e.g. dealumination, desilication) are used for the generation of mesopores, since they usually degrade the framework structure of zeolites. However, previous studies displayed high hydrothermal stability of novel hierarchical CHA zeolites (SSZ-13) [4] prepared by dual templates (one for the generation of micropores, and the other for the generation of mesopores, as was the case in our previous study [11]). Thus, the impact of a hydrothermal treatment on the main physico-chemical properties, active sites and catalytic activity (for the NH_3-SCR reaction) of our novel Cu-based hierarchical SAPO-34 catalysts was also thoroughly studied in Chapter IV. Therefore, to reach higher NH_3-SCR performance and hydrothermal stability, this PhD targets Cu-based hierarchical catalysts allowing efficient gas diffusion though mesopores. Nevertheless, it is well known that Cu-based catalysts are less active than Fe-based ones at higher temperatures. Thus, this PhD also aims at combining the activity of copper and iron sites in CHAbazite zeolite-zeolite core-shell structures (**Chapter V**).

[1] M. Helen McCay, Chapter 23 - Hydrogen: An Energy Carrier, in: T.M.B.T.-F.E. (Second E. Letcher (Ed.), Elsevier, Boston, 2014: pp. 495–510. https://doi.org/https://doi.org/10.1016/B978-0-08-099424-6.00023-5.

[2] I. Staffell, D. Scamman, A. Velazquez Abad, P. Balcombe, P.E. Dodds, P. Ekins, N. Shah, K.R. Ward, The role of hydrogen and fuel cells in the global energy system, Energy Environ. Sci. 12 (2019) 463–491. https://doi.org/10.1039/C8EE01157E.

[3] C.K. Lambert, Current state of the art and future needs for automotive exhaust catalysis, Nat. Catal. 2 (2019) 554–557. https://doi.org/10.1038/s41929-019-0303-x.

[4] C. Peng, R. Yan, Y. Mi, G. Li, Y. Zheng, Y. Luo, J. Liang, W. Liu, Z. Li, D. Wu, X. Wang, H. Peng, Toward rational design of a novel hierarchical porous Cu-SSZ-13 catalyst with boosted low-temperature NOx reduction performance, J. Catal. 401 (2021) 309–320. https://doi.org/https://doi.org/10.1016/j.jcat.2021.07.024.

[5] L. Han, S. Cai, M. Gao, J. Hasegawa, P. Wang, J. Zhang, L. Shi, D. Zhang, Selective Catalytic Reduction of NOx with NH3 by Using Novel Catalysts: State of the Art and Future Prospects, Chem. Rev. 119 (2019) 10916–10976. https://doi.org/10.1021/acs.chemrev.9b00202.

[6] S. Zhang, L. Pang, Z. Chen, S. Ming, Y. Dong, Q. Liu, P. Liu, W. Cai, T. Li, Cu/SSZ-13 and Cu/SAPO-34 catalysts for deNOx in diesel exhaust: Current status, challenges, and future perspectives, Appl. Catal. A Gen. 607 (2020) 117855. https://doi.org/10.1016/j.apcata.2020.117855.

[7] W.M. Bull, W.-M. Xue, P. Burk, R.S. Boorse, I. Jaglowski, G.S. Koermer, A. Moini, J.A. Patchett, J.C. Dettling, M.T. Caudle, Copper CHA Zeolinte Catalysts, U.S. Patent 0,226,545, 2008., 2009. https://patents.google.com/patent/US20080226545.

[8] S.J. Schmieg, S.H. Oh, C.H. Kim, D.B. Brown, J.H. Lee, C.H.F. Peden, D.H. Kim, Thermal durability of Cu-CHA NH3-SCR catalysts for diesel NOx reduction, Catal. Today. 184 (2012) 252–261. https://doi.org/10.1016/j.cattod.2011.10.034.

[9] T. Zhang, J. Li, J. Liu, D. Wang, Z. Zhao, K. Cheng, J. Li, High activity and wide temperature window of Fe-Cu-SSZ-13 in the selective catalytic reduction of NO with ammonia, AIChE J. 61 (2015) 3825–3837. https://doi.org/10.1002/aic.14923.

[10] F. Gao, E.D. Walter, E.M. Karp, J. Luo, R.G. Tonkyn, J.H. Kwak, J. Szanyi, C.H.F. Peden, Structure–activity relationships in NH3-SCR over Cu-SSZ-13 as probed by reaction kinetics and EPR studies, J. Catal. 300 (2013) 20–29. https://doi.org/https://doi.org/10.1016/j.jcat.2012.12.020.

[11] B.R.S. De Araujo, J.A. Onrubia-Calvo, I. Stambouli, G. Pétaud, J. Hidalgo-Carrillo, A. Nieto-Marquéz, B. Pereda-Ayo, J.R. González-Velasco, A. Caravaca, S. Gil, Towards the development of advanced hierarchical chabazite materials: Novel micro-mesoporous silicoaluminophosphate SAPO-34 zeolites, Mater. Today Commun. 31 (2022) 103580. https://doi.org/10.1016/j.mtcomm.2022.103580.

Chapter I

CHAPTER I: Context and state-of-the-art.

This chapter aspires to contextualize the aim and motivation of the PhD, giving information about the theory related to the envisaged application and the research topic. In the same way, this chapter is a review on the state-of-the-art, ready to settle a general background in order to facilitate the understanding of the following chapters of the manuscript. The NO_x emissions, environmental regulations, diesel after-treatment catalytic systems, including Selective Catalytic Reduction of nitrogen oxides (NO_x) via ammonia (NH_3-SCR), will be first described. The current catalysts used for NH_3-SCR reaction, including conventional microporous zeolites and, in particular, the so-called chabazite (CHA) zeolites, known to be highly efficient molecular sieves, will be also presented in this chapter. Furthermore, the current issues (background in low-temperature NH_3-SCR and diffusion limitations) and solutions (hierarchical zeolite possessing secondary porosity and core-shell structure) of these CHA-zeolite catalysts in operation conditions typical of modern engine exhaust systems, are also pointed out in this chapter.

1. Atmospheric pollution: focus on exhaust emissions from thermal combustion in engines.

Regarding the issue of air pollution, since the industrial revolution of the 19th century, the rapid technological advancement and industrialization in big cities has resulted in a profound alteration in the composition of the environment air. The initial connections between acid rain and air pollution were established at the same time than that of the greenhouse effect, which was introduced to explain the global warming of the earth [1,2]. This revolution has drastically altered the way in which humans interact with the environment, which had a significant impact on the levels of pollution in the air, water and land. The industrial era was made possible by the widespread use of coal as a main energy source, which replaced more traditional sources like wind, water and wood. However, this shift also brought about a first awareness of the negative effects of pollution on human health and the environment.

Large American cities, including New York, experienced issues with equestrian transport pollution, which was primarily based on horse excrement and carcasses, negatively impacting both, air quality and human health. New York was the first city to verify the pollution coming from such transport [3]. In this historical setting, horse transportation was replaced by

the gasoline vehicles during the Industrial Revolution, and when urbanization and population growth accelerated in the 1950s, the number of cars per inhabitant increased.

Among the air pollutants sources, the incomplete hydrocarbon combustion in thermal engines is considered as one of the major contributors to climate change, accounting for the vast majority of greenhouse gas (GHG) emissions (apart from CO_2). Without after-treatment depollution systems, the massive gasoline and diesel engines produce enormous amounts of gaseous and particulate exhaust pollutants that have a negative effect on both, health and environment. The most significant harmful pollutants coming from thermal combustion, in addition to carbon dioxide (CO_2) and water (H_2O), are carbon monoxide (CO), total hydrocarbons (THC), nitrogen oxides (NO_x) and particulate matter (PM) [4]. The main exhaust emissions as a function of the type of engine are summarized in Table I.1 [5]. In particular, NO_x (mainly NO and NO_2), which are not only emitted from mobile sources (thermal combustion engines - gasoline or diesel) but also from stationary sources (fossil-fuel power plants or fluid catalytic cracking units), are under scrutiny on account of their harmful influence on environment (acid rain, photochemical smog, ozone depletion) and human health, with morbidity and mortality effects, by spreading in respiratory tracts, up to Alveolar-cells [6–10].

Table I.1. Characteristic of the exhaust emissions as a function of the type of engine [5].

Chemical compounds	Diesel Engine	Gasoline engine operating at stoichiometry	Direct injection gasoline engine operating with an oxygen excess
$NO+NO_2$	200-1000 ppm	100-4000 ppm	800-2300 ppm
Total hydrocarbons	10-330 ppm	400-5000 ppm	350-1500 ppm
CO	150-1200 ppm	0.1-0.6 %	0.5-0.9 %
O_2	5-15 %	0.2-2 %	0.6-7 %
H_2O	1-7 %	10-12 %	10-12 %
CO_2	3-13 %	10-18 %	10-15 %
SO_2	10-100 ppm	15-60 ppm	10-50 ppm
Particles	50-400 mg m^{-3}	-	-
Temperature	973 K	1373 K	1173 K
Air/Fuel (A/F)	45-18	14.7	40-30

The first reports and measurements of pollution concentrations were made public in the United States in 1963. The "Clean Air Act" (CAA) and the "National Environmental Protection Act" (NEPA) were thus the first officially recognized emission standards [11]. In order to comply with these new environmental requirements, new catalytic converters were created in California, and the others nations soon followed it. However, in Europe, an emission control system was not required in vehicles like they were in America. Indeed, the European engine

was only created considering the World Health Organization (WHO)'s European Guide Values in 1987 [12]. Hence, 25 years after the United States, the use of a catalytic converter was adopted in Europe. That delay was justified on the basis that the small engines adopted in Europe would suffice to reduce around 70 or 80 percent of the pollution, which was strongly defended by Jacques Calvet, a chairman of Board of Directors of Peugeot Société Anonymes (PSA) [13]. Thus, the catalytic after-treatment systems were adopted in Europe in the 1980s thanks to the introduction of the first environmental regulation for automotive emissions, known as EURO I. These environmental standards have since continued to change with ever-more-strict reductions in emission limits. The evolution of environmental emission regulations must be closely followed, since it will indirectly determine the future directions of research and development for the automotive industry.

1.1. Environmental regulations for atmospheric pollution.

Despite the efforts that have been made to air pollution reduction since 1970, its impacts on climate, ecosystems and health are evident. Due to this growing environmental understanding, european authorities progressively restricted the acceptable exhaust emission limits by developing the denoted Euro emission standards, which are continually becoming stricter (Table I.2). Note that the emission standards for heavy duty engines (Euro I… VI) are written in Roman numerals, whereas those for light cars are written in Arabic (Euro 1… 6) [14]. Another distinction is that the emission control testing vary depending on whether the vehicle is considered heavy or light [15,16]. For instance, the emission limitations for trucks are determined by the amount of mass emitted per unit of mechanical work completed, which varies based on the torque that is applied when the vehicle is in motion. For this reason, the unit g/kWh is used. Contrary, for light vehicles the unit of g/km is employed, considering just the distance traveled. The different units make difficult to draw comparisons between these two categories.

Regarding the most recent European regulation for the emissions of light vehicles, EURO 6, which is being applied since 2014, is especially focused on NO_x emissions limitation by strongly reducing the NO_x emission standards compared to EURO 5 (from 0.18 g/km allowed in 2009 with Euro 5 to 0.08 fixed by Euro 6). Moreover, EURO 6 set new guidelines that takes into account particulate emissions not only in terms of their mass (particulate matter, or PM) but also their number (particulate number, or PN) [14,17]. Due to their significant impacts on environmental issues like acid rain and climate change, PM and NO_x are sometimes referred to as "primary pollutants of the atmosphere" [4,18,19].

Table I.2. Evolution of pollutant emission regulation for light vehicles [14].

	Gasoline (g km^{-1})					Diesel (g km^{-1})				
	CO	**HC**	**NO_x**	**PM**	**PN#**	**CO**	**HC + NO_x**	**NO_x**	**PM**	**PN#**
EURO II -2000	2.3	0.2	0.15	-	-	0.64	0.56	0.5	0.05	-
EURO IV -2005	1	0.1	0.08	-	-	0.5	0.3	0.25	0.025	-
EURO V -2006	1	0.1	0.06	0.005	-	0.5	0.23	0.18	0.005	6×10^{11}
EURO VI -2015	1	0.1	0.06	0.005	6×10^{11}	0.5	0.125	0.075	0.005	6×10^{11}

As a result of their great efficiency in combustion and fuel economy performance, diesel engines have found widespread application in the global automobile market. Despite their benefits, diesel combustion engines have a challenge to overcome: one of the most difficult technological issues that automobile manufacturers are facing nowadays is the task of reducing emissions of NO_x produced by diesel light vehicles. Indeed, the vehicles that use others petrol fuels produce much less amount of NO_x, as represented in the Figure I. 1 [16,20].

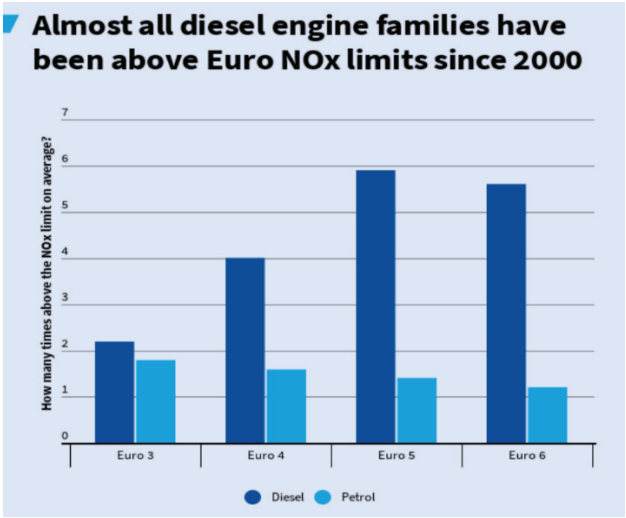

Figure I. 1. Average of NO_x emissions per Euro standard and per fuel type [21].

The previous Euro emission strandards are based on the emissions measured during a series of driving cycles, which defines a Global Harmonized Standard for determining the levels of pollutants and CO_2 emissions, fuel or energy consumption and electric range from light-duty [20,22]. These cycles need to reproduce faithfully the real traffic conditions. Thus, all new passenger cars shall be in accordance with NO_x emission limit during the European cycle of certification (New European Driving Cycle, NEDC - chassis dynamometer procedure). However, these testing commonly showed that the "real-world"

NO_x emissions from diesel passenger vehicles are much greater than the approved level, even though all automobile manufactures were able to achieve this criterion during controlled laboratory emissions tests, Figure I. 2 (a) and (b) [20]. The difference between measured and real-world emissions is indeed a huge problem.

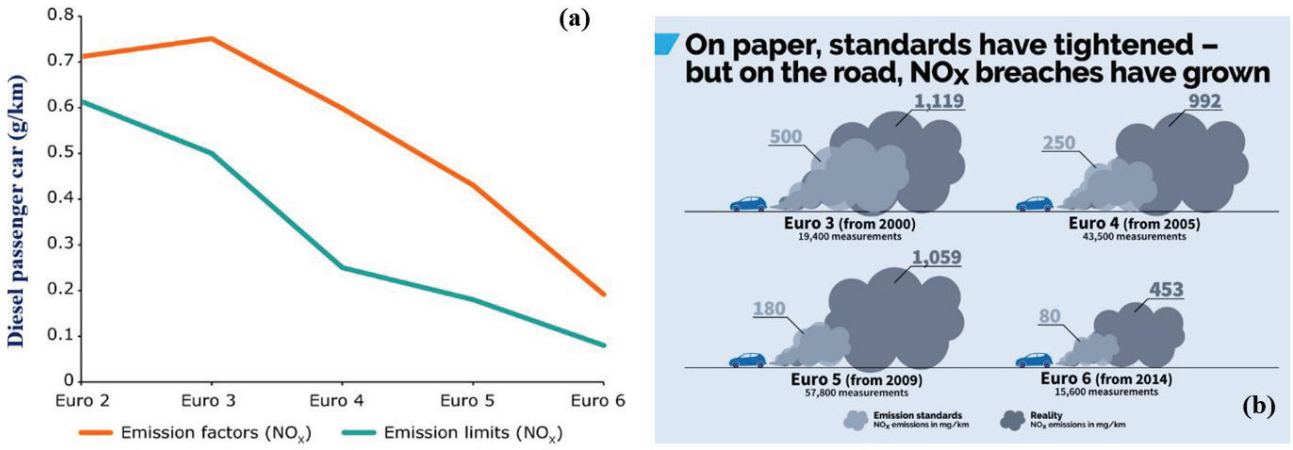

Figure I. 2 (a) The real-world NO_x emission factors in urban conditions for diesel cars with different Euro standards over the years and (b) Typical NO_x emissions measured in the real-world, against the European standards [21,23].

This discrepancy between the measured and real world emissions was spotlighted in 2015 by the scandal involving Volkswagen, in which it was discovered that the automobiles company hided the actual level of gaseous pollutants emissions [24]. The anti-pollution software implemented in the car only remained active while the automobile was undergoing laboratory testing. Once the testing was complete, the device was turned off. As a result, it was feasible to bring the NO_x emissions from the car under control, for a brief period of time and it made possible the vehicle to pass the emissions tests without any problems and get a certificate for environmentally responsible driving. That scandal unquestionably accelerated the stringency of regulations and the development of NO_x depollution systems, but it also brought the attention into the gap issue between laboratory emissions testing and measurements conducted under real-world settings [24].

Moreover, in 2017 the European Union (EU) introduced testing in real-world conditions (using portable emissions measurement systems), in addition to laboratory emission tests [25]. The Real Driving Emissions (RDE) tests (Euro 6d standards) are being progressive between 2017 and 2021[22] for NO_x (PM particle number being left for further study) in real operation in order to minimize the disparities that were discovered

between the pollutant emissions measured in the laboratory and those measured on the road, preventing the use of illegal strategies.

The RDE testing was established by EC Regulation (EU) 2017-1151 [26], which required that vehicle must be equipped with a Portable Emissions Measurement System (PEMS). The PEMS is, in general, a compact equipment composed of portable analyzers, an Exhaust mass Flow meter (EFM), a weather station and a Global Positioning System (GPS). This regulation also specifies the parameters for the journey, including time, distance traveled, speed ranges and ambient boundary conditions, which include its altitude and temperature [27]. The journey has to simulate a broad variety of real-world situations, with predetermined amounts of time spent in urban, suburban (also known as rural) a highway (also known as motorway) settings.

Emissions under a broad variety of operating circumstances are difficult to recreate in the laboratory, but that analysis can be provided by PEMS, which is a helpful tool for inventories in the automobile companies (e.g., large road gradients, strong accelerations, and variations in the altitude). The use of PEMS has increased over the past few years and it will continue for many reasons, including the fact that they are required under EU regulation as monitoring analyses [28,29]. However, even with all the benefits that PEMS provides, this system is not superior to laboratory analysis in all the requisites. For example, it has a lower accuracy, it is only possible to measure a limited number of gases and the response time is slower. Furthermore, there is a possibility that there will be a breakdown in communication between the computer and the onboard computer. For these reasons, the data obtained by the different measurement techniques needs to be cross-referenced, so that measurements may be optimized [30–32].

All in all, the main benefit in that development is, for the industry and laboratories involved, to be able to measure the closest of real conditions emissions that are being produced by the vehicles. This will allow them to respond more quickly to the regulatory norms and to be able to correct its failure. Nevertheless, even though air quality in Europe has improved over recent decades, it is important to keep a close eye on pollutant evolution, source and treatment. Thus, EURO 7 is currently being prepared, it is in process of acceptance by the commission that should be done in 2022 and its possible implementation is expected until 2025. The general purpose of EURO 7 evolves in the same direction, in order to decrease the pollutant emissions and limit as much as possible the probability of frauds and disobedience of the regulations [33,34].

2. Diesel after-treatment technologies : focus on NO_x technologies.

Environmental regulations for atmospheric pollution from automobile exhaust are continually becoming stricter. The development of innovative approaches to reduce pollutant emissions from automotive exhaust engines are strongly required. There are two ways to control NO_x: before and after the combustion, but the current levels required can only be reached through post-combustion methods, which are called "after-treatment systems" [5,35,36]. In the case of diesel engines, whether they are heavy or light, operating under lean-burn conditions (excess of oxygen in the exhaust), the current technologies are however more complex and required different bricks in order to control the amount of emitted pollutants. In particular, diesel vehicle engines must be equipped with a complex exhaust after-treatment system (Euro 6 emission standards), including a diesel oxidation catalyst (DOC) to oxidize NO, CO and unburned hydrocarbons, a Selective Catalytic Reduction system (SCR), which targets the reduction of NO_x to N_2 with urea, and a Diesel Particulate Filter (DPF). An example of the most widespread vehicle manufacturer's diesel exhaust after-treatment systems is illustrated in Figure I. 3. Note that sometimes the SCR is combined with Lean NO_x Traps (LNT) that firstly promote NO_x storage and then its reduction. Their position in exhaust line depend on their purpose, i.e. the target pollutants, chemical processes and operating temperature. Other processes also can be added in order to reinforce the system as filters and traps, and even Exhaust Gas Recirculation (EGR) valves.

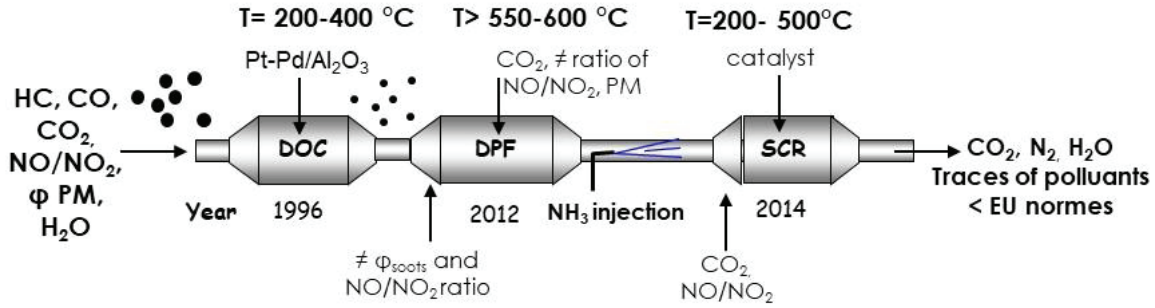

Figure I. 3. Exhaust after-treatment systems, according to Euro 6 emissions standards.

2.1. Diesel Oxidation Catalyst (DOC).

Oxidation catalysts were the initial after-treatment technologies used to remediate exhaust automobile emissions. The main function of DOC is the oxidation of unburned HC, CO and NO [5,37,38]. Nevertheless, the DOC catalysts also makes feasible to decrease the diesel particulate mass emissions by oxidation of a part of the organic fraction present on soot

carbon particles (soluble organic fraction (SOF) components), Figure I. 4 [5,37,38]. The most common diesel oxidation catalytic systems are consistent in a non-filter-based open ceramic monolith, Figure I. 4, which serves as a support for the DOC catalyst, normally containing noble metals dispersed onto a high surface area "washcoat" (hundreds of m^2/g). Indeed, the monolith support is coated with the above-mentioned "washcoat", commonly constituted by a combination of oxides such as alumina (Al_2O_3), ceria (CeO_2) and zirconia (ZrO_2) and then, the active catalytic metals (notably, nobles metals such as platinum (Pd), palladium (Pt) or rhodium (Rh)) are deposited through the washcoat's porosity [37,39,40].

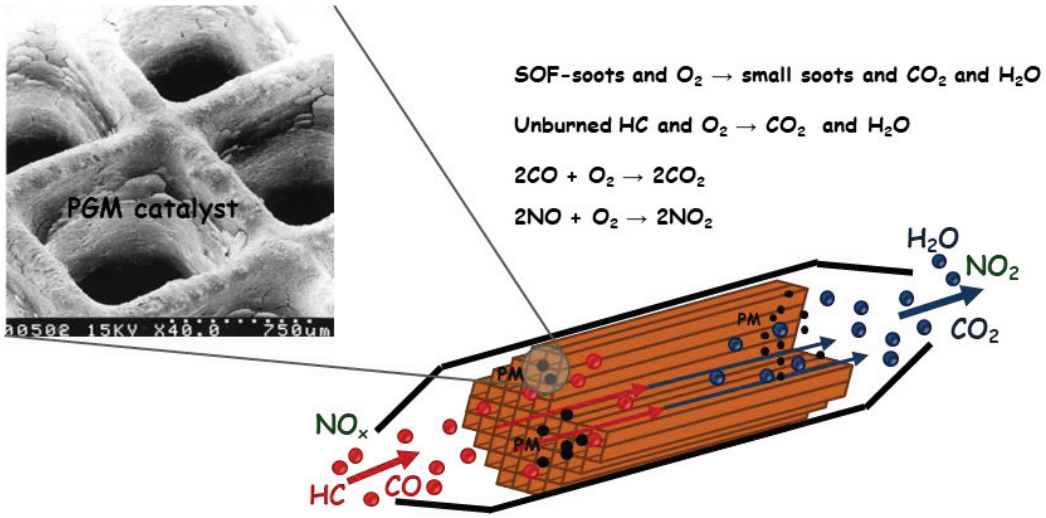

Figure I. 4. Diesel oxidation flow through monolith catalyst [5].

Thus, under lean-burn conditions in diesel engines, the DOC catalysts containing noble metals provide high oxidation activity for unburned HC, CO and SOF-soot to mainly form CO_2. Moreover, the oxidation of NO to NO_2 also occurs, which is essential for the correct functioning of downstream after-treatment systems, like the DPF and the SCR catalyst [37]. Thus, the three main reactions that takes place on DOC catalysts are the following ones:

$$C_nH_{2m} + (n + m/2)\ O_2 \rightarrow nCO_2 + mH_2O \quad (1)$$

$$CO + ½\ O_2 \rightarrow CO_2 \quad (2)$$

$$NO + ½\ O_2 \leftrightarrow NO_2 \quad (3)$$

However, the undesirable oxidation of SO_2 to SO_3 can also occur, which may react with water, leading to the formation of sulphates and sulfuric acid compounds (reactions (4) and (5)). These compounds can give rise to the catalyst aging, decreasing the overall depollution efficiency of the after-treatment system, and therefore casing harmful environmental and human health effects [37,41].

$$2\ SO_2 + O_2 \rightarrow 2\ SO_3 \quad (4)$$

$$SO_3 + H_2O \rightarrow H_2SO_4 \quad (5)$$

2.2. Diesel Particulate Filter (DPF).

As it was previously mentioned, the DOC catalytic systems allow the abatement of a part of the soluble organic fraction present on soot carbon particles. As a consequence, soot or particulate matter (PM) emissions have been reduced and mainly constituted by a large quantity of small particles, making necessary the incorporation of a specific technology to filtrate the PM. That effective abatement of soot requires the employment of filters that allow trapping the solid portion of PM from diesel exhaust. The Diesel Particulate Filter (DPF) is the most effective system, widely applied to a diesel engine due to the high filtration efficiency (> 98%) [42], which is essential to meet Euro emissions regulations.

DPFs are usually made of a porous material such as cordierite ($2MgO\text{-}2Al_2O_3\text{-}5SiO_2$) or silicon carbide (SiC), with thin longitudinal channels that are alternately blocked at the end, Figure I. 5 [43]. As a result, the exhaust gas is forced to pass through the porous channel walls. However, if the PM is too large to pass through the walls, it will accumulate in the inlet side of the DPF, generating a back pressure from the filter on the engine, which will reduce the engine efficiency [5]. Hence, a periodical regeneration of the DPF by soot total oxidation to CO_2 and water is required to control the pressure drop and prevent the DPF degradation. Indeed, the accumulating particles have to be continuously or periodically burned out of the DPF. However, the average temperature of the exhaust gases from a diesel engine is between 200 and 500 °C, which is lower than that generally required for the combustion of soot. In other words, temperatures greater than 600 °C are essential in the DPF for the total oxidation of soot [42]. To circumvent these issues, two types of regeneration processes, known as active regeneration [44,45] and passive regeneration [46], are commonly applied.

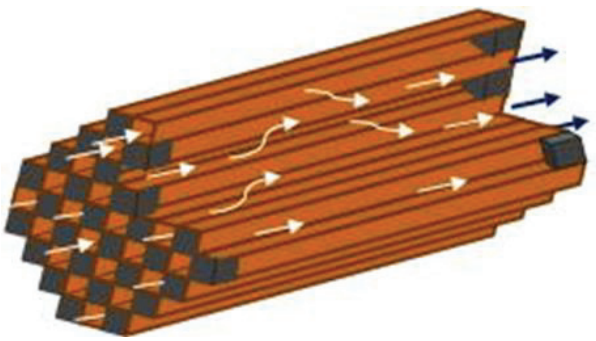

Figure I. 5. Diesel particulate filter.

Active regeneration

In the first regeneration process, the excessive accumulated soot is periodically removed through a controlled oxidation with O_2 in excess, which is already present on the exhaust gas. This active regeneration of soot, represented here as carbon (C), is carried out by the following reactions:

$$C + O_2 \rightarrow CO_2 \quad (6)$$

$$2\,C + O_2 \rightarrow 2\,CO \quad (7)$$

However, the heat required to oxidize PM comes from external sources, such as an electric or microwave heater, a flame-based burner, fuel injection in the exhaust, *etc.* Note that the previous DOC catalyst can also be used as a mean for increasing the DPF temperature [47]. Thus, regardless the specific strategy used as active regeneration, an additional energy input, quite high, is always required to heat the exhaust and the DPF system, which increases the production cost of the system. Moreover, the overheating regeneration temperatures close to the melting point of the DPF might compromise its integrity [48,49]. Due to these unfavorable consequences, active regeneration is not the preferred option for the regeneration of the DPF.

Passive regeneration

In the passive regeneration process, named Continuously Regenerating Trap (CRT) [5], Figure I. 6 (a), the oxidation of soot occurs between 250 and 500 °C in the presence of NO_2, which can be formed on the Pt-based DOC catalysts, as was previously mentioned, by the following reactions:

$$C + NO_2 \rightarrow CO + NO \quad (8)$$

$$C + 2\,NO_2 \rightarrow CO_2 + 2\,NO \quad (9)$$

Thus, a previous oxidation step will be first carried out to convert the NO that is already present in the exhaust gas into NO_2, which is a more powerful oxidant than oxygen. The later can take place, as previously mentioned, during DOC step. Nevertheless, an additional Pt catalyst, named Catalyzed Continuously Regenerating trap (CCRT), is sometimes directly coated within the DPF in order to enhance the effectiveness of the regeneration process by NO_2 [50], Figure I. 6 (b).

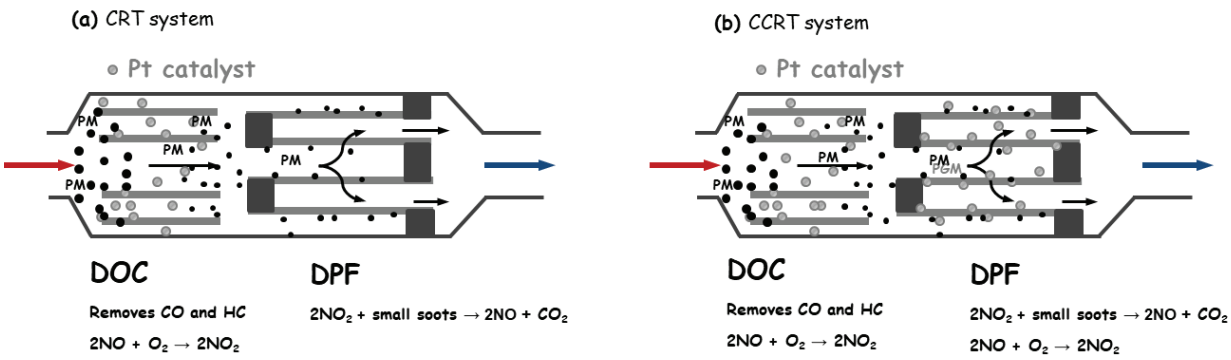

Figure I. 6. Passive soot regeneration by (a) CRT and (b) CCRT systems.

2.3. Technologies for NO_x abatement.

Two NO_x reduction technologies have been selected by vehicle manufacturers: lean NO_x trap (LNT) [51] and Selective Catalytic Reduction (SCR) performed notably by using ammonia as a reductant [52,53]. The aim of both technologies is to reduce NO_x in the gaseous automobile exhaust to harmless N_2, in order to meet the European emission standards. Note that the Exhaust Gas Recirculation (EGR) valve can also be used as auxiliary step for diesel engines to control NO_x emissions [54,55]. This latter methodology provides a second opportunity to clean the exhaust gases after the fuel has been burned. Thus, part of the exhaust is reintroduced into the combustion chamber, where is combined with new air during the intake stroke, that dilutes the O_2 in the inlet air stream and provides inert combustion gases. The later act as heat absorbers of combustion, reducing the cylinder temperature, which leads to lower NO_x levels. However, the fall in temperature inside the cylinder will reduce the efficiency of the combustion process, which results in an increase of unburnt HC and CO emissions [4]. For these reasons, the environmental standards cannot be achieved using the EGR after-treatment system alone.

- ***Lean NOx Traps (LNT)***

The LNT, also known as NO_x storage reduction (NSR), represent a promising technology that was implemented before NH_3-SCR [56]. The idea of LNT after-treatment system is based upon the storage and abatement of NO_x on a NO_x storage catalyst, which is also coated on a monolith and present specific acid-base and redox properties. Note that the LNT after-treatment system is generally placed upstream of the DPF because it needs reducing agents, which can remain trapped in the DPF, Figure I. 7 (a). Indeed, during the lean-burn period, NO is converted to NO_2, which is then stored on an alkaline earth oxide (such as barium oxide) in the form of nitrate species, reaction (10). The stored NO_x will be then desorbed during

intermittent rich/stoichiometric periods and reduced by hydrogen (H_2), CO or HC to N_2 over a Platinum group metals (PGM) catalyst, Figure I. 7 (a) and (b) [51,56–58].

$$BaO + 2\ NO_2^* + O^*\ Ba(NO_3)_2 \quad (10)$$

The most popular LNT catalyst is based on $Pt/BaO/Al_2O_3$ [59,60]. Nevertheless, other noble metals like Pd and Rh are also used. In this configuration, the role of the noble metal is essential to provide the required catalytic redox properties, firstly to oxidize NO in NO_2 and secondly to reduce NO_2 to N_2 [60].

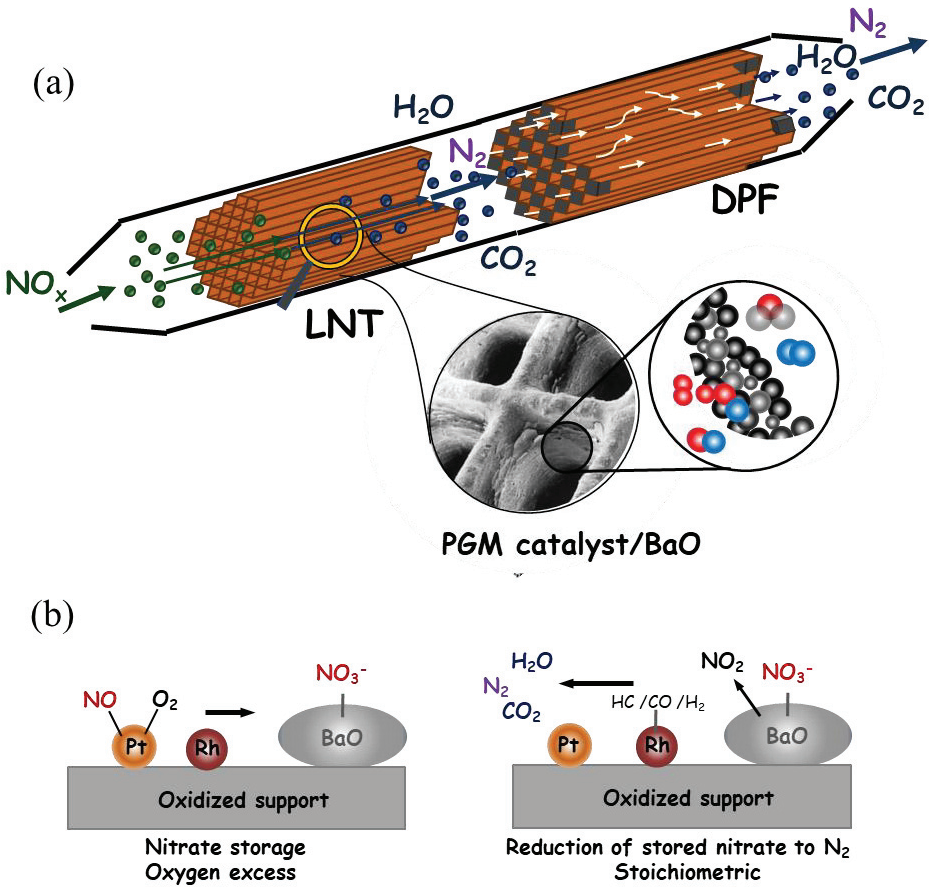

Figure I. 7. (a) Lean NOx Trap technology [5] and (b) Simplified mechanism of LNT catalyst containing Pt, Rh and BaO as active phases.

Although this first technology to NO_x abatement provides several advantages, from an economical point of view, the use of a significant amount of noble metals as well as the high amount of fuel consumption (notably during the intermittent rich periods) are not in favor of this technology. Moreover, like in the DOC catalysts, the LNT catalyst can be poisoned by sulfur compounds already present in the diesel exhaust. The formation of barium stable species such as $BaSO_4$ is indeed favored notably at high temperature, which will greatly reduce the performance of the LNT catalyst, reducing its ability to store NO_x [61,62].

- ***Selective Catalytic Reduction (SCR)***

The SCR is a proven NO_x abatement technology, which was initially applied in stationary power plants and industrial installations producing exhaust gas under lean combustion conditions, and is now installed in most of mobile diesel engines [52,53,63]. In the case of mobile applications, SCR catalytic systems can selectively reduce NO_x emissions in the exhaust gas in the presence of excess of O_2 with a reducing agent (e.g., HC, CO, H_2, NH_3, urea, *etc.*) yielding N_2 and water [52,56,63–67]. To date, SCR technology has been extensively reviewed with different reducing agents, with special focus on the reaction mechanism and catalyst development, being the most studied ones NH_3/urea and HC. Metal oxides (mainly Ag/Al_2O_3), Cu-ZSM-5 and Pt-based catalysts have been found to be active and hydrothermally stable for the HC-SCR catalytic reaction [52], where propane, octane and decane hydrocarbons are used as reductants. However, this technology exhibits poor selectivity towards N_2, inhibition by the high steam content and low-temperature activity [52]. Hence, it is considered that NH_3-SCR performed via Adblue® (precursor of ammonia) injection is the most used technology for NO_x abatement on account of its high efficiency, selectivity to nitrogen and wide operating temperature window [52,53]. The NO_x reduction efficiency is higher than 90% over a wide operating temperature window (200-450 °C). Note that the storage of NH_3 is not possible inside the vehicle due its toxicity, corrosive and flammability issues. To avoid these issues, the ammonia is in-situ obtained from a solution of urea, commercialized as AdBlue® in Europe. This solution contained a mixture of 32.5 %wt. of urea $(NH_2)_2CO$ and 67.5 %wt. of pure water. Thus, the first step of the NH_3-SCR process is the decomposition of urea into ammonia. Ideally, the ammonia formation process follows two reactions with the formation of isocyanic acid (HNCO) as intermediate. First, the thermolysis takes places as a result of pure water vaporisation, melting the solid urea [68].

$$(NH_2)_2CO \rightarrow NH_3 + HNCO \quad (11)$$

Then, the intermediate of isocyanic acid is converted by hydrolysis into NH_3 and CO_2 [68,69]:

$$HNCO + H_2O \rightarrow NH_3 + CO_2 \quad (12)$$

A temperature higher than 180 °C is required to complete urea decomposition by reactions (11) and (12), which is one of the reasons why urea SCR system has difficulty dealing with low temperature NO_x performance.

In an oxidizing environment, several chemical reactions can occur during the NH_3-SCR process depending in particular on the NO/NO_2 ratio, the main ones being:

$$2\ NH_3 + 2\ NO + 1/2\ O_2 \rightarrow 2\ N_2 + 3\ H_2O\ (13)\ \text{- Standard SCR}$$

$$2\ NH_3 + NO + NO_2 \rightarrow 2\ N_2 + 3\ H_2O\ (14)\ \text{- Fast SCR}$$

$$4\ NH_3 + 3\ NO_2 \rightarrow 7/2\ N_2 + 6\ H_2O\text{-}\ (15)\ \text{- } NO_2\text{-SCR}$$

It is well known that more than 90% of NO_x in diesel exhaust is usually composed by NO. Therefore, the equation (13), so-called Standard SCR will be the main SCR reaction with NH_3. This reaction implies a 1:1 stoichiometry for ammonia and NO, and the consumption of oxygen. On the other hand, when equimolar amounts of NO and NO_2 (1:1 $NO:NO_2$ ratio) are presented in exhaust gas, the so-called Fast SCR takes place (equation (14)), which is much faster than the Standard SCR reaction. Finally, if only NO_2 is presented in the exhaust gas, i.e. the NO is completely consumed, the reduction process is denoted NO_2-SCR, equation (15). Thus, the efficiency of NH_3-SCR catalytic process is strongly related to the NO/NO_2 ratio, in which the efficiency of the DOC after-treatment plays a role of paramount importance.

On the other hand, nitrous oxide (N_2O) can conversely be generated as an undesirable byproduct in NH_3-SCR systems, mainly following the reactions [52,70]:

$$2\ NH_3 + 2\ NO + O_2 \rightarrow N_2O + N_2 + 3\ H_2O\ (16)$$

$$2\ NH_3 + 2\ O_2 \rightarrow N_2O + 3\ H_2O\ (17)$$

$$NH_4NO_3 \rightarrow N_2O + 2\ H_2O\ (18)$$

Moreover, at higher temperatures, the undesirable oxidation of NH_3 to NO can also take place, which limits the overall NO_x conversion [63,71].

$$4\ NH_3 + 5\ O_2 \rightarrow 4\ NO + 6\ H_2O\ (19)$$

Nevertheless, it is well known that the catalyst is the key for the SCR reaction. It is important to recall that a relevant NH_3-SCR catalyst needs to ensure a dual function for the reduction of NO_x to be efficient: the support should present intrinsic acidic properties, while the active metal sites should possess redox properties [52,53,72]. The acidity of the support, of Lewis and Brønsted type, is critical to activate NH_3 by providing sites for NH_3 adsorption. The transition metal phase plays an important role for activating NO_x by catalyzing the NO oxidation ($NO + O_2 \rightarrow NO_2$) and the subsequent formation of surface NO_x adsorption complexes [52,53]. In the last decade, strong efforts have been paid to find efficient NH_3-SCR

catalysts and to maintain high efficiency over the largest possible temperature window. Moreover, the target catalysts need to exhibit high hydrothermal stability, together with a high selectivity towards N_2 in such temperature window.

3. NH_3-SCR catalysts.

The early SCR catalysts were composed of noble metals, which presented high performances for NO_x reduction at low temperature. However, these noble metal-based catalysts are no longer effective because they oxidize completely ammonia at low temperature (around 250 °C) [56]. In addition, other drawbacks of these catalysts are of course their high cost and the possible formation of N_2O [56,73]. In the 1970s, more economic and highly durable vanadium and titanium oxide mixtures (V_2O_5/TiO_2) catalysts were developed, which presented adequate activity at intermediate temperatures, particularly for stationary source emissions [74–76]. V_2O_5 constituted the active component in this common catalyst, which also includes TiO_2 as a support and tungsten or molybdenum oxide (WO_3 or MoO_3) as a promoter. The promoter acts to increase the number of acid sites, while decreasing the reactivity to oxidize SO_2 into SO_3 [77,78], which is the reason why these catalysts had a superior resistance to sulphur and therefore, good tolerance to lubricant poisoning [63,79]. Although these catalysts presented a high activity for NO_x reduction at the intermediate temperature range (300-400°C), both the activity and N_2 selectivity fall around 450 °C [80,81], Figure I. 8, and N_2O is also formed during the NH_3-SCR reaction [82,83], which requires an optimization in terms of vanadium composition. Note that in Figure I. 8 (a) the V_2O_5-WO_3/TiO_2 catalysts were indeed aged at low temperature because of their low thermal stability [80]. Together with this low thermal stability, the major issues of V_2O_5-WO_3/TiO_2 catalysts are related to their durability in terms of activity and selectivity, Figure I. 8 (b) [63,80,81,84–87], which has been explicitly considered as a drawback of its application. Moreover, around 500 °C, V_2O_5 begins to sublimate, which drastically reduce the catalytic performance and gives rise to the formation of highly toxic species, which are released through the exhaust gases [88]. For these reasons, such catalysts, which remain extensively used for stationary sources (power generation units) [75,76], are less effective for automobile exhaust removal applications, in which a good hydrothermal stability and durability are required. This feature is of paramount importance in view of the further implementation and commercialization of catalytic systems for the NH_3-SCR technology, since: i) water (steam) is one of the main products emitted from internal combustion engines, and ii) the exhaust temperature can reach over 700 ºC on account of the above-mentioned DPF

regeneration step [89]. However, the hydrothermal stability of these catalysts is still a concern until now.

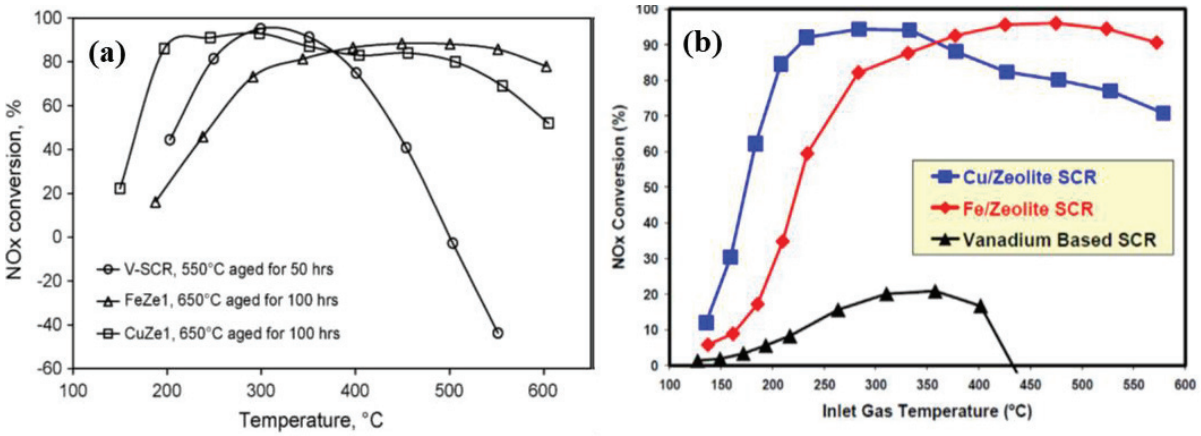

Figure I. 8. NO_x performance for Vanadium and zeolite SCR catalysts in Standard SCR reaction as a function of temperature after : (a) aging at different temperature [80]. Note that V_2O_5-WO_3/TiO_2 catalysts were aged at lower temperature than the others ones ; and (b) after aging for 64 h at 670 °C [63,90].

Hence, new catalysts thermally more stable must be designed and developed to overcome these issues. Thus, strong efforts have been paid in the last decade to find efficient NH_3-SCR catalysts and to maintain high efficiency over the largest possible temperature window. Metal-based zeolites have received much attention in these respects [52].

3.1. Zeolite-based NH_3-SCR catalysts.

The lack of thermal stability of V_2O_5-WO_3/TiO_2 in the exhaust gas removal made more advantageous to employ transition metals-based zeolites NH_3-SCR catalysts due to their higher activity for NO_x removal and low price [52]. Indeed, the crystalline aluminosilicate minerals, so-named zeolites, are promising materials for heterogeneous catalysis because of their well-defined crystallinity, porous structure (microporosity) and large interior surface. They are commonly constituted by a three-dimensional structure built up from TO_4 primary units forming $[SiO_4]^{4-}$ and $[AlO_4]^{5-}$ coordination polyhedral. The tetrahedron is indeed the primary building unit, Figure I. 9 (a). Thus, the T-atom of Si or Al are neighboring by four atoms of oxygen forming the above-mentioned TO_4 primary units [91], which are covalently assembled together in the corner by a shared oxygen atom, arranged into the secondary building units (sbus), Figure I. 9 (b). The framework of the zeolites is formed by repetition or assemblies of these secondary building units in different manners, giving rise to open microporous structures

(≤ 2 nm), in which the size of channel and pore opening is then variable [91,92]. To date, the International Zeolite Association (IZA) has recognized more than two hundred zeolites [93]. One of the most common differentiation between these different types of zeolite is based on the largest pore size opening of the zeolite framework structure: i.e. small pores such SAPO-34 (8-membered ring, ring dimensions of approximately 3.6 Å x 3.6 Å), medium such as ZMS-5 (10-membered ring, ~ 5.5 Å x 5.5 Å of ring dimensions), large and extra-large such as zeolite Beta and zeolite Y (12-membered ring or more with a membered ring of ~ 7.5 Å x 7.5 Å). These different sizes of pores and cavities will define the physico-chemical and structural properties of each zeolite for catalytic reactions in terms of activity and shape-selectivity, controlling the passage of reactants or by-products, but also in terms of stability. Indeed, medium and large pore zeolites are less stable under severe hydrothermal conditions as compared to the smaller pore zeolites [94].

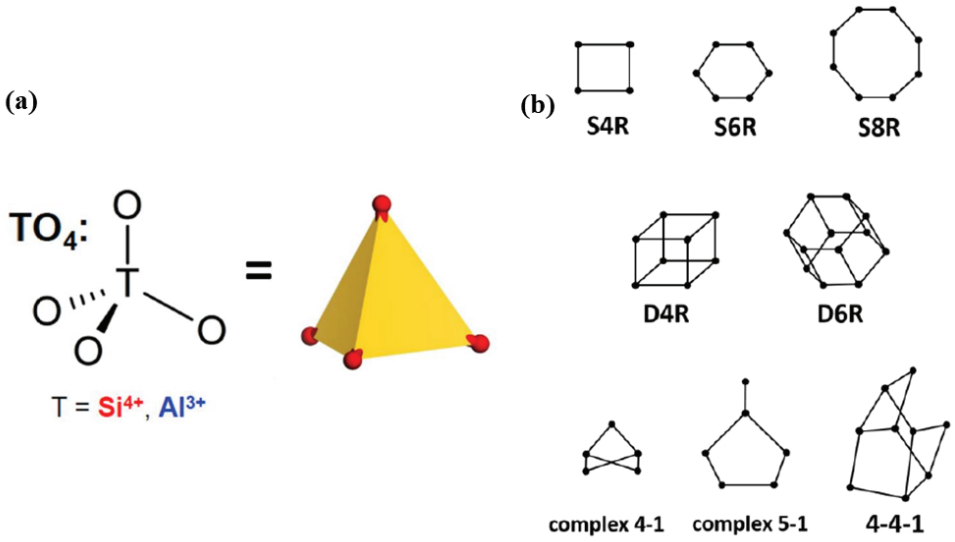

Figure I. 9. (a) TO_4 primary building unit of a zeolite and (b) Secondary building units (sbus) in zeolites [95].

Moreover, the negative charge related to Al^{3+} replacing Si^{4+} in the zeolite framework, provides the zeolites with both, acid properties and ion exchange capacity. The amount of aluminum in the zeolite framework is one of the most important parameters to control the acidity of the zeolites, increasing with the aluminum content [91,96]. Indeed, if the zeolite is only composed of SiO_4 units, the tetrahedral framework has a neutral charge. However, when Al-atoms are present or included, the framework will be negatively charged because of the charge difference between Si^{4+} and Al^{3+}. This negative charge can be then balanced by a counter ion in order to control the acid and redox properties of the zeolite materials. Thus, if the counter ion is a proton (H^+), the negative zeolite framework will stabilize and a bridging hydroxyl group

will be formed between the Si and Al atom, Figure I. 10. The formed hydroxyl group is known as a Brønsted acid site because a proton can be transferred from the site. Note that Brønsted acid sites are one of most important sites of adsorption of NH_3, as it was previously mentioned, which is crucial for NH_3-SCR reaction [52,53,72]. On the other hand, if transition metals, such as iron (Fe) or copper (Cu), which are the most common metals-based phases used for NO_x abatement by NH_3-SCR reaction, are exchanged, the zeolites can also function as redox catalysts. Thus, the special features of the zeolite-based materials are their adjustable acidic properties and their ability to stabilize transition metal redox couples such as Cu^+/Cu^{2+} and Fe^{2+}/Fe^{3+}, providing a dual function for the reduction of NO_x: intrinsic acidity and redox properties [52,53,72].

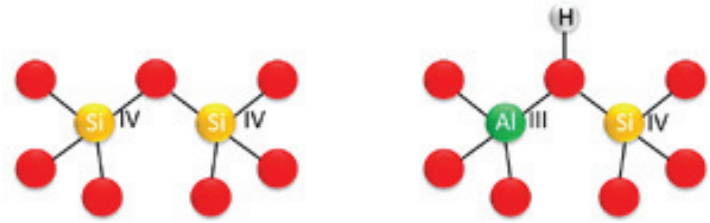

Figure I. 10. Stabilization of negatively charged zeolite framework by a proton: Brønsted acid site [95].

Thus, the crystallinity, microporosity and high internal surface area, in addition to the unique ion exchange and acidic properties of zeolites, make them good candidates to be used as catalytic supports for NH_3-SCR reaction.

Since 1986, Cu-/Fe-transition metals-based zeolite catalysts have been studied for the SCR reaction, starting by the work of Iwamoto et al. [97] related with Cu-based ZSM-5 medium pore zeolite SCR catalyst, and it has continued through the last three decades [53,98]. Thus, several large and medium pore zeolites have been used for this purpose, like mordenite (MOR) and beta (BEA) and ZSM-5 (MFI) and ferrierite (FER), respectively, between others. The zeolite-based catalysts had indeed a better hydrothermal stability in comparison with the vanadium oxide-based catalysts, Figure I. 8 (b) [63,81]. However, they are still limited, notably in terms of durability when they are aged at high temperature, which can give rise to the zeolite-based catalyst deactivation, Figure I. 11. Indeed, the deactivation of these SCR catalysts by hydrothermal treatment can be attributed to several phenomena (dealumination, sintering or thermal collapse), being the loss of NH_3 storage capacity due to zeolite dealumination considered the major cause of catalyst degradation [63,94,98–101].

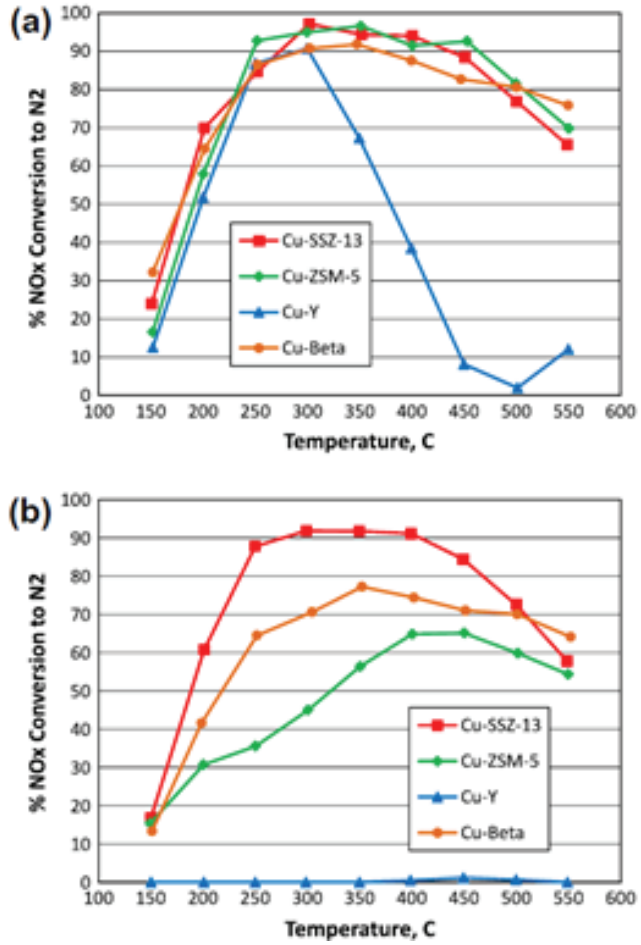

Figure I. 11. Comparison of NO_x conversion over Cu/zeolites (a) fresh and (b) after hydrothermal aging under Standard NH_3-SCR conditions [94].

3.2. CHAbazite-based zeolites as catalysts for NH_3-SCR reaction.

In order to improve the hydrothermal stability of the NH_3-SCR catalysts, a new generation of zeolite-based materials with a chabazite (CHA) structure, which features small pores (~3.8 Å), has emerged. Silicoaluminophosphate SAPO-34 and aluminosilicate SSZ-13 are the most popular CHA-zeolites [102]. The chabazite structure is composed by a succession of tetrahedral SiO_4 and AlO_4 units in SSZ-13, or SiO_4, AlO_4 and PO_4 units in SAPO-34 [103,104]. Note that this thesis manuscript is focused on SAPO-34 CHA-based zeolites. Thus, it's important to mention that the $[AlO_4]^{5-}$ and $[PO_4]^{3-}$ tetrahedral are the fundamental units to create the aluminophosphates (AlPOs) structure. Many zeolites can be derived from AlPOs by the incorporation of other T-atoms to the framework, such as Si, Co, Zn, Mg and Mn [104]. In the case of SAPO-34, a first aluminophosphate structure ($AlPO_4$) is formed and then the Si atom is incorporated in the structure forming a silicoaluminophosphate zeolite framework. Moreover, it's worth to mention that the CHA framework is composed of double six-membered

rings (6-MR, forming a hexagonal cage) linked by 4-member rings (4-MR) to form cavities with eight-membered windows (8-MR) who feature small pore sizes (~3.8 Å) [105,106]. This architecture consequently forms a unique organization by the interconnection of 8MR, 6MR and 4MR, Figure I. 12.

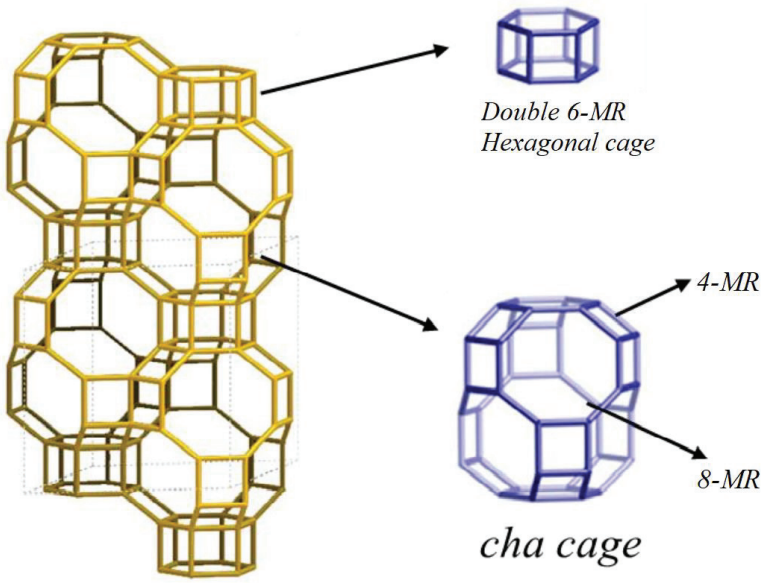

Figure I. 12. CHAbazite framework and building units [107].

These CHA-zeolites have been successfully used for several applications, mainly for separation purposes (CO_2/CH_4 or propane/propene) and catalysis (methanol-to-olefins, cluster encapsulation). Recently, BASF researchers have reported that aluminosilicate CHA loaded with Cu shows excellent activity for the SCR of NO_x, and more importantly, a higher hydrothermal stability than Cu-exchanged zeolites with medium and large pores [108]. The hydrothermal stability, in terms of preserved NH_3-SCR catalytic activity, of Cu-based SSZ-13 CHA-based catalyst is clearly observed in Figure I. 11 (b) compared to that observed for Cu-based medium and large pore zeolite catalysts. Indeed, it is well known that the small pore size on conventional microporous CHA zeolites impedes their structural dealumination (hence leading to high hydrothermal stability) since the hydrolysis phenomena between the structure and water molecules decrease [9,109–111]. Moreover, the superior performance of chabazite-based catalysts seems to be due to the narrow pores that allow the creation of a $[NH_4^+{}_x][NO]$ complex, which is one of the key intermediates in the NH_3-SCR process [112,113].

For an optimal hydrothermal stability, the structure and pore size of zeolites is indeed crucial. Nevertheless, the available Brønsted acid and ion exchanged sites play a crucial role in the NH_3-SCR reaction, in a similar way than that for medium and large pore zeolites.

Brønsted acid sites in SAPO-34 CHA-based zeolites are generated, as in the other zeolites, by proton (H^+) substitution and zeolite charge compensation, forming a bridging hydroxyl group. However, in this case, the negative charged zeolite framework, and so the creation of Brønsted acid sites, is related to substitution of P or Al by Si. Thus, the SAPO-34 zeolite acidity depends on the manner that Si is coordinated in the zeolite framework and the charge provided after its integration [114]. Thus, several substitution mechanisms can take place, Figure I. 13 [115–118].

SM1 - $Al^{3+} \rightarrow Si^{4+}$: An atom of Al is substituted for an atom of Si, leading to the formation of a Si-O-P bridges, which seem to be energetically unstable. This instability may be attributed to the existence of two positive charges [119,120].

SM2 - $P^{5+} \rightarrow Si^{4+} + H^+$: When P-O-Al is converted to Si-OH-Al, a P is replaced for a Si, forming Brønsted acid sites.

SM3 - $Al^{3+} + P^{5+} \rightarrow 2Si^{4+}$: Framework Al and P are replaced by two Si, forming undesired Si-islands without formation of Brønsted hydroxyl groups. These Si-islands could have adverse impacts on the acid properties and on the hydrothermal stability of the zeolite, eventually leading to the deactivation of the material when used as a catalyst [121–124].

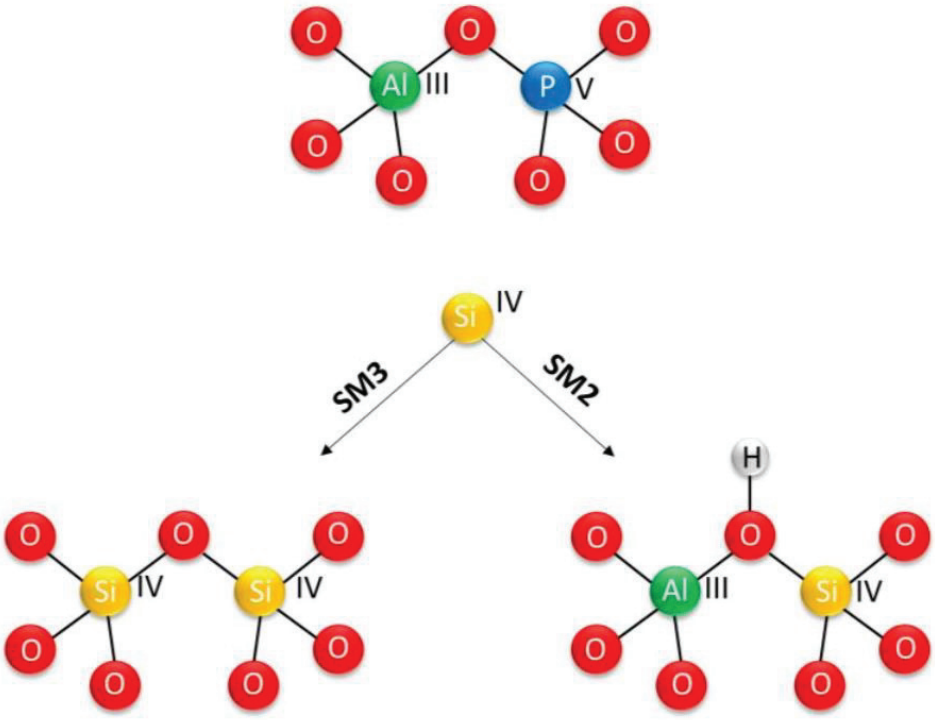

Figure I. 13. Schematic of the substitution mechanisms that commonly take place in SAPO-34 CHA-based zeolite [95].

The NH_3-SCR catalytic activity can be related with the strength of these Brønsted acid sites, and their location on the zeolite framework, strongly affecting their affinity to interact with NH_3 [117,122,124]. In particular, the surface or external hydroxyls, T-OH (with T = Si, Al and P) and the hydroxyl groups in the structure's defects present weak NH_3 interaction, whereas bridging hydroxyl groups, T-OH-T (with T = Si, Al and P) (e.g.: Si-OH-Al) have a moderate to strong interaction with NH_3. The second nature of active sites are the Lewis acid sites, produced by the framework Al and implemented transition metal species (notably Cu or Fe ions). As it was previously mentioned, they represent the redox species of the catalyst, and their synergy with the Brønsted acid sites will be determinant for the NH_3-SCR performances.

Thus, following these pioneering works of BASF researchers [108], a wide variety of fundamental and applied studies have been focused on CHA-zeolite catalysts, especially Fe- and Cu-loaded SAPO-34 and SZZ-13 in view of the NO_x abatement by NH_3-SCR [72,117,121,122,124–127]. Cu-loaded and Fe-loaded CHA-zeolites have superior SCR activity at low (<300°C) and high (>300°C) temperatures, respectively, Figure I. 14 (a). It is generally believed that the poor SCR activity for Fe-loaded zeolite-based catalysts at low temperature is due to NH_3 inhibition [52,128]. In the case of Cu, more N_2O is produced and SCR performance decays after prolonged hydrothermal treatment or more severe aging conditions (850 °C), mainly due to the undesirable non-selective NH_3 oxidation (previous equation (17)) catalyzed by CuO_x species [124]. Nevertheless, some previous studies showed the impact of the hydrothermal treatment on the migration of Cu species on conventional microporous Cu-loaded CHA-based zeolite catalysts [124,129–132]. Generally, it has been observed that after the hydrothermal treatment, CuO_x species re-disperse to occupy the ion-exchange sites in the CHA crystal framework, leading to the production of isolated Cu^{2+} species located in the six-membered rings of Cu-CHA catalysts. These latter have been indeed identified by many authors as a key catalytic active phase for the NH_3-SCR process [72,133–135]. However, with Fe, a good SCR activity is maintained at high temperature, and N_2O production is low [52,70,125]. The absence of N_2O yield over most Fe-loaded zeolite catalysts can be attributed to the N_2O decomposition and N_2O-SCR reactions [70,125]. However, Fe-loaded zeolites-based catalysts present some important drawbacks: some undesired Fe species (isolated cations or Fe-oxide particles) can be produced during the synthesis process depending on the zeolite structure, Si/Al ratio, iron content and aluminium distribution [136]. In addition, at high temperatures under hydrothermal conditions, they suffer dealumination caused by the iron coordination to inactive

oxide species. Thus, both Cu and Fe-based catalysts presented complementary properties in terms of the NH_3-SCR catalytic activity, selectivity and stability.

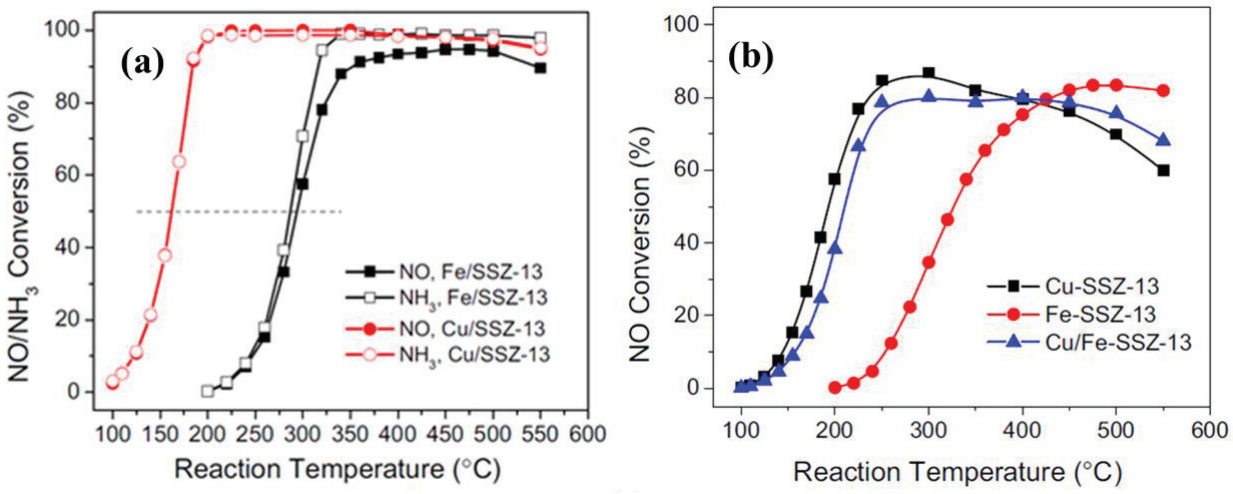

Figure I. 14. (a) NO/NH_3 conversions as a function of temperature over fresh Cu- and Fe-CHA-based catalysts (b) NO conversions as a function of temperature over hydrothermally treated Cu- and Fe-CHA-based catalysts and mixed (1/1) catalysts, during Standard NH_3-SCR. *Reaction conditions: 350 ppm NO, 350 ppm NH_3, 14% O_2, 2.5% H_2O balanced with N_2 at a GHSV of 200,000 h^{-1}* [125].

Combining Fe and Cu in CHA-zeolites appears naturally promising to take benefit of all advantages *i.e.,* to achieve durability, activity and N_2 selectivity in a large window of exhaust temperatures. Up to date, only few studies have explored this route. The use of a mixture and dual layer configuration of Cu- and Fe-loaded CHA-zeolite for NH_3-SCR has been reported at Pacific Northwest National Laboratory [125] and Chalmers University in collaboration with Ford Motor Company [126]. While an improved SCR performance in a large temperature range was claimed, the NO_x efficiency was only demonstrated at high temperatures and seems to be an average of the performance of individual zeolites catalysts, Figure I. 14 (b). At low reaction temperature on the contrary, the activity of the Cu-loaded CHA-zeolite is still limited. The incorporation of Fe cations in Cu-loaded CHA-zeolite to form bimetallic catalysts has been also recently considered by research groups in Tianjin, Beijing, and Oak Ridge National Laboratories [137–139]. However, the NO_x efficiency at low temperature was considerably lower compared to the corresponding Cu-loaded CHA-zeolite and even in the best case, the improved low temperature activity due to the proximity of Fe and Cu atoms, showed a moderate drop after hydrothermal aging. So far, the improvement of hydrothermal stability and NO_x efficiency at low temperature of Cu-loaded CHA zeolite remains a great challenge.

Among other reasons, this low NO_x efficiency at low temperature could be ascribed to the small pore size of CHA-zeolite, which strongly hinders the access of reactants to the catalytic active sites [138,140]. The kinetic diameters of NH_3-SCR reactants and by-products are presented in Table I.3. Considering the progress and further implementation of upgraded engine technologies together with the expected gradual fuel efficiency enhancement [141], this is a critical limitation so far of this kind of catalysts since the engine-exhaust temperatures are expected to drop sharply [142]. In addition, under "cold-start" operating conditions, the exhaust temperature is much lower compared to that "on-road". However, in such low temperature window, the above described Cu-CHA-based catalysts do not seem to exhibit sufficient activity to efficiently reduce NO_x [142]. Thus, the small pore size of CHA-zeolite has multiple advantages: pores represent well-defined sites for ion exchange, so highly dispersed and coordinately unsaturated cations can be obtained in these pores. These cations allow to reach the needed acidity to the active sites and the catalyst exhibits higher hydrothermal stability [126]. Despite these advantages, such zeolite channel structure might be unfavourable to high catalytic performance at low temperature. Indeed, intracrystalline diffusion limitations have been reported for NH_3-SCR over Cu-loaded CHA and Fe/Cu-loaded CHA-zeolite catalysts, mainly at low temperatures [127,138]. These reports suggest that it is difficult, with the CHA system, to improve activity by structure optimisation, as mass-transfer here is complex and its control still requires further work and understanding. As a result, automobile manufacturers are forced to improve the current after-treatment systems and to develop new catalytic materials or concepts that can meet current and future emission standards. The development of hierarchical zeolites with structured and ordered micropores and mesopores could be a promising solution to overcome such issue.

Table I.3. Kinetic diameters of reactants and products observed in NH_3-SCR reaction.

Molecules	H_2O	N_2	O_2	NO_2	NH_3	NO	N_2O	He	**Average diameter of CHA cages (6MR, 8MR)**
Kinetic diameter (nm)	0.265	0.364	0.346	0.240	0.260	0.317	0.330	0.260	**0.460**

4. Advanced SCR catalysts to ensure low and high temperature activity for NO_x removal.

4.1. Hierarchical meso-microporous CHA zeolite-based catalysts.

In this section we present the hierarchical zeolites, which include at least two types of pore sizes [143,144]. Thus, an improved reactant transfer can be achieved by extending the pore size of the CHA-zeolite-based catalysts [144,145]. In other words, introducing mesoporosity in the otherwise solely microporous CHA-zeolite-based catalysts is a promising solution to improve low-temperature NH_3-SCR activity. This approach could make active sites within the zeolite structure more accessible for reactants, permitting a better mass transport while keeping molecular sieving ability [146,147]. The resulting hierarchical structures should improve reactant diffusion and, as a consequence, NO_x efficiency. In the last decade, several strategies have been successfully developed to synthesize hierarchical porous aluminosilicate zeolites, and several reviews have been reported on the advances made in this field [144,145,147–151]. Among them, the most employed are: i) the post-treatment method, that relies on leaching Al or Si cations of pre-made zeolite framework, and ii) the hard-templating and soft-templating methods, i.e. hydrothermal crystallization methods in which a secondary organic structure direct agent (OSDA) or second larger template (such as nanocarbon and polymers, organosilanes and surfactants, respectively) is added in order to create the desired mesopores. Some details of these approaches to create hierarchical materials and their applications will be provided below.

Under the post-treatment method, the formation of mesoporous zeolites occurred by destructive dealumination or desilication leaching process, Figure I. 15, in which part of the pre-made crystalline zeolite is sacrificed to create larger external surface, i.e. the mesopores [149,152–155]. In particular, the dealumination post-treatment method is commonly accomplished by steaming or acid leaching. The term "steaming" refers to a hydrothermal treatment that is carried out at temperatures over 500 °C. Under these conditions, some Si–O–Al bonds will break, with the consequent leaching of Al cations of the pre-made zeolite framework. As a consequence, the less stable silicon species will move to different locations into the zeolite framework and can condense with silanols [146]. On the other hand, when the dealumination is done by acid leaching, organic acids such as oxalate or mineral acids such as nitric acid and hydrochloric acid are usually used [152]. The mesopores created by this methodology are based on isolated cavities rather than on interconnected mesopores [155,156]. For the desilication post-treatment method, on the contrary, a basic treatment of the calcined pre-made zeolite is performed by using notably NaOH [149]. This method is advantageous for

generating interconnected mesopores in zeolites, but it fails to generate abundant mesopores in large-particle-size crystals. Moreover, a strong leaching of Si leads to amorphization and can decrease the micropore volume and crystallinity of the bare CHA-based zeolite [149,157]. Moreover, the synthesis of crystalline and stable hierarchical zeolite by a post-treatment method is very complicated due to the instability of the framework structure under acid or alkaline treatment. This might also result in the destruction of Brønsted acid sites of the CHA zeolite, which are involved in NH_3 adsorption in the initial step of the NH_3-SCR reaction [148,158].

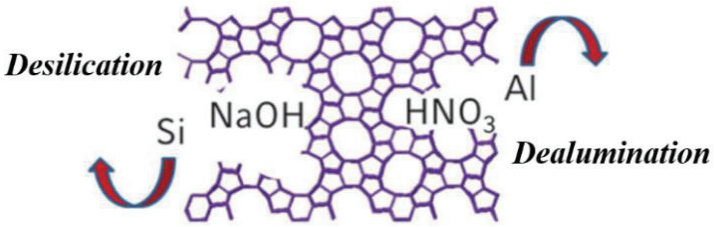

Figure I. 15. Post-treatment method: leaching Al or Si cations from pre-made zeolite framework [149].

In contrast, the creation of mesopores by hard-templating and soft-templating hydrothermal crystallization methods requires a secondary larger template (dual templating with micropores template). By adjusting these parameters, a high degree of control can be obtained on the hierarchical structure and morphology of the zeolite [148–150]. In particular, the hard-templating method uses solid substances such as polymers, biological materials, inorganic materials and carbonaceous materials as a mesopores template, Figure I. 16 [150,159–161]. This method often yields hierarchical materials with original zeolite properties and precise and controllable mesopore size distributions [162]. Using this approach, the zeolite gel is first combined with the hard template, and then the zeolite crystallization is accomplished through a controlled temperature and self-generated pressure. The template is finally eliminated by calcination in the case of organic templates or through a dissolution process involving strong acids and bases in the case of inorganic templates, which can readily damage the structure of the catalyst during the removal of the hard template [149,163,164]. Hard-templating method allows to improve reactants diffusion and catalytic efficiency comparing to bare microporous zeolites [165]. However, the accessibility to the created cavity-like mesopores produced by hard-templating method is through the micropores, hence they do not significantly enhance mass transfer [161]. Moreover, hard-templating approaches have been considered as expensive methods owing to the template price and the post-treatment together with long time-consuming mainly if the synthesis of the hard template used is included in the process [144,166].

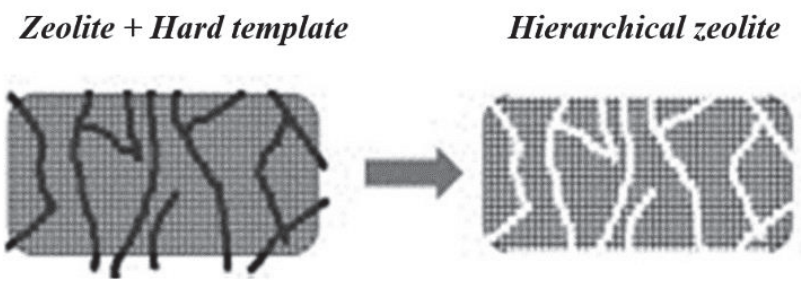

Figure I. 16. Hard-templating hydrothermal crystallization methods: hierarchical zeolite formation [150].

Adding a soft-template to the synthesis gels of zeolites is generally a straightforward, less expensive and even more versatile procedure than hard-templating methods [155,167]. The superior versatility relates to flexibility and tunability in terms of chemical composition, molar mass and surface charge. So far, the zeolite chemistry is regarded as already quite complex. Implementing mesoporosity might result in modified zeolite properties (namely their activity/selectivity, their stability related to their crystallinity as well as their defined acidity) that hence need to be carefully studied. Particularly, the nature and concentrations of precursors, the crystallization temperature and duration and the templates are the main factors to control the formation of pure, crystalline and interconnected micro-mesoporous zeolite structures with adequate acid properties. The choice of templates is vital for hierarchical zeolite formation. Various soft-templates have been used for this purpose such as cationic surfactants or polymers, organosilanes, silylane cationic polymers or surfactants, block copolymers and amphiphilic organosilanes [144,155,168,169]. Among them, ordinary surfactants such as cetyltrimethylammonium bromide (CTAB) have been proven to be the most effective mesoporous templates to create hierarchical zeolite structure [149,158,161,170–173]. CTAB interacts with the reactant raw materials (negatively charged) with the subsequent formation of mesoporous structures into the zeolite framework, Figure I. 17 [146,174]. Both microporous and soft mesoporous templates will be introduced at different stages of the synthesis procedure and removed by calcination.

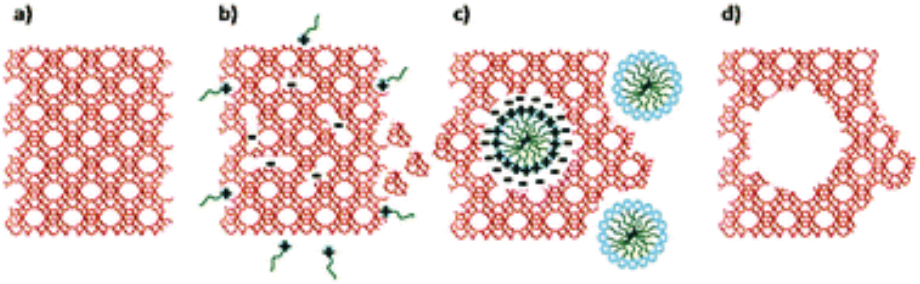

Figure I. 17. Soft-templating hydrothermal crystallization methods using CTAB as a secondary mesopores template: (a) zeolite framework without CTAB, (b) incorporation of CTAB mesopores template, (c) surfactant micelles formation and framework arrangement and (d) hierarchical structure created after removal of template [161].

A potential risk of this method is the formation of a phase-separated mixture of mesoporous and crystalline microporous zeolites due to the crystallization competition between meso- and microporous templates, Figure I. 18 (a) [158,172,173]. The formation of separated mesophases can be prevented by generating a large amount of sub-nanocrystalline zeolite seeds, with relatively high polymerization degree combined with the use of ethanol, prior to CTAB addition, Figure I. 18 (b). This alternative consists on the formation of nanocrystalline zeolite seeds prior to CTAB addition, by aging the zeolite precursor solution, and to perform the crystallization by hydrothermal treatment with CTAB thereafter [172]. This aging method, to the best of our knowledge, has only been used on medium and large pore size zeolites.

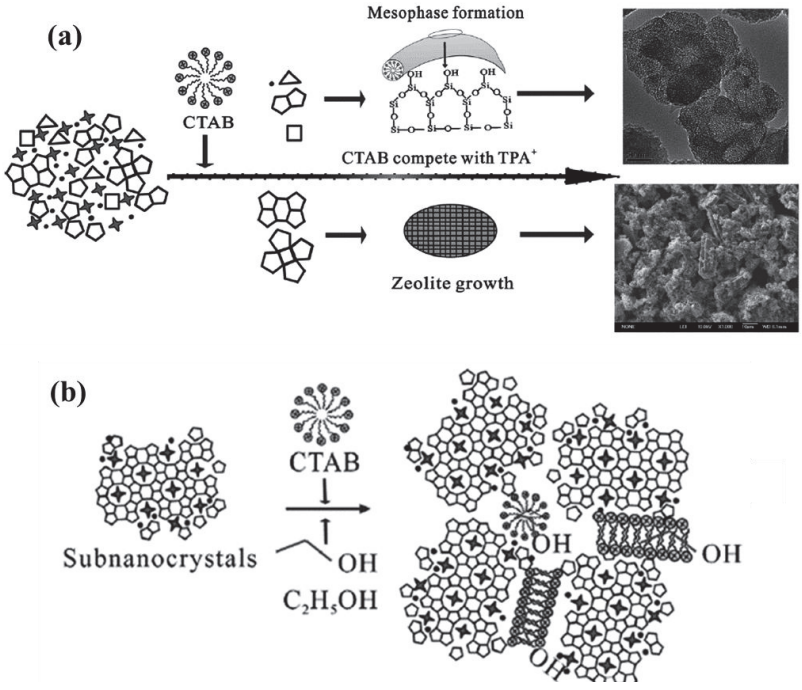

Figure I. 18 (a) Formation of a separated mesophases by adding CTAB template directly into the gel zeolite solution and (b) formation of subnanocrystals zeolite seeds [172].

Hierarchical CHA-based structures have been strongly used for methanol to hydrocarbon transformation and showed high product yield/selectivity [148–150,173,175,176]. For example, Sun et al. [175] reported the preparation of hierarchical porous SAPO-34 zeolites with intracrystalline micro-meso-macroporosity using TEA and polyethylene glycol (PEG 2000) polymer as micro and mesoporous templates, under hydrothermal conditions. These hierarchical zeolites were tested in the methanol-to-olefin (MTO) reaction, proving a good MTO performance with a prolonged catalytic lifetime (about 6 times more) due to the enhanced mass-transport within the hierarchical porous system and decreased acidity. Moreover, an increase of light olefins (C_2H_4 + C_3H_6) selectivity was observed, compared with the conventional SAPO-34 microporous catalyst. Likewise, Kong et al. [173] also demonstrated that the hierarchical SAPO-34 showed higher activity in the reaction of chloromethane to light olefins, together with higher catalytic stability than the conventional microporous CHA due to its optimal acidity and the enhanced diffusion efficiency. Álvaro-Mùnoz et al. [176] also synthesized SAPO-34 zeolites in a biphasic water-hexanol medium with two different surfactants, namely CTAB and HA (hexadecylamine), and TEAOH as microporous template. These materials were tested in the MTO process. They found that the use of the two-liquid phase medium synthesis causes greater incorporation and diversification of the silicon distribution in the SAPO-34 framework. Catalysts prepared with CTAB molar ratio in the range 0.14-0.12 rendered the best catalytic performance based on its small crystal size and mild acidity. Z. Zhou et al. [177] recently synthetized spherical hierarchical SAPO-34 zeolite by hydrothermal crystallization using TEAOH and morpholine (MOR) as composite template and CTAB as mesopores template and crystal growth inhibitor. These hierarchical SAPO-34 zeolite exhibited improved MTO catalytic performance and long catalytic lifetime.

It is only recently, that a few works acknowledged the potential of hierarchical CHA-based materials for exhaust after-treatment and, in particular, for NH_3-SCR of NO_x [9,165,178–184]. These works revealed the added-value of mesopores to greatly enhance diffusion of the reactants through the catalyst, and the greater accessibility and amount of active sites (mainly isolated Cu^{2+}) in the micropores [146,165,178,179,185], improving the NO_x reduction performance at low temperature. For example, J. Liu et al. [178] performed a reaction-kinetic approach, by careful quantification of the catalytic activity data, in order to calculate the intrinsic reaction rate constant k (sec^{-1}), which allows to understand the mesopores intrinsic effect and consequently the diffusion transport limitations. For the latter purpose, the authors quantified the catalyst effectiveness factors η, Thiele moduli ϕ (Grünert, 1998) and effective

diffusivities D (m^2/sec) and demonstrated that modifying the pore structure of the catalysts (by the presence of mesopores in the Cu-SAPO-34 catalysts) is indeed the primary way to improve mass transfer. Thus, the chemical reaction still takes place in the micropores, but the accessibility into the catalyst active sites needs to be enhanced.

Some of these studies also revealed the impact of mesopores incorporation on physico-chemical, redox and acid properties of Cu-loaded CHA-based catalysts, which indeed modify the catalytic performance for NO_x reduction. For example, Shin et al. [182] showed that the creation of mesopores by dealumination leaching or steaming destroys the ion exchange sites in Cu-SSZ-13-CHA based materials, decreasing the amount of Cu ions exchanged. Moreover, the ammonia oxidation activity at high temperature over Cu-loaded hierarchical-CHA is, however, much higher than that observed over conventional Cu-loaded CHA-based catalysts. For example, J. Liu et al. [178,180] developed several hierarchical Cu-SAPO-34 catalysts by a one-pot hydrothermal crystallization method combining a low-cost organometallic Cu-complex (copper-tetraethylenepentamine, Cu-TEPA) and an organic molecule (N,N-diisopropylethylamine DIPEA) as a secondary template. In both studies the hierarchical catalysts exhibited promising low-temperature NH_3-SCR performances, Figure I. 19, which are indeed attributed to the diffusion improvement. However, the NH_3-SCR performances of hierarchical catalysts were lower than that of the conventional catalyst at high temperature, which is indeed attributed to the non-selective ammonia oxidation, decreasing the NO_x conversion.

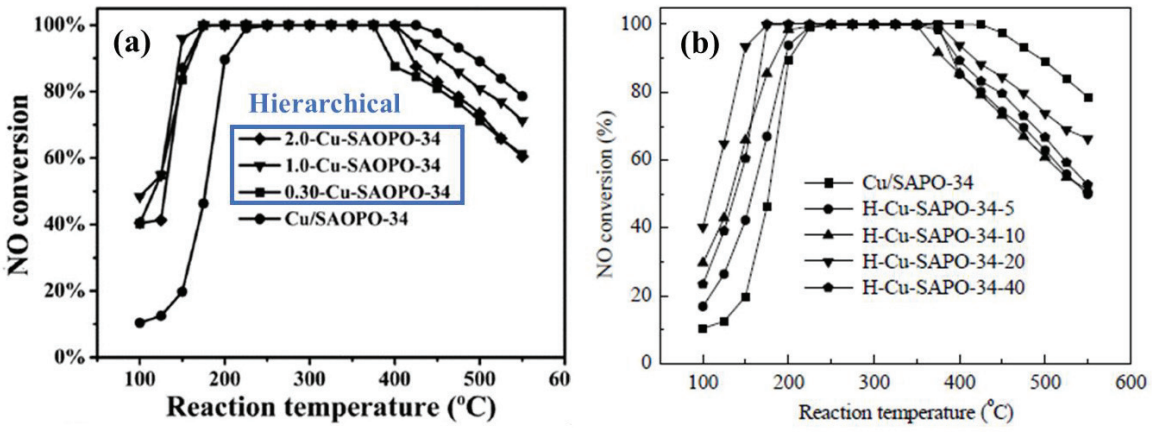

Figure I. 19. NO conversions as a function of reaction temperature over Cu-SAPO-34 hierarchical (H) and conventional catalysts (a) [178] and (b) [180]. *Reaction conditions: 1000 ppm NO, 1000 ppm NH_3, 3% O_2 with N_2 as a balance; GHSV = 50,000 h^{-1}.*

Besides, although the authors claimed that the NO_x efficiency temperature window is still wide, after a hydrothermal treatment the N_2O formation increased, compared to the fresh catalyst, Figure I. 20 (a) and (b) [178]. This phenomenon is related to the reduction of the amount of isolated Cu species and to the formation of CuO_x particles, overall making the oxidation of NH_3 more efficient.

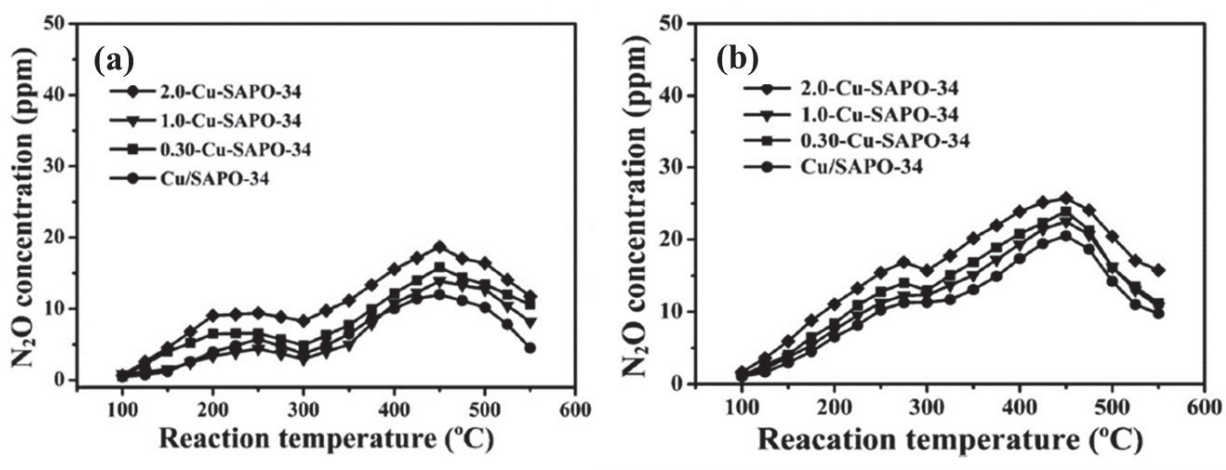

Figure I. 20. N_2O selectivity as a function of reaction temperature over (a) fresh and (b) aged Cu-SAPO-34 hierarchical and conventional catalysts [178]. *Reaction conditions: 1000 ppm NO, 1000 ppm NH_3, 3% O_2 with N_2 as a balance; GHSV = 50,000 h^{-1}.*

L. Liu et al. [184], however, demonstrated that the NH_3-SCR catalytic activity at high temperature was maintained over hierarchical Cu-SSZ-13 by dual template combining N,N,N-trimethyl-1-adamantammonium hydroxide (TMAdaOH) and $C_{16}H_{33}$-[N^+-methylpiperidine] (C_{16}MP) as micro-/meso-pores templates, Figure I. 21 (a). This feature was notably associated to the gradual decrease in the number of copper oxide clusters as the mesoporous agent content increased, improving the dispersion of copper species. Indeed, the latter indicates that the introduction of mesopores does not favor the non-selective ammonia oxidation at high temperature, Figure I. 21 (b). However, the creation of hierarchical Cu-SSZ-13 catalysts does not improve neither the low-temperature NH_3-SCR catalytic activity, Figure I. 18 (a).

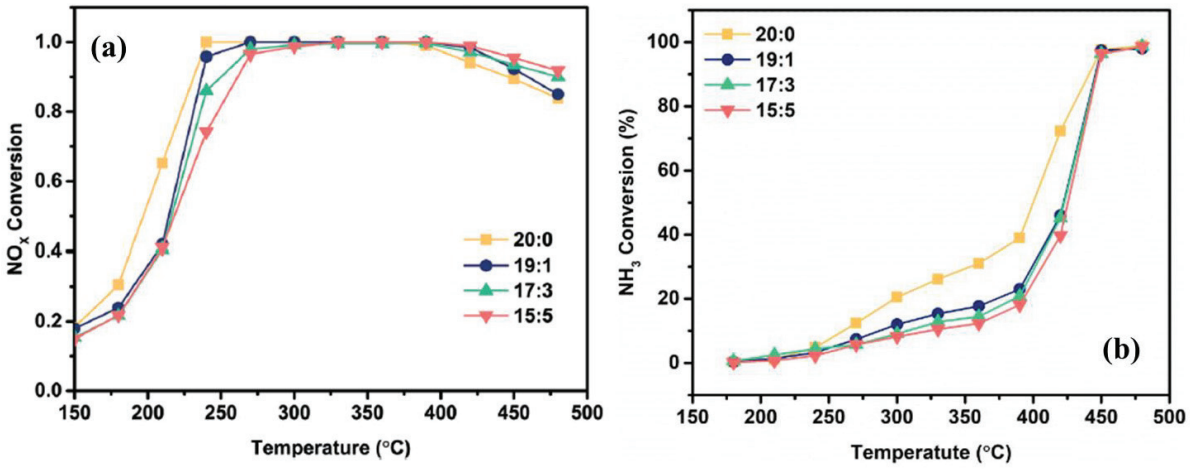

Figure I. 21. (a) NO conversions and (b) NH_3 conversions as a function of reaction temperature over conventional (20:0) and hierarchical Cu-SSZ-13 catalysts with different TMAdaOH/C_{16}MP molar ratios (19:1, 17:3 and 15:5) [184]. *Reaction conditions: 1000 ppm of NO and NH_3 and 5% of O_2 and H_2O; GHSV = 120,000 h^{-1}.*

Moreover, several authors showed that although the low-temperature NH_3-SCR catalytic activity was improved over hierarchical CHA-based catalysts, a decrease is, however, observed after hydrothermal treatment [9,165,181]. For example, R. Li et al. [165], who synthetized hierarchical SAPO-34 CHA-based zeolites by hard-templating hydrothermal crystallization method using $CaCO_3$ as a hard template, presented this material as a promising catalyst compared to conventional microporous SAPO-34, achieving 100% of NO_x conversion at 150 °C, Figure I. 22 (a). However, a slight decrease of NO_x conversion was observed at low temperature when the hierarchical catalyst is treated with 10% H_2O at 700 °C for 12 h, which came back higher as the hydrothermal treatment temperature increased (800 °C). Similar declines in low-temperature NH_3-SCR catalytic activity was observed by P. Wang et al. [181] after hydrothermal treatment at 700 °C, Figure I. 22 (b). Note that the hierarchical SAPO-34 CHA-based zeolites used in this paper were also synthetized by hard-templating method using $CaCO_3$ as hard template. The deactivation of hierarchical Cu/SAPO-34 catalysts was mainly attributed to the partial destruction of the CHA structure after hydrothermal treatment. This catalyst deactivation at low temperature was also observed by C. Peng at al. [9], Figure I. 23, which synthetized hierarchical Cu-SSZ-13-HP catalysts by a dual-template method using the bola-form organic $BC_{ph\text{-}10\text{-}6\text{-}6}$ as a mesopores template. However, the deactivation for the hierarchical catalyst was lower than that observed for the conventional Cu-SSZ-13-C catalyst after the hydrothermal treatment, which can mainly be attributed to the high-crystallinity of developed hierarchical micro-/mesoporous catalysts.

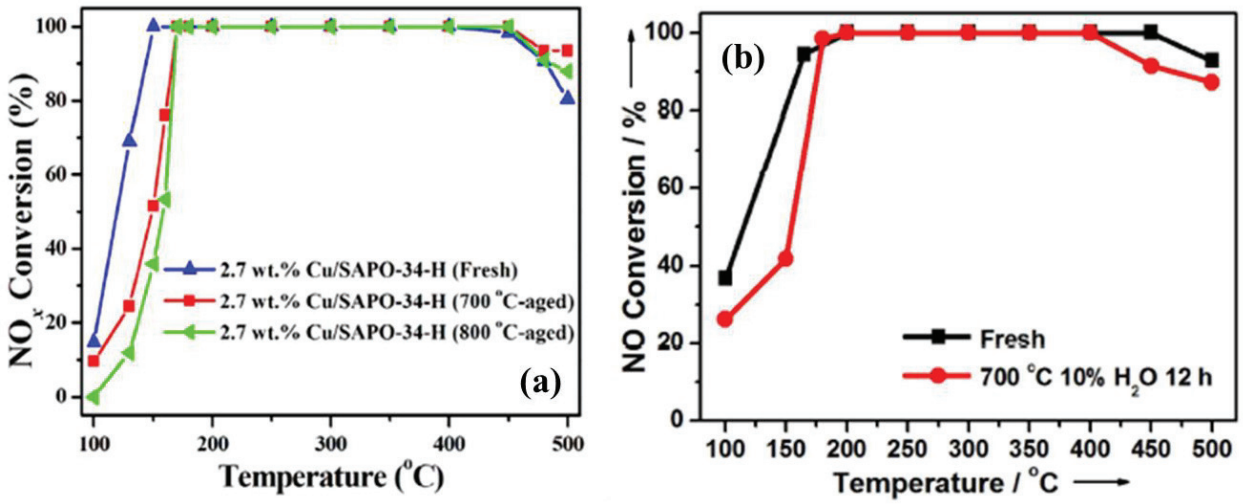

Figure I. 22. NO_x conversion by NH_3-SCR reaction as a function of reaction temperature over hierarchical Cu-SAPO-34 synthetized by hard-templating method fresh and aged at (a) 700 and 800 °C with 10% H_2O for 12 h [165]. *Reaction conditions: 1000 ppm NH_3, 1000 ppm NO, 3 vol% O_2 and H_2O, N_2 as balance gas; GHSV = 40,000 h^{-1}*; and (b) 700 °C with 10% H_2O for 12 h [181]. *Reaction conditions: 1000 ppm NH_3, 1000 ppm NO, 10 vol% O_2 and H_2O, N_2 as balance gas ; GHSV = 40,000 h^{-1}*.

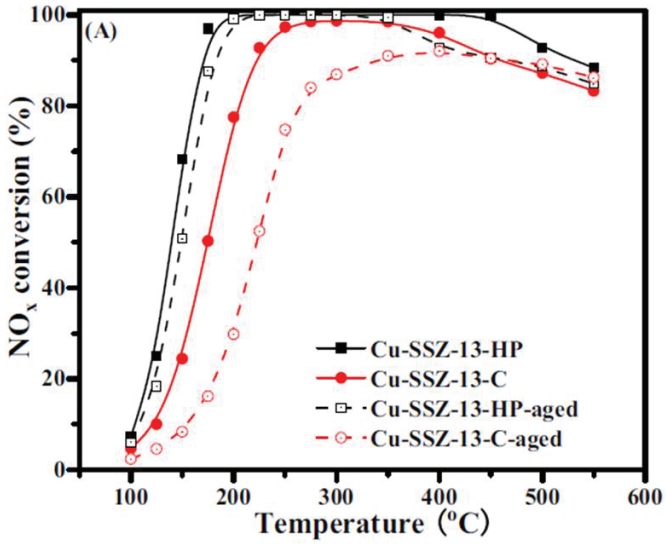

Figure I. 23. NO_x conversion as a function of reaction temperature over fresh and aged hierarchical and conventional Cu-SAPO-34 catalysts synthetized by dual-template method [9]. *Reaction conditions: 500 ppm NH_3, 500 ppm NO, 5 vol% of O_2 and H_2O, N_2 as balance ;* WHSV = 60,000 mL $g_{cat.}^{-1}$ h^{-1}.

Recently, Y. Mi et al. [185] and E. Gianotti et al. [183] developed hierarchical Cu-SAPO-34 CHA-based catalysts by soft-templating method using a long chain organic compound (C_6H_{13}–$N^+(CH_3)_2$–C_6H_{12}–$N^+(CH_3)_2$-$(CH_2)_6$–*O*–C_6H_4–C_6H_4–*O*–$(CH_2)_6$–$N^+(CH_3)_2$–C_6H_{12}–$N^+(CH_3)_2$–C_6H_{13} [$4Br^-$]) and CTAB as soft-templates, respectively. The potential of these hierarchical catalysts were clearly showed, in particular by Y. Mi et al. [185], Figure I. 24 (a). These catalysts also presented a high resistance to water and sulfur species at 300 °C, even higher than conventional SAPO-34 CHA-based zeolite, Figure I. 24 (b). However, the catalytic activity of hydrothermally aged hierarchical catalysts at low and high temperature was not presented for these authors.

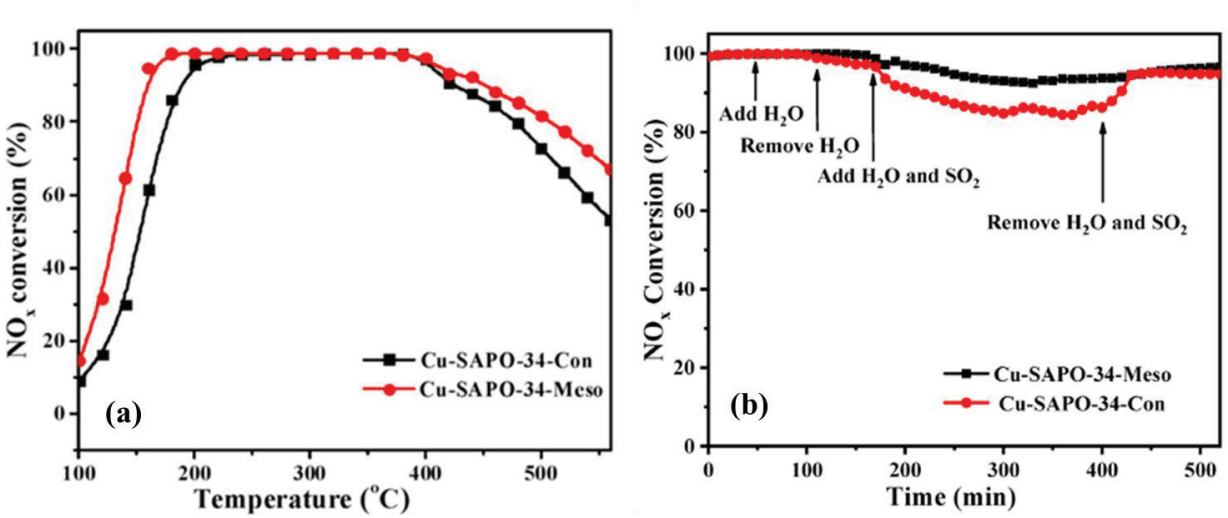

Figure I. 24. (a) NO_x conversion as a function of reaction temperature over fresh hierarchical and conventional Cu-SAPO-34 catalysts synthetized by soft-templating method (b) Stability test exposed to H_2O and SO_2 gas feed [185]. *Reaction conditions: 500 ppm NH_3, 500 ppm NO, 5 vol% of O_2 and H_2O, N_2 as balance ;* WHSV = 60,000 mL $g_{cat.}^{-1}$ h^{-1}.

The main conclusion here is that creation of mesopores is only slightly compatible with high hydrothermal stability, which seems to be mainly related to the synthesis process used to develop the hierarchical structured catalysts. This is a serious issue for high temperature operation such as needed for particle filter regeneration. Therefore, the above considerations illustrate the crucial and urgent need for even more stable, active and selective catalysts, bringing better eco- and health-friendliness. The next approach is to meet this need by means of a disruptive process leading to catalysts with advanced architecture, rather than by optimising existing materials.

4.2. Core-Shell structures.

The construction of a core-shell structure is potentially an optimal method to circumvent all the above-discussed issues, enhancing both NH_3-SCR performance and hydrothermal stability. Many efforts have been devoted to develop new core-shell materials, through modification of the components and structures of the core and of the shell. Unique chemical and physical properties and potential applications are foreseen in many areas [186–190]. Research on core-shell materials is mainly focused on metal nanoparticles-oxides core-shell structures [186,187] and some of them on metal oxides core/silicalite or aluminosilicate zeolite shell [188,189] notably synthesized by self-assembly method followed by a secondary hydrothermal growth, and even on hierarchical core-shell zeolites prepared by using a zeolite core as the nutrient for the growth of the zeolite shell [145,190–197]. Some of the latter are even related to the development of core-shell constituted by a medium pore size zeolite such as ZSM-5 and a SAPO-34 and/or SAPO-18 zeolite for biomass valorization or MTO reaction [191,195–197]. These works have proved that coating of shell-on-cores materials might alter the function and activity of the cores, but might prevent migration and coalescence of active sites during the catalytic reactions. Core–shell structures also provide a great opportunity for controlling the interaction among the different components in ways that might enhance structural stability or catalytic activity.

Despite the acknowledged potential of these core-shell materials for their application in catalysis, it is only recently that their added-value for exhaust after-treatment process has been explored [198–202]. In these studies, medium and large pore Fe-and Cu-based zeolites were coated with ceria or ceria loaded mesoporous-silica, resulting in a core-shell arrangement, Figure I. 25. It was also found that the ceria shell favors the so-called fast SCR reaction ($NO + NO_2 + 2\ NH_3 \rightarrow 2\ N_2 + 3\ H_2O$) at the location of the Fe-zeolite core, due to the oxidation of NO to NO_2 throughout the ceria shell. The core-shell structured catalysts showed indubitable advantages, improving the low-temperature NH_3-SCR reaction rate and the thermal stability compared to Fe- and physically mixed CeFe-based zeolite catalysts, while promoting new synergistic effects. Enhanced NH_3-SCR performance was also spotlighted by Z. Di et al. [202], which was related to the synergistic effect of Cu and ceria redox ability and medium zeolite acidity. These Cu-zeolite@ceria core-shell structures also showed an improved resistance to water and sulfur species. Similar synergistic effect was observed by using medium pore size zeolites such as ZSM-5 as a shell of ceria and Mn-Ce mixed oxides [203], improving the NH_3-SCR activity and poisoning resistance.

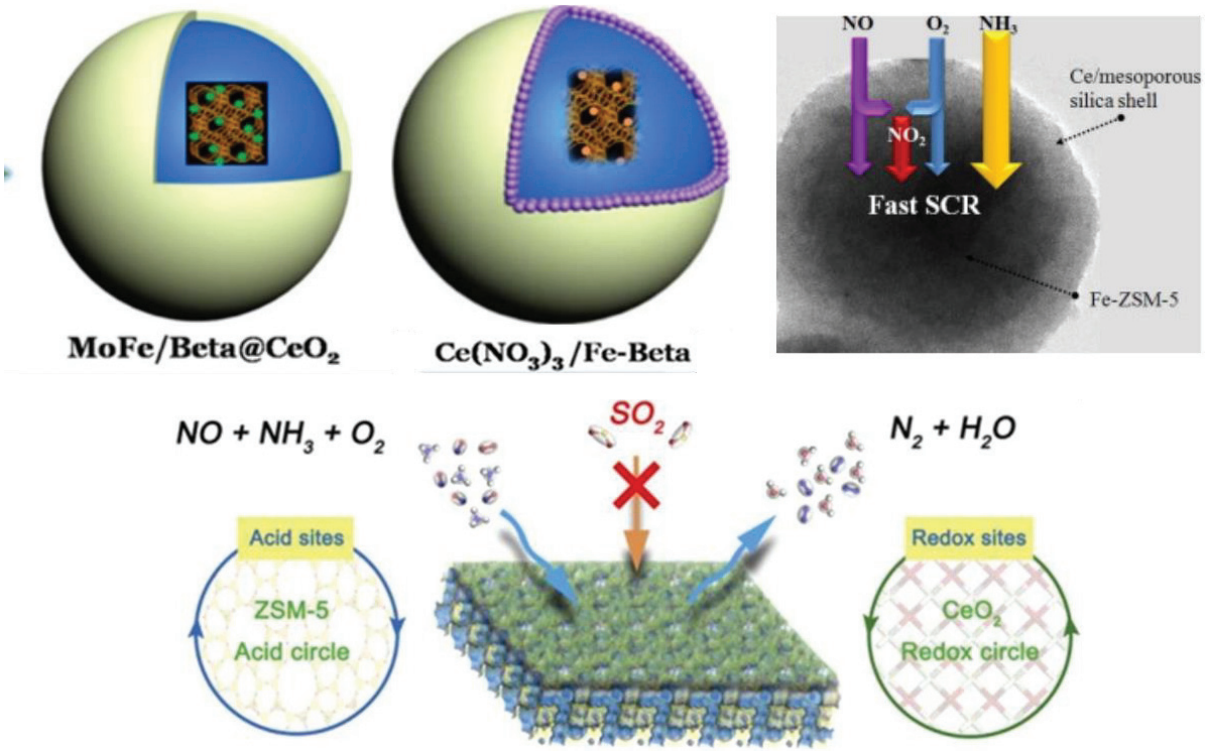

Figure I. 25. Core-shell arrangement where medium and large pore Fe-/Cu-based zeolites were coated with ceria or ceria loaded mesoporous-silica [198–200,202].

T. Zhang et al. [179] developed a core-shell structured catalyst with a mesoporous aluminosilicate shell (MAS) and Cu-loaded meso-SSZ-13 core by desilication and self-assembly methods with subsequent copper ion-exchange for the SCR reaction, that comprises only an active core, Figure I. 26. The corresponding core-shell catalyst showed an enhancement of NH_3-SCR activity at low temperature due to the reduced diffusion limitations by additional mesoporosity. In addition, the core-shell structure catalysts exhibited higher hydrothermal stability than the parent Cu-loaded micro/mesoporous-CHA catalysts. The hydrothermal stability improvement must be associated to the MAS shell, which prevents the collapse of the zeolite structure, maintaining the crystallinity and morphology of the zeolite core, as well as the formation of CuOx species. For all these advanced core-shell structures, the active temperature window (200-550°C) was, however, still undesirable.

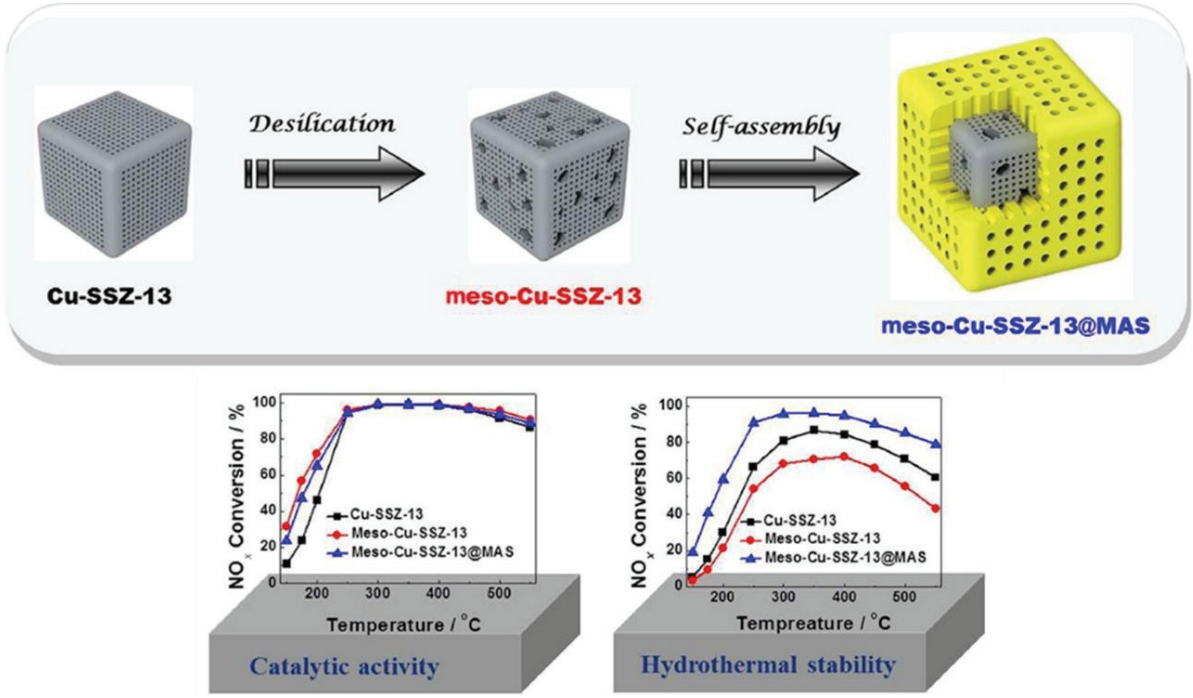

Figure I. 26. Preparation method to create core-shell Cu-based hierarchical SSZ-13 CHA with a mesoporous aluminosilicate shell, and NH_3-SCR activity and hydrothermal stability [179].

5. Position of the project, proposed research line and objectives.

Current and future regulations for gas emissions from mobile and stationary sources spotlight the strong limitations of current catalytic technologies. Among all air pollutants produced by vehicles (including CO, unburnt hydrocarbons and particulate matter), nitrogen oxides (NO_x) are known to cause alarming environmental issues, such as acid rain and photochemical smog [9,10]. In this sense, the NO_x emissions regulations are becoming increasingly more stringent, stimulating the continuous improvement of high-performance catalytic systems [141].

For NO_x abatement in particular, the selective catalytic reduction using urea or ammonia (urea- or NH_3-SCR) over copper- and iron-based zeolites catalysts is one of most effective and economic technologies [142]. Unfortunately, these catalytic systems exhibit serious practical limitations. First, current and future after-treatment systems of diesel engines contain a diesel particulate filter (DPF). High-temperatures (>600 °C) are commonly involved for DPF regeneration, which may cause irreversible damage to the SCR catalyst [89,178,179]. Second, under several operating conditions (cf. "cold-start" operating conditions), the temperature of the exhaust gas is not high enough to ensure a good catalytic performance. Then, low-

temperature SCR activity (150 °C) becomes more and more important. The above considerations illustrate the crucial and urgent need for even more stable, active and selective catalysts, bringing better eco- and health-friendliness.

In this sense, small-pore Cu-exchanged Chabazite (Cu-based CHA zeolites) catalysts, such as Cu-SAPO-34, were discovered and commercialized by researchers from BASF and Johnson Matthey, and are now widely applied to control vehicle exhausts emissions [108]. It is well known that the small pores on conventional microporous CHA zeolites impede their structural de-alumination (hence leading to high hydrothermal stability) [111]. This feature, as previously mentioned, is of paramount importance in view of the further implementation and commercialization of novel catalytic systems for the NH_3-SCR technology, since: i) water (steam) is one of the main products emitted from internal combustion engines, and ii) the exhaust temperature can reach over 700 ºC on account of the regeneration of the diesel particulate filter [89]. However, in the low temperature window, the above mentioned Cu-CHA catalysts do not seem to exhibit sufficient activity to efficiently reduce NO_x [142]. Among other reasons, the limited NO_x removal efficiency at low temperature is ascribed to the small pore size of CHA-zeolite, which strongly hinders the access of reactants to the catalytically active sites [138]. As a matter of fact, intra-crystalline (pore) diffusion limitations have been reported for NH_3-SCR over Cu-loaded CHA-zeolite catalysts at low temperature [127,138].

The approach of ANR JCJC project CHARO (*Hierarchical CHAbazite core-shell catalysts for Reduction of NO_x and N_2O*) and the present PhD is to meet this need by means of a disruptive process leading to catalysts with advanced architecture, optimising existing materials.

Thus, the development of hierarchical CHA-based zeolites with structured and ordered micropores and mesopores could be a promising solution to overcome these issues. The resulting hierarchical structures should improve reactant diffusion and, as a consequence, NO_x reduction efficiency. In the last decade, several strategies have been successfully developed to synthesize hierarchical porous aluminosilicate zeolites, and several reviews have been reported on the advances made in this field [145,146,148,149,158]. Among them, the most employed ones are: i) the post-treatment method, that relies on leaching Al or Si cations of pre-made zeolite framework, and ii) the combination of hard-templating and soft-templating methods. The synthesis of crystalline and stable hierarchical zeolites by a post-treatment method is more complicated due to the instability of the framework structure under acid or alkaline treatment. This might result in the destruction of Brønsted acid sites of the CHA zeolite, which are

involved in NH_3 adsorption in the initial step of the NH_3-SCR reaction [148,158]. In contrast, adding a soft-template to the synthesis gels of zeolites is generally a straightforward and even more versatile procedure than hard-template methods, such as using carbon additives. This alternative favors a superior flexibility and tunability of chabazite structure in terms of chemical composition, molar mass and surface charge. By adjusting these parameters, chabazite-type zeolite can be obtained with control on the hierarchical structure and morphology of the zeolite [148,149,158].

The target of the present PhD is to develop and thoroughly characterize novel hierarchical CHA based-materials (**Chapter III**) in order to improve their performance in the NO_x-reduction notably under *cold-start* operating conditions (**Chapter IV**). The strategy of soft-templating method, including a cationic surfactant such as cetyltrimethylammonium bromide (CTAB), was selected for hierarchical CHA-based zeolites synthesis in the present study. CTAB interacts with the reactant raw materials (negatively charged) with the subsequent formation of mesoporous structures into the zeolite framework [146,174]. A potential risk of this method is the formation of a mesoporous phase unconnected to the crystalline microporous zeolite, due to the competition between meso- and microporous templates during crystallization [158,172,173]. This PhD proposes a possible workaround, which is based on the principle that the formation of separated mesophases can be prevented by generating a large amount of sub-nanocrystals [172]. This alternative consists on the formation of nanocrystalline zeolite seeds prior to CTAB addition, by aging the zeolite precursor solution, and to perform the crystallization by hydrothermal treatment with CTAB thereafter. This aging method, to the best of author´s knowledge, has only been used on medium and large pore size zeolites. The synthesis procedure proposed in **Chapter III** was thoroughly studied and optimized. The physico-chemical, structural and acid properties of developed hierarchical materials were thus evaluated by several characterisation techniques in order to verify the incorporation of mesopores into the solely microporous chabazite framework.

Two hierarchical zeolite materials were further selected on account of their enhanced physico-chemical properties [204] and used as a support for Cu ions. Cu-exchanged hierarchical catalysts were also synthetized, carefully characterized and tested for NO_x reduction by the NH_3-SCR reaction (**Chapter IV**). A downside of mesopores creation, however, is that they can reduce hydrothermal stability. This is a serious issue for high temperature operation, as is the case during DPF regeneration. Thus, the impact of a hydrothermal treatment on the main physico-chemical properties, active sites and catalytic activity (for the NH_3-SCR reaction) of

our novel Cu-based hierarchical SAPO-34 catalysts was thoroughly studied in **Chapter IV**. Therefore, to reach higher NH_3-SCR performance and hydrothermal stability, this PhD targets Cu-based hierarchical catalysts allowing efficient gas diffusion though mesopores.

Nevertheless, it is well known that Cu-based catalysts are less active than Fe-based ones at higher temperatures [125]. Thus, this PhD also aims at combining the activity of copper and iron sites in CHAbazite zeolite-zeolite core-shell structures (**Chapter V**). The target novel core-shell structure, with a Cu-loaded hierarchical CHA-zeolite core and a Fe-loaded microporous CHA-zeolite shell, is expected to exhibit several advantages compared to the current catalysts based on combined individual Cu- and Fe-loaded phases, and compared to the existent NH_3-SCR core-shell structured catalysts. First, our interconnected core-shell catalytic systems will allow the free access of reactant species from the shell to the core and vice versa, where the active sites are located. This unique combination of Cu and Fe active sites, in a confined reaction environment and close interaction, will achieve superior NH_3-SCR activity at low and high temperatures, thanks to the complementary catalytic activity window of Cu- and Fe-based systems. The Fe-loaded microporous CHA-zeolite shell will also provide an effective protection against harsh operating conditions as well as a selective barrier against undesirable reactions. The complementary properties (activity/selectivity) of both interconnected catalysts, as well as the emergence of new synergetic features, mainly higher hydrothermal stability, will allow the development of materials with a unique architecture and excellent catalytic NH_3-SCR properties in extended ranges of operating conditions, achieving a higher simultaneous reduction of NO_x and N_2O.

As slightly explained in the General Introduction, this PhD manuscript will be organized in five chapters as follows. First, the experimental techniques and set-ups employed are summarized in Chapter II. Chapter III explores the development of hierarchical SAPO-34 CHA-based zeolites, showing the two soft-templating methods used in this study and its advantages and disadvantages in relation with the physico-chemical and acid properties of the novel hierarchical materials. Then, a chapter dedicated to the Cu-based hierarchical CHA-based catalysts synthesis, characterization and testing in NH_3-SCR reaction is presented (Chapter IV). Chapter V is devoted to the second objective of this PhD and shows the preliminary results concerning the development of all-zeolite core-shell materials. Finally, a general conclusion of the most relevant results and perspectives is presented in the Chapter VI.

Reference

[1] C.J. van der Veen, Fourier and the “greenhouse effect,” Polar Geogr. 24 (2000) 132–152. https://doi.org/10.1080/10889370009377693.

[2] D.W. Johnson, J. Turner, J.M. Kelly, The effects of acid rain on forest nutrient status, Water Resour. Res. 18 (1982) 449–461. https://doi.org/10.1029/WR018i003p00449.

[3] Imes Chiu, The Evolution from Horse to Automobile: A Comparative International Study, Cambria Pr, New York, 2009.

[4] İ.A. Reşitoğlu, K. Altinişik, A. Keskin, The pollutant emissions from diesel-engine vehicles and exhaust aftertreatment systems, Clean Technol. Environ. Policy. 17 (2015) 15–27. https://doi.org/10.1007/s10098-014-0793-9.

[5] S. Gil, J.M. Garcia-Vargas, L.F. Liotta, P. Vernoux, A. Giroir-Fendler, Single Brick Solution for Lean-Burn DeNO x and Soot Abatement, in: Perovskites Relat. Mix. Oxides, 2016: pp. 797–816. https://doi.org/https://doi.org/10.1002/9783527686605.ch35.

[6] C. İlkiliç, H. Aydin, The Harmful Effects of Diesel Engine Exhaust Emissions, Energy Sources, Part A Recover. Util. Environ. Eff. 34 (2012) 899–905. https://doi.org/10.1080/15567031003716709.

[7] T. Boningari, P.G. Smirniotis, Impact of nitrogen oxides on the environment and human health: Mn-based materials for the NOx abatement, Curr. Opin. Chem. Eng. 13 (2016) 133–141. https://doi.org/https://doi.org/10.1016/j.coche.2016.09.004.

[8] A.C. Lloyd, T.A. Cackette, Diesel Engines: Environmental Impact and Control, J. Air Waste Manage. Assoc. 51 (2001) 809–847. https://doi.org/10.1080/10473289.2001.10464315.

[9] C. Peng, R. Yan, Y. Mi, G. Li, Y. Zheng, Y. Luo, J. Liang, W. Liu, Z. Li, D. Wu, X. Wang, H. Peng, Toward rational design of a novel hierarchical porous Cu-SSZ-13 catalyst with boosted low-temperature NOx reduction performance, J. Catal. 401 (2021) 309–320. https://doi.org/https://doi.org/10.1016/j.jcat.2021.07.024.

[10] L. Han, S. Cai, M. Gao, J. Hasegawa, P. Wang, J. Zhang, L. Shi, D. Zhang, Selective Catalytic Reduction of NOx with NH3 by Using Novel Catalysts: State of the Art and Future Prospects, Chem. Rev. 119 (2019) 10916–10976. https://doi.org/10.1021/acs.chemrev.9b00202.

[11] R.E, Concil on environmental quality. Train, Statements on proposed feredral actions afffecting the environment, 1971.

[12] World Health Organization. Regional Office for Europe. Air quality guidelines for Europe. Copenhagen : WHO Regional Office for Europe, 1987.

[13] M. Scotto, La bataille des normes de pollution automobile va commencer à Luxembourg., Le Monde. (1985).

[14] Commission regulation (EU) No 136/2014, Amending Directive 2007/46/EC of the European Parliament and of the Council, Commission Regulation (EC) No 692/2008 as regards emissions from light passenger and commercial vehicles (Euro 5 and Euro 6), 2014. http://data.europa.eu/eli/reg/2014/136/oj.

[15] United Nations, Addendum Article 6: Agreement concerning greement the establishing of global technical regulations for wheeled vehicles, equipment and parts which can fitted and/or be used on wheeled vehicles, Geneve, 2007.

[16] L. Yang, V. Franco, A. Campestrini, J. German, P. Mock, NOx control technologies for Euro 6 Diesel passenger cars Market penetration and experimental performance assessment, Berlin, 2015.

[17] H.Y. Huang, R.Q. Long, R.T. Yang, The Promoting Role of Noble Metals on NOx Storage Catalyst and Mechanistic Study of NOx Storage under Lean-Burn Conditions, Energy & Fuels. 15 (2001) 205–213. https://doi.org/10.1021/ef0001235.

[18] H.-L. Chiang, Y.-M. Lai, S.-Y. Chang, Pollutant constituents of exhaust emitted from light-duty diesel vehicles, Atmos. Environ. 47 (2012) 399–406. https://doi.org/10.1016/j.atmosenv.2011.10.045.

[19] K. Skalska, J.S. Miller, S. Ledakowicz, Trends in NO abatement: A review, Sci. Total Environ. 408 (2010) 3976–3989. https://doi.org/10.1016/j.scitotenv.2010.06.001.

[20] L. Yang, V. Franco, A. Campestrini, J. German, P. Mock, NOx control technologies for Euro 6 Diesel passenger cars Market penetration and experimental performance assessment, Berlin, 2015.

[21] Florent Grelier, Cars with engine: can they ever be clean ?, Brussels, 2018.

[22] Emission Test Cycles - https://dieselnet.com/standards/cycles/index.php, (2022).

[23] European Environment Agency, Trends in diesel NOx emission factors and type

approval emission standards, Https://Www.Eea.Europa.Eu/Data-and-Maps/Figures/Trends-in-Diesel-Nox-Emission. (2012). https://www.eea.europa.eu/data-and-maps/figures/trends-in-diesel-nox-emission.

[24] S. Olson, Accusé de tricherie Volkswagen est menacé de sanctions aux Etats-Unis, Le Monde. (2015).

[25] No. 715/2007 of the European Parliament and of the Council on type-approval of motor vehicles with respect to emissions from light passenger and commercial vehicles (Euro 5 and Euro 6) and on access to vehicle repair and maintenance information, amending , Eur. Comm. (2017).

[26] Document 32017R1151, Commission Regulation (EU) 2017/1151 of 1 June 2017 supplementing Regulation (EC) No 715/2007 of the European Parliament and of the Council on type-approval of motor vehicles with respect to emissions from light passenger and commercial vehicles (Euro 5 a, Belgium, 2020.

[27] B. Giechaskiel, T. Vlachos, F. Riccobono, F. Forni, R. Colombo, F. Montigny, P. Le-Lijour, M. Carriero, P. Bonnel, M. Weiss, Implementation of Portable Emissions Measurement Systems (PEMS) for the Real-driving Emissions (RDE) Regulation in Europe, J. Vis. Exp. (2016). https://doi.org/10.3791/54753.

[28] B. Chelsea, U. Tietge, R. Muncrief, Y. Bernard, P. Mock, Road Tested: Comparative Overview of Real-World Versus Type-Approval NO_x and CO_2 Emissions from Diesel Cars in Europe, Washington, United States, 2017.

[29] J. Merkisz, J. Pielecha, P. Bielaczyc, J. Woodburn, Analysis of Emission Factors in RDE Tests As Well as in NEDC and WLTC Chassis Dynamometer Tests, in: 2016. https://doi.org/10.4271/2016-01-0980.

[30] H.C. Frey, A. Unal, N.M. Rouphail, J.D. Colyar, On-Road Measurement of Vehicle Tailpipe Emissions Using a Portable Instrument, J. Air Waste Manage. Assoc. 53 (2003) 992–1002. https://doi.org/10.1080/10473289.2003.10466245.

[31] S.C. Anenberg, J. Miller, R. Minjares, L. Du, D.K. Henze, F. Lacey, C.S. Malley, L. Emberson, V. Franco, Z. Klimont, C. Heyes, Impacts and mitigation of excess diesel-related NOx emissions in 11 major vehicle markets, Nature. 545 (2017) 467–471. https://doi.org/10.1038/nature22086.

[32] R. Varella, B. Giechaskiel, L. Sousa, G. Duarte, Comparison of Portable Emissions

Measurement Systems (PEMS) with Laboratory Grade Equipment, Appl. Sci. 8 (2018) 1633. https://doi.org/10.3390/app8091633.

[33] Normes européennes en matière d'émissions des véhicules — Euro 7 pour les voitures, les camionnettes, les camions et les autobus, 2022.

[34] New EU standard must reduce vehicle pollution to lowest level feasible, say cities and civil society, 2022.

[35] S. Koukiou, M. Konsolakis, R.M. Lambert, I.V. Yentekakis, Spectroscopic evidence for the mode of action of alkali promoters in Pt-catalyzed de-NOx chemistry, Appl. Catal. B Environ. 76 (2007) 101–106. https://doi.org/10.1016/j.apcatb.2007.05.014.

[36] M. Adamowska, A. Krztoń, M. Najbar, P. Da Costa, G. Djéga-Mariadassou, DRIFT study of the interaction of NO and O2 with the surface of Ce0.62Zr0.38O2 as deNOx catalyst, Catal. Today. 137 (2008) 288–291. https://doi.org/10.1016/j.cattod.2008.01.013.

[37] A. Russell, W.S. Epling, Diesel Oxidation Catalysts, Catal. Rev. 53 (2011) 337–423. https://doi.org/10.1080/01614940.2011.596429.

[38] F. -W. Schuetze, A. Woerz, G. Jeske, Diesel oxidation catalyst, Patent US 13/503,797, 2011. US20130202509A1.

[39] M.H. Wiebenga, C.H. Kim, S.J. Schmieg, S.H. Oh, D.B. Brown, D.H. Kim, J.-H. Lee, C.H.F. Peden, Deactivation mechanisms of Pt/Pd-based diesel oxidation catalysts, Catal. Today. 184 (2012) 197–204. https://doi.org/10.1016/j.cattod.2011.11.014.

[40] M. Haneda, K. Suzuki, M. Sasaki, H. Hamada, M. Ozawa, Catalytic performance of bimetallic PtPd/Al2O3 for diesel hydrocarbon oxidation and its implementation by acidic additives, Appl. Catal. A Gen. 475 (2014) 109–115. https://doi.org/10.1016/j.apcata.2014.01.023.

[41] W. Yang, J. Gong, X. Wang, Z. Bao, Y. Guo, Z. Wu, A Review on the Impact of SO2 on the Oxidation of NO, Hydrocarbons, and CO in Diesel Emission Control Catalysis, ACS Catal. 11 (2021) 12446–12468. https://doi.org/10.1021/acscatal.1c03013.

[42] C. Chen, A. Yao, C. Yao, G. Qu, Experimental study of the active and passive regeneration procedures of a diesel particulate filter in a diesel methanol dual fuel engine, Fuel. 264 (2020) 116801. https://doi.org/10.1016/j.fuel.2019.116801.

[43] John William, Investigation and development of the diesel particulate filter autoselective regeneration system, Loughborough University, 2006.

[44] S. Bensaid, C. J. Caroca, N. Russo, D. Fino, Detailed investigation of non-catalytic DPF regeneration, Can. J. Chem. Engeneering. 89 (2011) 401–407. https://doi.org/https://doi.org/10.1002/cjce.20408.

[45] B. R'Mili, A. Boréave, A. Meme, P. Vernoux, M. Leblanc, L. Noël, S. Raux, B. D'Anna, Physico-Chemical Characterization of Fine and Ultrafine Particles Emitted during Diesel Particulate Filter Active Regeneration of Euro5 Diesel Vehicles, Environ. Sci. Technol. 52 (2018) 3312–3319. https://doi.org/10.1021/acs.est.7b06644.

[46] A. Kotrba, T.P. Gardner, L. Bai, A. Yetkin, Passive Regeneration Response Characteristics of a DPF System, in: 2013. https://doi.org/10.4271/2013-01-0520.

[47] J. Ning, F. Yan, Composite Control of DOC-out Temperature for DPF regeneration, IFAC-PapersOnLine. 49 (2016) 20–27. https://doi.org/https://doi.org/10.1016/j.ifacol.2016.08.004.

[48] M. Belloir, N. Sakushima, H. Lahjaily, A CFD Study to Optimize the Injection Strategy for Diesel Particulate Filter Regeneration, in: 2007. https://doi.org/10.4271/2007-01-0164.

[49] G. C. Koltsakis, O. A. Haralampous, Z. C. Samaras, L. Kraemer, F. Heimlich, K. Behnk, Control Strategies for Peak Temperature Limitation in DPF Regeneration Supported by Validated Modeling, 2007. https://doi.org/https://doi.org/10.4271/2007-01-1127.

[50] B.R. Stanmore, V. Tschamber, J.-F. Brilhac, Oxidation of carbon by NOx, with particular reference to NO2 and N2O, Fuel. 87 (2008) 131–146. https://doi.org/10.1016/j.fuel.2007.04.012.

[51] N. Takahashi, H. Shinjoh, T. Iijima, T. Suzuki, K. Yamazaki, K. Yokota, H. Suzuki, N. Miyoshi, S. Matsumoto, T. Tanizawa, T. Tanaka, S. Tateishi, K. Kasahara, The new concept 3-way catalyst for automotive lean-burn engine: NOx storage and reduction catalyst, Catal. Today. 27 (1996) 63–69. https://doi.org/10.1016/0920-5861(95)00173-5.

[52] S. Brandenberger, O. Kröcher, A. Tissler, R. Althoff, The State of the Art in Selective Catalytic Reduction of NOx by Ammonia Using Metal-Exchanged Zeolite Catalysts,

Catal. Rev. 50 (2008) 492–531. https://doi.org/10.1080/01614940802480122.

[53] J. Wang, H. Zhao, G. Haller, Y. Li, Recent advances in the selective catalytic reduction of NOx with NH3 on Cu-Chabazite catalysts, Appl. Catal. B Environ. 202 (2017) 346–354. https://doi.org/https://doi.org/10.1016/j.apcatb.2016.09.024.

[54] M. Zheng, G.T. Reader, J.G. Hawley, Diesel engine exhaust gas recirculation—a review on advanced and novel concepts, Energy Convers. Manag. 45 (2004) 883–900. https://doi.org/10.1016/S0196-8904(03)00194-8.

[55] J. Thangaraja, C. Kannan, Effect of exhaust gas recirculation on advanced diesel combustion and alternate fuels - A review, Appl. Energy. 180 (2016) 169–184. https://doi.org/10.1016/j.apenergy.2016.07.096.

[56] R. Burch, Knowledge and Know-How in Emission Control for Mobile Applications, Catal. Rev. 46 (2004) 271–334. https://doi.org/10.1081/CR-200036718.

[57] N. Rankovic, A. Nicolle, D. Berthout, P. Da Costa, Extension of a kinetic model for NO oxidation and NOx storage to fixed-bed Pt/Ba/Al2O3 catalysts, Catal. Commun. 12 (2010) 54–57. https://doi.org/10.1016/j.catcom.2010.07.012.

[58] N. Rankovic, A. Nicolle, P. Da Costa, Detailed Kinetic Modeling Study of NOx Oxidation and Storage and Their Interactions over Pt/Ba/Al2O3 Monolith Catalysts, J. Phys. Chem. C. 114 (2010) 7102–7111. https://doi.org/10.1021/jp100192u.

[59] Y. Ji, J.-S. Choi, T.J. Toops, M. Crocker, M. Naseri, Influence of ceria on the NOx storage/reduction behavior of lean NOx trap catalysts, Catal. Today. 136 (2008) 146–155. https://doi.org/10.1016/j.cattod.2007.11.059.

[60] J. Klein, D. Wu, V. Tschamber, I. Fechete, F. Garin, Carbon–NSR catalyst interaction: Impact on catalyst structure and NOx storage efficiency, Appl. Catal. B Environ. 132–133 (2013) 527–534. https://doi.org/https://doi.org/10.1016/j.apcatb.2012.12.019.

[61] J.-S. Choi, W.P. Partridge, C.S. Daw, Sulfur impact on NOx storage, oxygen storage, and ammonia breakthrough during cyclic lean/rich operation of a commercial lean NOx trap, Appl. Catal. B Environ. 77 (2007) 145–156. https://doi.org/10.1016/j.apcatb.2007.07.025.

[62] Y. Jangjou, D. Wang, A. Kumar, J. Li, W.S. Epling, SO2 Poisoning of the NH3 -SCR Reaction over Cu-SAPO-34: Effect of Ammonium Sulfate versus Other S-Containing Species, ACS Catal. 6 (2016) 6612–6622. https://doi.org/10.1021/acscatal.6b01656.

[63] B. Guan, R. Zhan, H. Lin, Z. Huang, Review of state of the art technologies of selective catalytic reduction of NOx from diesel engine exhaust, Appl. Therm. Eng. 66 (2014) 395–414. https://doi.org/10.1016/j.applthermaleng.2014.02.021.

[64] Y. Guan, Y. Liu, Q. Lv, B. Wang, D. Che, Review on the selective catalytic reduction of NOx with H2 by using novel catalysts, J. Environ. Chem. Eng. 9 (2021) 106770. https://doi.org/https://doi.org/10.1016/j.jece.2021.106770.

[65] R. Mrad, A. Aissat, R. Cousin, D. Courcot, S. Siffert, Catalysts for NOx selective catalytic reduction by hydrocarbons (HC-SCR), Appl. Catal. A Gen. 504 (2015) 542–548. https://doi.org/https://doi.org/10.1016/j.apcata.2014.10.021.

[66] H. Hamada, M. Haneda, A review of selective catalytic reduction of nitrogen oxides with hydrogen and carbon monoxide, Appl. Catal. A Gen. 421–422 (2012) 1–13. https://doi.org/https://doi.org/10.1016/j.apcata.2012.02.005.

[67] M. Koebel, M. Elsener, M. Kleemann, Urea-SCR: a promising technique to reduce NOx emissions from automotive diesel engines, Catal. Today. 59 (2000) 335–345. https://doi.org/10.1016/S0920-5861(00)00299-6.

[68] S.D. Yim, S.J. Kim, J.H. Baik, I. Nam, Y.S. Mok, J.-H. Lee, B.K. Cho, S.H. Oh, Decomposition of Urea into NH3 for the SCR Process, Ind. Eng. Chem. Res. 43 (2004) 4856–4863. https://doi.org/10.1021/ie034052j.

[69] M. Kleemann, M. Elsener, M. Koebel, A. Wokaun, Hydrolysis of Isocyanic Acid on SCR Catalysts, Ind. Eng. Chem. Res. 39 (2000) 4120–4126. https://doi.org/10.1021/ie9906161.

[70] D. Zhang, R.T. Yang, N2O Formation Pathways over Zeolite-Supported Cu and Fe Catalysts in NH3-SCR, Energy & Fuels. 32 (2018) 2170–2182. https://doi.org/10.1021/acs.energyfuels.7b03405.

[71] G. Madia, M. Koebel, M. Elsener, A. Wokaun, Side Reactions in the Selective Catalytic Reduction of NOx with Various NO2 Fractions, Ind. Eng. Chem. Res. 41 (2002) 4008–4015. https://doi.org/10.1021/ie020054c.

[72] D. Wang, li Zhang, J. Li, K. Kamasamudram, W. Epling, NH3-SCR over Cu/SAPO-34 – Zeolite acidity and Cu structure changes as a function of Cu loading, Catal. Today. 231 (2014) 64–74. https://doi.org/10.1016/j.cattod.2013.11.040.

[73] U. Deka, I. Lezcano-Gonzalez, B.M. Weckhuysen, A.M. Beale, Local Environment

and Nature of Cu Active Sites in Zeolite-Based Catalysts for the Selective Catalytic Reduction of NO_x, ACS Catal. 3 (2013). https://doi.org/10.1021/cs300794s.

[74] P. Forzatti, Environmental catalysis for stationary applications, Catal. Today. 62 (2000) 51–65. https://doi.org/https://doi.org/10.1016/S0920-5861(00)00408-9.

[75] S.S.R. Putluru, L. Schill, A. Godiksen, R. Poreddy, S. Mossin, A.D. Jensen, R. Fehrmann, Promoted V2O5/TiO2 catalysts for selective catalytic reduction of NO with NH3 at low temperatures, Appl. Catal. B Environ. 183 (2016) 282–290. https://doi.org/https://doi.org/10.1016/j.apcatb.2015.10.044.

[76] Y. Long, Y. Su, Y. Xue, Z. Wu, X. Weng, V2O5–WO3/TiO2 Catalyst for Efficient Synergistic Control of NOx and Chlorinated Organics: Insights into the Arsenic Effect, Environ. Sci. Technol. 55 (2021) 9317–9325. https://doi.org/10.1021/acs.est.1c02636.

[77] N.N. Sazonova, L.T. Tsykoza, A. V. Simakov, G.B. Barannik, Z.R. Ismagilov, Relationship between sulfur dioxide oxidation and selective catalytic NO reduction by ammonia on V2O5−TiO2 catalysts doped with WO3 and Nb2O5, React. Kinet. Catal. Lett. 52 (1994) 101–106. https://doi.org/10.1007/BF02129856.

[78] T. Xu, X. Wu, Y. Gao, Q. Lin, J. Hu, D. Weng, Comparative study on sulfur poisoning of V2O5-Sb2O3/TiO2 and V2O5-WO3/TiO2 monolithic catalysts for low-temperature NH3-SCR, Catal. Commun. 93 (2017) 33–36. https://doi.org/10.1016/j.catcom.2017.01.021.

[79] A. P. Walker, P. G. Blakeman, T. Ilkenhans, B. Magnusson, A. C. McDonald, P. Kleijwegt, F. Stunnenberg, M. Sanchez, The Development and In-Field Demonstration of Highly Durable SCR Catalyst Systems, SAE Tech. Pap. 2004-01-1289. (2004) 548–558. https://doi.org/https://doi.org/10.4271/2004-01-1289.

[80] K. Kamasamudram, N.W. Currier, X. Chen, A. Yezerets, Overview of the practically important behaviors of zeolite-based urea-SCR catalysts, using compact experimental protocol, Catal. Today. 151 (2010) 212–222. https://doi.org/https://doi.org/10.1016/j.cattod.2010.03.055.

[81] S. Mohan, P. Dinesha, S. Kumar, NOx reduction behaviour in copper zeolite catalysts for ammonia SCR systems: A review, Chem. Eng. J. 384 (2020) 123253. https://doi.org/https://doi.org/10.1016/j.cej.2019.123253.

[82] M. Zhu, J.-K. Lai, I.E. Wachs, Formation of N2O greenhouse gas during SCR of NO

with NH3 by supported vanadium oxide catalysts, Appl. Catal. B Environ. 224 (2018) 836–840. https://doi.org/https://doi.org/10.1016/j.apcatb.2017.11.029.

[83] M. Yates, J.A. Martín, M.Á. Martín-Luengo, S. Suárez, J. Blanco, N2O formation in the ammonia oxidation and in the SCR process with V2O5-WO3 catalysts, Catal. Today. 107–108 (2005) 120–125. https://doi.org/https://doi.org/10.1016/j.cattod.2005.07.015.

[84] G. Madia, M. Elsener, M. Koebel, F. Raimondi, A. Wokaun, Thermal stability of vanadia-tungsta-titania catalysts in the SCR process, Appl. Catal. B Environ. 39 (2002) 181–190. https://doi.org/https://doi.org/10.1016/S0926-3373(02)00099-1.

[85] Z. Yan, W. Shan, X. Shi, G. He, Z. Lian, Y. Yu, Y. Shan, J. Liu, H. He, The way to enhance the thermal stability of V2O5-based catalysts for NH3-SCR, Catal. Today. 355 (2020) 408–414. https://doi.org/https://doi.org/10.1016/j.cattod.2019.07.037.

[86] G. Oliveri, G. Busca, V. Lorenzelli, Structure and surface area evolution of vanadia-on-titania powders upon heat treatment, Mater. Chem. Phys. 22 (1989) 511–521. https://doi.org/https://doi.org/10.1016/0254-0584(89)90063-1.

[87] G. Oliveri, G. Ramis, G. Busca, V.S. Escribano, Thermal stability of vanadia–titania catalysts, J. Mater. Chem. 3 (1993) 1239–1249. https://doi.org/10.1039/JM9930301239.

[88] Z.G. Liu, N.A. Ottinger, C.M. Cremeens, Vanadium and tungsten release from V-based selective catalytic reduction diesel aftertreatment, Atmos. Environ. 104 (2015) 154–161. https://doi.org/10.1016/j.atmosenv.2014.12.063.

[89] S.J. Schmieg, S.H. Oh, C.H. Kim, D.B. Brown, J.H. Lee, C.H.F. Peden, D.H. Kim, Thermal durability of Cu-CHA NH3-SCR catalysts for diesel NOx reduction, Catal. Today. 184 (2012) 252–261. https://doi.org/10.1016/j.cattod.2011.10.034.

[90] C.M. Giovanni, J. Girard, J. Patterson, K. Y. Cheng, C. Lambert, Laboratory Testing of Urea-SCR Formulations to Meet Tier 2 Bin 5 Emissions, SAE Tech. Pap. 2007-01-1575. (2007). https://doi.org/https://doi.org/10.4271/2007-01-1575.

[91] A. Dyer, An introduction to zeolite molecular sieves, J. Wiley, United States, 1988.

[92] I. Chorkendorff, J. W. Niemantsverdriet, Concepts of Modern Catalysis and Kinetics, 3rd Edition, Wiley-VHC, Netherlands, 2017.

[93] Database of Zeolite Structures, Http://Www.Iza-Structure.Org/Databases/. (n.d.).

[94] J.H. Kwak, D. Tran, S.D. Burton, J. Szanyi, J.H. Lee, C.H.F. Peden, Effects of hydrothermal aging on NH3-SCR reaction over Cu/zeolites, J. Catal. 287 (2012) 203–209. https://doi.org/https://doi.org/10.1016/j.jcat.2011.12.025.

[95] K. Kvande, A Study of Cu-loaded SAPO-34 for the Direct Conversion of Methane to Methanol, Faculty of Mathematics and Natural Sciences, University of Oslo, 2019.

[96] S. M. Auerbach, K. A. Carrado, P. K. Dutta, Handbook of Zeolite Science and Technology, Marcel Dek, New York, 2003.

[97] M. Iwamoto, H. Furukawa, Y. Mine, F. Uemura, S. Mikuriya, S. Kagawa, Copper(II) ion-exchanged ZSM-5 zeolites as highly active catalysts for direct and continuous decomposition of nitrogen monoxide, J. Chem. Soc. Chem. Commun. (1986) 1272–1273. https://doi.org/10.1039/C39860001272.

[98] A.M. Beale, F. Gao, I. Lezcano-Gonzalez, C.H.F. Peden, J. Szanyi, Recent advances in automotive catalysis for NOx emission control by small-pore microporous materials, Chem. Soc. Rev. 44 (2015) 7371–7405. https://doi.org/10.1039/C5CS00108K.

[99] G. Cavataio, H.-W. Jen, J.R. Warner, J.W. Girard, J. Y. Kim, C. K. Lambert, Enhanced Durability of a Cu/Zeolite Based SCR Catalyst, SAE Int. J. Fuels Lubr. 1 (2009) 477–487. https://doi.org/https://doi.org/10.4271/2008-01-1025.

[100] J. M. Fedeyko, H.-Y. Chen, T.H. Ballinger, E.C. Weigert, H.-L. Chang, J.P. Cox, P.J., Andersen, Development of Thermally Durable Cu/SCR Catalysts, SAE Tech. Pap. 2009-01-0899. (2009) 7. https://doi.org/https://doi.org/10.4271/2009-01-0899.

[101] O. Mihai, C.R. Widyastuti, A. Kumar, J. Li, S.Y. Joshi, K. Kamasamudram, N.W. Currier, A. Yezerets, L. Olsson, The Effect of NO2/NOx Feed Ratio on the NH3-SCR System Over Cu–Zeolites with Varying Copper Loading, Catal. Letters. 144 (2014) 70–80. https://doi.org/10.1007/s10562-013-1133-0.

[102] M. Moliner, C. Martínez, A. Corma, Synthesis Strategies for Preparing Useful Small Pore Zeolites and Zeotypes for Gas Separations and Catalysis, Chem. Mater. 26 (2014) 246–258. https://doi.org/10.1021/cm4015095.

[103] G. Pétaud, Réduction catalytique sélective des oxydes d'azotes par l'ammoniac : cinétique, mécanisme et modélisation du système cuivre Chabazite, l'Université Claude Bernard Lyon 1, 2019.

[104] P. A. Jacobs, E.M. Flanigen, J.C. Jansen, H. van Bekkum, Introduction to Zeolite Science and Practice, first Else, Amsterdan, 2001.

[105] L. S. Dent, J.V. Smith, Crystal Structure of Chabazite, a Molecular Sieve, Nature. 181 (1958) 1794–1796. https://doi.org/10.1038/1811794b0.

[106] S. Wilson, P. Barger, The characteristics of SAPO-34 which influence the conversion of methanol to light olefins, Microporous Mesoporous Mater. 29 (1999) 117–126. https://doi.org/10.1016/S1387-1811(98)00325-4.

[107] D. Yuan, A. Xing, P. Miao, Q. Sun, L. Cui, H. Wang, L. Ma, F. Chiang, J. Kong, Assembly of Sub-Crystals on the Macroscale and Construction of Composite Building Units on the Microscale for SAPO-34, Chem. - An Asian J. 13 (2018) 3063–3072. https://doi.org/10.1002/asia.201801069.

[108] W.M. Bull, W.-M. Xue, P. Burk, R.S. Boorse, I. Jaglowski, G.S. Koermer, A. Moini, J.A. Patchett, J.C. Dettling, M.T. Caudle, Copper CHA Zeolinte Catalysts, U.S. Patent 0,226,545, 2008., 2009. https://patents.google.com/patent/US20080226545.

[109] J. Pérez-Ramírez, C.H. Christensen, K. Egeblad, C.H. Christensen, J.C. Groen, Hierarchical zeolites: enhanced utilisation of microporous crystals in catalysis by advances in materials design, Chem. Soc. Rev. 37 (2008) 2530. https://doi.org/10.1039/b809030k.

[110] T. Fjermestad, S. Svelle, O. Swang, Mechanistic Comparison of the Dealumination in SSZ-13 and the Desilication in SAPO-34, J. Phys. Chem. C. 117 (2013) 13442–13451. https://doi.org/10.1021/jp4028468.

[111] P.G. Blakeman, E.M. Burkholder, H.-Y. Chen, J.E. Collier, J.M. Fedeyko, H. Jobson, R.R. Rajaram, The role of pore size on the thermal stability of zeolite supported Cu SCR catalysts, Catal. Today. 231 (2014) 56–63. https://doi.org/https://doi.org/10.1016/j.cattod.2013.10.047.

[112] R.Q. Long, R.T. Yang, Reaction Mechanism of Selective Catalytic Reduction of NO with NH3 over Fe-ZSM-5 Catalyst, J. Catal. 207 (2002) 224–231. https://doi.org/10.1006/jcat.2002.3528.

[113] R.Q. Long, R.T. Yang, Catalytic Performance of Fe–ZSM-5 Catalysts for Selective Catalytic Reduction of Nitric Oxide by Ammonia, J. Catal. 188 (1999) 332–339. https://doi.org/10.1006/jcat.1999.2674.

[114] R. Vomscheid, M. Briend, M.J. Peltre, P.P. Man, D. Barthomeuf, The Role of the Template in Directing the Si Distribution in SAPO Zeolites, J. Phys. Chem. 98 (1994) 9614–9618. https://doi.org/10.1021/j100089a041.

[115] G. Liu, P. Tian, Y. Zhang, J. Li, L. Xu, S. Meng, Z. Liu, Synthesis of SAPO-34 templated by diethylamine: Crystallization process and Si distribution in the crystals, Microporous Mesoporous Mater. 114 (2008) 416–423. https://doi.org/10.1016/j.micromeso.2008.01.030.

[116] J. Tan, Z. Liu, X. Bao, X. Liu, X. Han, C. He, R. Zhai, Crystallization and Si incorporation mechanisms of SAPO-34, Microporous Mesoporous Mater. 53 (2002) 97–108. https://doi.org/10.1016/S1387-1811(02)00329-3.

[117] L. Wang, W. Li, S.J. Schmieg, D. Weng, Role of Brønsted acidity in NH3 selective catalytic reduction reaction on Cu/SAPO-34 catalysts, J. Catal. 324 (2015) 98–106. https://doi.org/https://doi.org/10.1016/j.jcat.2015.01.011.

[118] S. Ashtekar, S.V. V Chilukuri, D.K. Chakrabarty, Small-Pore Molecular Sieves SAPO-34 and SAPO-44 with Chabazite Structure: A Study of Silicon Incorporation, J. Phys. Chem. 98 (1994) 4878–4883. https://doi.org/10.1021/j100069a018.

[119] E.M. Flanigen, R.L. Patton, S.T. Wilson, Structural, Synthetic and Physicochemical Concepts in Aluminophosphate-Based Molecular Sieves, 37 (1988) 13–27. https://doi.org/10.1016/S0167-2991(09)60578-4.

[120] C.S. Blackwell, R.L. Patton, Solid-state NMR of silicoaluminophosphate molecular sieves and aluminophosphate materials, J. Phys. Chem. 92 (1988) 3965–3970. https://doi.org/10.1021/j100324a055.

[121] C. Lin, Y. Cao, X. Feng, Q. Lin, H. Xu, Y. Chen, Effect of Si islands on low-temperature hydrothermal stability of Cu/SAPO-34 catalyst for NH3-SCR, J. Taiwan Inst. Chem. Eng. 81 (2017) 288–294. https://doi.org/https://doi.org/10.1016/j.jtice.2017.09.050.

[122] T. Yu, J. Wang, M. Shen, W. Li, NH3-SCR over Cu/SAPO-34 catalysts with various acid contents and low Cu loading, Catal. Sci. Technol. 3 (2013) 3234–3241. https://doi.org/10.1039/C3CY00453H.

[123] T. Fjermestad, S. Svelle, O. Swang, Mechanism of Si Island Formation in SAPO-34, J. Phys. Chem. C. 119 (2015) 2086–2095. https://doi.org/10.1021/jp510845z.

[124] Z. Chen, C. Bian, C. Fan, T. Li, The role of Si coordination structures in the catalytic properties and durability of Cu-SAPO-34 as NH3-SCR catalyst for NOx reduction, Chinese Chem. Lett. 33 (2022) 893–897. https://doi.org/10.1016/j.cclet.2021.06.071.

[125] F. Gao, Y. Wang, M. Kollár, N.M. Washton, J. Szanyi, C.H.F. Peden, A comparative kinetics study between Cu/SSZ-13 and Fe/SSZ-13 SCR catalysts, Catal. Today. 258 (2015) 347–358. https://doi.org/https://doi.org/10.1016/j.cattod.2015.01.025.

[126] S. Andonova, S. Tamm, C. Montreuil, C. Lambert, L. Olsson, The effect of iron loading and hydrothermal aging on one-pot synthesized Fe/SAPO-34 for ammonia SCR, Appl. Catal. B Environ. 180 (2016) 775–787. https://doi.org/https://doi.org/10.1016/j.apcatb.2015.07.007.

[127] F. Gao, E.D. Walter, E.M. Karp, J. Luo, R.G. Tonkyn, J.H. Kwak, J. Szanyi, C.H.F. Peden, Structure–activity relationships in NH3-SCR over Cu-SSZ-13 as probed by reaction kinetics and EPR studies, J. Catal. 300 (2013) 20–29. https://doi.org/https://doi.org/10.1016/j.jcat.2012.12.020.

[128] I. Nova, M. Colombo, E. Tronconi, V. Schmeisser, M. Weibel, The NH3 Inhibition Effect in the Standard SCR Reaction over a Commercial Fe-zeolite Catalyst for Diesel Exhaust Aftertreatment: An Experimental and Modeling Study, SAE Int. J. Engines. 4 (2011) 1822–1838. https://doi.org/10.4271/2011-01-1319.

[129] X. Li, Y. Zhao, H. Zhao, M. Liu, Y. Ma, X. Yong, H. Chen, Y. Li, The Cu migration of Cu-SAPO-34 catalyst for ammonia selective catalytic reduction of NOx during high temperature hydrothermal aging treatment, Catal. Today. 327 (2019) 126–133. https://doi.org/10.1016/j.cattod.2018.05.029.

[130] D. Wang, Y. Jangjou, Y. Liu, M.K. Sharma, J. Luo, J. Li, K. Kamasamudram, W.S. Epling, A comparison of hydrothermal aging effects on NH3-SCR of NO over Cu-SSZ-13 and Cu-SAPO-34 catalysts, Appl. Catal. B Environ. 165 (2015) 438–445. https://doi.org/10.1016/j.apcatb.2014.10.020.

[131] X. Liu, X. Wu, D. Weng, Z. Si, R. Ran, Evolution of copper species on Cu/SAPO-34 SCR catalysts upon hydrothermal aging, Catal. Today. 281 (2017) 596–604. https://doi.org/10.1016/j.cattod.2016.05.021.

[132] L. Wang, J.R. Gaudet, W. Li, D. Weng, Migration of Cu species in Cu/SAPO-34 during hydrothermal aging, J. Catal. 306 (2013) 68–77.

https://doi.org/https://doi.org/10.1016/j.jcat.2013.06.010.

[133] L. Wang, W. Li, G. Qi, D. Weng, Location and nature of Cu species in Cu/SAPO-34 for selective catalytic reduction of NO with NH3, J. Catal. 289 (2012) 21–29. https://doi.org/https://doi.org/10.1016/j.jcat.2012.01.012.

[134] U. Deka, A. Juhin, E.A. Eilertsen, H. Emerich, M.A. Green, S.T. Korhonen, B.M. Weckhuysen, A.M. Beale, Confirmation of Isolated Cu2+ Ions in SSZ-13 Zeolite as Active Sites in NH3-Selective Catalytic Reduction, J. Phys. Chem. C. 116 (2012) 4809–4818. https://doi.org/10.1021/jp212450d.

[135] J. Xue, X. Wang, G. Qi, J. Wang, M. Shen, W. Li, Characterization of copper species over Cu/SAPO-34 in selective catalytic reduction of NO x with ammonia: Relationships between active Cu sites and de-NO x performance at low temperature, J. Catal. 297 (2013) 56–64. https://doi.org/https://doi.org/10.1016/j.jcat.2012.09.020.

[136] K. Johansen, H. Bentzer, A. Kustov, K. Larsen, T.V.W. Janssens, R.G. Barfod, Integration of Vanadium and Zeolite Type SCR Functionality into DPF in Exhaust Aftertreatment Systems - Advantages and Challenges. SAE Technical Paper 2014-01-1523, 2014. https://doi.org/10.4271/2014-01-1523.

[137] R. Zhang, Y. Li, T. Zhen, Ammonia selective catalytic reduction of NO over Fe/Cu-SSZ-13, RSC Adv. 4 (2014) 52130–52139. https://doi.org/10.1039/C4RA09290B.

[138] T. Zhang, J. Li, J. Liu, D. Wang, Z. Zhao, K. Cheng, J. Li, High activity and wide temperature window of Fe-Cu-SSZ-13 in the selective catalytic reduction of NO with ammonia, AIChE J. 61 (2015) 3825–3837. https://doi.org/10.1002/aic.14923.

[139] X. Yang, Z. Wu, M. Moses-Debusk, D.R. Mullins, S.M. Mahurin, R.A. Geiger, M. Kidder, C.K. Narula, Heterometal Incorporation in Metal-Exchanged Zeolites Enables Low-Temperature Catalytic Activity of NO_x Reduction, J. Phys. Chem. C. 116 (2012) 23322–23331. https://doi.org/10.1021/jp3056043.

[140] G. Sørli, Effect of Porosity on the Hydrothermal Stability of CuSAPO-34 for the deNOx Process, Norwegian University of Science and Technology , 2016.

[141] C.K. Lambert, Current state of the art and future needs for automotive exhaust catalysis, Nat. Catal. 2 (2019) 554–557. https://doi.org/10.1038/s41929-019-0303-x.

[142] S. Zhang, L. Pang, Z. Chen, S. Ming, Y. Dong, Q. Liu, P. Liu, W. Cai, T. Li, Cu/SSZ-13 and Cu/SAPO-34 catalysts for deNOx in diesel exhaust: Current status, challenges,

and future perspectives, Appl. Catal. A Gen. 607 (2020) 117855. https://doi.org/10.1016/j.apcata.2020.117855.

[143] M. Hartmann, A.G. Machoke, W. Schwieger, Catalytic test reactions for the evaluation of hierarchical zeolites, Chem. Soc. Rev. 45 (2016) 3313–3330. https://doi.org/10.1039/C5CS00935A.

[144] X. Jia, W. Khan, Z. Wu, J. Choi, A.C.K. Yip, Modern synthesis strategies for hierarchical zeolites: Bottom-up versus top-down strategies, Adv. Powder Technol. 30 (2019) 467–484. https://doi.org/10.1016/j.apt.2018.12.014.

[145] N. Masoumifard, R. Guillet-Nicolas, F. Kleitz, Synthesis of Engineered Zeolitic Materials: From Classical Zeolites to Hierarchical Core–Shell Materials, Adv. Mater. 30 (2018) 1704439. https://doi.org/10.1002/adma.201704439.

[146] A. Feliczak-Guzik, Hierarchical zeolites: Synthesis and catalytic properties, Microporous Mesoporous Mater. 259 (2018) 33–45. https://doi.org/https://doi.org/10.1016/j.micromeso.2017.09.030.

[147] M. Hartmann, M. Thommes, W. Schwieger, Hierarchically-Ordered Zeolites: A Critical Assessment, Adv. Mater. Interfaces. 8 (2021) 2001841. https://doi.org/https://doi.org/10.1002/admi.202001841.

[148] Q. Sun, Z. Xie, J. Yu, The state-of-the-art synthetic strategies for SAPO-34 zeolite catalysts in methanol-to-olefin conversion, Natl. Sci. Rev. 5 (2017) 542–558. https://doi.org/10.1093/nsr/nwx103.

[149] K. Möller, T. Bein, Mesoporosity – a new dimension for zeolites, Chem. Soc. Rev. 42 (2013) 3689–3707. https://doi.org/10.1039/C3CS35488A.

[150] J. Zhong, J. Han, Y. Wei, P. Tian, X. Guo, C. Song, Z. Liu, Recent advances of the nano-hierarchical SAPO-34 in the methanol-to-olefin (MTO) reaction and other applications, Catal. Sci. Technol. 7 (2017) 4905–4923. https://doi.org/10.1039/C7CY01466J.

[151] I.I. Ivanova, E.E. Knyazeva, Micro–mesoporous materials obtained by zeolite recrystallization: synthesis, characterization and catalytic applications, Chem. Soc. Rev. 42 (2013) 3671–3688. https://doi.org/10.1039/C2CS35341E.

[152] A. Zukal, V. Patzelová, U. Lohse, Secondary porous structure of dealuminated Y zeolites, Zeolites. 6 (1986) 133–136. https://doi.org/10.1016/S0144-2449(86)80011-2.

[153] Y. Sasaki, T. Suzuki, Y. Takamura, A. Saji, H. Saka, Structure Analysis of the Mesopore in Dealuminated Zeolite Y by High Resolution TEM Observation with Slow Scan CCD Camera, J. Catal. 178 (1998) 94–100. https://doi.org/10.1006/jcat.1998.2130.

[154] S. Ren, G. Liu, X. Wu, X. Chen, M. Wu, G. Zeng, Z. Liu, Y. Sun, Enhanced MTO performance over acid treated hierarchical SAPO-34, Chinese J. Catal. 38 (2017) 123–130. https://doi.org/https://doi.org/10.1016/S1872-2067(16)62557-3.

[155] W. Khan, X. Jia, Z. Wu, J. Choi, A.C.K. Yip, Incorporating Hierarchy into Conventional Zeolites for Catalytic Biomass Conversions: A Review, Catalysts. 9 (2019) 127–149. https://doi.org/https://doi.org/10.3390/catal9020127.

[156] P. Kortunov, S. Vasenkov, J. Kärger, R. Valiullin, P. Gottschalk, M. Fé Elía, M. Perez, M. Stöcker, B. Drescher, G. McElhiney, C. Berger, R. Gläser, J. Weitkamp, The Role of Mesopores in Intracrystalline Transport in USY Zeolite: PFG NMR Diffusion Study on Various Length Scales, J. Am. Chem. Soc. 127 (2005) 13055–13059. https://doi.org/10.1021/ja053134r.

[157] D. Verboekend, J. Pérez-Ramírez, Design of hierarchical zeolite catalysts by desilication, Catal. Sci. Technol. 1 (2011) 879–890. https://doi.org/10.1039/C1CY00150G.

[158] J. Zhong, J. Han, Y. Wei, P. Tian, X. Guo, C. Song, Z. Liu, Recent advances of the nano-hierarchical SAPO-34 in the methanol-to-olefin (MTO) reaction and other applications, Catal. Sci. Technol. 7 (2017) 4905–4923. https://doi.org/10.1039/C7CY01466J.

[159] A.G. Machoke, A.M. Beltrán, A. Inayat, B. Winter, T. Weissenberger, N. Kruse, R. Güttel, E. Spiecker, W. Schwieger, Micro/Macroporous System: MFI-Type Zeolite Crystals with Embedded Macropores, Adv. Mater. 27 (2015) 1066–1070. https://doi.org/10.1002/adma.201404493.

[160] I. Schmidt, A. Krogh, K. Wienberg, A. Carlsson, M. Brorson, C.J.H. Jacobsen, Catalytic epoxidation of alkenes with hydrogen peroxide over first mesoporous titanium-containing zeolite, Chem. Commun. (2000) 2157–2158. https://doi.org/10.1039/b006460m.

[161] Y. Wei, T.E. Parmentier, K.P. de Jong, J. Zečević, Tailoring and visualizing the pore

architecture of hierarchical zeolites, Chem. Soc. Rev. 44 (2015) 7234–7261. https://doi.org/10.1039/C5CS00155B.

[162] R. Bai, Y. Song, Y. Li, J. Yu, Creating Hierarchical Pores in Zeolite Catalysts, Trends Chem. 1 (2019) 601–611. https://doi.org/10.1016/j.trechm.2019.05.010.

[163] D.P. Serrano, J.M. Escola, P. Pizarro, Synthesis strategies in the search for hierarchical zeolites, Chem. Soc. Rev. 42 (2013) 4004–4035. https://doi.org/10.1039/C2CS35330J.

[164] A. Thomas, F. Goettmann, M. Antonietti, Hard Templates for Soft Materials: Creating Nanostructured Organic Materials, Chem. Mater. 20 (2008) 738–755. https://doi.org/10.1021/cm702126j.

[165] R. Li, P. Wang, S. Ma, F. Yuan, Z. Li, Y. Zhu, Excellent selective catalytic reduction of NOx by NH3 over Cu/SAPO-34 with hierarchical pore structure, Chem. Eng. J. 379 (2020) 122376. https://doi.org/10.1016/j.cej.2019.122376.

[166] R.J. White, A. Fischer, C. Goebel, A. Thomas, A Sustainable Template for Mesoporous Zeolite Synthesis, J. Am. Chem. Soc. 136 (2014) 2715–2718. https://doi.org/10.1021/ja411586h.

[167] K. Jackowska, A.T. Bieguński, M. Tagowska, Hard template synthesis of conducting polymers: a route to achieve nanostructures, J. Solid State Electrochem. 12 (2008) 437–443. https://doi.org/10.1007/s10008-007-0453-7.

[168] J. Zhou, Z. Hua, X. Cui, Z. Ye, F. Cui, J. Shi, Hierarchical mesoporous TS-1 zeolite: a highly active and extraordinarily stable catalyst for the selective oxidation of 2,3,6-trimethylphenol, Chem. Commun. 46 (2010) 4994. https://doi.org/10.1039/c0cc00499e.

[169] T. Pan, Z. Wu, A. Yip, Advances in the Green Synthesis of Microporous and Hierarchical Zeolites: A Short Review, Catalysts. 9 (2019) 274. https://doi.org/10.3390/catal9030274.

[170] P. Prokešová-Fojtíková, S. Mintova, J. Čejka, N. Žilková, A. Zukal, Porosity of micro/mesoporous composites, Microporous Mesoporous Mater. 92 (2006) 154–160. https://doi.org/10.1016/j.micromeso.2005.12.017.

[171] L. Huang, W. Guo, P. Deng, Z. Xue, Q. Li, Investigation of Synthesizing MCM-41/ZSM-5 Composites, J. Phys. Chem. B. 104 (2000) 2817–2823. https://doi.org/10.1021/jp990861y.

[172] Y. Zhu, Z. Hua, J. Zhou, L. Wang, J. Zhao, Y. Gong, W. Wu, M. Ruan, J. Shi, Hierarchical Mesoporous Zeolites: Direct Self-Assembly Synthesis in a Conventional Surfactant Solution by Kinetic Control over the Zeolite Seed Formation, Chem. – A Eur. J. 17 (2011) 14618–14627. https://doi.org/10.1002/chem.201101401.

[173] L. Kong, Z. Jiang, J. Zhao, J. Liu, B. Shen, The Synthesis of Hierarchical SAPO-34 and its Enhanced Catalytic Performance in Chloromethane Conversion to Light Olefins, Catal. Letters. 144 (2014) 1609–1616. https://doi.org/10.1007/s10562-014-1296-3.

[174] X.-Y. Yang, L.-H. Chen, Y. Li, J.C. Rooke, C. Sanchez, B.-L. Su, Hierarchically porous materials: synthesis strategies and structure design, Chem. Soc. Rev. 46 (2017) 481–558. https://doi.org/10.1039/C6CS00829A.

[175] Q. Sun, N. Wang, G. Guo, X. Chen, J. Yu, Synthesis of tri-level hierarchical SAPO-34 zeolite with intracrystalline micro–meso–macroporosity showing superior MTO performance, J. Mater. Chem. A. 3 (2015) 19783–19789. https://doi.org/10.1039/C5TA04642D.

[176] T. Álvaro-Muñoz, C. Márquez-Álvarez, E. Sastre, Enhanced stability in the methanol-to-olefins process shown by SAPO-34 catalysts synthesized in biphasic medium, Catal. Today. 215 (2013) 208–215. https://doi.org/https://doi.org/10.1016/j.cattod.2013.03.015.

[177] Z. Zhou, X. Wang, R. Jiang, X. Chen, H. Hou, Synthesis of stacked spherical hierarchical SAPO-34 zeolite and its methanol to olefin catalytic performance, Adv. Powder Technol. 33 (2022) 103414. https://doi.org/https://doi.org/10.1016/j.apt.2021.103414.

[178] J. Liu, F. Yu, J. Liu, L. Cui, Z. Zhao, Y. Wei, Q. Sun, Synthesis and kinetics investigation of meso-microporous Cu-SAPO-34 catalysts for the selective catalytic reduction of NO with ammonia, J. Environ. Sci. 48 (2016) 45–58. https://doi.org/https://doi.org/10.1016/j.jes.2016.01.027.

[179] T. Zhang, F. Qiu, J. Li, Design and synthesis of core-shell structured meso-Cu-SSZ-13@mesoporous aluminosilicate catalyst for SCR of NO with NH3: Enhancement of activity, hydrothermal stability and propene poisoning resistance, Appl. Catal. B Environ. 195 (2016) 48–58. https://doi.org/10.1016/j.apcatb.2016.04.058.

[180] J. Liu, J. Liu, Z. Zhao, W. Song, Y. Wei, A. Duan, G. Jiang, Synthesis of a chabazite-supported copper catalyst with full mesopores for selective catalytic reduction of nitrogen oxides at low temperature, Chinese J. Catal. 37 (2016) 750–759. https://doi.org/10.1016/S1872-2067(15)61072-5.

[181] P. Wang, Z. Li, X. Wang, Y. Tong, F. Yuan, Y. Zhu, One-pot synthesis of Cu/SAPO-34 with hierarchical pore using cupric citrate as a copper source for excellent NH_3 - SCR of NO performance, ChemCatChem. 12 (2020) 4871–4878. https://doi.org/10.1002/cctc.202000818.

[182] H.S. Shin, I.J. Jang, N.R. Shin, S.H. Kim, S.J. Cho, Dealumination and characterization of chabazite for catalytic application, Res. Chem. Intermed. 37 (2011) 1239–1246. https://doi.org/10.1007/s11164-011-0390-z.

[183] E. Gianotti, J.C.F.P. Brito, I. Miletto, L. Marchese, Rational Design of Hierarchical Porous Cu/Sapo-34 Obtained with Sustainable Templates, SSRN Electron. J. (2022). https://doi.org/10.2139/ssrn.4185991.

[184] L. Liu, Z. Chen, H. Qu, J. Yuan, M. Yu, H. Xie, Q. Zhong, Dual-template assembled hierarchical Cu-SSZ-13: morphology evolution, crystal growth and stable high-temperature selective catalytic reduction performance, CrystEngComm. 22 (2020) 7036–7045. https://doi.org/10.1039/D0CE01144D.

[185] Y. Mi, G. Li, Y. Zheng, Y. Luo, W. Liu, Z. Li, D. Wu, H. Peng, Insights into novel mesoporous Cu-SAPO-34 with enhanced deNOx performance for diesel emission control, Microporous Mesoporous Mater. 323 (2021) 111245. https://doi.org/10.1016/j.micromeso.2021.111245.

[186] Q. Zhang, I. Lee, J.B. Joo, F. Zaera, Y. Yin, Core–Shell Nanostructured Catalysts, Acc. Chem. Res. 46 (2013) 1816–1824. https://doi.org/10.1021/ar300230s.

[187] K. Bakhmutsky, N.L. Wieder, M. Cargnello, B. Galloway, P. Fornasiero, R.J. Gorte, A Versatile Route to Core-Shell Catalysts: Synthesis of Dispersible M@Oxide (M=Pd, Pt; Oxide=TiO2, ZrO2) Nanostructures by Self-Assembly, ChemSusChem. 5 (2012) 140–148. https://doi.org/10.1002/cssc.201100491.

[188] E.A. Khan, E. Hu, Z. Lai, Preparation of metal oxide/zeolite core–shell nanostructures, Microporous Mesoporous Mater. 118 (2009) 210–217. https://doi.org/10.1016/j.micromeso.2008.08.031.

[189] N. Masoumifard, K. Kim, S. Kaliaguine, P.M. Arnal, F. Kleitz, Synthesis of microporous/mesoporous core–shell materials with crystalline zeolitic shell and supported metal oxide silica core, CrystEngComm. 18 (2016) 4452–4464. https://doi.org/10.1039/C6CE00286B.

[190] X.-Y. Yang, L.-H. Chen, Y. Li, J.C. Rooke, C. Sanchez, B.-L. Su, Hierarchically porous materials: synthesis strategies and structure design, Chem. Soc. Rev. 46 (2017) 481–558. https://doi.org/10.1039/C6CS00829A.

[191] J. Zheng, G. Wang, M. Pan, D. Guo, Q. Zhao, B. Li, R. Li, Hierarchical core–shell zeolite composite ZSM-5@SAPO-34 fabricated by using ZSM-5 as the nutrients for the growth of SAPO-34, Microporous Mesoporous Mater. 206 (2015) 114–120. https://doi.org/10.1016/j.micromeso.2014.12.011.

[192] Y. Bouizi, L. Rouleau, V.P. Valtchev, Factors Controlling the Formation of Core−Shell Zeolite−Zeolite Composites, Chem. Mater. 18 (2006) 4959–4966. https://doi.org/10.1021/cm0611744.

[193] J. Zheng, X. Sun, Y. Du, B. Qin, Y. Zhang, H. Zhang, M. Pan, R. Li, Structural features of core–shell zeolite–zeolite composite and its performance for methanol conversion into gasoline and diesel, J. Mater. Res. 31 (2016) 2302–2316. https://doi.org/DOI: 10.1557/jmr.2016.208.

[194] T. Meng, N. Ren, Z. Ma, Silicalite-1@Cu-ZSM-5 core-shell catalyst for N2O decomposition, J. Mol. Catal. A Chem. 404–405 (2015) 233–239. https://doi.org/https://doi.org/10.1016/j.molcata.2015.05.006.

[195] X. Li, F. Rezaei, D.K. Ludlow, A.A. Rownaghi, Synthesis of SAPO-34@ZSM-5 and SAPO-34@Silicalite-1 Core–Shell Zeolite Composites for Ethanol Dehydration, Ind. Eng. Chem. Res. 57 (2018) 1446–1453. https://doi.org/10.1021/acs.iecr.7b05075.

[196] W. Jin, J. Ma, H. Ma, X. Li, Y. Wang, Hydrothermal synthesis of core-shell ZSM-5/SAPO-34 composite zeolites and catalytic performance in methanol-to-aromatics reaction, J. Solid State Chem. 267 (2018) 6–12. https://doi.org/https://doi.org/10.1016/j.jssc.2018.08.004.

[197] Z. Xu, J. Li, W. Qian, H. Ma, H. Zhang, W. Ying, Synthesis of core–shell SAPO-34@SAPO-18 composites by the epitaxial growth method and their catalytic properties for the MTO reaction, RSC Adv. 7 (2017) 54866–54875.

https://doi.org/10.1039/C7RA11395A.

[198] L. Zhang, T. Du, H. Qu, B. Chi, Q. Zhong, Synthesis of Fe-ZSM-5@Ce/mesoporous-silica and its enhanced activity by sequential reaction process for NH3-SCR, Chem. Eng. J. 313 (2017) 702–710. https://doi.org/10.1016/j.cej.2016.12.108.

[199] J. Liu, Y. Du, J. Liu, Z. Zhao, K. Cheng, Y. Chen, Y. Wei, W. Song, X. Zhang, Design of MoFe/Beta@CeO2 catalysts with a core−shell structure and their catalytic performances for the selective catalytic reduction of NO with NH3, Appl. Catal. B Environ. 203 (2017) 704–714. https://doi.org/10.1016/j.apcatb.2016.10.039.

[200] J. Liu, J. Liu, Z. Zhao, Y. Wei, W. Song, Fe-Beta@CeO $_2$ core-shell catalyst with tunable shell thickness for selective catalytic reduction of NO $_x$ with NH $_3$, AIChE J. 63 (2017) 4430–4441. https://doi.org/10.1002/aic.15743.

[201] L. Chen, X. Wang, Q. Cong, H. Ma, S. Li, W. Li, Design of a hierarchical Fe-ZSM-5@CeO2 catalyst and the enhanced performances for the selective catalytic reduction of NO with NH3, Chem. Eng. J. 369 (2019) 957–967. https://doi.org/https://doi.org/10.1016/j.cej.2019.03.055.

[202] Z. Di, H. Wang, R. Zhang, H. Chen, Y. Wei, J. Jia, ZSM-5 core–shell structured catalyst for enhancing low-temperature NH3-SCR efficiency and poisoning resistance, Appl. Catal. A Gen. 630 (2022) 118438. https://doi.org/https://doi.org/10.1016/j.apcata.2021.118438.

[203] H. Peng, G. Li, T. An, Core–Shell Confinement MnCeOx@ZSM-5 Catalyst for NOx Removal with Enhanced Performances to Water and SO2 Resistance BT - Core-Shell and Yolk-Shell Nanocatalysts, in: H. Yamashita, H. Li (Eds.), Springer Singapore, Singapore, 2021: pp. 165–179. https://doi.org/10.1007/978-981-16-0463-8_10.

[204] B.R.S. De Araujo, J.A. Onrubia-Calvo, I. Stambouli, G. Pétaud, J. Hidalgo-Carrillo, A. Nieto-Marquéz, B. Pereda-Ayo, J.R. González-Velasco, A. Caravaca, S. Gil, Towards the development of advanced hierarchical chabazite materials: Novel micro-mesoporous silicoaluminophosphate SAPO-34 zeolites, Mater. Today Commun. 31 (2022) 103580. https://doi.org/10.1016/j.mtcomm.2022.103580.

Chapter II

CHAPTER II: Experimental section

1. Synthesis of micro- and micro-mesoporous (hierarchical) CHA-based zeolites.

The synthesis of novel hierarchical SAPO-34 CHA-based zeolites was accomplished by thoroughly exploring the complementarity between the optimized one-pot hydrothermal crystallization method previously reported by the authors [1,2] and state-of-art hydrothermal routes, in particular soft-templating methods [1–6]. All hierarchical materials were prepared by hydrothermal crystallization method using tetraethylammonium hydroxide (TEAOH) as a microporous template and a secondary organic structure direct agent, CTAB, as mesoporous soft-template. Sequential approaches were explored to control and better understand the heterogeneous nucleation mechanism: a) hydrothermal synthesis of the gel mixture, containing both TEAOH and CTAB (Scheme II. 1), and b) addition of CTAB to the pre-aged microporous gel solution and subsequent hydrothermal synthesis (Scheme II. 2).

1.1. Synthesis of microporous SAPO-34 CHA-based zeolites (micro-SAPO-34).

The SAPO-34 material was synthesized via conventional hydrothermal crystallization method using TEAOH as template with the following molar composition of the initial zeolite gel solution: 1.0 Al_2O_3/1.0 P_2O_5/0.3 SiO_2/3.2 TEAOH/34 H_2O. Detailed description and operation conditions for the preparation of microporous SAPO-34 chabazite can be found in previous works [1,2]. Thus, the TEAOH (Sigma-Aldrich, 35%) is firstly mixed with aluminium isopropoxide ($Al(OPri)_3$, Sigma-Aldrich, 85%) for 90 min, after that the proper amount of silica precursor (Fumed silica, SiO_2, Sigma-Aldrich, CAS 112945-52-5) is stirred with the initial suspension during 30 min until homogeneity. Next, phosphoric acid (85wt% H_3PO_4 CAS 7664-38-2) is diluted with water under stirring for 30 min. Finally, the generated mixture is sealed in an autoclave with Teflon chamber and placed in a furnace at 200°C for 96 hours. This material is denoted as *"Micro (Fumed silica)"* in supporting information Chapter III.

For comparison purpose, however, the time of crystallization and the nature of the silica precursor were optimized, concluding that 48 h are needed to obtain a crystalline SAPO-34 phase using Tetraethyl orthosilicate (TEOS) (used as a Si precursor, Sigma-Aldrich, 98%) (Supporting Information Chapter III). Thus, the previous described zeolite gel solution was hydrothermally synthetized at 200 °C for 48 h in a Teflon-lined stainless-steel autoclave (TOP Industries ASA, reference number 2071 000, volume: 0.025 L). This material is denoted as *"Micro"* in the next chapters of the present manuscript.

After crystallization, the materials were centrifuged, washed and dried at 110 °C overnight. Finally, the synthesized powders were calcined at 550 °C for 6 h in synthetic air (total flow rate = 4.5 L · h^{-1}) to remove the template.

1.2. Synthesis of SAPO-34 hierarchical CHA-based zeolites.

a) One-pot hydrothermal crystallization method (One-pot Meso).

The hierarchical SAPO-34 CHA-based zeolites were prepared by one-pot hydrothermal crystallization method (Scheme II. 1) using TEAOH as a microporous template, and a secondary mesoporous template cetyltrimethylammonium bromide (CTAB). The main idea behind this method is the formation of surfactant micelles, which serve as templates for the mesostructure, while TEAOH promotes the crystallization of the zeolite [5,7]. The molar composition of zeolite gel solution was: 1.0 Al_2O_3/1.0 P_2O_5/0.3 SiO_2/3.2 TEAOH/0.3 CTAB/8.8 EtOH/80 H_2O.

Firstly, the aluminum isopropoxide was mixed with a solution of phosphoric acid (Sigma-Aldrich, 85%) diluted in water and stirred for 2 h. The TEAOH was then added to the mixture and stirred for 2 h. Finally, a solution containing Si precursor, TEOS (Sigma-Aldrich, 98%), the secondary template CTAB (Sigma-Aldrich, 98%), and a biphasic mixture of water and ethanol, were added to the mixture and stirred for another 2 h. Note that the ethanol was used as a self-assembly modulator, which favors the self-assembly of nanocrystalline zeolite seeds under the direction by mesopore secondary organic structure direct agent, CTAB [8,9]. The resulting gel was then transferred into a 100 mL Teflon-lined stainless-steel autoclave and heated at 200 °C and autogenous pressure for 48 h. As for the microporous material, after crystallization, the product was thoroughly washed with water and then dried at 110 °C overnight, followed by calcination at 550 °C for 6 h. This material is denoted as *"One-pot Meso"*.

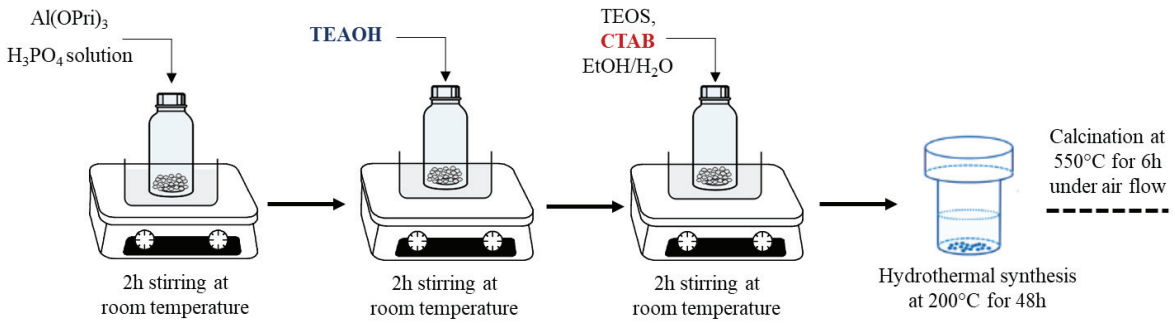

Scheme II.1. Synthesis of hierarchical SAPO-34 by one-pot hydrothermal.

b) Aging heat method and hydrothermal crystallization (Aged Meso).

As previously mentioned, the presence of both templates in the starting gel solution could eventually result in a microporous zeolite crystal embedded in a physical mixture containing mesoporous structures [4,9,10]. In order to overcome this issue, an additional step was implemented before the incorporation of CTAB to the microporous gel solution (Scheme II. 2). The molar composition of the zeolite gel solution was: 1.0 Al_2O_3/1.0 P_2O_5/0.3 SiO_2/3.2 TEAOH/0.3 CTAB/8.8 EtOH/80 H_2O.

Firstly, the $Al(OPri)_3$ and TEAOH were mixed at room temperature. After stirring for 90 min, the Si precursor, TEOS, was added and stirred for 1 h. The solution was mixed with the a H_3PO_4 solution and stirred for 3 h at room temperature. This solution, containing TEOS, $Al(OPri)_3$ and H_3PO_4 as Si, Al and P precursors and TEAOH as a microporous template, was aged in a sealed Schott Duran bottle at 100 °C for 64 h under continuous stirring, to form nanocrystalline zeolite seeds. After aging, the solution was mixed with CTAB solution at 100 °C. After stirring for 2 h, absolute ethanol was added to the mixture and stirred for 3 h at 100 °C. This solution was placed in a Teflon-lined stainless-steel autoclave at 200 °C under autogenous pressure for 24 h for hydrothermal crystallization. After crystallization, the sample was washed, dried at 110 °C overnight and finally calcined at 550 °C for 6 h. This sample is firstly denoted as *"Aged Meso-0.15"*.

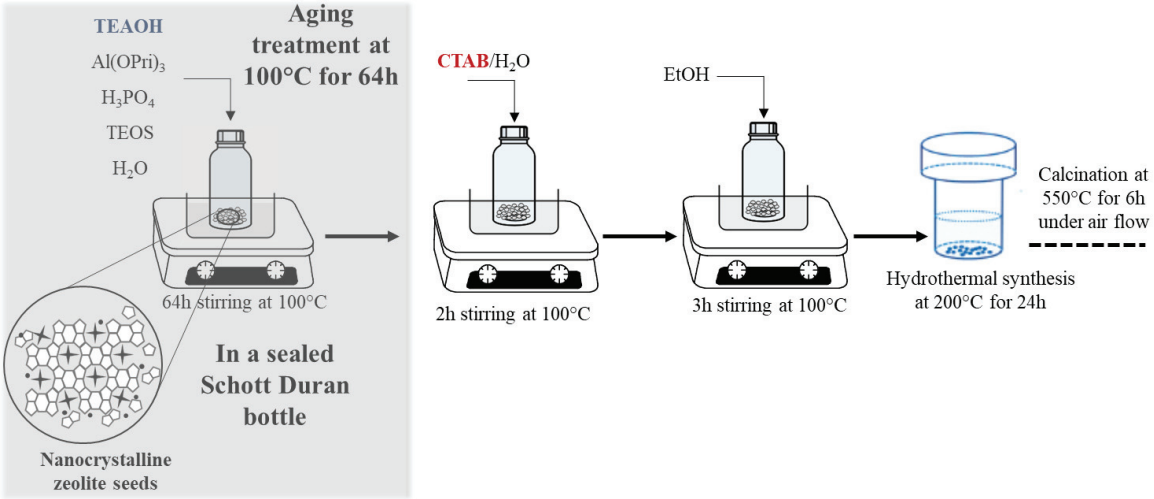

Scheme II. 2. Synthesis of hierarchical SAPO-34 by aging heat hydrothermal crystallization method.

The effect of aging time of hierarchical SAPO-34 zeolites was also evaluated by varying the aging time between 24, 48 and 64 h (before addition of CTAB template and hydrothermal crystallization). The same procedure and precursor amounts were used. These materials are

denoted as *"Aged Meso-24h", "Aged Meso-48h"* and *"Aged Meso-64h"*, respectively. Note that the last one ("*Aged meso-64h*") corresponds to the previously denoted "*Aged Meso-0.15*" material.

Moreover, the mesoporosity of the hierarchical materials was adjusted by varying the amount of the secondary mesoporous template (CTAB) of the samples aged during 64 h. The molar compositions of the precursor mixtures were: 1.0 Al_2O_3/1.0 P_2O_5/0.3 SiO_2/3.2 TEAOH/x CTAB/8.8 EtOH/80 H_2O (with x = 0.33, 0.66 and 1.33). These hierarchical CHA-based zeolites are denoted as *"Aged Meso-0.15", "Aged Meso-0.33" and "Aged Meso-S-0.66"* based on the molar ratio of CTAB/Al of 0.15, 0.33 and 0.66, respectively. Note that the first one ("*Aged Meso-0.15*") corresponds to the previously denoted as "*Aged Meso-64h*".

2. Synthesis of microporous and hierarchical Cu-based SAPO-34 catalysts.

First of all, both microporous and hierarchical SAPO-34 zeolite supports were synthesized as described above [11]. Briefly, the microporous SAPO-34 zeolite was prepared via hydrothermal crystallization using TEAOH as template with the following molar composition of the initial zeolite gel solution: 1.0 Al_2O_3/1.0 P_2O_5/0.3 SiO_2/3.2 TEAOH/34 H_2O. This microporous zeolite support is denoted as *"Micro-fresh (support)"*. Regarding the hierarchical zeolite supports, the aging method followed by hydrothermal crystallization was used to synthetized the Cu-based hierarchical catalysts. After crystallization, the support was washed, dried at 110 ^oC overnight and finally calcined at 550 ^oC for 6 h. Two hierarchical materials were selected as catalytic supports. The molar compositions of the precursor mixtures were: 1.0 Al_2O_3/1.0 P_2O_5/0.3 SiO_2/3.2 TEAOH/*x* CTAB/8.8 EtOH/80 H_2O (with x = 0.33 and 1.33). These hierarchical SAPO-34-based zeolite supports are denoted as *"0.15-fresh (support)"* and *"0.66-fresh (support)"* based on the molar ratio of CTAB/Al of 0.15 and 0.66, respectively.

The Cu-loaded catalysts were prepared by two steps ionic exchange (IE) method over the above described zeolite supports, Scheme II.3. The first IE step was performed under an excess of 0.1M NH_4NO_3 (98 wt.%, Sigma-Aldrich) solution at 70 ^oC for 4 h, in order to generate NH_4/SAPO-34-based materials. After washing, separating and drying the solid materials, a 0.01 M $Cu(OAc)_2$ solution (99 wt.%, Aldrich) was heated at 80 ^oC and added to the NH_4-SAPO-34 zeolites during vacuum filtration by using a Büchner funnel. This latter filtration step was performed three times to assure a proper Cu incorporation (2%wt. Cu nominal loading target) on the zeolite supports. After that, the catalyst was washed, dried at 110 ^oC overnight and finally

calcined at 550 ºC for 6 h. The catalysts obtained are denoted as "*Cu/micro-fresh*", "*Cu/0.15-fresh*", and "*Cu/0.66-fresh*", which were prepared on the *"Micro-fresh (support)"*, *"0.15-fresh (support)"* and *"0.66-fresh (support)"*, respectively.

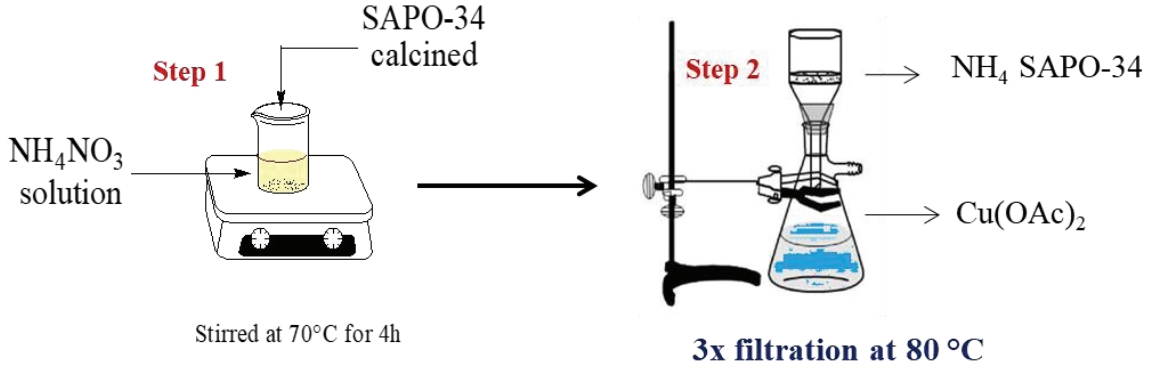

Scheme II. 3. Synthesis of Cu-loaded catalysts by two steps ionic exchange (IE) method.

3. Hydrothermal treatment of Cu-hierarchical based catalysts.

The hydrothermal treatment of the above described Cu-based catalysts, both microporous and hierarchical, was performed under a gas stream of 10% steam in air at 750 ºC. Water was introduced by means of a temperature-controlled saturator. The total gas flow (Air + H_2O) was 100 mL min^{-1}. The catalysts obtained after the hydrothermal treatment are denoted as *"Cu/micro-HT"*, *"Cu-0.15-HT"*, and "*Cu-0.66-HT"*, which were prepared by subjecting to the hydrothermal treatment the *"Cu/micro-fresh"*, *"Cu/0.15-fresh"* and *"Cu/0.66-fresh"* catalysts, respectively. *"*

4. Synthesis of core-shell structures.

The second objective of this PhD is the development of core-shell catalysts with metal-loaded hierarchical CHA-zeolites. The Fe-based shell will be synthesized onto the Cu-based core using a self-assembly method followed by a secondary hydrothermal growth promoted by a seed precursor solution [6,12,13]. This multi-steps method was selected due to its versatility. Several approaches were used to optimize the formation of a core-shell, which will be described in detail in Chapter V. Nevertheless, a general description will present below.

The main methodology used to achieve the formation of novel core-shell materials involves several steps, Scheme II. 4, and uses, as a starting point the core catalyst (Cu-loaded hierarchical CHA-zeolite catalysts) and the zeolite seed (seed layer with composition equivalent to shell zeolite without metal loading). The first step will be the surface modification of the

negatively charged core catalyst by a polyelectrolyte for example cationic surfactant CTAB that will transfer charges to the core material. This surface modification is a critical step for the formation of uniform zeolite shell as it will facilitate the effective interaction between core and shell materials [6]. The next step is the adjunction of seeds onto the core, i.e. the adsorption of negatively charged seed on the external surface of core crystal, which will induce a faster growth of the shell [6]. The next step is the secondary shell growth using a conventional hydrothermal crystallization method. For this step, the core catalyst with its surface seeds will be immersed in a solution containing the precursor of shell CHA-zeolite, and will be subjected to a secondary hydrothermal treatment inducing crystallization. After that, the core-shell material will be washed, dried at 110 °C overnight and finally calcined at 550 °C for 6 h. Finally, the obtained core-shell materials will be loaded with iron species by conventional ion-exchange method.

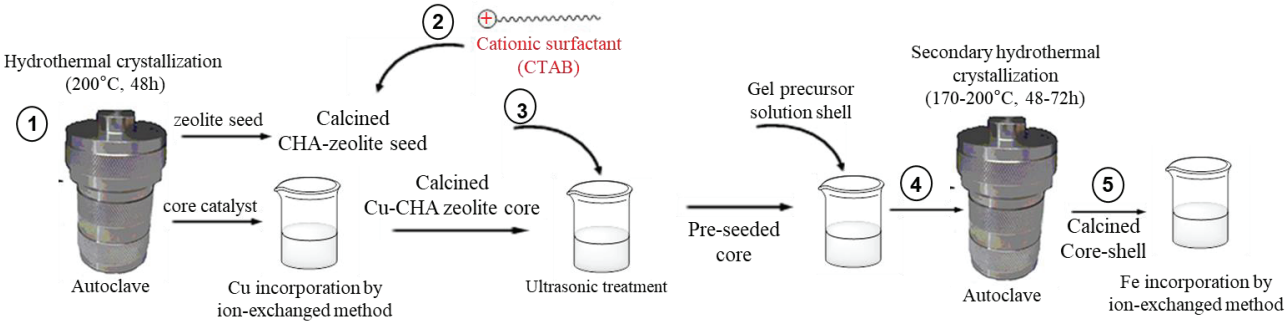

Scheme II. 4. Core-shell synthesis steps: **1)** Preparation of core catalyst and zeolite seed, **2)** surface modification of core catalyst, **3)** core seeding (suspension ultrasonically treated), **4)** secondary shell growth and **5)** Fe-incorporation by ion-exchanged method.

A main risk is to achieve only low control on core-shell attractions and secondary growth, hence low control on the structure of the targeted architectures, due to the cross influence of several parameters during synthesis. To limit this risk, the zeolite crystal size, the pH, the type of polyelectrolyte for surface modification (CTAB and TEAOH), the previous treatment of the core and/or seed shell prior to secondary hydrothermal crystallization, *etc.* were modified and will be presented in Chapter V.

4.1. Zeta Potential measurements.

The zeta potential measurements were carried out to evaluate the surface charges of core and seed shell materials before and after surface modification with above-mentioned polyelectrolytes during the development of core-shell structures. Indeed, the zeta potential is

correlated to the surface charge of nanoparticles in a colloidal solution (colloids in suspension) [14]. A charged particle will move with a fixed velocity in a voltage field. This phenomenon is called electrophoresis. The mobility of the particles is related to i) the dielectric constant and viscosity of the colloid liquid suspension and ii) the electrical potential at the interface between the moving particle and the liquid. Thus, the electrical potential, which is called zeta potential, could be related to the mobility of the particle.

The Zeta Potential Analyzer (*Zetaphoremeter*) measures the potential of colloidal particles based on their movement and trajectory in response to a known applied voltage. The voltage is applied between two electrodes, which are in separate compartments. The voltage applied produces a homogenous electric field, and in the connect chamber between the two compartments, the attracted particles travel toward the electrode. Thus, zeta potential is measured by tracking the motion of charged particles in an applied voltage field. As previously mentioned, this is a direct measurement called electrophoretic mobility. Electrophoretic mobility is, therefore, a relative measure of how fast a particle moves in an electric field. Zeta potential can be calculated from the measured electrophoretic mobility using a theoretical relation between the two that is also dependent on the dielectric constant and the viscosity of the suspending liquid.

The zeta potential analysis was performed on the Zetaphoremeter IV model Z4000. The preparation of the colloidal solution required the preparation of two solutions. The first one consists of 20 mg of the material to be analyzed, which is dispersed in 100 ml of water and kept under ultrasound for 30 min to guarantee a proper dispersion. To obtain the colloidal solution 5 mL of the first solution is diluted in 50 mL of water. The analysis was carried out at different basic pHs levels, and the pH change was adjusted manually using drops of a solution of 0.5 mL of NH_4OH in 10 mL.

5. Supports and catalysts characterization.

5.1. Inductively coupled plasma optical emission spectroscopy (ICP-OES).

The chemical composition of the zeolites and Cu loading of catalysts (before and after the hydrothermal treatment) was quantitatively assessed by inductively coupled plasma optical emission spectroscopy (ICP-OES) on an Activa instrument from Horiba Jobin Yvon. Before the measurement, the zeolite-based materials were dissolved using a mixture of lithium tetra-borate and hydrofluoric acid (HF) and a mixture of inorganic acids (H_2SO_4, HNO_3 and HF) for Si and P and Al determination, respectively.

5.2. *Thermogravimetric analyses (TGA).*

Thermogravimetric analyses (TGA) were carried out over the dried samples (non-calcined materials) in the temperature range 25–700 °C (5 °C · min^{-1}) on a Thermobalance Mettler MX1, using 5 mg of sample, under flowing air (5 mL · min^{-1}).

5.3. *Wide-angle and low-angle X-ray Diffraction (XRD).*

The zeolite formation and crystalline structure of synthetized SAPO-34-based zeolite, as well as the creation of ordered mesopores, were characterized by wide-angle and low-angle X-ray Diffraction (XRD), respectively. XRD is based on the diffracted ray produced by the interaction of monochromatic X-rays generated by a cathode ray tube, and a crystalline sample. The law of Bragg, equation (1) relates the wavelength of electromagnetic radiation to the diffraction angle and the lattice spacing in the crystalline sample. To identify the phases on the material, the diffraction peaks obtained through a range of 2θ angles, are converted to d-spacing and compared with standard reference patterns.

$$2 \cdot d_{hkl} \cdot \sin\theta = n \cdot \lambda \quad (1)$$

where: d_{hkl} is the lattice spacing, θ is the angle of incidence (rad), n is the integer and λ is the wavelength of the incident X-ray beam (Å).

For that, a Bruker D8 diffractometer (0.154184 nm CuK radiation) equipped with a Ni filter and 1-D fast multistrip detector (LynxEye, 192 channels on 2.95) was used. The diffractograms were taken at 2θ steps with a 0.02° increment. For phase identification and for crystallinity calculus, Bruker's Diffrac.Eva program and the ICDD-PDF4 + database were used.

Note that for calculation of crystallinity, EVA program is based on the global area of crystallinity and the reduced area related to the amorphous area.

$$\%\ Amorphous = \frac{Global\ area - reduced\ area}{Global\ area}\ x\ 100 \quad (2)$$

5.4. *N_2-adsoprtion/desorption.*

The creation of mesoporores in the original chabazite-based materials, to form hierarchical structures, the effect of Cu incorporation and hydrothermal treatment on the physico-chemical properties of the catalysts were evaluated by N_2-adsoprtion/desorption at -196 ºC. Nitrogen adsorption represents the most widely used technique to determine catalyst surface area and to characterize its porous texture. Gas molecules close to the solid surface area are attracted by forces arising from solid-surface atoms. In order to measure de adsorption, the

quantity of a nitrogen gas molecule on the solid surface at different partial pressure is determined at constant temperature (isotherm). The adsorption isotherm obtained is characteristic of each material and the quantity of gas adsorbed can provide a measure of surface area. According to IUPAC classification [15] six types can be distinguished, but only four are usually found in catalyst characterization, Figure II-1.

Once saturation is reached, the adsorbate desorption takes place. However, the evaporation usually takes place at a pressure lower than that of capillary condensation giving a hysteresis. This is due to pore shape and four types of hysteresis have been recognized, according to IUPAC classification [15], Figure II-2.

A Micromeritics ASAP 2020 specific surface area and porosity analyzer was used for N_2-adsorption/desorption measurements. Prior to the measurements, the samples were outgassed at 400 °C for 4 h under vacuum. At $P/P_0 < 0.3$, the specific surface area (S_{BET}) was determined using the multipoint Brunauer-Emmett-Teller (BET) analysis. The model developed by Brunauer, Emmet and Teller in 1940s [16], still remains the most used method to determine the specific surface area of a porous material. They defined an equation for multimolecular adsorption using a generalization method of Langmuir's treatment of unimolecular layer [17]. Thus, the specific surface area S_{BET} of solids would be calculated by the equation (3):

$$S_{BET} = \frac{V \cdot N_A \cdot \sigma}{V_m \cdot m} \qquad (3)$$

where: S_{BET} is the specific surface area ($m^2 g^{-1}$), V is the volume of N_2 adsorbed (mL), N_A is the Avogadro number ($6.023 \cdot 10^{23}$ molecules mol^{-1}), σ is the area covered by one nitrogen molecule (generally 0.162 nm^2), V_m is the molar volume (mL mol^{-1}) and m is the masse of the analyzed sample.

Pore size distribution and the corresponding data were determined by using Horvath-Kawazoe (HK) and Barrett-Joyner-Halenda (BJH) methods for microporous and mesoporous size distribution, respectively. Both of them were applied to the desorption branch.

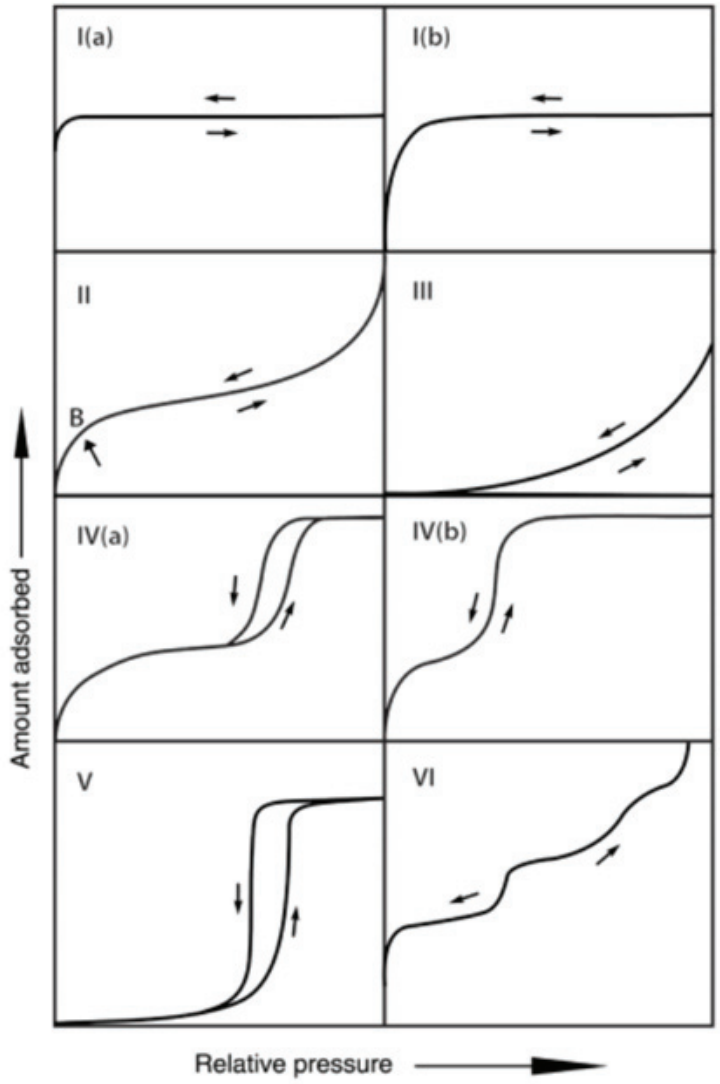

Figure II.1. IUPAC Classification of Isotherms [15].

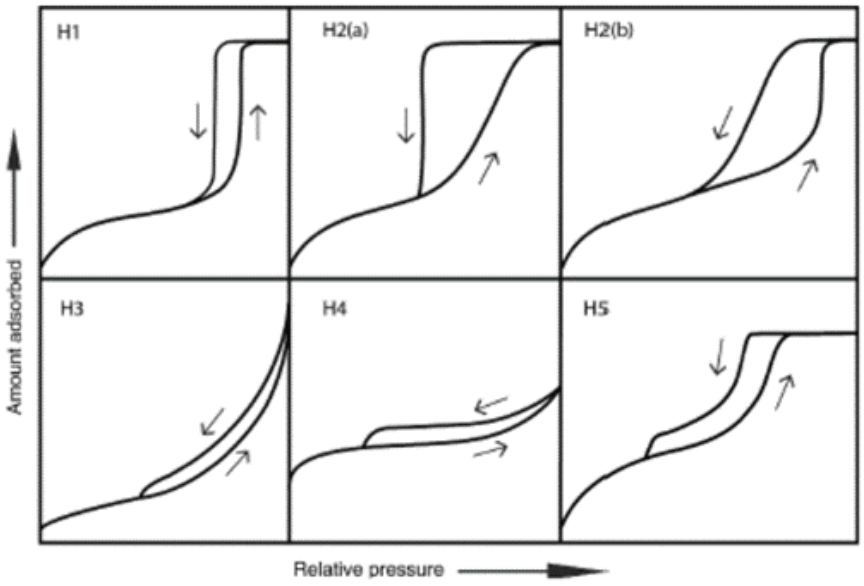

Figure II. 2. IUPAC Classification of Hysteresis Loops [15].

5.5. *Magic Angle Spinning Nuclear Magnetic Resonance (MAS NMR).*

Magic Angle Spinning Nuclear Magnetic Resonance (MAS NMR) semi-quantitative technique was employed to identify the different chemical bulk architectures of zeolites. The ^{27}Al, ^{29}Si and ^{31}P MAS NMR measurements were performed on Bruker AVANCE III 500 WB spectrometer at resonance frequencies of 130, 99 and 202 MHz, respectively. A sample spinning rates of 10 kHz was used in a commercial 2.5 mm MAS probe at room temperature.

5.6. *Transmission Electron Microscopy (TEM) and Environmental TEM (E-TEM).*

The existence of intracrystalline mesoporosity was evaluated by Transmission Electron Microscopy (TEM) using a JEM-2100 microscope with EDX detector. All samples are embedded in epoxy resin before cutting by ultramicrotomy. The method of epoxy impregnation in combination with ultramicrotomy can produce thin section specimens with a uniform thickness. The cuts are collected on a grid to be observed in TEM. Special attention was paid to the creation and distribution of wall-crystallized mesopores.

The high-resolution environmental TEM (E-TEM) were carried out to prove the formation of core-shell structure. A FEI TITAN environmental microscope (80–300 keV), with a spherical aberration corrector and equipped with an EDS detector, was used for this purpose. E-TEM analysis require stable catalysts. The equipment radiation damages the zeolite material structure; therefore, the images were captured swiftly. In order to prepare the samples for E-TEM analysis, a little amount of sample powder was ground in a mortar and pestle, diluted in alcohol, and kept in ultrasound per 5 min. Drops of the solution were put on a microscope grid specific for the studies (a MEMS SiNx chip adapted for a DensSolutions heating holder or a 200-mesh holey-carbon copper grid adapted to the high-tilt Fischione 2020 holder).

5.7. *Temperature programmed desorption of ammonia (NH_3-TPD).*

Temperature-Programmed ammonia Desorption (NH_3-TPD) was used to assess the acidic properties (relative quantity and strength of acid sites) of the target catalysts. Samples were loaded into a U-shaped quartz tube to acquire the NH_3-TPD profiles. All samples were initially pre-treated at 500°C for 0.5 h in an oxidative environment (10% O_2, 20 mL min^{-1}, heating rate of 10 ^oC min^{-1}). After 0.5 h, a He stream (20 mL min^{-1}) was introduced, and the temperature was decreased to 150 ^oC, where NH_3 adsorption occurred (a total flow of 40 mL min^{-1} of 1000 ppm NH_3 was introduced until saturation). After that, the samples were exposed to He for 0.5 h to eliminate the physically adsorbed species. Then, the NH_3-desorption

experiments were performed by heating (at 2 °C min^{-1}) from 150 to 500 ºC. A NICOLET Fourier Transform Infrared (FTIR) analyzer, equipped with a heated 2 m gas cell and a DTGS detector, was used to continually monitor desorbed ammonia. For semi-quantitative deconvolution, all profiles were fitted using the Gaussian approach.

5.8. *Temperature programmed reduction (H_2-TPR).*

The reducibility of the samples was investigated by temperature programmed reduction (H_2-TPR) experiments using a Micromeritics AutoChem II equipment. The quartz tube reactor was loaded with 0.1 g of sample and pretreated under a gas stream of 30 mL min^{-1} of 5% O_2/He mixture at 500 °C for 0.25 h to remove adsorbed water and impurities as well as to ensure reducible species total oxidation, and then cooled down to 35 °C. Afterwards, samples were heated from 35 to 900 °C (heating rate of 10 °C min^{-1}) in a 5% H_2/Ar gas mixture (30 mL min^{-1}). Water generated during sample reduction was removed by using a cold trap before gas analysis by a thermal conductivity detector.

5.9. *Diffuse Reflectance Infrared Fourier Transform Spectroscopy (DRIFTS).*

Diffuse Reflectance Infrared Fourier Transform Spectroscopy (DRIFTS) was used to determine the zeolite framework modifications on account of the incorporation of Cu species in the ionic exchange sites of the support. Two different probe molecules (NH_3 and CO) were used. The DRIFTS studies were performed in a NICOLET FTIR analyzer, equipped with a *Praying Mantis* (Harris Scientific). Prior the measurements, the catalysts were subjected to a pre-treatment at 500 °C under a gas stream of 10% O_2 (20 mL min^{-1}, heating rate of 10 ºC min^{-1}) for 0.5 h. Then, the cell was cooled down to 35 ºC, and the adsorption process was carried out under a gas composition of 1000 ppm of the probe molecule (NH_3 or CO). After He sweeping (to remove the physically adsorbed species), DRIFTS spectra were acquired under He at 35°C.

6. Catalytic performance evaluations: NH_3-SCR reaction.

The SCR experiments were performed in a down-flow stainless steel reactor. The reactor tube, with 0.15 g of 0.3–0.5 mm pelletized catalysts inside, was located into a three-zone tube furnace. The temperature was measured by a thermocouple at the top of the catalyst bed. The reaction temperature was varied from 100 to 450 °C in steps of 50 °C. The composition of the feed gas mixture was 650 ppm NO (610-620 ppm NO + 30-40 ppm NO_2 under equilibrium), 650 ppm NH_3, 6% O_2 and 5% of H_2O using Ar as the balance gas. Gases were

fed via mass flow controllers, and the total flow rate was set at 730 mL min^{-1}, which corresponded to a space velocity (gas hourly space velocity) of 115.000 h^{-1}. The NO, NO_2, NH_3, and N_2O concentrations at the reactor exit were continuously monitored by an online Fourier transform infrared (FTIR) multigas analyzer (MKS 2030). The used setup is presented in Figure II. 3.

Figure II. 3. Experimental setup for NH_3-SCR measurements.

- ***Feed system:*** The feeding system contains separate lines for the reagents NO, NH_3, NO_2, and O_2. The water vapor was introduced via a saturator. Flow management is accomplished by valves and flowmeter, as previously mentioned. To prevent ammonium nitrate precipitation from obstructing the system lines during NH_3-SCR operation, all system lines were heated to 200 °C [18]. The standard SCR reaction operating conditions were 650 ppm NO, 650 ppm NH_3, 5% H_2O, and 6% O_2.
- ***Reaction system:*** In down-flow stainless steel reactor, 0.15 g of 0.3–0.5 mm pelletized catalyst was introduced. The reactor was located into a three-zone tube furnace, and the temperature was monitored by a K-type thermocouple placed at the top of the catalyst bed and controlled by the oven temperature controller.
- ***Analysis system:*** The reactants and by-products were continuously monitored by an online Fourier transform infrared (FTIR) multigas analyzer (MKS 2030).

Once different compound concentrations were stabilized for at least 0.25 h, the catalytic parameters were determined. The NO (X_{NO}) and NH_3 (X_{NH_3}) conversions were determined according to:

$$X_{NO}(\%) = \frac{F_{NO}^{in} - F_{NO}^{out}}{F_{NO}^{in}} \quad (4)$$

$$X_{NH_3}(\%) = \frac{F_{NH_3}^{in} - F_{NH_3}^{out}}{F_{NH_3}^{in}} \quad (5)$$

where $F_{NH_3}^{in}$ and $F_{NH_3}^{out}$ are the molar flow (µmol min^{-1}) of NH_3 in the inlet and the outlet, respectively; meanwhile, F_{NO}^{in} and F_{NO}^{out} are the molar flow (µmol min^{-1}) of the NO in the inlet and the outlet.

Furthermore, the catalytic behavior of the SCR system was evaluated in terms of the selectivity towards the different nitrogen containing products (NO_2, N_2O and N_2).

$$S_{NO_2}(\%) = \frac{F_{NO_2}^{out}}{F_{NH_3}^{in} \times X_{NH_3} + F_{NO}^{in} \times X_{NO}} \quad (6)$$

$$S_{N_2O}(\%) = \frac{2\ xF_{N_2O}^{out}}{F_{NH_3}^{in} \times X_{NH_3} + F_{NO}^{in} \times X_{NO}} \quad (7)$$

$$S_{N_2}(\%) = \frac{2 \times F_{N_2}^{out}}{F_{NH_3}^{in} \times X_{NH_3} + F_{NO}^{in} \times X_{NO}} \quad (8)$$

where $F_{NO_2}^{out}$, $F_{NH_3}^{out}$, $F_{N_2O}^{out}$ and $F_{N_2}^{out}$ are the molar flow (µmol min^{-1}) of NH_3, N_2O and N_2 at the reactor outlet, respectively.

Finally, the NO reaction rate was estimated as follow:

$$r_{STD\ SCR}^{NO} = \frac{F_{NO}^{in}\ x\ X_{NO}}{m_{cat}\ \times\ \%wt_{Cu}} \quad (9)$$

with $r^{NO}{}_{STD\ SCR}$ = reaction rates (mol_{NO} min^{-1} g_{Cu}^{-1}), F_{NO}^{in} is the molar flow (mol min^{-1}) of NO in the reactor inlet, X_{NO} is the NO conversion, m_{cat}= sample mass (g) and $\%wt._{Cu}$ = Weight Copper percentage from ICP OES results.

References

[1] G. Pétaud, F. Gaillard, M. Tayakout, S. Gil, A. Giroir-Fendler, Spotlight on Large Surface Copper Cluster Role of Cu-SAPO-34 Catalyst in Standard NH3-SCR Performances, ChemCatChem. 12 (2020) 2807–2822. https://doi.org/10.1002/cctc.201902036.

[2] G. Pétaud, S. Gil, A.G. Fendler, Cu SAPO 34 One Pot Hydrothermal Preparation Method for Particular Copper Configuration, Top. Catal. 62 (2019) 63–71. https://doi.org/10.1007/s11244-018-1107-y.

[3] L. Jin, S. Liu, T. Xie, Y. Wang, X. Guo, H. Hu, Synthesis of hierarchical ZSM-5 by cetyltrimethylammonium bromide assisted self-assembly of zeolite seeds and its catalytic performances, React. Kinet. Mech. Catal. 113 (2014). https://doi.org/10.1007/s11144-014-0743-x.

[4] J. Zhong, J. Han, Y. Wei, P. Tian, X. Guo, C. Song, Z. Liu, Recent advances of the nano-hierarchical SAPO-34 in the methanol-to-olefin (MTO) reaction and other applications, Catal. Sci. Technol. 7 (2017) 4905–4923. https://doi.org/10.1039/C7CY01466J.

[5] A. Feliczak-Guzik, Hierarchical zeolites: Synthesis and catalytic properties, Microporous Mesoporous Mater. 259 (2018) 33–45. https://doi.org/https://doi.org/10.1016/j.micromeso.2017.09.030.

[6] N. Masoumifard, R. Guillet-Nicolas, F. Kleitz, Synthesis of Engineered Zeolitic Materials: From Classical Zeolites to Hierarchical Core–Shell Materials, Adv. Mater. 30 (2018) 1704439. https://doi.org/10.1002/adma.201704439.

[7] X.-Y. Yang, L.-H. Chen, Y. Li, J.C. Rooke, C. Sanchez, B.-L. Su, Hierarchically porous materials: synthesis strategies and structure design, Chem. Soc. Rev. 46 (2017) 481–558. https://doi.org/10.1039/C6CS00829A.

[8] S. Hu, H. Jia, J. Ma, W. Hao, R. Li, A hierarchical zeolite microsphere prepared by an eco-friendly and practical route for efficient reaction of bulky molecules, Microporous Mesoporous Mater. 294 (2020) 109931. https://doi.org/https://doi.org/10.1016/j.micromeso.2019.109931.

[9] Y. Zhu, Z. Hua, J. Zhou, L. Wang, J. Zhao, Y. Gong, W. Wu, M. Ruan, J. Shi, Hierarchical Mesoporous Zeolites: Direct Self-Assembly Synthesis in a Conventional

Surfactant Solution by Kinetic Control over the Zeolite Seed Formation, Chem. – A Eur. J. 17 (2011) 14618–14627. https://doi.org/10.1002/chem.201101401.

[10] L. Kong, Z. Jiang, J. Zhao, J. Liu, B. Shen, The Synthesis of Hierarchical SAPO-34 and its Enhanced Catalytic Performance in Chloromethane Conversion to Light Olefins, Catal. Letters. 144 (2014) 1609–1616. https://doi.org/10.1007/s10562-014-1296-3.

[11] B.R.S. De Araujo, J.A. Onrubia-Calvo, I. Stambouli, G. Pétaud, J. Hidalgo-Carrillo, A. Nieto-Marquéz, B. Pereda-Ayo, J.R. González-Velasco, A. Caravaca, S. Gil, Towards the development of advanced hierarchical chabazite materials: Novel micro-mesoporous silicoaluminophosphate SAPO-34 zeolites, Mater. Today Commun. 31 (2022) 103580. https://doi.org/10.1016/j.mtcomm.2022.103580.

[12] J. Zheng, G. Wang, M. Pan, D. Guo, Q. Zhao, B. Li, R. Li, Hierarchical core–shell zeolite composite ZSM-5@SAPO-34 fabricated by using ZSM-5 as the nutrients for the growth of SAPO-34, Microporous Mesoporous Mater. 206 (2015) 114–120. https://doi.org/10.1016/j.micromeso.2014.12.011.

[13] Y. Bouizi, L. Rouleau, V.P. Valtchev, Factors Controlling the Formation of Core−Shell Zeolite−Zeolite Composites, Chem. Mater. 18 (2006) 4959–4966. https://doi.org/10.1021/cm0611744.

[14] S. Mohammadi-Jam, K.E. Waters, R.W. Greenwood, A review of zeta potential measurements using electroacoustics, Adv. Colloid Interface Sci. 309 (2022) 102778. https://doi.org/https://doi.org/10.1016/j.cis.2022.102778.

[15] M. Thommes, K. Kaneko, A. V Neimark, J.P. Olivier, F. Rodriguez-Reinoso, J. Rouquerol, K.S.W. Sing, Physisorption of gases, with special reference to the evaluation of surface area and pore size distribution (IUPAC Technical Report), Pure Appl. Chem. 87 (2015) 1051–1069. https://doi.org/https://doi.org/10.1515/pac-2014-1117.

[16] G. Leofanti, M. Padovan, G. Tozzola, B. Venturelli, Surface area and pore texture of catalysts, Catal. Today. 41 (1998) 207–219. https://doi.org/https://doi.org/10.1016/S0920-5861(98)00050-9.

[17] S. Brunauer, P.H. Emmett, E. Teller, Adsorption of Gases in Multimolecular Layers, J. Am. Chem. Soc. 60 (1938) 309–319. https://doi.org/10.1021/ja01269a023.

[18] H. Nishiyama, Y. Tanaka, T. Adachi, S. Kawamura, Y. Daisho, H. Suzuki, H. Ishii, K. Yamaguchi, A Study on the Improvement of NOx Reduction Efficiency for a Urea SCR System, in: 2015. https://doi.org/10.4271/2015-01-2014.

Chapter III

CHAPTER III: Towards the development of advanced hierarchical chabazite materials: novel micro-mesoporous silicoaluminophosphate SAPO-34 zeolites.

The target of chapter III is to develop and thoroughly characterize novel hierarchical CHA based-materials in order to improve their performance in the NO_x-reduction under *cold-start* operating conditions, i.e. low-temperature NH_3-SCR activity. The synthesis of novel hierarchical SAPO-34 CHA-based zeolites was accomplished by thoroughly exploring the complementarity between the optimized one-pot hydrothermal crystallization method previously reported by our group [1,2] and state-of-art hydrothermal routes, in particular soft-templating methods [1–6]. A cationic surfactant, such as cetyltrimethylammonium bromide (CTAB) was used as a secondary soft template in addition to tetraethylammonium hydroxide (TEAOH) as a microporous template. As explained in the *Chapter I*, the CTAB interacts with the reactant raw materials (negatively charged) with the subsequent formation of mesoporous structures into zeolite framework [5,7]. A potential risk of this method is the formation of a mesoporous phase unconnected to the crystalline microporous zeolite, due to the competition between meso- and microporous templates during crystallization [4,8,9]. In this chapter, we propose, for the first time, a possible workaround, supported on previous results obtained for other zeolites with larger pores, which is based on the principle that the formation of separated mesophases, from zeolite crystals, can be prevented by generating a large amount of subnanocrystals with relatively high polymerization degree combined with the use of ethanol [8]. Therefore, this alternative consists on the formation of nanocrystalline zeolite seeds prior to CTAB addition, by aging the zeolite precursor solution, and to perform the crystallization by hydrothermal treatment with CTAB thereafter. This aging method, to the best of author´s knowledge, has only been used on medium and large pore size zeolites. The synthesis procedure proposed in this study was thoroughly studied, optimized and the resultant materials were characterized by a wide variety of characterization techniques.

Thus, sequential approaches were explored to control and better understand the heterogeneous nucleation mechanism: a) hydrothermal synthesis of the gel mixture, containing both TEAOH and CTAB, and b) addition of CTAB to the pre-aged microporous gel solution and subsequent hydrothermal synthesis. The experimental details of both approaches are reported in previous *Chapter II*. The material synthetized by approach a) is denoted as *"One-*

pot Meso", whereas the material synthetized by method b) is denoted as "*Aged Meso-0.15*" based on a CTAB/Al molar ratio of 0.15. Note that the molar composition of zeolite gel solution was the same for both synthetized zeolites: 1.0 Al_2O_3/1.0 P_2O_5/0.3 SiO_2/3.2 TEAOH/0.3 CTAB/8.8 EtOH/80 H_2O.

The effect of aging time of hierarchical SAPO-34 zeolites was also evaluated by varying the aging time between 24, 48 and 64 h (before addition of CTAB template and hydrothermal crystallization). The same procedure b) and precursor amounts were used. These materials are denoted as *"Aged Meso-24h", "Aged Meso-48h"* and *"Aged Meso-64h"*, respectively. Note that the last one ("*Aged meso-64h*") corresponds to the previously denoted "*Aged Meso-0.15*" material. Some characterization results concerning the aging time effect are presented in Supporting Information of the present *Chapter III* (Table III. S1, Figure III. S3, *Influence of aging time* section).

Alternatively, the mesoporosity of the hierarchical materials was adjusted by varying the amount of the secondary mesoporous template (CTAB) of the materials aged during 64 h. The molar compositions of the precursor mixtures were: 1.0 Al_2O_3/1.0 P_2O_5/0.3 SiO_2/3.2 TEAOH/x CTAB/8.8 EtOH/80 H_2O (with x = 0.33, 0.66 and 1.33). These hierarchical CHA-based zeolites are denoted as *"Aged Meso-0.15", "Aged Meso-0.33" and "Aged Meso-S-0.66"* based on the molar ratio of CTAB/Al of 0.15, 0.33 and 0.66, respectively.

For comparison purposes, conventional microporous SAPO-34 CHA-based zeolite was also synthesized via conventional hydrothermal crystallization method using TEAOH as template with the following molar composition of the initial zeolite gel solution: 1.0 Al_2O_3/1.0 P_2O_5/0.3 SiO_2/3.2 TEAOH/34 H_2O [1,2]. Note that the time of crystallization and the nature of the silica precursor were optimized (Figure III. S1 (a), *XRD analysis of micro-SAPO-34*), concluding that 48 h are needed to obtain a crystalline SAPO-34 phase using TEOS (Aldrich, 98%) as a Si precursor. The latter presented an average of micropores pore size bigger than that corresponding to conventional CHA-based zeolite synthetized using Fumed Silica as a Si precursor (Figure III. S1 (b), HK pore size distribution), This material is denoted as *"Micro"*.

The experimental conditions used for the synthesis, including conventional microporous and hierarchical CHA-based catalysts, are summarized on Table III.1.

Table III.1. The experimental conditions of synthetized SAPO-34 CHA-based zeolites.

Samples	Method	Crystallization time (h)	Aging time (h)	Micro template	Meso template	CTAB/Al molar ratio
Micro	One-pot	48	-	TEAOH	-	-
One-pot Meso	One-pot	48	-	TEAOH	CTAB	0.15
Aged Meso-24h	Aged[a]	24	**24**	TEAOH	CTAB	0.15
Aged Meso-48h	Aged[a]	24	**48**	TEAOH	CTAB	0.15
Aged Meso-0.15 (or Aged Meso-64h in Supporting information)	Aged[a]	24	**64**	TEAOH	CTAB	**0.15**
Aged Meso-0.33	Aged[a]	24	64	TEAOH	CTAB	**0.33**
Aged Meso-0.66	Aged[a]	24	64	TEAOH	CTAB	**0.66**

[a] *aged heat treatment previous to the hydrothermal crystallization synthesis.*

1. Influence of the preparation method.

Firstly, the effect of the incorporation of a secondary template (mesoporous: CTAB surfactant) was studied by thermogravimetric analysis. The TGA/DTG curves of non-calcined microporous and micro-mesoporous zeolites are plotted in Figure III. 1 (a), (b) and (c). Weight loss curves show a higher decrease for micro-mesoporous CHA-based zeolites (~ 30%, Figure III.1 (b) and (c)) than for the microporous CHA-based zeolite (~ 20%, Figure III. 1 (a)). This could be attributed to the presence of two templates (micro- and mesoporous) in these materials compared to a single one in the microporous zeolite. In other words, the amount of precursors to be removed during calcination in the case of micro-mesoporous zeolites was higher. Three weight loss steps (noticed as I, II and III on Figure III. 1 (b) and (c)) appear on the TGA curves of micro-mesoporous CHA-based zeolites in the temperature range from 25 to 700 °C. The first weight loss (I) at a temperature below 200 °C is related to the desorption of adsorbed water. The second weight loss (II), between 200 and 450 °C, could be attributed to the decomposition of the microporous template TEAOH and to the main process of CTAB decomposition [10–12]. Finally, the third weight loss (III) at temperatures higher than 450 °C is more likely associated with the further removal of organic residues blocked in channels and cages of SAPO-34 structure or to organic species associated to CTAB [10–12]. Therefore, all the templates were almost completely decomposed at 550 °C in the synthesized materials (Figure III. 1 (b), (c) and (d)). As a consequence, the selected calcination temperature was fixed at 550 °C to ensure that all organic were entirely removed. Beyond this temperature, the catalyst structure can be weakened.

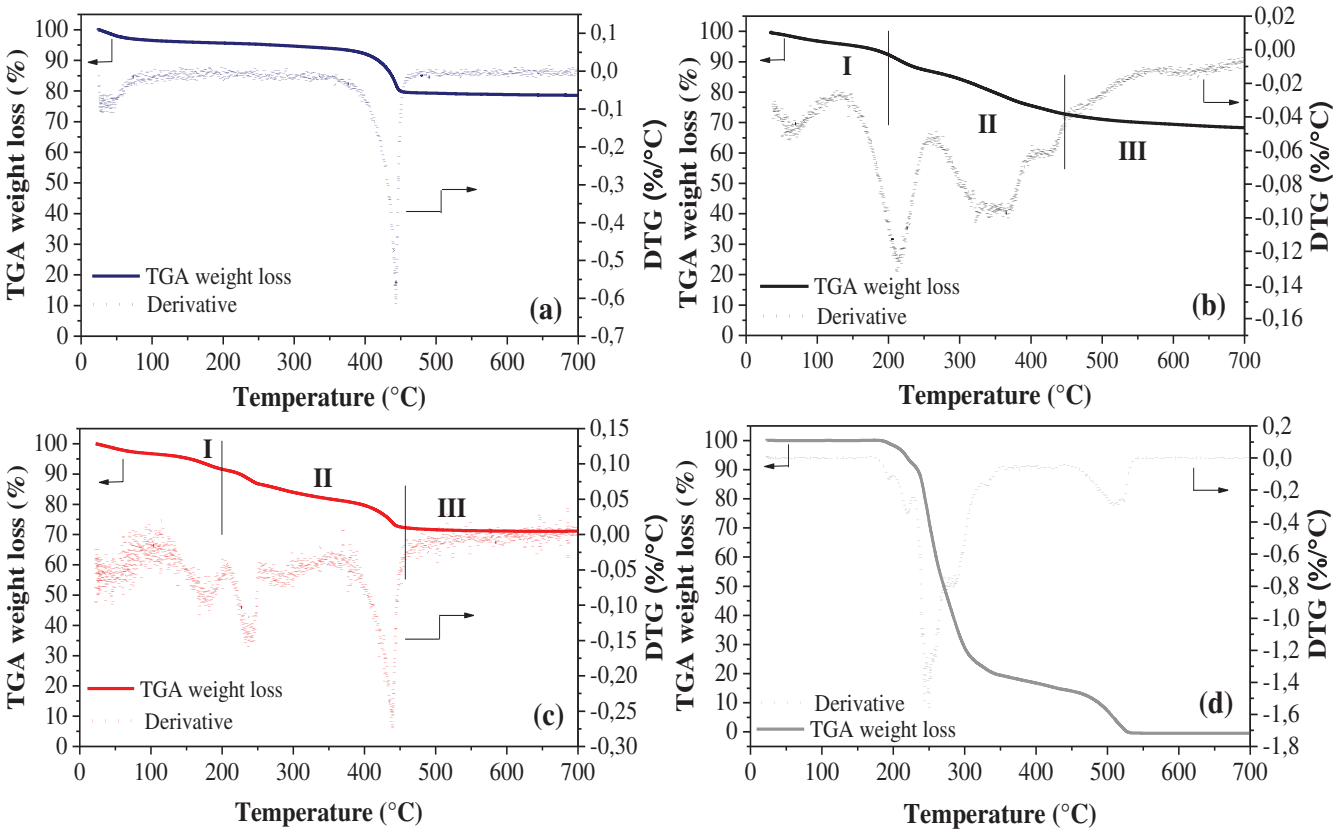

Figure III. 1. TGA/DTA curves of non-calcined (a) conventional micropores SAPO-34, (b) One-pot meso-SAPO-34, (c) Aged meso-SAPO-34 and (d) CTAB precursor.

Table III.2 summarizes the chemical composition and textural properties of the materials. These properties were measured by ICP-OES and N_2 adsorption/desorption experiments, respectively. The experimental elemental composition, which is illustrated by the Si/Al molar ratio, is similar for both, Micro- and Aged Meso-0.15 SAPO-34 materials, whereas a non-negligible gap is observed for One-pot Meso material. A Si/Al molar ratio of 0.15 is targeted. Moreover, the (Si+P)/Al molar ratio is given in order to monitor and control whether values of this ratio remain beyond the critical value of 1 [13,14]. A lower ratio tends to increase adsorption capacity of basic molecules due to the increasing acidity of the material [13,15]. However, if the ratio becomes higher than 1, with larger amount of Si, it could indicate the presence of undesired Si-islands. These structures could have adverse impacts on the acid properties and on the hydrothermal stability of the zeolite, eventually leading to the deactivation of the material when used as a catalytic support [15–17]. All the zeolites prepared presented a (Si+P)/Al molar ratio below the critical threshold of 1. Therefore, no Si-islands are expected within these materials, as it was further verified by Nuclear Magnetic Resonance (MAS NMR) in Figure III. S2. No peak is detected in the -110 ppm chemical shift region of ^{29}Si MAS NMR

profiles of Micro, One-pot and Aged Meso-0.15, indicating that these bulk structures are free of Si-island $Si(OSi)_4$ [14,16,18–21].

Table III. 2. Chemical composition and textural properties of conventional microporous and micro-mesoporous SAPO-34 zeolites.

Materials	Si/Al molar ratio	(Si+P)/Al molar ratio	S_{BET} ($m^2 \cdot g^{-1}$)	S_{ext} ($m^2 \cdot g^{-1}$)	V_{micro} ($cm^3 \cdot g^{-1}$)	V_{meso} ($cm^3 \cdot g^{-1}$)	Average mesopores size (nm)	HF[a]
Micro	0.13	0.95	**690**	53	**0.25**	**0.09**	-	0.06
One-pot Meso	0.09	0.70	**437**	344	**0.09**	**0.68**	9	0.09
Aged Meso-0.15	0.15	0.58	**587**	257	**0.19**	**0.40**	10	0.14

[a]*Hierarchy Factor (HF): HF = (V_{micro}/V_{total}) × (S_{ext}/S_{BET}), where $V_{total} = V_{micro} + V_{meso}$ and $S_{BET} = S_{micro}$ (not shown) + S_{meso}.*

The N_2 adsorption/desorption isotherms and the pore size distributions of conventional microporous and both micro-mesoporous SAPO-34 CHA-based zeolites are presented in Figure III. 2 (a) and (b). The Micro-SAPO-34 showed a characteristic microporous Type I(a) isotherm, according to IUPAC classification, and comparable with those reported in the literature [22,23]. Together with the large adsorption at low partial pressures, corresponding to microporosity, a transition to Type IV(a) isotherms is observed in micro-mesoporous CHA-based modified zeolites [24], which reveals the presence of mesoporosity within the microporous-CHA framework. The non-reversibility of these isotherms indicates the presence of pores larger than 4 nm. The shape of the hysteresis loops is also indicative of the texture of the developed materials. The existence of H2-type hysteresis in both CHA-based modified zeolites reveals the presence of ink-bottle pores. Moreover, the high adsorption volume at low pressures ($P/P_0 < 0.1$) is substantially decreased for one-pot Meso zeolite, presenting a large hysteresis loop at higher partial pressures, which could indicate a large loss of microporosity [8] (Figure III. 2 (a)). Accordingly, the pore size distributions of One-pot Meso and Aged Meso-0.15 modified CHA-based zeolites (Figure III. 2 (b)), obtained using the BJH method, clearly show the presence of mesopore structures with pore sizes centered at 8 and 10 nm, respectively.

N_2 adsorption/desorption results also showed a significantly increased external surface area (S_{ext} = 344-257 m^2g^{-1}) and mesoporous volume (V_{meso} = 0.68-0.40 cm^3g^{-1}) for One-pot Meso et Aged Meso-0.15 modified CHA-based zeolites, respectively, as compared with the conventional microporous SAPO-34 zeolite (S_{ext} = 53 m^2g^{-1}, V_{meso} = 0.09 cm^3g^{-1}). Note that the external surface area of microporous SAPO-34 zeolites has been associated to the defects of the external surface and/or the external voids created between zeolites particles (inter-

crystalline porosity) [22]. It has been demonstrated that the BET analysis are not applicable to microporous materials to obtain the true accessible surface area, but this value obtained can be used as an apparent or fingerprint area of the material [25]. The Aged Meso-0.15 zeolite showed a BET specific surface area (S_{BET}) lower than that of Micro SAPO-34 (587 versus 690 m^2g^{-1}) but higher than that of the One-pot Meso zeolite (437 m^2g^{-1}). This lower value makes the latter new material potentially less attractive than the Aged Meso-0.15 SAPO-34 zeolite.

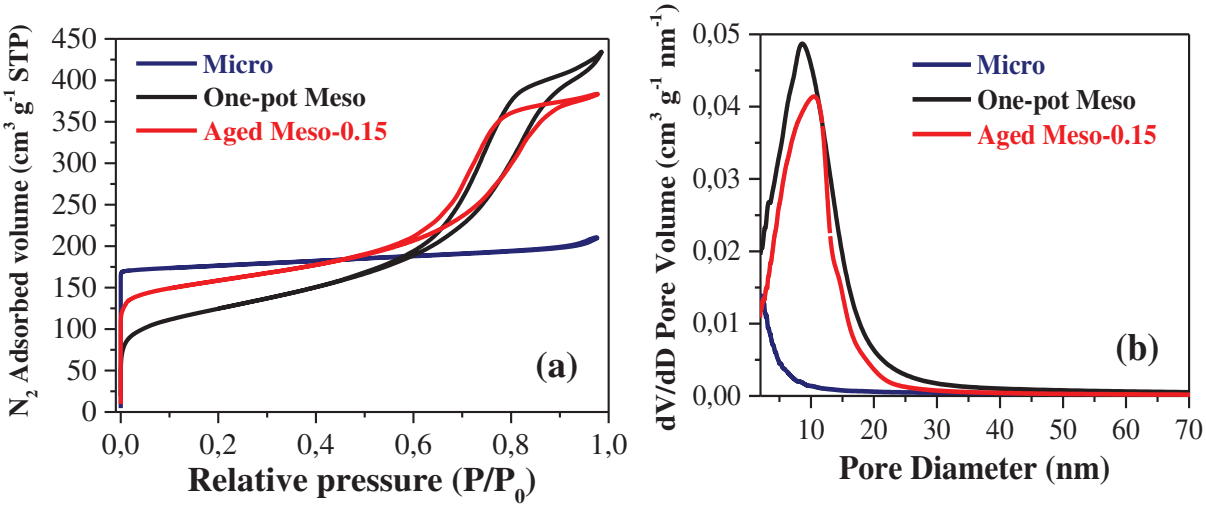

Figure III. 2. (a) N_2 adsorption/desorption isotherms of conventional microporous and micro-mesoporous CHA-based zeolites and (b) BJH pore diameter distributions of hierarchical CHA-based zeolites.

The introduction of mesoporosity into microporous-CHA framework was further evaluated using the hierarchy factor (HF). This parameter was firstly introduced by Perez-Ramirez et al. [26,27], and is defined as the product of the relative mesopore surface area (S_{meso}/S_{total}) multiplied by a relative microporous volume (V_{micro}/V_{total}). This HF has been recently applied to classify the porous characteristics of several materials as a function of its framework and the preparation method. In other words, the hierarchy factor could be understood as a parameter that comprises the enhancement of the mesopore surface area without a severe sacrifice of the micropore volume. This is of paramount importance for the design of efficient hierarchical zeolites, considering that the active sites for a given reaction are in the micropores, while the added mesopores enhance the diffusion and molecular transport of reactants to such active sites. Accordingly, the HF allowed comparing hierarchically structured zeolites independently of the synthetic methodology. The micro-mesoporous modified CHA-based zeolites exhibited a higher hierarchy factor (HF values of 0.10 and 0.14 for One-pot Meso and Aged Meso zeolites, respectively) compared with that of conventional microporous CHA-

zeolites (HF value of 0.06), which clearly indicates the incorporation of mesopores in the conventional zeolite. Thus, considering the hierarchy factor as a measurement of the extent of the external surface increase without an important decrease in the micropore volume, the so-called Aged Meso SAPO-34 zeolite presents the most promising hierarchical properties.

These results clearly demonstrate the possibility to create a significant amount of mesopores into the microporous SAPO-34 materials. It is worth highlighting that the aging treatment of the zeolite precursor solution before performing the crystallization by hydrothermal synthesis with CTAB allows keeping to an important extent the microporosity even after the incorporation of the mesoporous template.

The XRD patterns at low and wide-angles of the conventional microporous and the micro-mesoporous SAPO-34 CHA-based materials are shown in Figure III. 3 (a) and (b). Both micro-mesoporous materials exhibited XRD characteristic peaks at 2θ = 9.5, 12.9, 16.2, 17.8, 19.2, 20.8, 23.3, 24.9, 26.2, 30.6 and 32.0° (Figure III. 3 (a)) in good agreement with the patterns of conventional SAPO-34 CHA-based zeolite (reference: PDF 00-047-0429) reported in literature [9,20,21,28,29]. These results suggest that the original zeolite structure is maintained, regardless the synthesis approach and the potential incorporation of mesopores. However, an additional peak at 2θ = 19.7° is observed for micro-mesoporous SAPO-34 chabazite synthesized by the *one-pot* method, which can be attributed to the formation of an expected secondary phase of aluminum phosphate hydrate (ICDD-PDF4+).

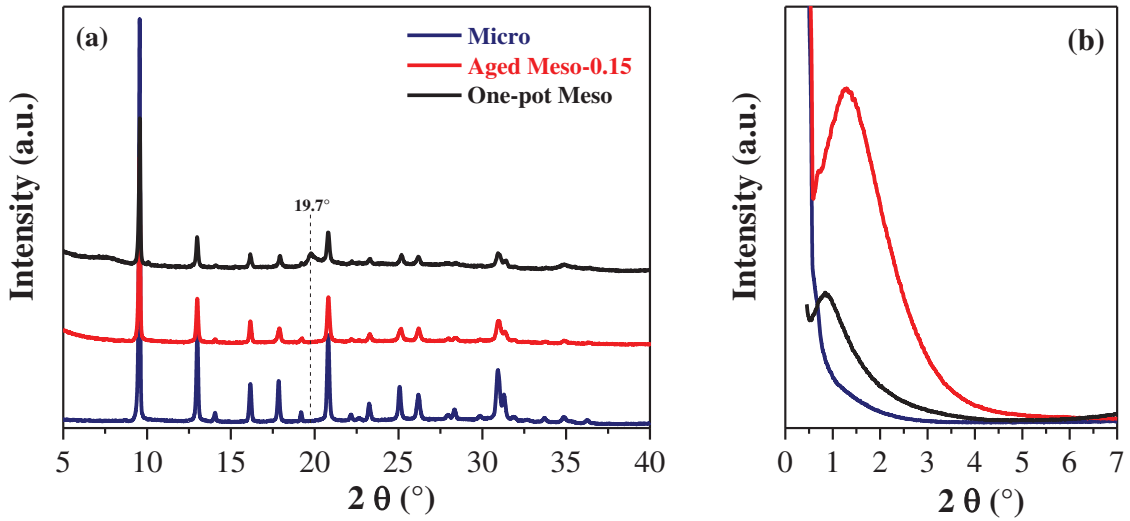

Figure III. 3. XRD patterns (a) wide- and (b) low-angle of conventional microporous SAPO-34 CHA-based zeolite and micro-mesoporous SAPO-34 CHA-based zeolites synthesized with different methods.

Regarding low angle XRD patterns (Figure III. 3 (b)), a broad diffraction peak at 2θ = 1-3° for micro-mesoporous materials can be noticed. This peak is usually attributed to the formation of an ordered mesoporous structure, in good agreement with the N_2 adsorption/desorption results. The previously calculated hierarchy factor provided significant information about the formation of mesopores in micro-mesoporous zeolites. However, this parameter is "blind" to the nature and order of such mesopores. The intensity of the XRD signal is higher as the structural ordering increases, which could be therefore indicative of some long-range order. In other words, the intensity of the peak by low-angle XRD could be linked to the creation of mesopores with some periodicity [30–35], being it higher in the case of the Aged Meso-0.15 SAPO-34 material. In addition and as expected, compared with the conventional Micro-SAPO-34, the intensities of the wide-angle X-ray diffraction peaks for micro-mesoporous SAPO-34 materials decreased, which suggests some crystallinity loss [23,36], as confirmed by the calculation of the relative crystallinity (Table III.3). Thus, it seems that the addition of CTAB has a slightly detrimental effect on the SAPO-34 crystal structure [9]. Moreover, the crystal size (according to Scherrer equation) slightly decreases for both modified CHA-based zeolites, which could be attributed to the crystal growth inhibitor (CGI) effect of CTAB, as recently reported in literature [37]. Nevertheless, the main lattice parameters (calculated by Diffrac.Eva software using PDF 00-047-0429 as a standard SAPO-34 reference patterns, a=13.78) were not significantly modified after the incorporation of mesopores.

Table III. 3. Relative crystallinity, crystallite size and lattice parameters of conventional microporous and micro-mesoporous SAPO-34 zeolites.

Materials	Crystal size (nm)[a]	Relative crystallinity (%)[a,b]	Lattice parameter a (Å)[a]
Micro	104.3	100	13.60
One-pot Meso	80.3	71.2	13.64
Aged Meso-0.15	82.7	86.8	13.63

[a] *Crystal size, relative crystallinity and lattice parameter were calculated by Diffrac.Eva software.*

[b] *Relative crystallinity correspond to the normalized crystallinity of micro-mesoporous materials with respect to the micro-SAPO-34 material.*

To sum up, according to the XRD results, all materials exhibited a crystalline structure typical of SAPO-34 CHA-based zeolite, and the use of CTAB did not seem to drastically affect its crystalline properties. However, only in the case of micro-mesoporous CHA-based zeolite synthetized via the aging treatment, a pure and crystalline phase with no obvious impurity phase

peaks is obtained. Together with the experimental evidences previously observed by N_2 adsorption/desorption, these results point out the paramount importance of the aging procedure during the synthesis of micro-mesoporous SAPO-34 zeolites, which is reported for the very first time in this study.

TEM micrographs were carried out to analyze the introduction of mesoporosity into the materials framework. The results included in Figure III. 4 clearly reveal the existence of mesoporosity with different pore sizes (6-10 nm) on the surface of Aged Meso-SAPO-34 CHA-based zeolite (Figure III. 4 (a) and (b)), which are not observed in TEM images of conventional microporous one (Figure III. 4 (e) and (f)) [21]. These results are in good agreement with the N_2 adsorption/desorption and low-angle XRD data. The identification of mesoporosity of One-pot Meso CHA-based zeolite, Figure III. 4 (c) and (d), was complicated due to the instability of this sample under electron beam. Some evidences about the creation of mesopores in this material can be appreciated in both TEM images, together with the presence of a secondary unidentified phase unconnected to the crystalline microporous zeolite (highlighted in Figure III. 4 (c)), which points out the lower purity of such material compared with the Aged Meso-SAPO-34 CHA-based zeolite, in which a quasi-homogeneous distribution of wall-crystallized mesopores can be observed in Figure III. 4 (b). The latter confirms the presence of intracrystalline mesoporosity, where mesopores and micropores seem to coexist within the same SAPO-34 crystal.

The above described characterization techniques, i.e., XRD, N_2 adsorption/desorption and TEM images clearly demonstrated the existence of an important mesoporosity with both methods (one-pot and aged approaches). However, only in the case of Aged Meso-0.15 zeolite, a pure and crystalline SAPO-34 phase (Figure III. 3, XRD) with an interconnected hierarchical structure (Figure III. 4, TEM) and a BET specific surface area comparable to the original zeolite is obtained. According to these results, the aging treatment was chosen as the enhanced method to synthetize hierarchical SAPO-34 zeolites. In other words, this method exhibits very promising features in order to develop an even more stable, active and selective catalyst for NH_3-SCR reaction. Thus, the next step of this study was to optimize the operating conditions of the aged treatment method: aging time (Table III. S1, Figure III. S3 – *See Supporting Information*) as well as to evaluate the influence of mesoporous template amount on the textural properties (mesoporous incorporation).

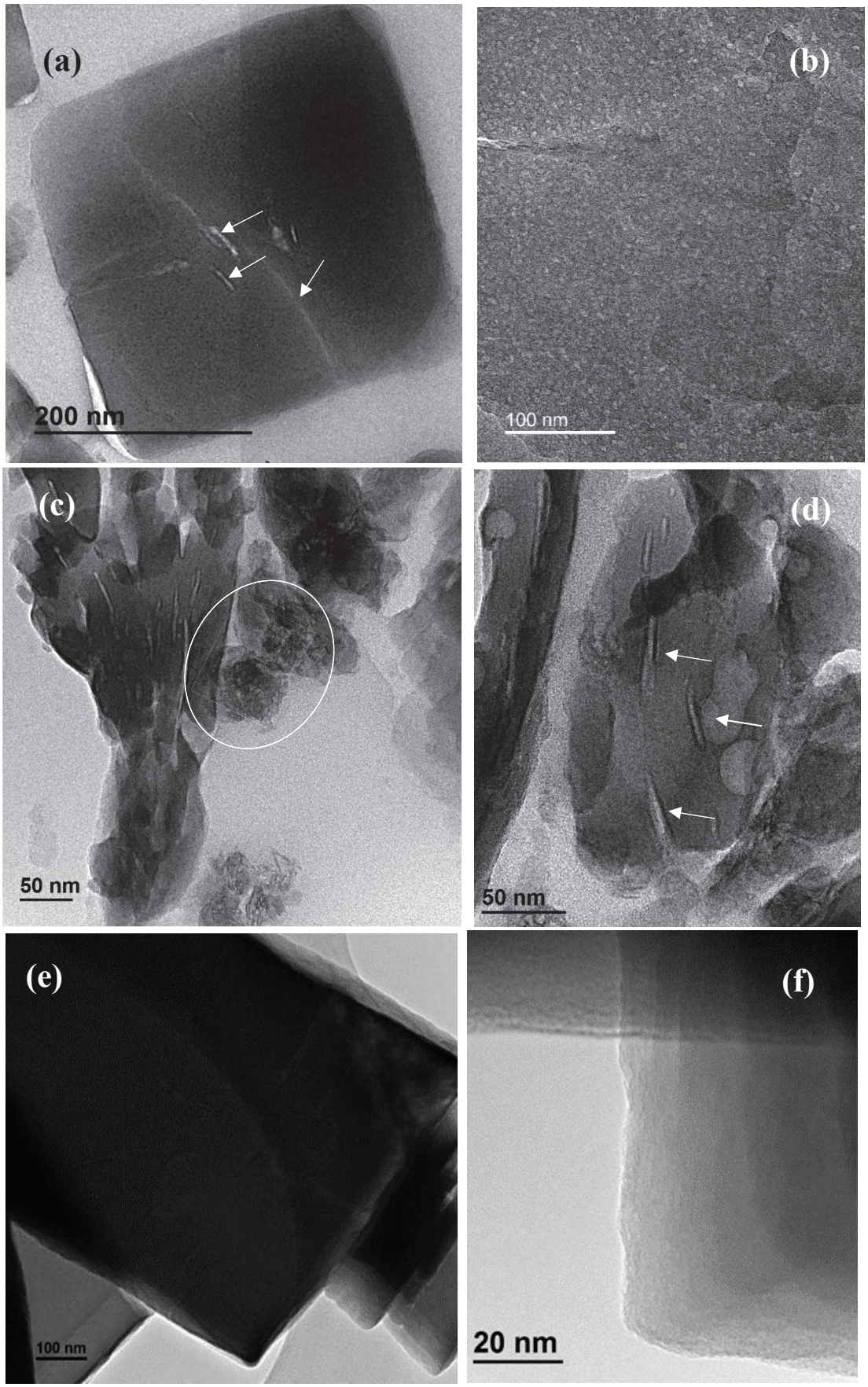

Figure III. 4. TEM images of (a, b) Aged Meso-0.15, (c, d) One-pot Meso and (e, f) Micro SAPO-34 CHA-based materials.

2. Effect of mesoporous template (CTAB) amount

The influence of the amount of CTAB as a mesoporous template on the crystalline structures and textural properties of hierarchical Aged-SAPO-34 CHA-based zeolites was evaluated. With that purpose, the CTAB/Al molar ratio was set at 0.15, 0.33 and 0.66. As a result, the hierarchical CHA-based zeolites were denoted as Aged Meso-0.15, Aged Meso-0.33 and Aged Meso-0.66, based on the molar ratio of CTAB/Al. Note that the first one (Aged Meso-0.15) corresponds with that denoted as Aged meso-64h (*See Supporting Information section*).

The XRD patterns at low- and wide-angles of conventional micro-SAPO-34 and hierarchical SAPO-34 zeolites synthetized with different CTAB amounts are shown in Figure III.5. Crystalline phases and the main lattice parameters (Table III.4) are preserved for all hierarchical SAPO-34 CHA-based zeolites, maintaining the SAPO-34 structure without apparent phase impurity [9,21]. In general terms, compared with conventional micro-SAPO-34, the X-ray diffraction peak intensities of hierarchical CHA-based zeolites are less intense, Figure III. 5 (a), which is associated to the incorporation of mesoporosity [9,23,36]. These results suggest that the SAPO-34 partially lose its crystallinity due to the incorporation of CTAB, which is consistent with the calculated relative crystallinity. This parameter seems to reach a minimum value for the Aged Meso-0.33 material, Figure III. 6. A slight decrease of the crystal size is also observed for these Aged hierarchical materials, Table III.4. Some differences were also observed in the low-angle XRD patterns of the three hierarchical zeolites, Figure III. 5 (b). As previously explained, the appearance and intensity of diffraction peaks in this low-range (2θ = 1.5-2.0º) could be related to the formation and periodicity of mesopore phases [31–35]. The results obtained clearly indicate a decrease in the maximum diffraction intensity as the amount of CTAB template increased, which is indicative of a loss of periodicity in the mesopores.

Table III. 4. Crystal size and relative crystallinity of hierarchical SAPO-34 zeolites synthesized with different CTAB amount.

Materials	Crystal size (nm)	Relative crystallinity (%)	Lattice parameter a (Å)
Micro	104.8	100	13.60
Aged Meso-0.15	82.7	86.8	13.63
Aged Meso-0.33	82.8	70.4	13.61
Aged Meso-0.66	82.7	86.6	13.63

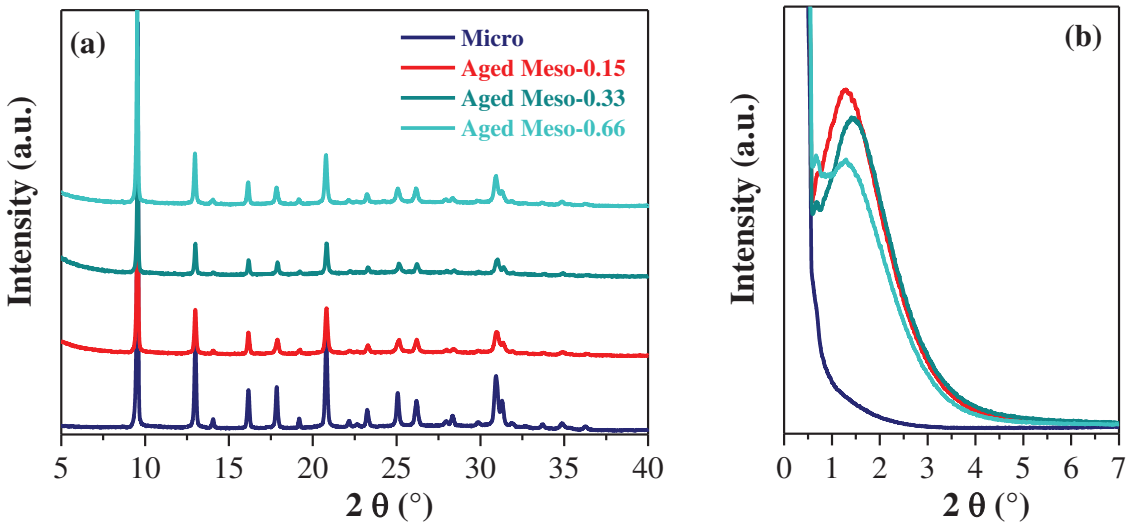

Figure III. 5. XRD patterns (a) wide- and (b) low-angles of conventional micropores CHA-based zeolite and hierarchical SAPO-34 CHA-based zeolites synthetized with different amount of CTAB.

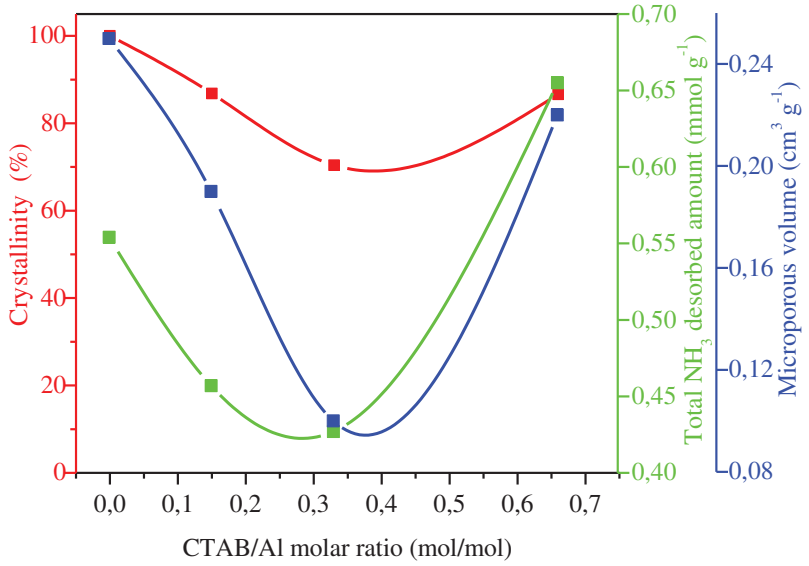

Figure III. 6. Inverted-volcano trend: Crystallinity, microporous volume and acidity as a function of CTAB/Al molar ratio.

The influence of CTAB amount on textural properties was also evaluated by N_2 adsorption-desorption. The N_2 adsorption/desorption isotherms and pore size distributions of the aged Meso-SAPO-34 zeolites synthetized with different CTAB amount are shown in Figure III. 7. All hierarchical SAPO-34 CHA-based zeolites present a combination of type I and IV isotherms with an increase of adsorbed amount at low pressure as well as a pronounced hysteresis loop at high P/P_0. These loops, which can be classified as H2, as commented above,

are indicative of ink-bottle pores, in the range of mesopores. Regarding the textural properties listed in Table III.5, as expected, the BET surface area and micropores volume generally decreased due to the addition of CTAB, while the formation of mesopores was clearly observed with the concomitant increase of the external surface area. It is worth noting that the specific surface area and micropore volume exhibited minimum values for the material with CTAB/Al molar ratio = 0.33, leading to a slight decrease of the hierarchical factor. A similar phenomenon was observed in a previous study by Zhang et al. [38], although the reasons leading to this inverted-volcano trend, Figure III. 6, are still unclear. In any case, the results obtained by N_2 adsorption/desorption point out the strong influence of the amount of CTAB template on the formation of mesopores and the related sacrifice of the micropore phases with both, Aged Meso-0.15 and Aged Meso-0.66 exhibiting the most interesting structural properties. Note that the reproducibility of the preparation method and CTAB amount influence was evaluated comparing the isotherms of two or three materials synthetized in different batch (*See Figure III. S4 Supporting Information section*).

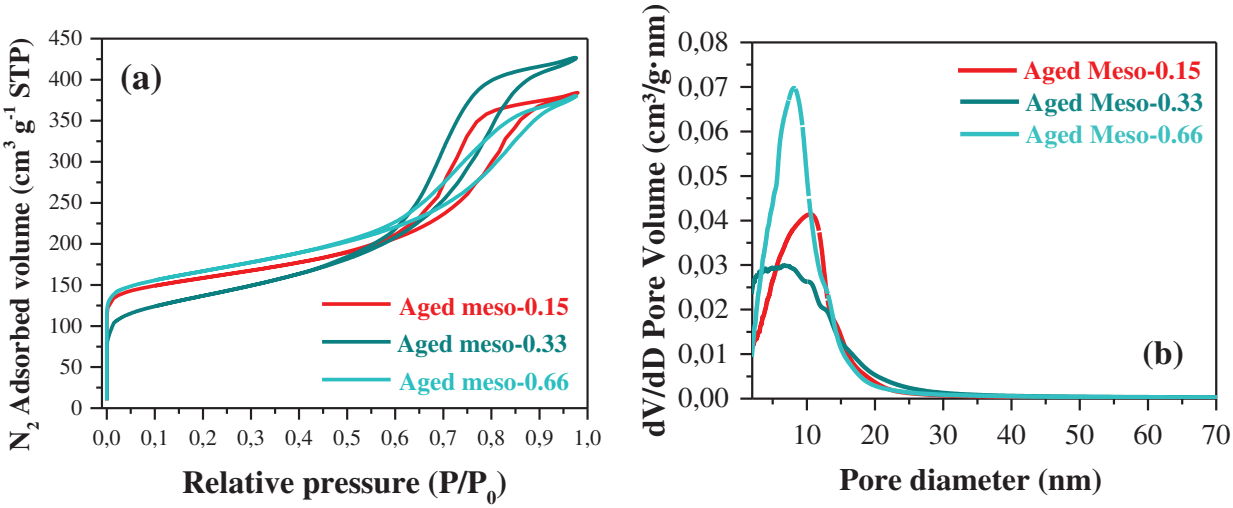

Figure III. 7. (a) N_2 adsorption-desorption isotherms and (b) BJH pore size distributions curves of hierarchical CHA-based zeolites synthetized with different CTAB amount.

Table III.5. Influence of different amounts of CTAB: chemical composition and textural properties.

Materials	CTAB/Al Molar ratio	Si/Al Molar ratio	(Si+P)/Al Molar ratio	S_{BET} ($m^2 \cdot g^{-1}$)	S_{ext} ($m^2 \cdot g^{-1}$)	V_{micro} ($cm^3 \cdot g^{-1}$)	V_{meso} ($cm^3 \cdot g^{-1}$)	Average mesopores size (nm)	HF[a]
Micro	-	0.13	0.95	**690**	53	0.25	0.09	-	0.06
Aged Meso-0.15	0.15	0.15	0.58	**587**	257	0.19	0.40	10	0.14
Aged Meso-0.33	0.33	0.15	0.50	**485**	387	0.10	0.56	7	0.12
Aged Meso-0.66	0.66	0.15	0.64	**611**	281	0.22	0.37	8	0.17

[a]*Hierarchy Factor (HF): HF = (V_{micro}/V_{total}) × (S_{ext}/S_{BET}), where $V_{total} = V_{micro} + V_{meso}$ and $S_{BET} = S_{micro}$ (not shown) + S_{meso}.*

The chemical composition, Si, Al and P contents, of the materials synthetized with higher amount of CTAB was determined by ICP-OES analysis. The experimental Si/Al molar ratio was close to the Aged Meso-0.15 and theoretical ones (Si/Al = 0.15) regardless of the CTAB amount. Nuclear Magnetic Resonance experiment (MAS NMR) were also performed to evaluate the chemical bulk architecture of synthetized hierarchical zeolites. Figure III. 8. A shows the ^{29}Si MAS NMR spectra of all hierarchical zeolites, Figure III. 8 (a), in which the main chemical shifts of a tetrahedrally coordinated chabazite structure are underlined (dash lines). The building unit $Si(OAl)_x$ with x = 4, 3, 2, 1, 0, gives rise to a chemical shift at -89, -95, -99.6, -104,3 and -110 ppm respectively, according to the literature [13,16,19–21,39]. These results showed that no resonance peak was detected in the -110 ppm chemical shift region, indicating that these bulk structures are free of Si-island $Si(OSi)_4$ [14,16,18–21], which is in good agreement with the value of molar ratio (Si+P)/Al lower than 1 (Table III.5).

For Aged Meso-0.15 and Aged Meso-0.66, a well-defined signal centered between -89 and -95 ppm, which is similar to the conventional Micro-SAPO-34, seems to indicate that these hierarchical materials presented isolated Si atoms mainly in $Si(OAl)_3$ and $Si(OAl)_4$ building unit configuration. On the contrary, a broader peak is observed for Aged Meso-0.33 zeolite, which could underline a disordered state of Si on this material [39], which is in good agreement to its lower crystallinity, Table III.4. Besides, in accordance with the literature [40–42], the incorporation of isolated Si atoms into the neutral framework of AlPO-34 generates surface bridge hydroxyl groups, which give rise to the Brønsted sites, T-OH-T groups (e.g.: Si-OH-Al) with moderate and/or strong-acid properties. Thus, although a quantitative evaluation is not possible, the lower relative intensity of both Aged Meso-0.15 and Aged Meso-0.33 ^{29}Si NMR spectra compared to that of the Micro and Aged Meso-0.66 materials could indicate a lower density of Brønsted acid sites in the former materials. This suggestion was confirmed by NH_3-TPD results below.

Significant differences were also observed with the corresponding ^{31}P NMR data (Figure III. 8 (b)), in which two main resonance peaks at -27 and -17 ppm are visible for Micro and Aged Meso-0.15 and -0.33 zeolites, whereas only the former is clearly appreciable for Aged Meso-0.66 SAPO-34 zeolite. The former one, which seems to be common for all materials, is correlated to the tetrahedral coordinated P [20,21]. However, the latter is assigned to disordered P atoms perturbed with water, $P(OAl)_4(H_2O)_y$ [20,21], which suggests that at least some of these phosphorus atoms are located at defects caused by a reversible hydrolysis of SAPO-34 framework. This coordination with water is also visible in ^{27}Al NMR data (Figure III. 8 (c)), in

which the small peak with a chemical shift of ca. 7 ppm (12 ppm for Micro-SAPO-34) represents pentacoordinated extra-framework aluminum atoms formed by the additional coordination of one water molecule ($Al(OP)_4(H_2O)$), while that of -10 ppm is attributed to octahedral aluminum atoms formed by the additional coordination of two water molecules ($Al(OP)_4(H_2O)_2$) [63]. The presence of these two resonance peaks in all profiles indicates the existence of extra-framework Al species in all the materials. Note that the relative intensity of these peak increases with the increasing CTAB/Al molar ratio following the same inverted-volcano tendency observed in term of microporosity and crystallinity, Figure III. 6.

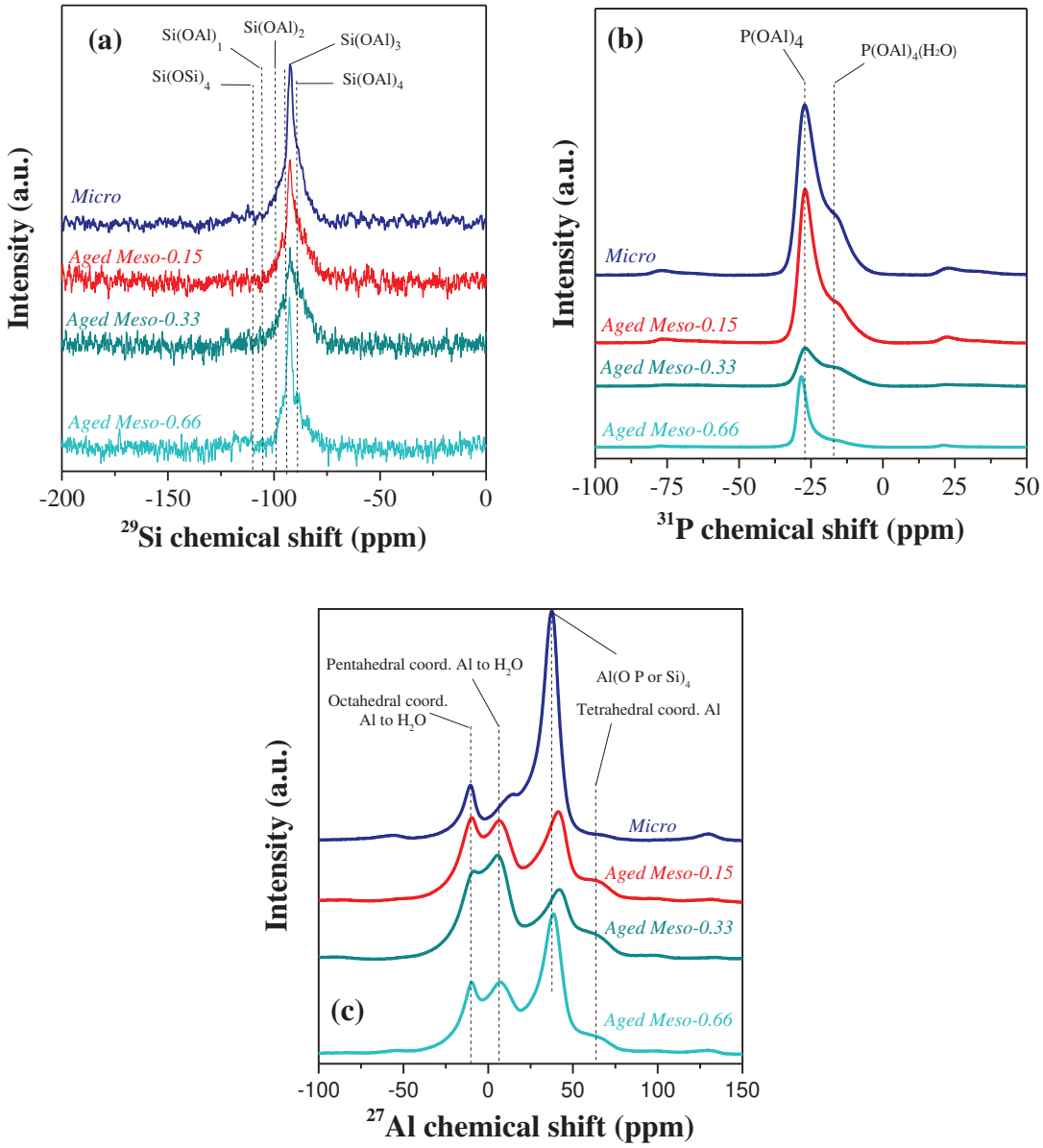

Figure III. 8. NMR spectra (a) ^{29}Si, (b) ^{31}P and (c) ^{27}Al of hierarchical SAPO-34 chabazites synthesized with different amount of CTAB.

Thus, the lower intensity of these peaks together with the well-defined signals correlated to the $P(OAl)_4$, $Si(OAl)_3$ and $Si(OAl)_4$ coordinated atoms observed on ^{31}P NMR and ^{29}Si NMR spectra for Aged Meso-0.66 material seems to indicate that a higher amount of CTAB (CTAB/Al molar ratio = 0.66) give rise to a building unit environment closer to that of the theoretical tetrahedral CHA configuration (exclusively constituted by isolated elements). This idea is also evidenced in ^{27}Al NMR spectra, Figure III. 8 (c), by the peak centered at a chemical shift of 39–42 ppm, attributed to tetrahedral framework aluminum atoms ($Al(OP\ or\ Si)_4$), whose relative intensity increases with the increasing CTAB/Al molar ratio for Aged Meso-0.15 and Aged Meso-0.66. Furthermore, a weak and broad peak with a chemical shift of 63 ppm is observed in ^{27}Al NMR spectra for all hierarchical materials, which is not observed for conventional Micro-SAPO-34. According to the literature [42], this peak could be related to the formation of tetrahedral coordination aluminum atoms from Al_2O_3 clusters, which could explain the lower value of (Si+P)/Al molar ratio as well as lower crystallinity obtained for hierarchical Aged materials compared to the microporous one. Note that the relative intensity of this peak also follows the above mentioned inverted-volcano tendency, where the Aged Meso-0.33 seems to be the most disordered material with a chemical environmental framework far away from the theoretical CHA configuration.

All in all, the NMR results seem to indicate that the Aged Meso-0.66 and 0.15 hierarchical materials exhibit the closest building units compared to the traditional microporous CHA zeolite. These features are of paramount importance, since the aim of this chapter is to develop a hierarchical material with added mesoporosity (to enhance its diffusion properties), where the main advantages of the CHA zeolite are preserved, namely its volume of micropores, crystallinity and acidity.

To gain a better understanding on CTAB influence on acidity and specially on strength and density of Brønsted sites in hierarchical CHA-based zeolites, NH_3 temperature-programmed desorption (NH_3-TPD) was performed. Note that the Brønsted acid sites have an important role in NH_3-SCR reaction, acting as NH_3 storage centers, which become a source of NH_3 at high temperature [43,44]. As shown in Figure III. 9, both microporous and hierarchical CHA-based zeolites presented a similar NH_3 desorption profile, which can be deconvoluted into three main desorption regions at low, medium and high temperature, denoted as LT, MT and HT, respectively [21,44]. The peak at LT could be attributed to the NH_3 desorption from weak Brønsted acid sites like surface or external hydroxyls, T-OH (with T = Si, Al and P), whereas the peaks at MT and HT could be assigned to the NH_3 desorption from moderate and

strong structural bridged Brønsted sites, T-OH-T (e.g.: Si-OH-Al) and/or Lewis acid sites such as tri-coordinated extra-framework Al [17,44–46]. The amount of each acid site was calculated by integrating the deconvoluted desorption peaks, Table III.6.

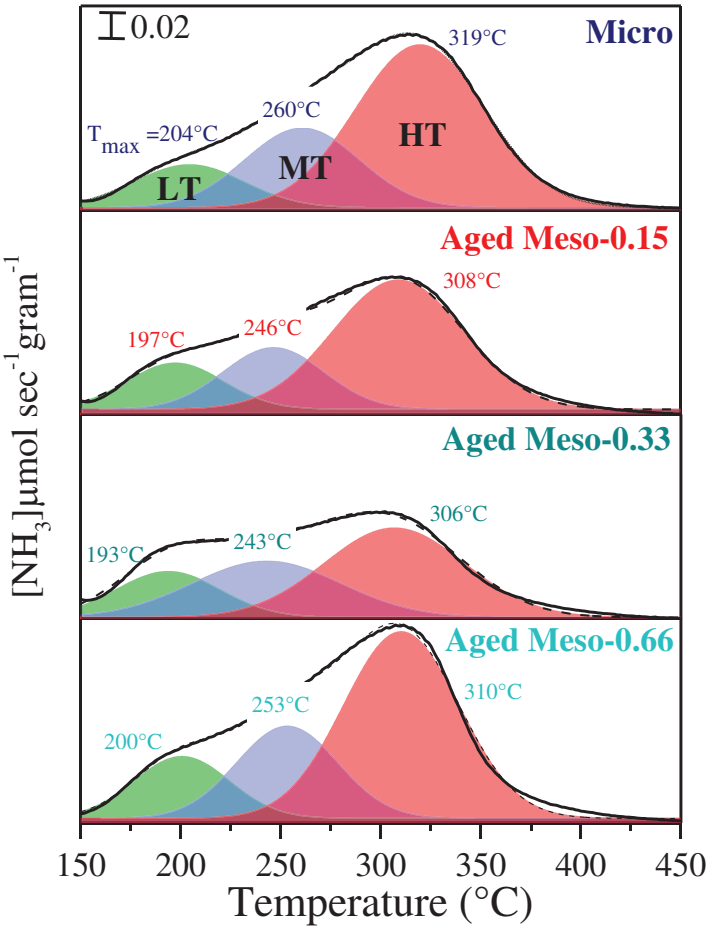

Figure III. 9. NH_3-TPD profiles of Micro and hierarchical Aged Meso-0.15, Aged Meso-0.33 and Aged Meso-0.66 SAPO-34 zeolites with the corresponding deconvoluted peaks at LT, MT and HT.

Table III. 6. Desorbed NH_3 amount according to NH_3-TPD measurements with related maximum peak temperature.

	NH_3 desorbed amount (mmol · $g_{zeolite}^{-1}$)				**Temperature peak (°C)**		
Zeolites	**Weak acid sites (LT)**	**Medium acid sites (MT)**	**Strong acid sites (HT)**	**Total desorbed NH_3 amount**	**LT**	**MT**	**HT**
Micro	0.069	0.152	0.332	0.554	204	260	319
Aged Meso-0.15	0.081	0.088	0.287	0.457	197	246	308
Aged Meso-0.33	0.095	0.073	0.259	0.427	193	243	306
Aged Meso-0.66	0.116	0.147	0.392	0.655	200	253	310

Compared with the conventional microporous SAPO-34 zeolite, the total number of acid sites are reduced for both 0.15 and 0.33 hierarchical CHA-based zeolites, whereas the total acidity of conventional micro-SAPO-34 is maintained and even slightly higher for Aged Meso-0.66 hierarchical zeolite. An inverted volcano-type dependence with the CTAB/Al amount was also found, Figure III. 6, where the total acidity highly decreased for Aged Meso-0.33 zeolite. Note that a similar tendency was observed by L. Kong et al. [9]. The decrease of total acid sites for both mentioned hierarchical zeolites suggests that part of the Brønsted acid sites are removed by the creation of additional mesoporosity, i.e. the addition of CTAB had a significant impact on the distribution of acidity [9,23,36]. This could be assigned to the loss of micropore volume and crystallinity and probably to the lower Si incorporation into the zeolite framework [21,36,47]. In other words, the SAPO-34 structure was partially modified during the additional aging treatment and/or the hydrothermal crystallization process, removing a substantial part of the Brønsted acid sites [23,48]. Besides, the amount of weak acid sites (LT), i.e. the extra-lattice species (external hydroxyl groups, T-OH), which are bounded to the defect sites [36], increased as the CTAB content increased. For hierarchical Aged Meso-0.15 and -0.33, some of strong acid sites (HT) were replaced with weak acid sites (LT). On the contrary, although the total acidity and the amount of moderate and strong acid sites are preserved for Aged Meso-0.66, an increase of weak acid sites is also observed. The latter matches to the loss of crystallinity, compared to the conventional microporous one. Furthermore, the desorption peaks, Table III. 6 and Figure III. 9, are slightly shifted towards lower temperatures for Aged Meso-0.15 and 0.66 and even more for Aged Meso-0.33 hierarchical CHA-based zeolites (e.g. 246, 253 and 243 °C of MT desorption temperature, respectively) compared to that of the conventional Micro-SAPO-34 (260 °C), which indicates that the strength of acid sites is slightly lowered for all hierarchical materials [9,36]. Hence, the acidic properties in SAPO-34 molecular sieve [9] are significantly affected by CTAB mesopore template, decreasing density and strength of moderate and strong acid sites, which could be again correlated with the existence of some defects in the crystalline structure and/or the less incorporation of Si species into the framework of both hierarchical materials, according to the XRD and NMR results (Table III.4 and Figure III.8. (a)) [36]. Nevertheless, although some structural changes, notably loss of crystallinity and order/periodicity of mesopores, are occurred on Aged Meso-0.66, both NMR and NH_3-TPD results confirm that the acidity is preserved for this hierarchical material.

3. Discussion and Conclusions

Microporous silicoaluminophosphate SAPO-34 is commonly used for the reduction of NO_x with NH_3 for automotive applications. Nevertheless, the main issue is the limited access of reactants to the zeolite active sites under certain reaction conditions. In this sense, we propose a new approach for the development of hierarchical micro-mesoporous SAPO-34 zeolites. The main idea is to avoid the competition between microporous (TEAOH) and mesoporous templates (CTAB) by introducing the latter after a defined aging period, which allowed for the pre-formation of the microporous zeolite seeds. Thus, the so-called Aged Meso-0.15 material, prepared by the above-mentioned procedure, was compared with the One-pot Meso material, where both templates (CTAB and TEAOH) were introduced at the same time. The results obtained demonstrated very clearly that an aging procedure allowed to obtain a material with much more interesting structural properties. The Aged material exhibited a higher specific surface area than the One-pot material, with a similar amount of mesopores, leading to a higher hierarchy factor. In addition, the low-angle XRD clearly pointed out not only to the presence of mesopores, but also to a higher order and periodicity of these mesopores. Moreover, no impurities or secondary phases were observed by the aging procedure, as opposed to the One-pot, where an aluminium phosphate hydrate phase appeared. Hence, the advantages of the synthesis procedure proposed in this chapter were outstanding.

In order to get more insights and to optimize this original material, a series of hierarchical zeolites was prepared by the same method, but by varying the CTAB amount. In all the characterization techniques used, a strong influence of this parameter was observed, including physicochemical and acidic properties. The formation of mesopores was achieved for all of them. Indeed, as the amount of CTAB increased, the mesoporous volume increased. However, the microporous volume (together with the relative crystallinity) seemed to follow an unexpected inverted-volcano trend, where the sample with an intermediate amount of CTAB (called Aged Meso-0.33) exhibited the lowest values compared with Aged Meso-0.15 and Aged Meso-0.66 hierarchical materials. That led to higher hierarchy factors for the two latter materials, since the amount of micropores sacrificed to produce mesopores was smaller. A similar trend was observed in the total acidity, suggesting that a substantial part of the Brønsted acid sites are removed by the creation of additional mesoporosity. In addition, it is clearly showed that the increase of CTAB had a detrimental effect on the order/periodicity of mesopores, which could be the differentiating factor between Aged Meso-0.15 and Aged Meso-0.66 materials. Ideally, the hierarchical materials should exhibit structural properties such as

crystallinity, micropores volume and acidity as close as possible to the base CHA microporous SAPO-34 zeolite. The introduction of mesopores will clearly enhance the diffusion of reactants, but it should not affect in a significant manner the rest of physico-chemical parameters. Therefore, it is believed that the highest total acidity of the Aged Meso-0.66 makes it the most promising hierarchical material for future automotive applications. Next chapter will deal with the incorporation of metallic active sites in the conventional and latter hierarchical zeolites together with the study of their catalytic performance.

4. Supporting Information

Synthesis of microporous SAPO-34 CHA-based zeolites (Micro).

Detailed description and operation conditions of microporous SAPO-34 CHA-based zeolites can be found elsewhere in our previous works [1,2]. In the present PhD, the time of hydrothermal synthesis and silica precursor were optimized. Comparing to our previous work, the time of hydrothermal crystallization was decreased, 48 h instead of 96 h, using the same Si precursor, Fumed silica. Moreover, XRD patterns suggest that 48 h are need to obtain a crystalline SAPO-34 phase, using TEOS as a Si precursor. The later protocol was used to synthetized materials denoted as a *"Micro"* in the present manuscript.

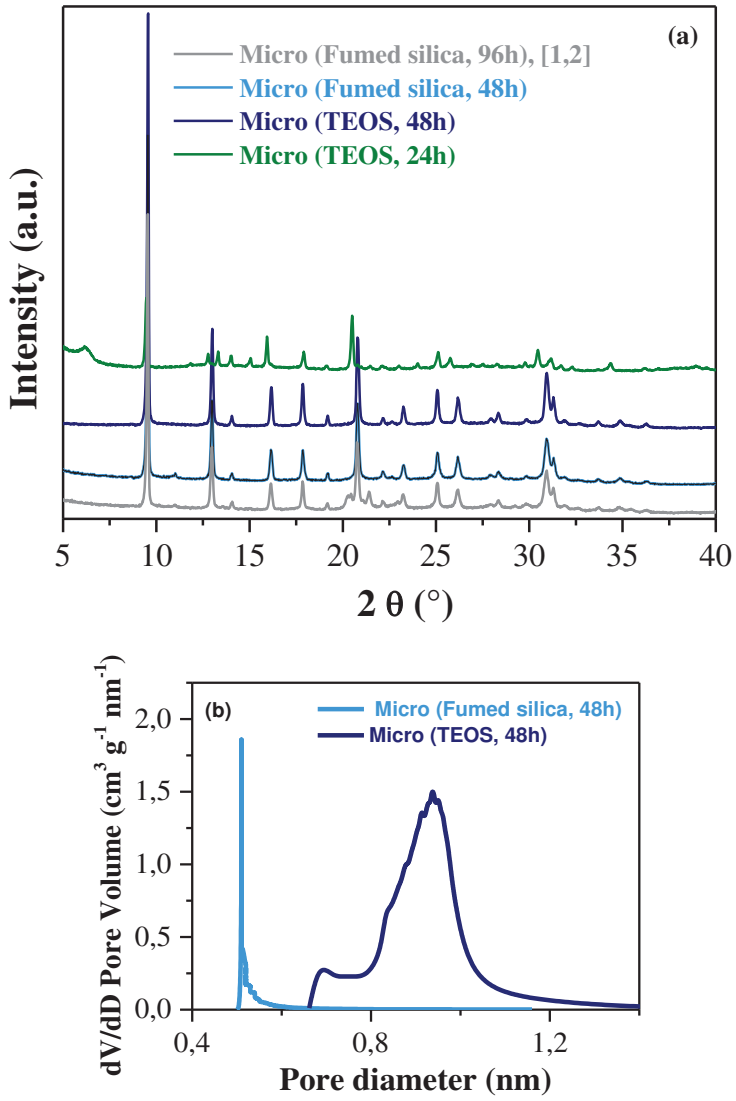

Figure III. S1. (a) XRD patterns of conventional micropores SAPO-34 CHA-based zeolites at different times of hydrothermal synthesis and silica precursors and (b) HK pore size distribution of Micro (Fumed silica, 48h) and Micro (TEOS, 48).

- *Catalyst characterization*

MAS NMR experiments were performed to evaluate the chemical bulk architecture of synthetized supports. Figure III. S2 (a) shows the ^{29}Si MAS NMR spectra of Micro, One-pot Meso and Aged Meso-0.15 zeolites, in which the main chemical shifts of a tetrahedrally coordinated chabazite structure are underlined (dash lines). The building unit $Si(OAl)_x$ with x = 4, 3, 2, 1, 0, gives rise a chemical shift at -89, -95, -99.6, -104,3 and -110 ppm respectively, according to the literature [13,16,19–21,39]. These results showed that no resonance peak was detected in the -110 ppm chemical shift region, indicating that these bulk structures are free of Si-island $Si(OSi)_4$ [16,18,19,21]. For Aged Meso-0.15 material, a well-defined signal centered between -89 and -95 ppm, similar to that of the conventional microporous one, seems to indicate that this material presented isolated Si atoms mainly in $Si(OAl)_3$ and $Si(OAl)_4$ building unit configuration. On the contrary, only isolated Si atoms in $Si(OAl)_4$ configuration seems to be presented on One-pot Meso SAPO-34. Comparing the intensity of both ^{29}Si NMR spectra, a disordered state of Si on One-pot Meso material could be underlined [39].

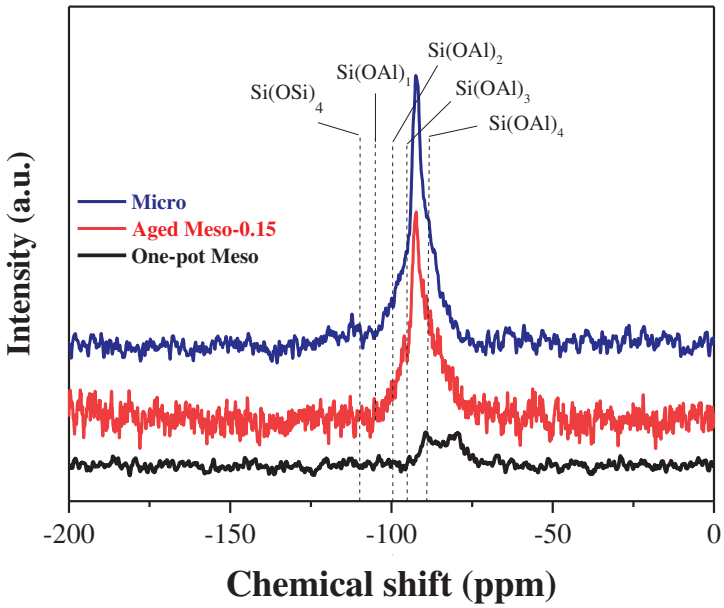

Figure III. S2. ^{29}Si MNR spectra of Micro, One-pot and Aged Meso-0.15 SAPO-34 materials.

- ***Influence of aging time***

The effect of aging time of hierarchical SAPO-34 zeolites is then studied. The hierarchical materials were synthesized by hydrothermal crystallization with a previous aging treatment at 100°C varying the aged time between 24, 48 and 64h (before addition of CTAB template and hydrothermal crystallization). These materials will be denoted as "Aged Meso-24h", "Aged

Meso-48h" and "Aged Meso-64h", respectively. Note that the last one ("Aged Meso-64h") corresponds with the previous denoted "Aged Meso-0.15" CHA-based zeolite.

The chemical composition of these hierarchical CHA-based zeolites is listed in Table III. S1. As previously shown, it was possible to obtain materials with CHA structure as a pure and crystalline phase using this adapted method. However, the duration of aging treatment has an important influence in the formation of these crystalline hierarchical structures, Figure S3. The materials previously aged for 24 or 48h exhibited an amorphous structure by XRD analysis, indicating that 24h or 48h of aged heat treatments is not long enough to form these nanocrystalline zeolite seeds. As previously mentioned, the formation of the zeolite seeds (negatively charged) is required to ensure the assembly with the cationic CTAB (positively charged) for mesoporosity creation [4,5,7,8]. However, if the aging time is not enough to form the nanocrystalline zeolite seeds, the zeolite gel solution (before crystallization) will be constituted by oligomers and/or nanoparticles with low crystallization degree, which are responsible for the formation of amorphous mesophases [8]. These characterization results showed that the formation of CHA sieve structure required a specific aged time (about 64h) to form nanocrystalline zeolite seeds and, as a consequence, to form pure and crystalline hierarchical CHA-based zeolites.

Table III. S1. Influence of aging time - chemical composition of Aged Meso SAPO-34 CHA-based zeolites.

Support	Aging time (h)	Si/Al Molar ratio	(Si+P)/Al molar ratio
Aged meso-64h[a]	64	0.12	0.73
Aged meso-48h[b]	48	0.13	0.37
Aged meso-24h[c]	24	0.14	0.37

[a,b] and [c] Hierarchical SAPO-34 CHA-based zeolite synthetized by soft-templating method (using TEAOH and CTAB as micro and meso-templates) with a previous aging heat treatment at 100°C for 64h, 48h and 24h, respectively.

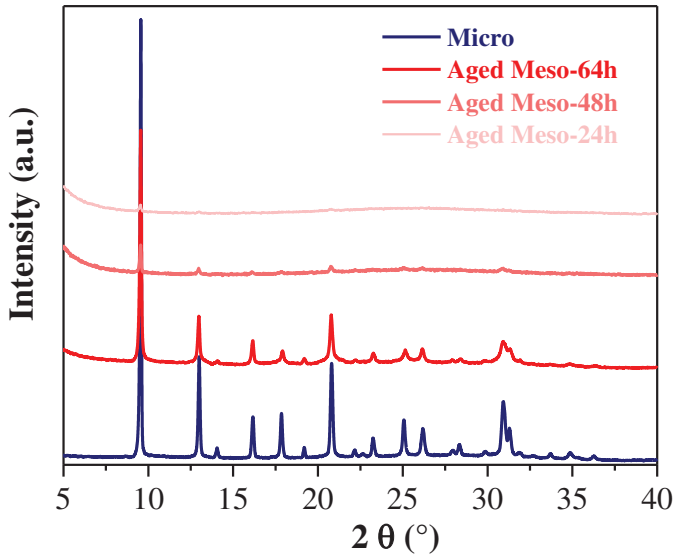

Figure III. S3. XRD patterns of conventional micropores CHA-based zeolite and hierarchical SAPO-34 CHA-based zeolites synthetized using different aging time.

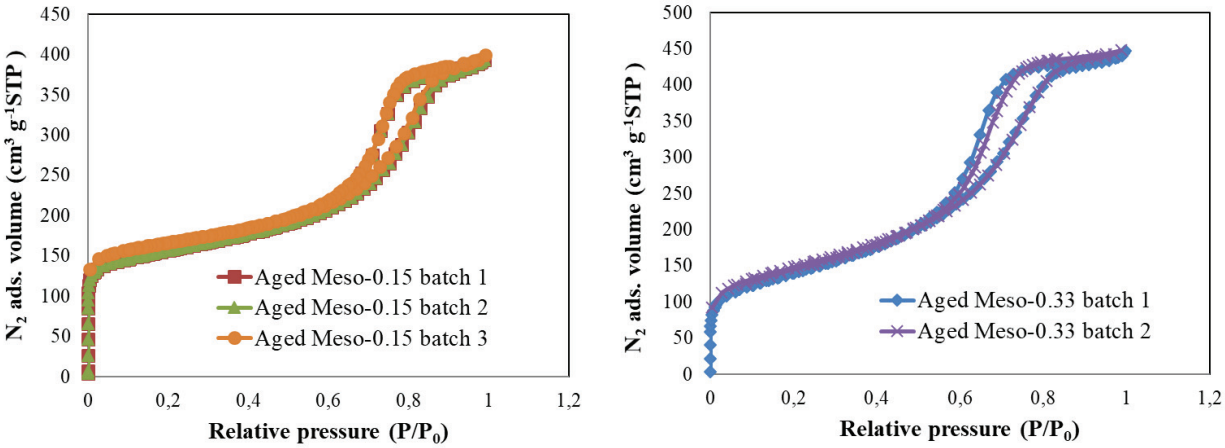

Figure III. S4. N_2 adsorption-desorption isotherms (a) Aged Meso-0.15 and (b) Aged Meso-0.33 hierarchical materials.

References

[1] G. Pétaud, F. Gaillard, M. Tayakout, S. Gil, A. Giroir-Fendler, Spotlight on Large Surface Copper Cluster Role of Cu-SAPO-34 Catalyst in Standard NH3-SCR Performances, ChemCatChem. n/a (2020). https://doi.org/10.1002/cctc.201902036.

[2] G. Pétaud, S. Gil, A.G. Fendler, Cu SAPO 34 One Pot Hydrothermal Preparation Method for Particular Copper Configuration, Top. Catal. 62 (2019) 63–71. https://doi.org/10.1007/s11244-018-1107-y.

[3] L. Jin, S. Liu, T. Xie, Y. Wang, X. Guo, H. Hu, Synthesis of hierarchical ZSM-5 by cetyltrimethylammonium bromide assisted self-assembly of zeolite seeds and its catalytic performances, React. Kinet. Mech. Catal. 113 (2014). https://doi.org/10.1007/s11144-014-0743-x.

[4] J. Zhong, J. Han, Y. Wei, P. Tian, X. Guo, C. Song, Z. Liu, Recent advances of the nano-hierarchical SAPO-34 in the methanol-to-olefin (MTO) reaction and other applications, Catal. Sci. Technol. 7 (2017) 4905–4923. https://doi.org/10.1039/C7CY01466J.

[5] A. Feliczak-Guzik, Hierarchical zeolites: Synthesis and catalytic properties, Microporous Mesoporous Mater. 259 (2018) 33–45. https://doi.org/https://doi.org/10.1016/j.micromeso.2017.09.030.

[6] N. Masoumifard, R. Guillet-Nicolas, F. Kleitz, Synthesis of Engineered Zeolitic Materials: From Classical Zeolites to Hierarchical Core–Shell Materials, Adv. Mater. 30 (2018) 1704439. https://doi.org/10.1002/adma.201704439.

[7] X.-Y. Yang, L.-H. Chen, Y. Li, J.C. Rooke, C. Sanchez, B.-L. Su, Hierarchically porous materials: synthesis strategies and structure design, Chem. Soc. Rev. 46 (2017) 481–558. https://doi.org/10.1039/C6CS00829A.

[8] Y. Zhu, Z. Hua, J. Zhou, L. Wang, J. Zhao, Y. Gong, W. Wu, M. Ruan, J. Shi, Hierarchical Mesoporous Zeolites: Direct Self-Assembly Synthesis in a Conventional Surfactant Solution by Kinetic Control over the Zeolite Seed Formation, Chem. – A Eur. J. 17 (2011) 14618–14627. https://doi.org/10.1002/chem.201101401.

[9] L. Kong, Z. Jiang, J. Zhao, J. Liu, B. Shen, The Synthesis of Hierarchical SAPO-34 and its Enhanced Catalytic Performance in Chloromethane Conversion to Light Olefins, Catal. Letters. 144 (2014) 1609–1616. https://doi.org/10.1007/s10562-014-

1296-3.

[10] T. Álvaro-Muñoz, C. Márquez-Álvarez, E. Sastre, Enhanced stability in the methanol-to-olefins process shown by SAPO-34 catalysts synthesized in biphasic medium, Catal. Today. 215 (2013) 208–215. https://doi.org/https://doi.org/10.1016/j.cattod.2013.03.015.

[11] Y.D. Wang, S. Zhang, C.L. Ma, H.D. Li, Synthesis and room temperature photoluminescence of ZnO/CTAB ordered layered nanocomposite with flake-like architecture, J. Lumin. 126 (2007) 661–664. https://doi.org/https://doi.org/10.1016/j.jlumin.2006.10.018.

[12] M. Briend, R. Vomscheid, M.J. Peltre, P.P. Man, D. Barthomeuf, Influence of the Choice of the Template on the Short- and Long-Term Stability of SAPO-34 Zeolite, J. Phys. Chem. 99 (1995) 8270–8276. https://doi.org/10.1021/j100020a060.

[13] J. Wang, T. Yu, X. Wang, G. Qi, J. Xue, M. Shen, W. Li, The influence of silicon on the catalytic properties of Cu/SAPO-34 for NOx reduction by ammonia-SCR, Appl. Catal. B Environ. 127 (2012) 137–147. https://doi.org/https://doi.org/10.1016/j.apcatb.2012.08.016.

[14] P. Wang, A. Lv, J. Hu, J. Xu, G. Lu, The synthesis of SAPO-34 with mixed template and its catalytic performance for methanol to olefins reaction, Microporous Mesoporous Mater. 152 (2012) 178–184. https://doi.org/https://doi.org/10.1016/j.micromeso.2011.11.037.

[15] T. Fjermestad, S. Svelle, O. Swang, Mechanism of Si Island Formation in SAPO-34, J. Phys. Chem. C. 119 (2015) 2086–2095. https://doi.org/10.1021/jp510845z.

[16] C. Lin, Y. Cao, X. Feng, Q. Lin, H. Xu, Y. Chen, Effect of Si islands on low-temperature hydrothermal stability of Cu/SAPO-34 catalyst for NH3-SCR, J. Taiwan Inst. Chem. Eng. 81 (2017) 288–294. https://doi.org/https://doi.org/10.1016/j.jtice.2017.09.050.

[17] T. Yu, J. Wang, M. Shen, W. Li, NH3-SCR over Cu/SAPO-34 catalysts with various acid contents and low Cu loading, Catal. Sci. Technol. 3 (2013) 3234–3241. https://doi.org/10.1039/C3CY00453H.

[18] C.S. Blackwell, R.L. Patton, Solid-state NMR of silicoaluminophosphate molecular sieves and aluminophosphate materials, J. Phys. Chem. 92 (1988) 3965–3970.

https://doi.org/10.1021/j100324a055.

[19] G.A. V Martins, G. Berlier, S. Coluccia, H.O. Pastore, G.B. Superti, G. Gatti, L. Marchese, Revisiting the Nature of the Acidity in Chabazite-Related Silicoaluminophosphates: Combined FTIR and 29Si MAS NMR Study, J. Phys. Chem. C. 111 (2007) 330–339. https://doi.org/10.1021/jp063921q.

[20] F. Gao, E.D. Walter, N.M. Washton, J. Szanyi, C.H.F. Peden, Synthesis and Evaluation of Cu-SAPO-34 Catalysts for Ammonia Selective Catalytic Reduction. 1. Aqueous Solution Ion Exchange, ACS Catal. 3 (2013) 2083–2093. https://doi.org/10.1021/cs4004672.

[21] J. Liu, F. Yu, J. Liu, L. Cui, Z. Zhao, Y. Wei, Q. Sun, Synthesis and kinetics investigation of meso-microporous Cu-SAPO-34 catalysts for the selective catalytic reduction of NO with ammonia, J. Environ. Sci. 48 (2016) 45–58. https://doi.org/https://doi.org/10.1016/j.jes.2016.01.027.

[22] Q. Sun, Y. Ma, N. Wang, X. Li, D. Xi, J. Xu, F. Deng, K.B. Yoon, P. Oleynikov, O. Terasaki, J. Yu, High performance nanosheet-like silicoaluminophosphate molecular sieves: synthesis, 3D EDT structural analysis and MTO catalytic studies, J. Mater. Chem. A. 2 (2014) 17828–17839. https://doi.org/10.1039/C4TA03419H.

[23] X. Chen, A. Vicente, Z. Qin, V. Ruaux, J.-P. Gilson, V. Valtchev, The preparation of hierarchical SAPO-34 crystals via post-synthesis fluoride etching, Chem. Commun. 52 (2016) 3512–3515. https://doi.org/10.1039/C5CC09498D.

[24] M. Thommes, K. Kaneko, A. V Neimark, J.P. Olivier, F. Rodriguez-Reinoso, J. Rouquerol, K.S.W. Sing, Physisorption of gases, with special reference to the evaluation of surface area and pore size distribution (IUPAC Technical Report), Pure Appl. Chem. 87 (2015) 1051–1069. https://doi.org/https://doi.org/10.1515/pac-2014-1117.

[25] F. Sotomayor, K. Cychosz, M. Thommes, Characterization of Micro/Mesoporous Materials by Physisorption: Concepts and Case Studies, (2018).

[26] J. Pérez-Ramírez, D. Verboekend, A. Bonilla, S. Abelló, Zeolite Catalysts with Tunable Hierarchy Factor by Pore-Growth Moderators, Adv. Funct. Mater. 19 (2009) 3972–3979. https://doi.org/10.1002/adfm.200901394.

[27] D. Verboekend, J. Pérez-Ramírez, Design of hierarchical zeolite catalysts by

desilication, Catal. Sci. Technol. 1 (2011) 879–890. https://doi.org/10.1039/C1CY00150G.

[28] A.M. Prakash, S. Unnikrishnan, Synthesis of SAPO-34: high silicon incorporation in the presence of morpholine as template, J. Chem. Soc. Faraday Trans. 90 (1994) 2291–2296. https://doi.org/10.1039/FT9949002291.

[29] T. Ishihara, M. Kagawa, F. Hadama, Y. Takita, Copper Ion-Exchanged SAPO-34 as a Thermostable Catalyst for Selective Reduction of NO with C3H6, J. Catal. 169 (1997) 93–102. https://doi.org/https://doi.org/10.1006/jcat.1997.1681.

[30] M. Zienkiewicz-Strzałka, M. Skibińska, S. Pikus, Small-angle X-ray scattering (SAXS) studies of the structure of mesoporous silicas, Nucl. Instruments Methods Phys. Res. Sect. B Beam Interact. with Mater. Atoms. 411 (2017) 72–77. https://doi.org/https://doi.org/10.1016/j.nimb.2017.03.028.

[31] R.A. García, D.P. Serrano, D. Otero, Catalytic cracking of HDPE over hybrid zeolitic–mesoporous materials, J. Anal. Appl. Pyrolysis. 74 (2005) 379–386. https://doi.org/https://doi.org/10.1016/j.jaap.2004.11.002.

[32] M. Choi, H.S. Cho, R. Srivastava, C. Venkatesan, D.-H. Choi, R. Ryoo, Amphiphilic organosilane-directed synthesis of crystalline zeolite with tunable mesoporosity, Nat. Mater. 5 (2006) 718–723. https://doi.org/10.1038/nmat1705.

[33] I.I. Ivanova, E.E. Knyazeva, Micro–mesoporous materials obtained by zeolite recrystallization: synthesis, characterization and catalytic applications, Chem. Soc. Rev. 42 (2013) 3671–3688. https://doi.org/10.1039/C2CS35341E.

[34] Y.P. Khitev, Y.G. Kolyagin, I.I. Ivanova, O.A. Ponomareva, F. Thibault-Starzyk, J.-P. Gilson, C. Fernandez, F. Fajula, Synthesis and catalytic properties of hierarchical micro/mesoporous materials based on FER zeolite, Microporous Mesoporous Mater. 146 (2011) 201–207. https://doi.org/https://doi.org/10.1016/j.micromeso.2011.05.003.

[35] D. Verma, R. Kumar, B.S. Rana, A.K. Sinha, Aviation fuel production from lipids by a single-step route using hierarchical mesoporous zeolites, Energy Environ. Sci. 4 (2011) 1667–1671. https://doi.org/10.1039/C0EE00744G.

[36] A. Varzaneh, J. Towfighi, S. Sahebdelfar, H. Bahrami, Carbon nanotube templated synthesis of hierarchical SAPO-34 catalysts with different structure directing agents for catalytic conversion of methanol to light olefins, J. Anal. Appl. Pyrolysis. 121 (2016)

11–23. https://doi.org/https://doi.org/10.1016/j.jaap.2016.06.007.

[37] S. ul H. Bakhtiar, X. Wang, S. Ali, F. Yuan, Z. Li, Y. Zhu, CTAB-assisted size controlled synthesis of SAPO-34 and its contribution toward MTO performance, Dalt. Trans. 47 (2018) 9861–9870. https://doi.org/10.1039/C8DT01811A.

[38] W. Zhang, W. Ming, S. Hu, B. Qin, J. Ma, R. Li, A feasible one-step synthesis of hierarchical zeolite Beta with uniform nanocrystals via CTAB, Materials (Basel). 11 (2018). https://doi.org/10.3390/ma11050651.

[39] J. Tan, Z. Liu, X. Bao, X. Liu, X. Han, C. He, R. Zhai, Crystallization and Si incorporation mechanisms of SAPO-34, Microporous Mesoporous Mater. 53 (2002) 97–108. https://doi.org/10.1016/S1387-1811(02)00329-3.

[40] M. Popova, C. Minchev, V. Kanazirev, Methanol conversion to light alkenes over SAPO-34 molecular sieves synthesized using various sources of silicon and aluminium, Appl. Catal. A Gen. 169 (1998) 227–235. https://doi.org/https://doi.org/10.1016/S0926-860X(98)00003-9.

[41] B. Zibrowius, E. Löffler, M. Hunger, Multinuclear MAS n.m.r. and i.r. spectroscopic study of silicon incorporation into SAPO-5, SAPO-31, and SAPO-34 molecular sieves, Zeolites. 12 (1992) 167–174. https://doi.org/https://doi.org/10.1016/0144-2449(92)90079-5.

[42] M. Wang, Z. Wang, S. Liu, R. Gao, K. Cheng, L. Zhang, G. Zhang, X. Min, J. Kang, Q. Zhang, Y. Wang, Synthesis of hierarchical SAPO-34 to improve the catalytic performance of bifunctional catalysts for syngas-to-olefins reactions, J. Catal. 394 (2021) 181–192. https://doi.org/https://doi.org/10.1016/j.jcat.2020.08.020.

[43] T. Yu, T. Hao, D. Fan, J. Wang, M. Shen, W. Li, Recent NH3-SCR Mechanism Research over Cu/SAPO-34 Catalyst, J. Phys. Chem. C. 118 (2014) 6565–6575. https://doi.org/10.1021/jp4114199.

[44] L. Wang, W. Li, S.J. Schmieg, D. Weng, Role of Brønsted acidity in NH3 selective catalytic reduction reaction on Cu/SAPO-34 catalysts, J. Catal. 324 (2015) 98–106. https://doi.org/https://doi.org/10.1016/j.jcat.2015.01.011.

[45] S. Ashtekar, S.V. V Chilukuri, D.K. Chakrabarty, Small-Pore Molecular Sieves SAPO-34 and SAPO-44 with Chabazite Structure: A Study of Silicon Incorporation, J. Phys. Chem. 98 (1994) 4878–4883. https://doi.org/10.1021/j100069a018.

[46] C. Wang, C. Wang, J. Wang, J. Wang, M. Shen, W. Li, Effects of Na+ on Cu/SAPO-34 for ammonia selective catalytic reduction, J. Environ. Sci. 70 (2018) 20–28. https://doi.org/https://doi.org/10.1016/j.jes.2017.11.002.

[47] H. Yang, Z. Liu, H. Gao, Z. Xie, Synthesis and catalytic performances of hierarchical SAPO-34 monolith, J. Mater. Chem. 20 (2010) 3227–3231. https://doi.org/10.1039/B924736J.

[48] W. Khan, X. Jia, Z. Wu, J. Choi, A.C.K. Yip, Incorporating Hierarchy into Conventional Zeolites for Catalytic Biomass Conversions: A Review, Catalysts. 9 (2019) 127–149. https://doi.org/https://doi.org/10.3390/catal9020127.

Chapter IV

CHAPTER IV: Cu-hierarchical-SAPO-34 catalysts with enhanced low-temperature NO_x removal and high hydrothermal stability.

Considering the expected gradual fuel efficiency enhancement [1], together with the progress and further implementation of upgraded engine technologies, the engine-exhaust temperatures are expected to drop sharply [2]. In addition, under "cold-start" operating conditions, the exhaust temperature is much lower compared to that "on-road". However, in such low temperature window, the above described Cu-CHA catalysts do not seem to exhibit sufficient activity to efficiently reduce NO_x [2]. Among other reasons, this could be attributed to the small pore size of CHA-zeolite, which strongly hinders the access of reactants to the catalytically active sites. It leads to significant intra-crystalline diffusion limitations, even at low temperatures [3,4]. The development of hierarchical zeolites with structured and ordered micropores and mesopores could be a promising solution to overcome such issue. In this sense, in previous chapter III [5] novel hierarchical CHA-based (SAPO-34) materials were developed and optimized by the strategy of soft-templating method (never used before for small-pore zeolites). Both microporous and soft mesoporous templates where introduced at different stages of the synthesis procedure. Hence, by using different amounts of cetyltrimethylammonium bromide (CTAB, mesoporous template), the obtained materials exhibited both, micro and mesopores (without drastically damaging the zeolite structure), with different structural (crystallinity, micropores/mesopores ratio) and acidic properties, which will potentially influence their catalytic performance for the NH_3-SCR reaction. Indeed, two hierarchical zeolite materials were selected on account of their enhanced physico-chemical properties [5]: On the one hand, the material so-called "*Aged-Meso-0.15*" (with a CTAB/Al molar ratio = 0.15) exhibited a significant volume of mesopores (without a drastic sacrifice of micropores), and the highest long-range order of mesopores among the developed hierarchical materials, together with an important amount of acid sites. On the other hand, the material so-called "*Aged-Meso-0.66*" (with a CTAB/Al molar ratio = 0.66) also exhibited a similar hierarchical porosity, and even a higher amount of acid sites than the "*Aged-Meso-0.15*", although the long-range order of mesopores was lower. Hence, both materials are very promising for the NO_x reduction by the NH_3-SCR reaction, since the hierarchical pore formation may potentially enhance the low temperature diffusion of reactants, while their acidity may promote the kinetics for such catalytic process [6,7].

This chapter aims to move one-step forward into the development of advanced catalysts for the NH_3-SCR reaction. Seeing as the above-described hierarchical zeolite materials exhibit very promising features, they will be used as catalytic supports for the development of new Cu/SAPO-34 catalysts. These hierarchical SAPO-34-based zeolite supports are denoted as "*0.15-fresh (support)"* and "*0.66-fresh (support)"* based on the molar ratio of CTAB/Al of 0.15 and 0.66, respectively, and the microporous one is denoted as "*Micro-fresh (support)"*. However, as previously mentioned in *Chapter I*, the hydrothermal stability is a key feature in view of the further implementation of such catalytic materials. It is well-known that the small pores on conventional microporous CHA zeolites inhibit their structural de-alumination, leading to high hydrothermal stability [8]. Hence, one may think that the creation of mesopores could eventually weaken the zeolite structure, decreasing therefore its hydrothermal stability. This is expected if aggressive post-treatment methods (e.g. dealumination, desilication) are used for the generation of mesopores, since they usually degrade the framework structure of zeolites. However, previous studies displayed high hydrothermal stability of novel hierarchical CHA zeolites (SSZ-13) [9] prepared by dual templates (one for the generation of micropores, and the other for the generation of mesopores, as was the case in our previous study [5]).

On the other hand, the impact of the hydrothermal treatment on the migration of Cu species on conventional microporous Cu-CHA catalysts has been reported [10–13]. Generally, it has been observed that after the hydrothermal treatment, CuO species re-disperse to occupy the ion-exchange sites in the CHA crystal framework, leading to the production of isolated Cu^{2+} species. These latter have been identified as a key catalytic active phase for the NH_3-SCR process. Hence, in this work the impact of a hydrothermal treatment on the main physico-chemical properties, active sites and catalytic activity (for the NH_3-SCR reaction) of the novel hierarchical Cu/SAPO-34 catalysts will be thoroughly studied. The catalysts obtained after the hydrothermal treatment are denoted as "*Cu/micro-HT*", "*Cu-0.15-HT*" and "*Cu-0.66-HT*", which were prepared by subjecting to the hydrothermal treatment the "*Cu/micro-fresh*", "*Cu/0.15-fresh*" and "*Cu/0.66-fresh*" catalysts, respectively.

All in all, this chapter will allow to get more insights into the understanding of these catalytic materials, from their structural features to the role of the different Cu species and acid sites in the chemical reactions involved for the catalytic reduction of NO_x.

1. Physico-chemical properties of Cu/SAPO-34 catalysts before and after hydrothermal treatment.

The structural properties of the microporous and hierarchical Cu-based catalysts, before (*"Cu/micro-fresh"*, *"Cu/0.15-fresh"* and *"Cu/0.66-fresh"*) and after the hydrothermal treatment (*"Cu/micro-HT"*, *"Cu/0.15-HT"* and *"Cu/0.66-HT"*), were investigated by XRD, N_2 adsorption/desorption and ICP-OES analysis.

First of all, Figure IV. 1 (a-c) (left) show the XRD patterns at wide-angles for the fresh Cu-based microporous catalyst (*"Cu/micro-fresh"*) and the above-mentioned hierarchical catalysts (*"Cu/0.15-fresh"* and *"Cu/0.66-fresh"*), respectively. All these fresh catalysts exhibit XRD characteristic peaks of conventional SAPO-34 CHA-based zeolite, with their main peak located at $2\theta = 9.5^{o}$ [5,14]. The crystal size (according to the Scherrer equation) and the relative crystallinity of such catalysts (compared to the crystallinity of the *"Cu/micro-fresh"* catalyst) are shown in Table IV. 1, as well as the final Cu loading obtained by ICP-AES. In addition, a minor decrease of both, the crystal size and crystallinity, was observed for the Cu-based hierarchical catalysts compared to those of the Cu-based microporous catalyst. As a matter of fact, similar crystal sizes and relative crystallinity values were obtained for the hierarchical supports in our previous study (*Chapter III*) [5]. It can be attributed to both, the slight detrimental effect on the SAPO-34 crystal structure due to the addition of the mesoporous template (CTAB) during the synthesis procedure [14], and its crystal growth inhibitor effect [15]. This seems to indicate that neither the introduction of mesopores into the microporous SAPO-34, nor the introduction of Cu by ionic exchange, drastically affected to its crystalline structure, in good agreement with previous studies [10,16]. Indeed, this is a feature of paramount importance. Ideally, the addition of mesopores and Cu species, while enhancing the diffusion of reactants into the catalyst active sites and the reaction kinetics, should not compromise the high stability and robustness of the zeolite material, which are typically ascribed to its microporous structure with small-size pores. In view of these results, it can be expected therefore that these materials may exhibit a significant hydrothermal stability.

Hence, the same catalysts were also characterized after the hydrothermal treatment, and the wide-angle XRD patterns of the so-called *"Cu/micro-HT"*, *"Cu/0.15-HT"* and *"Cu/0.66-HT"* catalysts are shown in Figures IV. 1 (a-c) (left), respectively, together with their fresh counterparts. Very interestingly, this series of catalysts exhibited almost identical crystalline features (see Table IV. 1) than the fresh materials, which points out that the main CHA structure of the hierarchical catalysts was well preserved after the harsh hydrothermal treatment. It is

worth noting that the diffraction peaks ascribed to Copper oxides (CuO) (2θ = 35.6° and 38.8°) cannot be observed for any sample, likely due to the fact that the Cu species (2%wt. Cu nominal loading target) were homogeneously dispersed in all these catalysts [9]. The type, role and ratio of the different Cu species will be thoroughly discussed in the next sections.

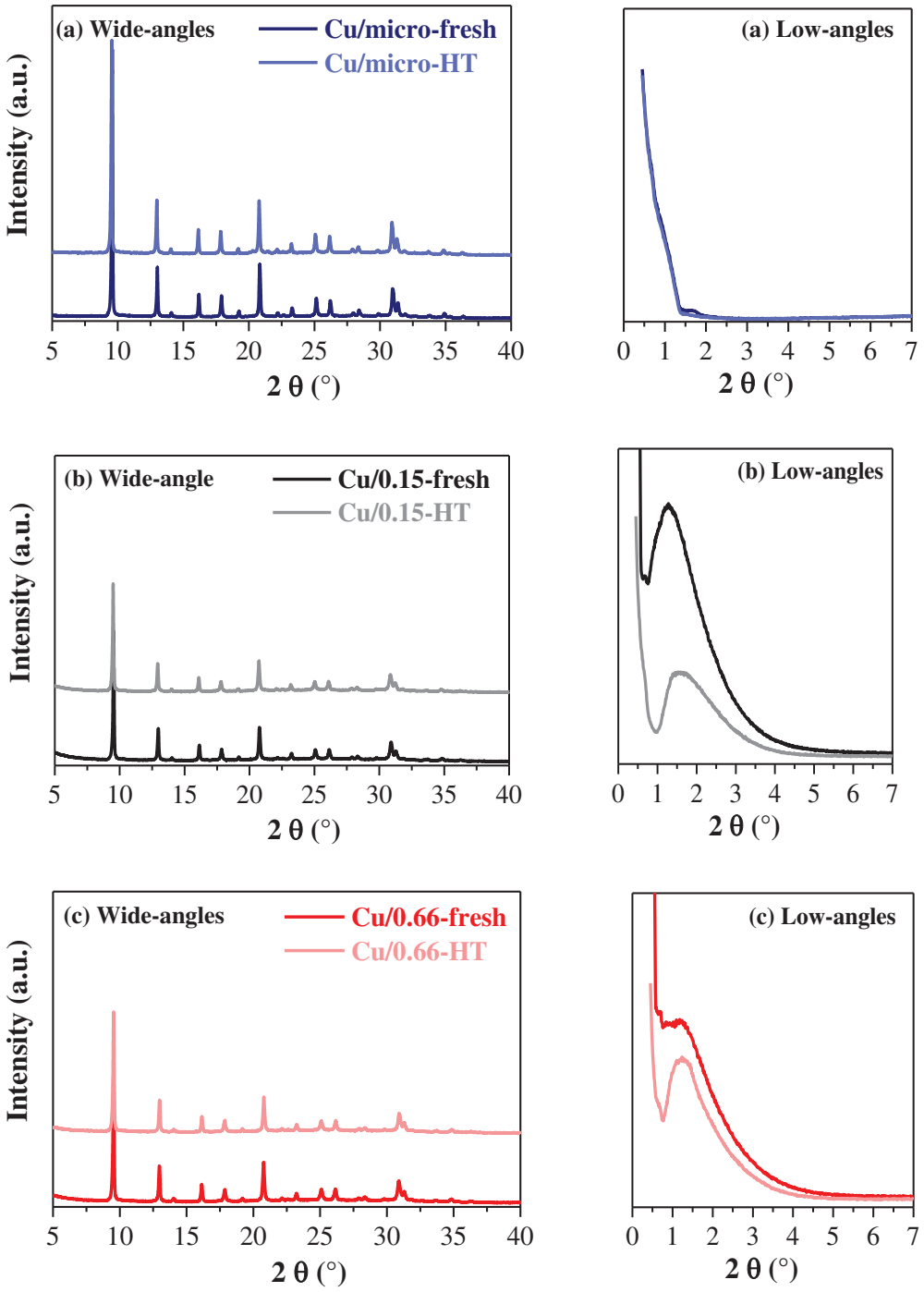

Figure IV. 1. XRD patterns for wide- (left) and low-angles (right) of microporous and hierarchical Cu-based catalysts before (fresh) and after hydrothermal treatment (HT): (a) "Cu/micro-fresh" and "Cu/micro-HT" (b) "Cu/0.15-fresh" and "Cu/0.15-HT" (c) "Cu/0.66-fresh" and "Cu/0.66-HT".

While the wide-angle XRD provides relevant information about the bulk structure of these materials, low-angle XRD is commonly used to determine the relative order of the mesopores created in the hierarchical materials. Figures IV. 1 (a-c) (right) show the low-angle XRD patterns (2θ = 0.5-7°) of *"Cu/micro-HT"*, *"Cu/0.15-HT"* and *"Cu/0.66-HT"* catalysts, respectively, together with their fresh counterparts. Regarding the fresh catalysts, they exhibit almost identical profiles compared to those of their zeolite-based supports [5]. Among the Cu-based hierarchical catalysts, *"Cu/0.15-fresh"* exhibits the highest intensity of the peak at 1.6°, which could be related with a more important long-range order (i.e., higher periodicity) of mesopores [17,18]. As expected, the XRD pattern of the *"Cu/micro-fresh"* and *"Cu/micro-HT"* catalysts did not depict such peak, since these materials are mainly based on small micropores. However, a clear decrease of the representative peak for the hierarchical catalysts after the hydrothermal treatment can be observed in these figures, suggesting a slight detrimental impact on the periodicity of the mesopores of those catalysts.

Table IV. 1. Crystal size, relative crystallinity and Cu loading and textural properties of Cu-based microporous and hierarchical catalysts before (fresh) and after hydrothermal treatment (HT). Data of the counterpart fresh zeolite supports from ref. [5] are included as reference.

Materials	Crystal size (nm)[a]	Relative crystallinity (%)[a,b]	Cu (%)[c]
Micro-fresh (support) [5]	*104.8*	*100*	-
Cu/micro-fresh	89.4	100	1.60
Cu/micro-HT	83.2	99.7	1.56
0.15-fresh (support) [5]	*82.7*	*86.8*	-
Cu/0.15-fresh	78.9	82.8	1.21
Cu/0.15-HT	79	78.3	1.13
0.66-fresh (support) [5]	*82.7*	*86.6*	-
Cu/0.66-fresh	76	84.7	1.48
Cu/0.66-HT	77.5	83.8	1.19

[a]*Crystal size and normalized crystallinity were calculated by Diffrac.Eva software.*

[b]*Relative crystallinity correspond to the normalized crystallinity of Cu-based materials with respect to the "Cu/micro-fresh" catalyst.*

[c]*Cu loading was obtained by ICP-AOS - 2%wt. Cu nominal loading target.*

In order to understand whether the minor loss of periodicity was related to a loss of mesopores, the textural properties of the materials studied in this work were characterized by N_2 adsorption/desorption. Figures IV. 2 (a-c) show the isotherms for the target Cu-based catalysts before and after the hydrothermal treatment, while Figures IV. 2 (d, e) depict the BJH pore diameter distribution of the Cu-based hierarchical catalysts. As expected, the fresh

microporous catalyst (*"Cu/micro-fresh"*) shows a Type I isotherm, characteristic of microporous materials according to the IUPAC classification [19,20]. Regarding the fresh hierarchical catalysts (*"Cu/0.15-fresh"* and *"Cu/0.66-fresh"*), they exhibit a combination of Type I and Type IV isotherms, with a significant adsorption at low partial pressures (attributed to microporosity) and a pronounced hysteresis loop at high P/P_0. As a matter of fact, the shapes of these isotherms are very similar to those reported in our previous study for the hierarchical zeolite supports [5]. It reveals the presence of mesoporosity within the microporous-CHA framework, while the hysteresis can be classified as H2-type, associated with ink-bottle pores. In addition, the pore size distributions of the *"Cu/0.15-fresh"* and *"Cu/0.66-fresh"* catalysts, which were obtained by the BJH method, indicate that the mesopore sizes in such materials are centered at about 9 nm. Regarding the materials exposed to the hydrothermal treatment, it is worth noting that the N_2 adsorption/desorption isotherms exhibit the same trend. However, while the adsorption volume at low pressures (associated to micropores) did not seem to be significantly modified, the adsorption volume at higher pressures was slightly lower for the catalysts after the hydrothermal treatment. This observation suggests a minor decrease of the mesoporosity of these catalysts.

Based on the N_2 adsorption/desorption isotherms, Table IV. 2 shows the values of S_{BET} (BET specific surface area), S_{ext} (external surface area), V_{micro} (microporous volume) and V_{meso} (mesoporous volume) of the target catalysts, together with the values obtained in our previous study [5] for their counterpart supports for further comparison. For hierarchical materials, the external surface area is tightly related to their volume of mesopores (intra-crystalline porosity) [5], while the S_{ext} for the microporous SAPO-34-based materials can be associated to the defects of the external surface and inter-crystalline porosity [19]. First of all, the Cu-based microporous catalyst exhibits a higher S_{BET} and V_{micro} than both fresh hierarchical catalysts (*"Cu/0.15-fresh"* and "*Cu/0.66-fresh"*), which show very similar values. However, as expected, the latter catalysts depict higher values of S_{ext}, which led to higher V_{meso}. In good agreement with our previous study and with the N_2 adsorption/desorption isotherms previously described (Figure IV. 2), this proves the development of mesopores in the microporous CHA framework. However, it is worth noting that, for all the fresh catalysts, a significant decrease of the external surface area and mesoporous volume (leading to an overall decrease of the S_{BET}) was observed compared to their bare supports. Hence, the hierarchy factor values (HF, Table IV. 2) of the Cu-based hierarchical catalysts were slightly lower than those of the hierarchical zeolite support but much higher than the HF for the *"Cu/micro-fresh"* catalyst. The high HF values obtained

for the Cu-based hierarchical catalysts can be interpreted as an efficient development of mesopores without a severe sacrifice of the micropore volume of the base material [5,21].

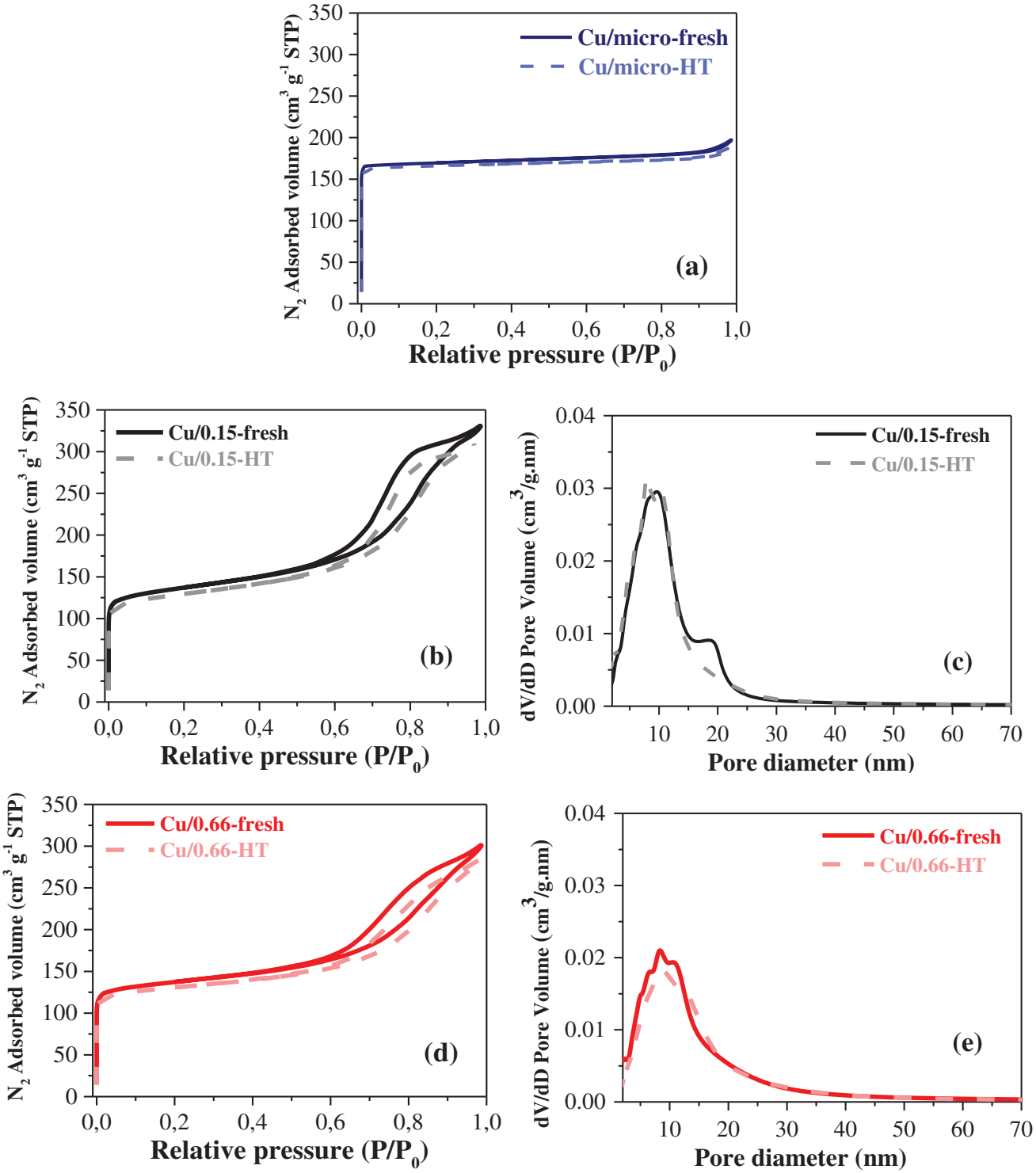

Figure IV. 2. N_2 adsorption-desorption isotherms of Cu-based: (a) microporous and (b, c) hierarchical catalysts before (fresh) and after hydrothermal treatment (HT). BJH pore diameter distributions of (d, e) Cu-based hierarchical catalysts before (fresh) and after hydrothermal treatment (HT).

According to previous studies, the loss of external surface upon the introduction of Copper could be attributed to the partial coverage of the external surface area of the zeolite-based supports with CuO_x species [12]. Even though the role of the different Copper species in CHA-based catalysts is still under debate, it is generally accepted that isolated Cu^{2+} ions (incorporated by ionic exchange into the zeolite framework) are relevant active sites for the NH_3-SCR reaction [6,7,11,12,22]. However, the presence of CuO_x species covering the surface (mainly the mesopores) of these materials cannot be neglected. One can expect therefore that the materials exhibiting a higher mesoporous volume (i.e., the hierarchical catalysts in this study) could accommodate a higher concentration of CuO_x species. In view of these results, it can expect a higher amount of CuO_x species in *"Cu/0.15-fresh"* and *"Cu/0.66-fresh"* than in *"Cu/micro-fresh"*.

Table IV. 2. Textural properties of Cu-based microporous and hierarchical catalysts before (fresh) and after hydrothermal treatment (HT). Data of the counterpart fresh zeolite supports from ref. [5] are included as reference.

Materials	S_{BET} (m^2/g)	S_{ext} (m^2/g)	V_{micro} (cm^3/g)	V_{meso} (cm^3/g)	Average mesopores size (nm)	HF[a]
Micro-fresh (support) [5]	*690*	*53*	*0.25*	*0.09*		*0.06*
Cu/micro-fresh	664	28	0.25	0.05	-	0.03
Cu/micro-HT	651	21	0.24	0.04	-	0.02
0.15-fresh (support) [5]	*587*	*257*	*0.19*	*0.40*	*10*	*0.14*
Cu/0.15-fresh	512	181	0.18	0.33	9	0.12
Cu/0.15-HT	485	162	0.17	0.32	9	0.11
0.66-fresh (support) [5]	*611*	*281*	*0.22*	*0.37*	*8*	*0.17*
Cu/0.66-fresh	519	145	0.19	0.28	9	0.11
Cu/0.66-HT	496	125	0.18	0.26	10	0.10

[a]*Hierarchy Factor (HF): HF = $(V_{micro}/V_{total}) \times (S_{ext}/S_{BET})$, where $V_{total} = V_{micro} + V_{meso}$.*

After the hydrothermal treatment, a minor decrease of the specific surface area (S_{BET}) was observed for all the target catalysts, mainly related with a slight decrease of their external surface. This may justify the minor loss of long-range mesoporous order previously observed for the hierarchical catalysts after the hydrothermal treatment (low-angle XRD, Figure IV. 1). It is already well-known that microporous Cu/SAPO-34 catalysts exhibit an outstanding hydrothermal stability, since their small pores inhibit the structural de-alumination [8,10]. Nevertheless, these results suggest that, even for the Cu-based hierarchical catalysts, their

framework is robust enough to resist the harsh hydrothermal treatment, since only minor structural changes were observed. In addition, the Cu loading after such treatment remained very similar to that of the fresh catalysts. All in all, the results obtained in this section point out the excellent structural properties and hydrothermal resistance of the Cu-based hierarchical catalysts developed in this study.

2. Characterization of catalytic active sites: Cu species and surface acidity.

Even though the reaction mechanism for the NH_3-SCR reaction over Cu/SAPO-34 catalysts is still under debate, it is generally accepted that both, the nature of the Cu species and the acid sites of the catalyst constitute the main active sites for that catalytic process.

Regarding the Cu species, isolated Cu^{2+} ions are generally considered as the main Cu active sites for the NH_3-SCR reaction [12,23]. In addition, it is well-stablished that, under standard NH_3-SCR reaction conditions, isolated Cu^{2+} and Cu^{+} ionic species coexist, and interconvert one into the other through a redox mechanism [24,25]. However, as already pointed out in the previous section, there is a high probability of finding a different type of cupper species in the target catalysts, i.e. CuO_x, since the external surface of the catalysts drastically decreased upon the introduction of Copper. It is well-known that the state of Copper species is strongly affected by the preparation method [26,27] and by the exposure of the catalyst to a hydrothermal treatment [10,12,13]. Therefore, in this section the presence of different Cu species will be firstly evaluated by Diffuse reflectance infrared Fourier transform spectroscopy (DRIFTS) with pre-adsorption of different two probe molecules (NH_3 and CO) and by H_2-Temperature Programmed Reduction (H_2-TPR) measurements.

Figure IV. 3 (a) shows the DRIFTS spectra after NH_3 adsorption for the Cu-based fresh microporous *"Cu/micro-fresh"* catalyst. The bands at 891 and 844 cm^{-1} are commonly related to the internal asymmetric SAPO-34 framework vibration perturbed by Copper cations at the exchanged sites. Previous studies (on Cu/ZSM-5 catalysts) proposed that the band at the lower wavenumber is related to Cu^{2+} ions, while that at the higher wavenumber is ascribed to Cu^{+} ions [28,29]. Hence, the presence of these two bands provides direct evidence for the Cu species occupying the exchange sites in the microporous SAPO-34 support. However, lower signal was observed for the fresh Cu-based hierarchical catalysts, Figure IV. 3 (b) and (c), in comparison to Cu/micro fresh catalyst, which suggests that these catalysts might exhibit a significantly lower concentration of isolated Copper ions.

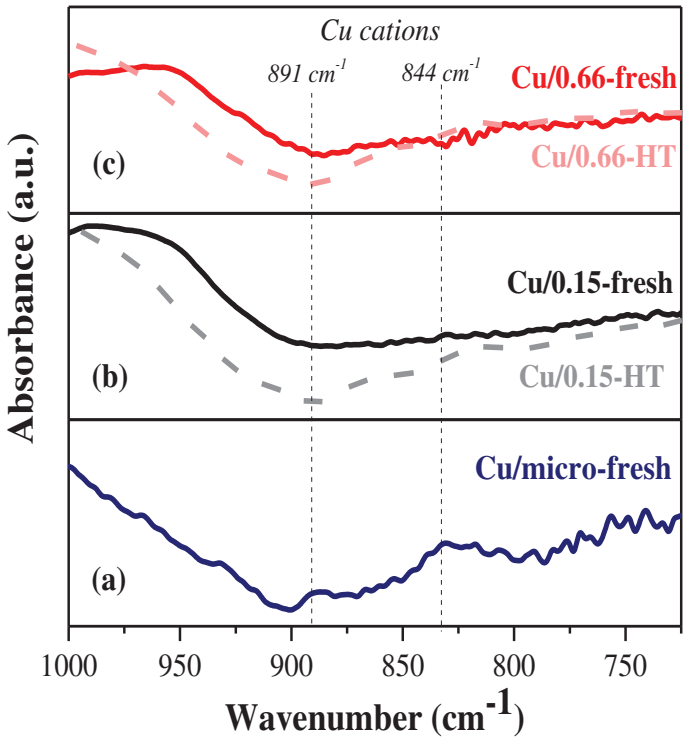

Figure IV. 3. DRIFTS spectra after previous adsorption of NH_3 at 35 °C (1000 ppm NH_3/He) for the fresh Cu-based microporous and hierarchical catalysts before (fresh) and after hydrothermal treatment (HT): (a) "Cu/micro-fresh", (b) "Cu/0.15-fresh" and "Cu/0.15-HT", (c) "Cu/0.66-fresh" and "Cu/0.66-HT".

In order to support this technique, additional information was obtained by DRIFTS after CO adsorption on the *"Cu/0.15-fresh"* and *"Cu/0.66-fresh"* hierarchical catalysts, Figure IV. 4. For both catalysts, two main bands centered at 2136 and 2154 cm^{-1} were observed, which according to previous studies [30] can be attributed to Cu^+–CO carbonyl species, which are bonded to framework O atoms at two different sites of the SAPO-34 zeolite. The CHA framework is composed of double 6-membered ring units (6-MR, forming an hexagonal prism) linked by 4-member rings (4-MR) to form cavities, accessible through 8-membered ring windows (8-MR). The incorporation of Copper cations in this structure is due to charge deficit compensation [31] and it happens in the 6-MR and 8-MR positions. Qu et al. [30] suggested that the band at 2136 cm^{-1} is due to Cu^+ ions located in the center of 6-MR connected to the large cages of the CHA structure, while the band at 2154 cm^{-1} is characteristic of Cu^+ species in the 8-MR. Hence, even if the isolated Cu ions (Cu^{2+} and Cu^+) signal obtained by NH_3 DRIFTS on the fresh Cu-based hierarchical catalysts was minor but not inexistent, the results obtained after CO adsorption are consistent with the presence of isolated Cu^+ ions occupying

the exchange sites of the hierarchical supports. In addition, among the Cu-based hierarchical catalysts, it seems that the relative amount of Cu^+ cations is more significant for the *"Cu/0.66-fresh"* catalyst, which exhibits more pronounced bands in the infrared spectra.

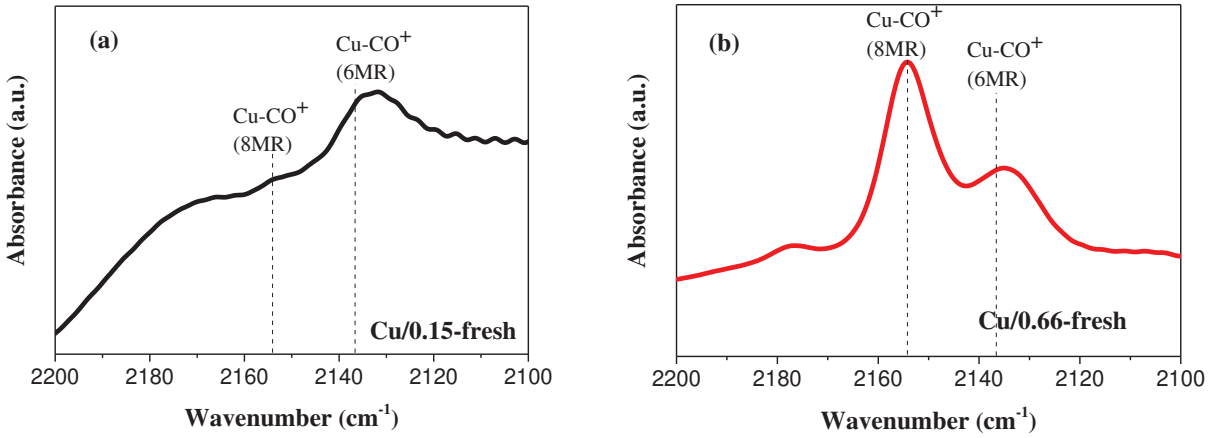

Figure IV. 4. DRIFTS spectra after previous adsorption of CO at 35 °C (1000 ppm CO/He) for: (A) "Cu/0.15-fresh", (B) "Cu/0.66-fresh" hierarchical catalysts.

In addition, Figure IV. 3 (b) and (c) also show the DRIFTS spectra after NH_3 adsorption for the hierarchical *"Cu/0.15-HT"* and *"Cu/0.66-HT"* catalysts after the hydrothermal treatment. As opposed to the Cu-based fresh hierarchical catalysts, weak bands at 891 and 844 cm^{-1} could be observed. As previously described for the fresh Cu-based microporous catalyst, those bands could be attributed to the presence of isolated Cu ions (likely Cu^+ and Cu^{2+} ions, respectively) occupying the exchange sites of the hierarchical zeolite supports. Thus, the slight (but non-negligible) appearance of these two bands in the Cu-based hierarchical catalysts after the hydrothermal treatment provide direct evidence that the Cu species were transferred, from the external surface to the exchange sites, in the hierarchical zeolite support during the hydrothermal treatment. Note that the migration and evolution of Cu species during hydrothermal treatment has received increasing attention in the last decade, mainly motivated by the application of Cu/SAPO-34 catalysts for automotive applications. In this sense, many studies reported (for microporous catalysts) that CuO migrate and re-disperse to occupy the ion exchange sites in the crystal framework during the hydrothermal treatment [10–13]. This is indeed a very interesting feature, considering that isolated Cu ions are relevant species for the NO_x reduction by the NH_3-SCR process. Once again, the Cu-based hierarchical catalysts developed in this study exhibit very promising features, since the hydrothermal treatment not only did not significantly affect to their structure, but also led to the evolution of CuO_x species

(likely placed in their mesoporous external surface) towards the exchange positions of the zeolite-based support framework.

The above described DRIFTS experiments allowed to qualitatively assess the presence of Cu^{2+}/Cu ions in the catalysts proposed in this study. With the aim of confirming and quantifying the presence of such species, as well as their increase after subjecting the hierarchical samples to hydrothermal treatment, H_2-Temperature-Programmed reduction (H_2-TPR) measurements were performed. Figure IV. 5 shows the H_2 consumption profiles for the fresh Cu-based microporous catalyst, together with the Cu-based hierarchical catalysts before and after the hydrothermal treatment, while Figure IV. S1-*Supporting Information* shows, in addition to those, the reduction profile of a physical mixture of non-calcined CuO and microporous SAPO-34 (used as a reference).

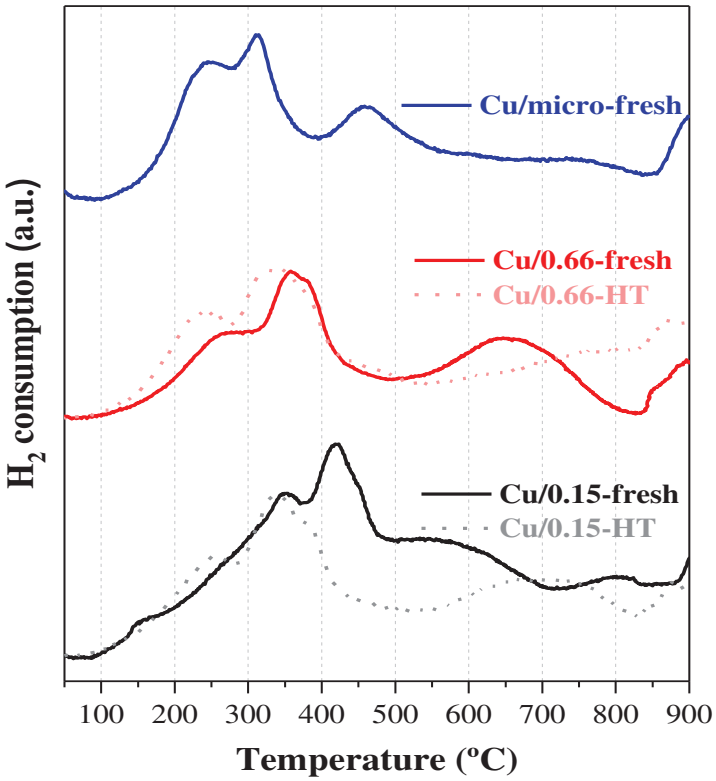

Figure IV. 5. H_2 consumption profiles normalized per Copper content during H_2-TPR experiments for the Cu-based fresh microporous catalyst and the Cu-based hierarchical catalysts before (fresh) and after HT.

A complex reduction profile, with multiple contributions is observed for all the catalysts studied (Figure IV. 5). It is generally accepted that the reduction of Cu^{2+} in zeolite-based materials takes place through two consecutive steps. First, Cu^{2+} ions are reduced to Cu^{+} at low

temperatures, followed by the reduction of Cu^+ into Cu^0 at high temperatures [32]. Hence, in agreement with previous studies, the peak observed at the lower temperature (around 230 ºC) represents the reduction of Cu^{2+} to Cu^+ [6,26,32,33]. With regards to the reduction of Cu^+ to Cu^0, it seems to be dependent, among other factors, on the Cu loading [34]. For instance, Dong. et al. [35] described that two different contributions (centered at ca. 435 and 720 ºC, respectively) were needed to depict the reduction of Cu^+ ions for a Cu/SAPO-34 catalyst with 1.6 % of copper content. The higher temperature peak was attributed to the reduction of highly stable Cu^+ species. It is worth noting that the hierarchical catalysts developed in this study exhibit a Cu loading of the same order. Hence, the peaks observed in the H_2-TPR profiles at temperatures between 425 ºC and 750 ºC (Figure IV. 5) will be ascribed to the reduction of Cu^+, whereas those at the higher temperatures could be assigned to highly stable Cu^+ ions. Moreover, Richter et al. [36] reported that the reduction of CuO nanoparticles (clusters) to Cu^0 occurs in a single step at around 300 ºC. It seems reasonable therefore to assign the peaks observed on our catalysts, Cu-based microporous and hierarchical catalysts, at ca. 310 ºC to the reduction of such species. In addition, it was also determined experimentally that a physical (un-calcined) mixture of CuO and SAPO-34 zeolite presented a single reduction peak located at ca. 260 ºC (Figure IV. S1-*Supporting Information*). In agreement with previous studies [26,37], such reduction step will be ascribed to the single-step reduction of CuO aggregates to Cu^0. Such peak is not observed in the H_2-TPR profiles of Cu-based microporous and hierarchical catalysts synthetized in this study, probably because it is overlapped by some of the other contributions above described.

Thus, four main Cu species will be considered in this study according to these considerations: Cu^{2+} isolated ions in exchange position (reduction peak at ca. 230 ºC), CuO aggregates (reduction peak at ca. 260 ºC), CuO clusters (reduction peak at ca. 310 ºC) and Cu^+ isolated ions in exchange position (reduction peaks at ca. 425 - 750 ºC). As it was previously discussed, the CuO_x species (i.e. CuO aggregates and Cu nanoparticles) are likely to be found in the external surface of the zeolite-based supports. The integration of the deconvoluted peaks allowed to calculate the H_2 consumption (in μmol H_2 g^{-1}_{Cu}, Table IV. 3) normalized per mass of Cu (according to the ICP results, Table IV. 1) attributed to those reduction steps.

Table IV. 3. Quantification of H_2 Consumption ascribed to the reduction of different Copper species, along with their distribution.

	H_2 consumption (μmol · g_{Cu}^{-1})			
Catalysts	**Cu^{2+}→Cu^{+} exchanged**	**CuO→Cu^0 aggregates**	**CuO→Cu^0 clusters**	**Cu^{+}→Cu^0 exchanged**
Cu/micro-fresh	953.8	1239.9	2938.4	5065.3
Cu/0.15-fresh	519.4	3804.3	3950.5	3617.9
Cu/0.15-HT	1048.1	1183.7	4127.3	4464.2
Cu/0.66-fresh	583.5	2121.3	5371.1	3753.9
Cu/0.66-HT	953.8	1239.9	2938.4	5065.3

Regarding the H_2-TPR profiles, two main differences can be clearly observed on account of the induced mesoporosity (i.e., microporous vs. hierarchical fresh catalysts) and the hydrothermal treatment. On the one hand, the *"Cu/micro-fresh"* catalyst exhibits a significantly higher overall reducibility compared to the *"Cu/0.15-fresh"* and *"Cu/0.66-fresh"* catalysts. On the other hand, a clear shift towards lower temperatures of the reduction peaks below 500 ºC is observed for the hydrothermally treated hierarchical catalysts. The latter observation confirms that the hydrothermal treatment leads to a significant framework modification due to the Copper species migration from the external surface into the exchange sites of the hierarchical zeolite-based supports, as suggested by the DRIFTS experiments (Figure IV. 3). Note that the shift towards lower reduction temperatures seems to be higher for *"Cu/0.15-HT"* catalyst, in good agreement with the previous NH_3 DRIFTS measurements, in which the appearance of the two bands, related to the internal asymmetric SAPO-34 framework vibration perturbed by Copper cations at the exchanged sites, are clearly more evident after the hydrothermal treatment for this catalyst than for *"Cu/0.66-HT"* catalyst.

In order to quantify the above described phenomena, considering the hydrogen consumption (in μmol H_2 g^{-1}, Table IV. 3), and the stoichiometry of the different reducible species, the relative abundance (in %, Table IV. 4) of the different Copper species in the original sample was determined. For instance, the *"Cu/micro-fresh"* catalyst presents a hydrogen consumption of 953.8 μmol H_2 g_{Cu}^{-1} for the reduction of Cu^{2+} ions to Cu^{+} ions. Taking into account the reduction reaction: $Cu^{2+} + 1/2H_2 \rightarrow Cu^{+} + H^{+}$, this value suggests that the original catalyst contained 1907.6 μmol Cu^{2+} g_{Cu}^{-1}. In increasing order of temperature, the reduction of CuO aggregates and CuO clusters consumed 1239.9 and 2938.4 μmol H_2 g_{Cu}^{-1}, respectively. Both phases follow the same reduction stoichiometry ($CuO + H_2 \rightarrow Cu^0 + H_2O$). Following the same reasoning, it results in Copper contents of aggregates and clusters of 1239.9 and 2938.4

μmol H_2 g_{Cu}^{-1}, respectively. Finally, the hydrogen consumption during the reduction of Cu^+ ions to metallic Copper was 5065.3 μmol H_2 g_{Cu}^{-1}. However, it is worth noting that the calculation of the amount of Cu^+ ions in the original catalyst requires subtraction of the hydrogen consumption due to reduction of Cu^+ ions coming from Cu^{2+} ion reduction. Thus, the hydrogen consumption attributed to Cu^+ ion reduction can be calculated as 5065.3–953.8 μmol H_2 = 4111.5 μmol H_2 g_{Cu}^{-1}. Considering the reduction reaction: $Cu^+ + 1/2H_2 \rightarrow Cu^0 + H^+$, the content of Cu^+ ions results in 8223.0 μmol g_{Cu}^{-1}.

Table IV. 4. Distribution of different copper species quantify by previous H_2 Consumption.

	Cu species distribution (%)				
Catalysts	**Cu^{2+} exchanged**	**CuO aggregates**	**CuO clusters**	**Cu^+ exchanged**	**(Cu^{2+}+Cu^+) exchanged**
Cu/micro-fresh	13.3	8.7	20.5	57.5	70.8
Cu/0.15-fresh	6.9	25.4	26.4	41.3	48.3
Cu/0.15-HT	14.7	8.3	29.0	48.0	62.7
Cu/0.66-fresh	7.8	14.1	35.8	42.3	50.1
Cu/0.66-HT	16.5	7.3	35.0	41.2	57.7

Considering the values depicted in Table IV. 3 and IV. 4, the Cu-based hierarchical fresh catalysts show significantly lower hydrogen consumption ascribed to the combined amount of isolated Cu ionic species (Cu^{2+} + Cu^+) reduction than the "Cu/micro-fresh" catalyst, in line with the results observed by NH_3-DRIFTS experiments (Figure IV. 3). More specifically, the proportion of Cu ions decreased from 70.8 % for the microporous material to values below 50 % for the hierarchical ones. However, the latter catalysts exhibit a higher ratio of CuO species (both agglomerate and clusters). Note that the *"Cu/0.15-HT"* catalyst presented the highest amount of these CuO species. These results confirm the trends previously observed in N_2 adsorption/desorption measurements. The Cu-based hierarchical fresh catalysts suffered a significant decrease of the external (and hence the S_{BET}, Table IV. 2) surface area upon the introduction of Copper, which can be attributed to the partial loading of their mesopores by CuO species. Thus, these results suggest that the creation of mesopores for the hierarchical catalysts decreased (as expected) their microporous volume, and therefore limited the placement of isolated Cu^{2+} species in exchange positions, leading to the formation of CuO species. Nevertheless, in agreement with the NH_3-DRIFTS experiments (Figure IV. 3), the fraction of isolated Cu ions (Cu^{2+} + Cu^+) significantly increased for the Cu-based hierarchical catalysts after the hydrothermal treatment. Taking into account that those species are supposed

to play a key role for the NH_3-SCR reaction, an improved performance of the hierarchical *"Cu/0.15-HT"* and *"Cu/0.66-HT"* catalysts is expected for the efficient reduction of NO_x. Moreover, the migration of CuO species from the external surface into the exchange sites upon hydrothermal treatment seems to be also more pronounced for *"Cu/0.15-HT"* catalyst, which was the catalyst that presented less evidence of Cu^+ species (CO DRIFTS, Figure IV. 4) and high amount of CuO aggregates (H_2-TPR, Table IV. 4). Hence, one may think that the migration of CuO aggregates, in weak interaction with the zeolite structure, is preferential.

On the other hand, the acidity of the zeolite-based catalyst is known to influence, in a significant manner, the catalytic activity towards the NH_3-SCR process. In this study, the acidic properties of the target catalysts were studied via NH_3-Temperature Programmed Desorption (NH_3-TPD) experiments. NH_3 is accepted as an efficient probe molecule to characterize zeolite acidity [38,39]. Figure IV. 6 shows the NH_3-desorption profiles of *"Cu/micro-fresh"* catalyst, together with the Cu-based hierarchical catalysts before and after the hydrothermal treatment. Three NH_3 desorption peaks could be clearly observed for all these materials, although the temperature and area below such peaks vary among them. As previously reported, in the absence of Cu, the desorption peaks are commonly attributed to Brønsted acid sites of the zeolite-based support referred to weak, moderate and strong acidity, respectively [5,12]. This acidity originates from the proton, for compensating the unbalanced electronic charges due to Si incorporation into the neutral framework of aluminophosphates. However, when Cu is loaded, the acidic properties of the support drastically change. Previous studies suggested that, after Cu loading, Cu^{2+} species substitute some protons of the zeolite support, resulting in the increase of the number of Lewis acid sites, while the number of Brønsted acid sites decreased [12,32,37]. It seems therefore that both Lewis and Brønsted sites with different strength coexist in the Cu/CHA-based catalysts. Hence, the three peaks observed in the NH_3-desorption profiles (Figure IV. 6) at low, medium and high temperature could be attributed to the NH_3 adsorption at weak, moderate and strong Brønsted acid sites at the zeolite support, together with weak, moderate and strong Lewis acid sites related to Cu species, respectively.

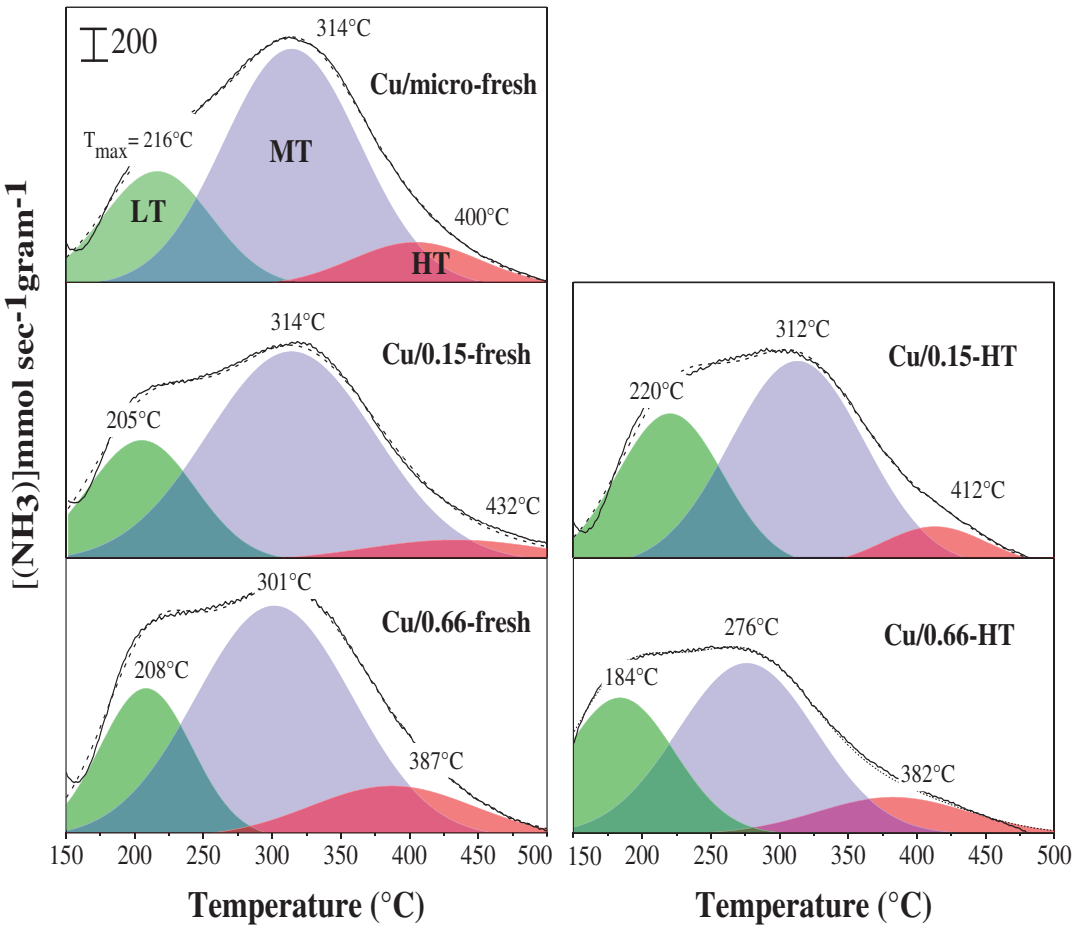

Figure IV. 6. NH_3-TPD profiles of for the fresh Cu-based microporous catalyst and the Cu-based hierarchical catalysts before (fresh) and after hydrothermal treatment (HT) with the corresponding deconvoluted peaks at LT, MT and HT.

The distribution of acid sites is a feature of paramount importance, since it has been reported that both, Brønsted and Lewis acid sites on Cu/SAPO-34 catalysts are necessary and important for NH_3 adsorption. While NH_3 molecules adsorbed on Lewis acid sites are readily reactive with NO_x, the Brønsted acid sites may act as an NH_3 reservoir, supplying additional NH_3 via migration to the Lewis acid sites for the NH_3-SCR reaction, mainly at high temperature [12,40]. The NH_3-desorption amounts (in mmol $g^{-1}_{catalyst}$) are obtained by integration of the de-convoluted peaks observed in Figure IV. 6, and shown in Table IV. 5 (together with the peak temperature). Regarding the Cu-based fresh catalysts, a slight decrease of the total amount of acid sites was observed for the *"Cu/0.15-fresh"* hierarchical catalyst compared to the *"Cu/micro-fresh"* catalyst, while the total acidity of the *"Cu/0.66-fresh"* hierarchical catalyst is very similar to the latter. The differences in total acidity between both Cu-based hierarchical fresh catalysts could be attributed to the higher formation of CuO species (i.e. CuO aggregates

and Cu nanoparticles clusters), in detriment to Cu^{2+} ions, in *"Cu/0.15-fresh"* hierarchical catalyst, which presented the highest and lowest amount of CuO species and Cu^{2+} ions (Table IV. 4), respectively. The availability of Lewis acid sites to store NH_3 is then disfavored in the latter, decreasing its total acidity [41]. A similar trend was observed in our previous study [5] for their counterpart supports, although the distribution of the acid sites and the temperature of the peaks drastically changed, as expected, upon the introduction of Copper. This points out the important framework modification on account of the Cu^{2+} species placed in ionic-exchange positions of the zeolite-based supports.

Table IV. 5. Desorbed NH_3 amount according to NH_3-TPD measurements with related maximum peak temperature.

	NH_3 desorbed amount (mmol · $g_{catalyst}^{-1}$)				**Temperature peak (°C)**		
Catalysts	**Weak acid sites (LT)**	**Medium acid sites (MT)**	**Strong acid sites (HT)**	**Total desorbed NH_3 amount**	**LT**	**MT**	**HT**
Cu/micro-fresh	0.28	0.79	0.14	1.21	216	314	400
Cu/0.15-fresh	0.23	0.80	0.07	1.09	205	314	432
Cu/0.15-HT	0.30	0.63	0.07	1.00	220	312	412
Cu/0.66-fresh	0.21	0.76	0.20	1.17	208	301	387
Cu/0.66-HT	0.18	0.59	0.19	0.96	184	276	382

After the hydrothermal treatment, although the NH_3-desorption profiles were similar to those of the fresh Cu-based hierarchical catalysts, a general decrease of the total acidity was observed. One may think that such acidity may increase, on account of the higher amount of isolated Cu ionic species (as observed by H_2-TPR measurements, Table IV. 4) after the hydrothermal treatment. However, the slight decrease of the external surface area observed for *"Cu/0.15-HT"* and *"Cu/0.66-HT"* catalysts (Table IV. 2) suggests a minor damage of the Cu-based hierarchical catalysts, which could eventually decrease the total acidity of these materials, in good agreement with the obtained results. In addition, most of the desorption peaks are slightly shifted towards lower temperatures after the hydrothermal treatment, which indicates that the strength of the acid sites of the Cu-based hierarchical catalysts is slightly lowered [5,42]. Nevertheless, even considering these aspects, the overall acidity of the hierarchical materials did not seem to dramatically decrease after the hydrothermal treatment.

3. Catalytic activity before and after hydrothermal treatment.

In this section, the influence of the structural parameters (Table IV. 2) and the presence of different Cu species (Table IV. 4) and acid sites (Table IV. 5) on the catalytic activity and selectivity of the Cu-based hierarchical catalysts subjected to the hydrothermal stability treatment will be studied.

The NH_3-SCR performance of the fresh Cu-based catalysts (both microporous and hierarchical) was assessed as a function of the reaction temperature. Figure IV. 7 shows the NO and NH_3 conversions, together with the selectivity towards the main reaction products: N_2 (desired product), NO_2 and N_2O. In addition, aiming for a clearer comparative view, Figure IV. S2 (a)-*Supporting Information* shows the variation of the NO conversion in the whole temperature range (100-450 ºC) and the NO reaction rate in a selected low temperature window (Figure IV. S2 (b)-*Supporting Information*, 105-130 ºC) for *"Cu/micro-fresh"*, *"Cu/0.15-fresh"* and *"Cu/0.66-fresh"* catalysts. Although the fresh Cu-based hierarchical catalysts exhibit a slightly higher activity in the lower temperature range, Figure IV. S2 (b), the overall NO_x reduction activity of the Cu-based microporous fresh catalyst was higher in the rest of the studied temperature range, Figure IV. S2 (a). The higher activity of the Cu-based hierarchical catalysts at the lower temperatures could be ascribed to the mesopores created in the zeolite framework (Table IV. 2). As discussed in the introduction section, the small pore-size of conventional microporous CHA-zeolite leads to important diffusion limitations, even at low temperatures [3,4,16]. Considering that both, the acidity (Table IV. 5) and the concentration of isolated Cu ionic species (Table IV. 4) are lower for the fresh Cu-based hierarchical catalysts (compared to the fresh Cu-based microporous catalyst), the most plausible explanation is that the ordered mesopores created enhanced the diffusion of the reactants towards the catalyst active sites, increasing the performance for the NH_3-SCR reaction in the lower temperature range (T < 130 ºC).

In order to understand the higher activity (in the wider temperature range) of the Cu-based microporous fresh catalyst compared to the Cu-based hierarchical fresh catalysts, the two key features above mentioned should be thoroughly considered: the *"Cu/micro-fresh"* catalyst shows a higher amount of isolated Cu species (both Cu^{2+} and Cu^{+}), and a higher total acidity. In this sense, many studies agree that isolated Cu^{2+} ions are the active sites for the NH_3-SCR process [6,7,11,12,22], mainly at low temperatures (< 300 ºC). Note that the amount of both isolated Cu species is slightly lower in the case of *"Cu/0.15-fresh"* catalyst (CO DRIFTS, H_2-TPR), which can explain the differences in activity observed between both hierarchical catalyst

at the medium range of temperatures. However, at higher temperatures, the catalytic performance may be affected by the acid content in the catalysts [6,7]. The results shown in Figure IV. 7 clearly point out that several competitive reactions take place, since the products distribution is significantly affected by the reaction temperature. First of all, considering that equal amounts of NO and NH_3 are introduced to the feed stream (in the absence of NO_2), similar NO and NH_3 conversions should be expected according to the *Standard SCR process* (reaction 1) [26]:

$$4\ NH_3 + 4\ NO + O_2 \rightarrow 4\ N_2 + 6\ H_2O\ (1)$$

However, for all the fresh catalysts, although this is true at low temperatures (< 300 ^oC), at higher temperatures, the NH_3 conversion surpassed the NO conversion. These results evidenced that the NH_3 oxidation is the main side reaction to influence the NO conversion at high temperature [6,7]. The steadiness (for *"Cu/micro-fresh"* and *"Cu/0.15-fresh"* catalysts) and decrease (for *"Cu/0.66-fresh"* catalyst) of the NO conversion while increasing the NH_3 conversion at high temperature could be ascribed to two reasons. First, part of the NO in the feed stream cannot react with insufficient adsorbed NH_3 species, since they are partially consumed by NH_3 oxidation. Second, more NO (and NO_2 in a minor extent) is produced during NH_3 oxidation (reaction 2), decreasing therefore the NO conversion values. In addition, a minor (but non-negligible) amount of N_2O was observed for all these catalysts. It is reported that the N_2O formation could be ascribed to the decomposition of NH_4NO_3 [6,7], previously formed by reaction 3:

$$4\ NH_3 + 5\ O_2 \rightarrow 4\ NO + 6\ H_2O\ (2)$$

$$2NO_2 + 2\ NH_3 \rightarrow N_2 + NH_4NO_3 + H_2O\ (3)$$

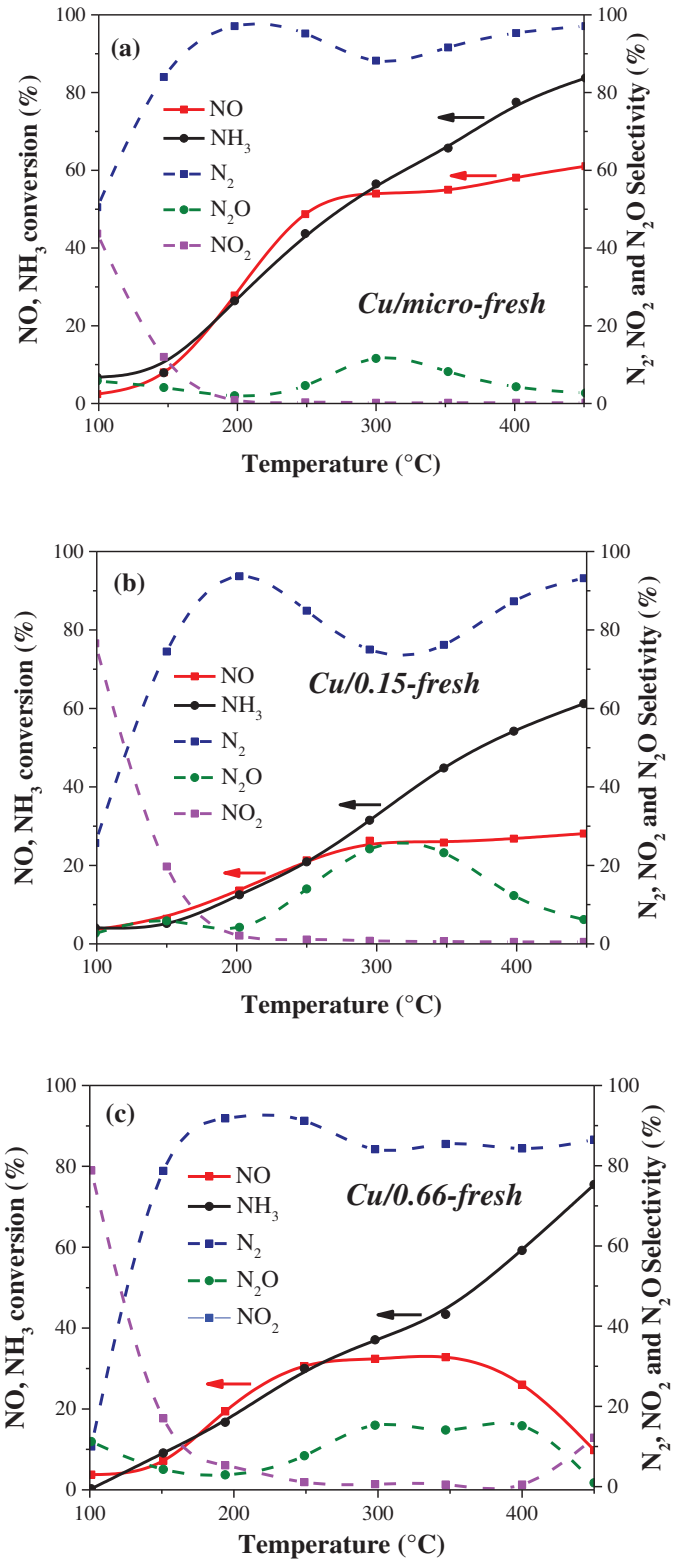

Figure IV. 7. Evolution of NO and NH_3 conversion (left axis), and N_2, N_2O and NO_2 selectivity (right axis) with temperature for: (a) "Cu/micro-fresh" (b) "Cu/0.15-fresh" and (c) "Cu/0.66-fresh". *Reaction conditions for Standard NH_3-SCR: 650 ppm NO, 650 ppm NH_3, 5% H_2O, 6% O_2.*

Nevertheless, as previously mentioned, even though all the fresh catalysts exhibit similar trends regarding their catalytic performance and selectivity, the overall activity in the whole temperature range was higher for the Cu-based microporous catalyst. At low temperatures, isolated Cu^{2+} ions are reported as the key active sites. These species are reduced to Cu^{+} in the presence of NO and NH_3, leading to the production of N_2 [24,43]. The isolated Cu^{+} species may be then re-oxidized to Cu^{2+} in the presence of NO and O_2, in the low temperature region, through the formation of nitrite/nitrate reaction intermediates [25,44]. Therefore, it seems that both isolated Cu^{2+} and Cu^{+} species are relevant to catalyse the NH_3-SCR reaction in the low temperature range, which explains the higher NOx reduction activity for the fresh Cu-based microporous catalyst at T < 300 ºC was generally higher, since it exhibits a higher amount of Cu^{+}/Cu^{2+} species (Table IV. 4). In addition, the NO_2 production observed at low temperatures could be attributed to the presence of CuO species (present in all the catalysts), as suggested by Liu et al. [12], which may favour the oxidation of NO to NO_2. The NO_2 produced could eventually favour the SCR process via the so-called fast-SCR route (reaction 4).

$$2\ NH_3 + NO + NO_2 \rightarrow 2\ N_2 + 3\ H_2O \quad (4)$$

However, as it was previously mentioned, at higher temperatures, the catalytic performance may be affected by competitive side reactions, mainly the oxidation of NH_3. In this sense, previous studies reported that such oxidation reaction (as well as the decomposition of ammonium nitrate to produce N_2O) may be inhibited by the increase of the concentration of acid sites [6,7]. In other words, the higher concentration of both, Brønsted and Lewis sites, might enhance the NH_3-SCR reaction instead of the undesired NH_3 oxidation. While the former reaction takes place on the Lewis sites, the Brønsted sites act as a reservoir for the adsorption of additional NH_3 species, that might be transferred to the Lewis sites [12,40]. This is in good agreement with our results, where the higher activity for NO_x reduction was observed, also in the high temperature range, for the fresh Cu-based microporous catalyst (together with a lower selectivity to undesired N_2O), which might be attributed to the higher total acidity of this catalyst compared to the fresh Cu-based hierarchical catalysts (Figure IV. 6, Table IV. 5). Moreover, the higher contents of large Cu aggregates (Table IV. 4) in both fresh Cu-based hierarchical catalysts could be also responsible of the formation of N_2O and the enhanced NH_3 oxidation at medium and high temperature [41], favoring the formation of NO_2 notably in the case of *"Cu/0.66-HT"* hierarchical catalyst. Note that the latter presented the highest amount of CuO clusters and a bigger gap between NH_3 conversion and NO conversion at high

temperatures. These surface CuO clusters could be responsible to the more drastically decrease of NH_3-SCR performance at high temperatures in the case of *"Cu/0.66-HT"* hierarchical catalyst, since the catalytic activity for NH_3 oxidation is enhanced [12].

On the other hand, Figure IV. 8 shows the activity and selectivity of the Cu-based hierarchical catalysts (*"Cu/0.15-HT"* and *"Cu/0.66-HT"*) after the hydrothermal treatment. For a clearer visualization, Figures IV. S3 (b)-*Supporting Information* show the comparative performance (reaction rate in a selected low temperature window, 100-250 ^oC) of such Cu-based hierarchical catalysts hydrothermally treated with the fresh catalysts previously discussed in Figure IV. 7. The conversions and products selectivity trends observed for the hierarchical *"HT"* catalysts is very similar to the trends previously explained. However, the magnitude of the different catalytic processes involved seemed to be different. It suggests, as expected, that the different concentration of isolated Cu ionic species and acid sites drastically affects the performance of these catalysts. Hence, at low temperature, NO reaction rate (attributed to the NH_3-SCR reaction) was higher for both hydrothermally treated *"Cu/0.15-HT"* and *"Cu/0.66-HT"* hierarchical catalysts than that for the *"Cu/micro-fresh"* one, Figure IV. S3 (b). This is in good agreement with the previous discussion, since the concentration of isolated Cu^{2+} ions drastically increased in the Cu-based hierarchical catalysts after the hydrothermal treatment (Table IV. 4), on account of the migration of CuO species to the exchange positions in the zeolite-based framework. The higher activity of *"Cu/0.15-HT"* compared to that of the *"Cu/0.66-HT"* catalyst can be explained by the highest amount of isolated Cu species (both Cu^{2+} and Cu^{+}) probably due to the easier migration of CuO aggregates, weakly connected to the zeolite structure, to the zeolite exchanged positions after HT, as it was previously mentioned. This phenomenon, together with the enhanced diffusion of reactants through the created mesopores, seemed to increase the catalytic performance of both *"Cu/0.15-HT"* and *"Cu/0.66-HT"* hierarchical catalysts at low temperatures. This is a very interesting feature considering that the main purpose of this study is to advance one step forward to the development of novel catalysts with enhanced activity at low temperature.

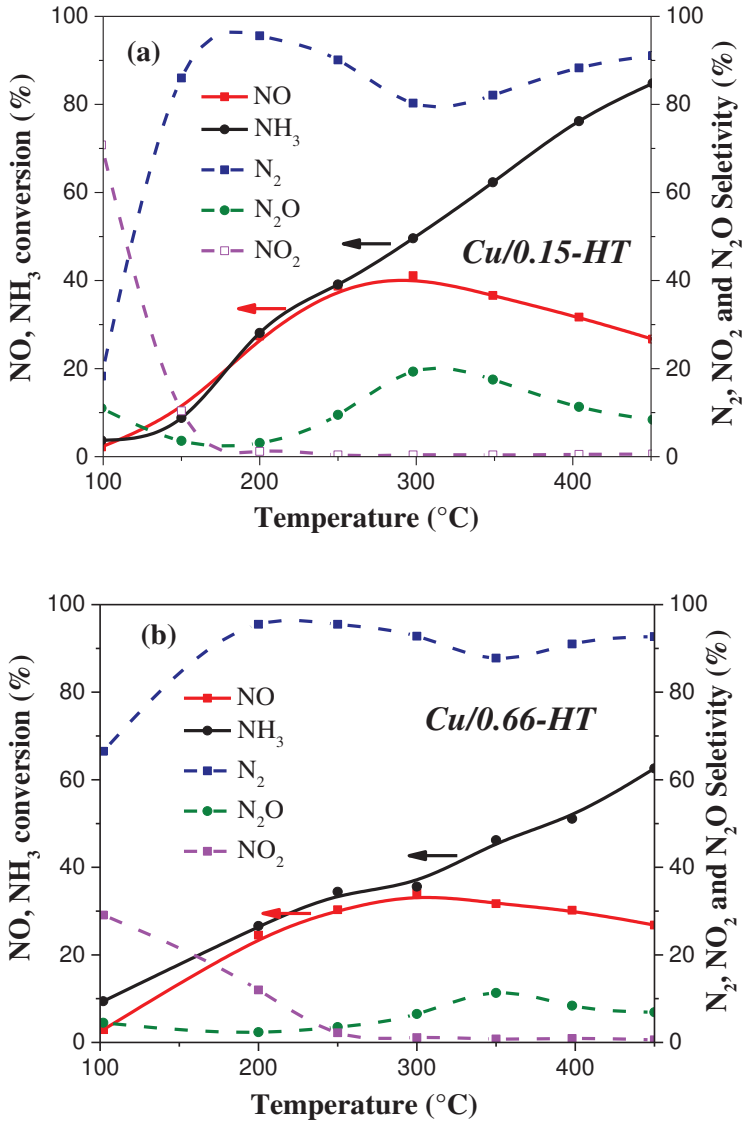

Figure IV. 8. Evolution of NO and NH_3 conversion (left axis), and N_2, N_2O and NO_2 selectivity (right axis) with temperature for: (a) "Cu/0.15-HT" and (b) "Cu/0.66-HT". *Reaction conditions for Standard NH_3-SCR: 650 ppm NO/ 650 ppm NH_3 / 5% H_2O/ 6% O_2.*

However, very interestingly, even though the performance of the Cu-based hierarchical catalysts was higher after the hydrothermal treatment (compared to their fresh counterparts), the overall NO_x reduction activity in the high temperature window was lower compared to the microporous fresh catalyst (*"Cu/micro-fresh",* Figure IV. 9). These results suggest that the higher amount of isolated Cu ions (and the lower amount of CuO species) in the latter still favored the activity at high temperatures. However, the decreased specific surface area and total amount of acid sites (Tables IV. 2 and 5), and the still high amount of nanosized Cu clusters

presented in hierarchical catalysts (Table IV. 4), seemed to partially affect the NH_3-SCR reaction at high temperatures, in favor of the undesired NH_3 oxidation reaction [41,45,46].

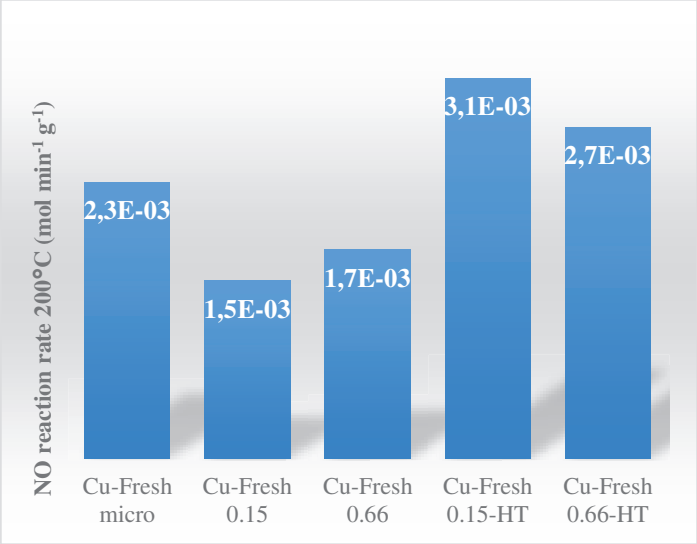

Figure IV. 9. NO reaction rate at 200 °C for the fresh and HT catalysts. *Reaction conditions for Standard NH_3-SCR: 650 ppm NO/ 650 ppm NH_3 / 5% H_2O/ 6% O_2.*

All in all, the results obtained in this study clearly suggest that the Cu-based hierarchical catalysts subjected to a hydrothermal treatment exhibit very interesting and promising features. Both, the mesoporosity created (enhanced reactants diffusion), together with the enhanced concentration of isolated Cu ions (active sites) after the hydrothermal treatment, seemed to drastically improve their activity at low temperatures for the NH_3-SCR reaction, which is a relevant feature in view of their further practical implementation.

4. Discussion and Conclusions

In our previous chpater, novel hierarchical SAPO-34 zeolites were developed by the soft-templating synthesis procedure. These materials exhibited very interesting structural properties, with a significant mesoporous volume and an important concentration of acid sites. Hence, in this study those materials were used as supports for the development of Cu-based hierarchical SAPO-34 catalysts. The purpose of this work was to characterize and assess the hydrothermal stability and catalytic activity (for NO_x reduction via NH_3-SCR) of these novel materials, and to compare them with a typical Cu-based microporous SAPO-34 catalyst.

The physico-chemical characterization of the Cu-based hierarchical catalysts by XRD, BET and ICP-AOS demonstrated that these catalysts exhibit a very important hydrothermal stability, since their structural properties suffered minor changes after the hydrothermal

treatment. In addition, by H_2-TPR and NH_3-DRIFTS it was shown that such treatment led to the migration of CuO species to the ionic exchange positions of the hierarchical zeolite frameworks. This is especially relevant, considering that isolated Cu^{2+} species are generally considered as the key active sites of the NH_3-SCR catalytic process at low temperatures. Unfortunately, the total amount of acid sites (considered as the main active sites for the NH_3-SCR at high temperatures) decreased on account of the hydrothermal treatment (as demonstrated by NH_3-TPD).

The catalytic activity of these catalysts was evaluated and compared with the Cu-based microporous SAPO-34 catalyst. As expected, at high temperatures, the NH_3-SCR activity of the Cu-based hierarchical catalysts hydrothermally treated did not surpass that of the microporous catalyst, likely due to their lower concentration of acid sites and specific surface area, which might favour the undesired NH_3-oxidation reaction. However, very interestingly, their NH_3-SCR activity at low temperatures overcame that of the reference microporous catalyst. It seems therefore that both, the increase of the isolated Cu^{2+} active sites, and the (likely) enhanced diffusion of reactants through the mesopores, upgraded their performance for an efficient reduction of NO_x at low temperatures, which is a feature of paramount importance in view of their further practical implementation.

5. Supporting information

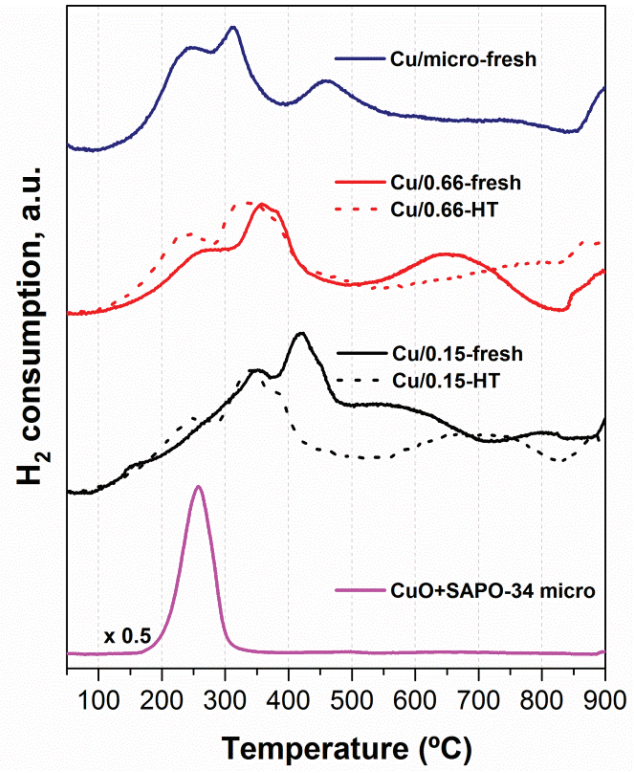

Figure IV. S1. H_2 consumption profiles normalized per copper content during H_2-TPR experiments for the fresh Cu-based microporous catalyst and the Cu-based hierarchical catalysts before (fresh) and after hydrothermal treatment (HT). The physical mixture of CuO and microporous SAPO-34 zeolite is also included as reference.

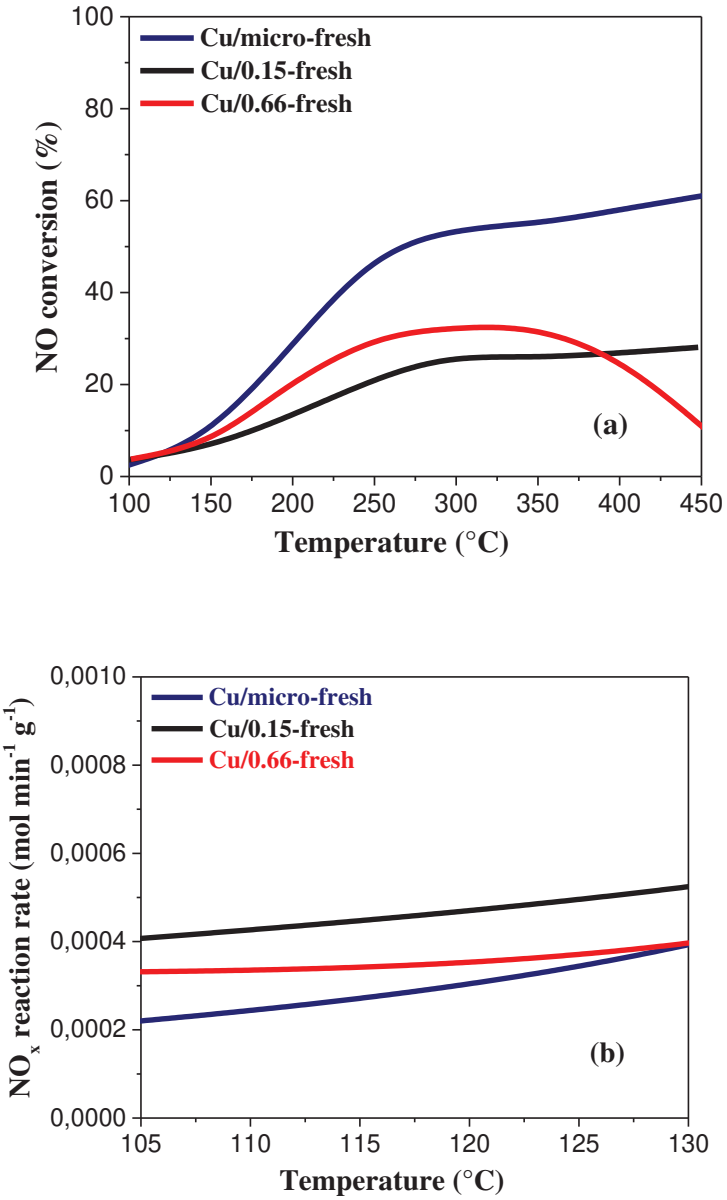

Figure IV. S2. Comparison of (a) NO conversion as a function of temperature in a wide temperature region and (b) NO reaction rate as a function of temperature in a low temperature 105 – 130 °C region, for the fresh catalytic materials ("Cu/micro-fresh", "Cu/0.15-fresh" and "Cu/0.66-fresh")). *Reaction conditions for Standard NH_3-SCR: 650 ppm NO/ 650 ppm NH_3 / 5% H_2O/ 6% O_2.*

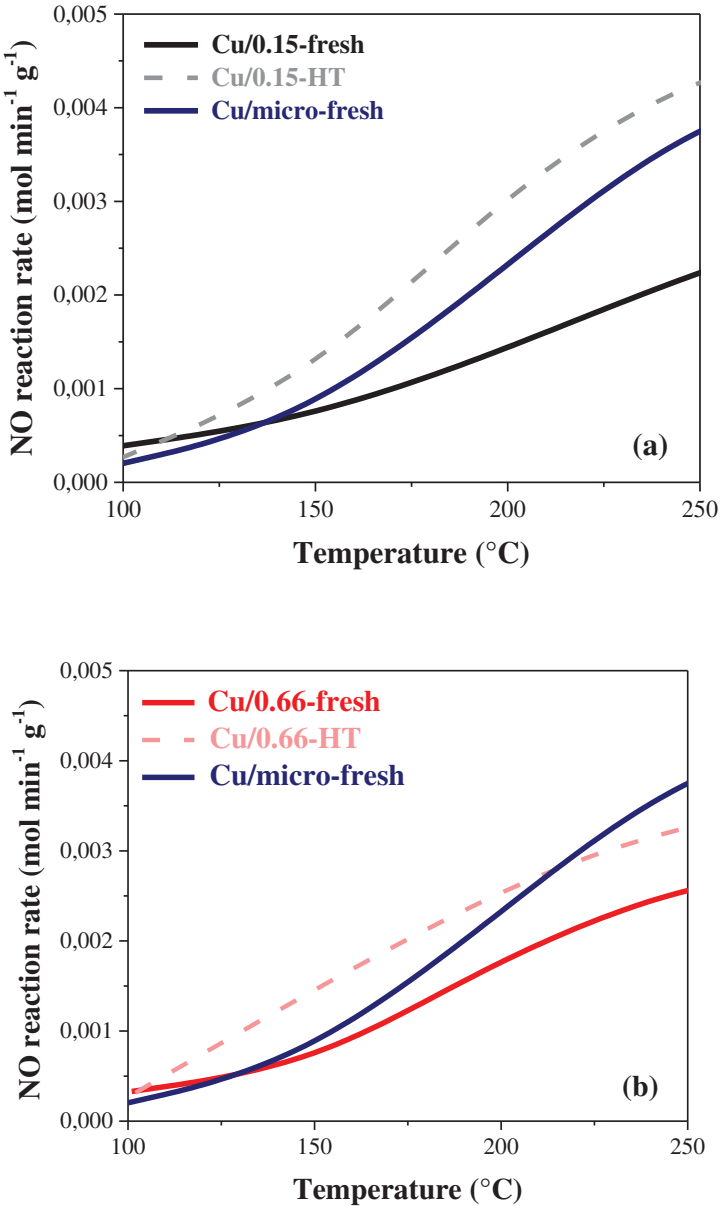

Figure IV. S3. Comparison of the NOx reaction rate as a function of temperature for the hierarchical catalysts before and after the hydrothermal treatment, with the fresh microporous catalyst: (a) "Cu/micro-fresh", "Cu/0.15-fresh" and "Cu/0.15-HT" and (b) "Cu/micro-fresh", "Cu/0.66-fresh" and "Cu/0.66-HT". *Reaction conditions for Standard NH_3-SCR: 650 ppm NO/ 650 ppm NH_3 / 5% H_2O/ 6% O_2.*

References

[1] C.K. Lambert, Current state of the art and future needs for automotive exhaust catalysis, Nat. Catal. 2 (2019) 554–557. https://doi.org/10.1038/s41929-019-0303-x.

[2] S. Zhang, L. Pang, Z. Chen, S. Ming, Y. Dong, Q. Liu, P. Liu, W. Cai, T. Li, Cu/SSZ-13 and Cu/SAPO-34 catalysts for deNOx in diesel exhaust: Current status, challenges, and future perspectives, Appl. Catal. A Gen. 607 (2020) 117855. https://doi.org/10.1016/j.apcata.2020.117855.

[3] T. Zhang, J. Li, J. Liu, D. Wang, Z. Zhao, K. Cheng, J. Li, High activity and wide temperature window of Fe-Cu-SSZ-13 in the selective catalytic reduction of NO with ammonia, AIChE J. 61 (2015) 3825–3837. https://doi.org/10.1002/aic.14923.

[4] F. Gao, E.D. Walter, E.M. Karp, J. Luo, R.G. Tonkyn, J.H. Kwak, J. Szanyi, C.H.F. Peden, Structure–activity relationships in NH3-SCR over Cu-SSZ-13 as probed by reaction kinetics and EPR studies, J. Catal. 300 (2013) 20–29. https://doi.org/https://doi.org/10.1016/j.jcat.2012.12.020.

[5] B.R.S. De Araujo, J.A. Onrubia-Calvo, I. Stambouli, G. Pétaud, J. Hidalgo-Carrillo, A. Nieto-Marquéz, B. Pereda-Ayo, J.R. González-Velasco, A. Caravaca, S. Gil, Towards the development of advanced hierarchical chabazite materials: Novel micro-mesoporous silicoaluminophosphate SAPO-34 zeolites, Mater. Today Commun. 31 (2022) 103580. https://doi.org/10.1016/j.mtcomm.2022.103580.

[6] T. Yu, J. Wang, M. Shen, W. Li, NH3-SCR over Cu/SAPO-34 catalysts with various acid contents and low Cu loading, Catal. Sci. Technol. 3 (2013) 3234–3241. https://doi.org/10.1039/C3CY00453H.

[7] T. Yu, T. Hao, D. Fan, J. Wang, M. Shen, W. Li, Recent NH3-SCR Mechanism Research over Cu/SAPO-34 Catalyst, J. Phys. Chem. C. 118 (2014) 6565–6575. https://doi.org/10.1021/jp4114199.

[8] P.G. Blakeman, E.M. Burkholder, H.-Y. Chen, J.E. Collier, J.M. Fedeyko, H. Jobson, R.R. Rajaram, The role of pore size on the thermal stability of zeolite supported Cu SCR catalysts, Catal. Today. 231 (2014) 56–63. https://doi.org/https://doi.org/10.1016/j.cattod.2013.10.047.

[9] C. Peng, R. Yan, Y. Mi, G. Li, Y. Zheng, Y. Luo, J. Liang, W. Liu, Z. Li, D. Wu, X. Wang, H. Peng, Toward rational design of a novel hierarchical porous Cu-SSZ-13

catalyst with boosted low-temperature NOx reduction performance, J. Catal. 401 (2021) 309–320. https://doi.org/https://doi.org/10.1016/j.jcat.2021.07.024.

[10] X. Li, Y. Zhao, H. Zhao, M. Liu, Y. Ma, X. Yong, H. Chen, Y. Li, The Cu migration of Cu-SAPO-34 catalyst for ammonia selective catalytic reduction of NOx during high temperature hydrothermal aging treatment, Catal. Today. 327 (2019) 126–133. https://doi.org/10.1016/j.cattod.2018.05.029.

[11] D. Wang, Y. Jangjou, Y. Liu, M.K. Sharma, J. Luo, J. Li, K. Kamasamudram, W.S. Epling, A comparison of hydrothermal aging effects on NH3-SCR of NO over Cu-SSZ-13 and Cu-SAPO-34 catalysts, Appl. Catal. B Environ. 165 (2015) 438–445. https://doi.org/10.1016/j.apcatb.2014.10.020.

[12] X. Liu, X. Wu, D. Weng, Z. Si, R. Ran, Evolution of copper species on Cu/SAPO-34 SCR catalysts upon hydrothermal aging, Catal. Today. 281 (2017) 596–604. https://doi.org/10.1016/j.cattod.2016.05.021.

[13] L. Wang, J.R. Gaudet, W. Li, D. Weng, Migration of Cu species in Cu/SAPO-34 during hydrothermal aging, J. Catal. 306 (2013) 68–77. https://doi.org/https://doi.org/10.1016/j.jcat.2013.06.010.

[14] L. Kong, Z. Jiang, J. Zhao, J. Liu, B. Shen, The Synthesis of Hierarchical SAPO-34 and its Enhanced Catalytic Performance in Chloromethane Conversion to Light Olefins, Catal. Letters. 144 (2014) 1609–1616. https://doi.org/10.1007/s10562-014-1296-3.

[15] S. ul H. Bakhtiar, X. Wang, S. Ali, F. Yuan, Z. Li, Y. Zhu, CTAB-assisted size controlled synthesis of SAPO-34 and its contribution toward MTO performance, Dalt. Trans. 47 (2018) 9861–9870. https://doi.org/10.1039/C8DT01811A.

[16] F. Gao, E.D. Walter, N.M. Washton, J. Szanyi, C.H.F. Peden, Synthesis and Evaluation of Cu-SAPO-34 Catalysts for Ammonia Selective Catalytic Reduction. 1. Aqueous Solution Ion Exchange, ACS Catal. 3 (2013) 2083–2093. https://doi.org/10.1021/cs4004672.

[17] R.A. García, D.P. Serrano, D. Otero, Catalytic cracking of HDPE over hybrid zeolitic–mesoporous materials, J. Anal. Appl. Pyrolysis. 74 (2005) 379–386. https://doi.org/https://doi.org/10.1016/j.jaap.2004.11.002.

[18] I.I. Ivanova, E.E. Knyazeva, Micro–mesoporous materials obtained by zeolite

recrystallization: synthesis, characterization and catalytic applications, Chem. Soc. Rev. 42 (2013) 3671–3688. https://doi.org/10.1039/C2CS35341E.

[19] Q. Sun, Y. Ma, N. Wang, X. Li, D. Xi, J. Xu, F. Deng, K.B. Yoon, P. Oleynikov, O. Terasaki, J. Yu, High performance nanosheet-like silicoaluminophosphate molecular sieves: synthesis, 3D EDT structural analysis and MTO catalytic studies, J. Mater. Chem. A. 2 (2014) 17828–17839. https://doi.org/10.1039/C4TA03419H.

[20] X. Chen, A. Vicente, Z. Qin, V. Ruaux, J.-P. Gilson, V. Valtchev, The preparation of hierarchical SAPO-34 crystals via post-synthesis fluoride etching, Chem. Commun. 52 (2016) 3512–3515. https://doi.org/10.1039/C5CC09498D.

[21] J. Pérez-Ramírez, D. Verboekend, A. Bonilla, S. Abelló, Zeolite Catalysts with Tunable Hierarchy Factor by Pore-Growth Moderators, Adv. Funct. Mater. 19 (2009) 3972–3979. https://doi.org/10.1002/adfm.200901394.

[22] J. Wang, T. Yu, X. Wang, G. Qi, J. Xue, M. Shen, W. Li, The influence of silicon on the catalytic properties of Cu/SAPO-34 for NOx reduction by ammonia-SCR, Appl. Catal. B Environ. 127 (2012) 137–147. https://doi.org/https://doi.org/10.1016/j.apcatb.2012.08.016.

[23] L. Wang, W. Li, G. Qi, D. Weng, Location and nature of Cu species in Cu/SAPO-34 for selective catalytic reduction of NO with NH3, J. Catal. 289 (2012) 21–29. https://doi.org/https://doi.org/10.1016/j.jcat.2012.01.012.

[24] K.A. Lomachenko, E. Borfecchia, C. Negri, G. Berlier, C. Lamberti, P. Beato, H. Falsig, S. Bordiga, The Cu-CHA deNOx Catalyst in Action: Temperature-Dependent NH3-Assisted Selective Catalytic Reduction Monitored by Operando XAS and XES, J. Am. Chem. Soc. 138 (2016) 12025–12028. https://doi.org/10.1021/jacs.6b06809.

[25] M. Moreno-González, R. Millán, P. Concepción, T. Blasco, M. Boronat, Spectroscopic Evidence and Density Functional Theory (DFT) Analysis of Low-Temperature Oxidation of Cu+ to Cu2+NOx in Cu-CHA Catalysts: Implications for the SCR-NOx Reaction Mechanism, ACS Catal. 9 (2019) 2725–2738. https://doi.org/10.1021/acscatal.8b04717.

[26] M. Urrutxua, B. Pereda-Ayo, U. De-La-Torre, J.R. González-Velasco, Evaluation of Cu/SAPO-34 Catalysts Prepared by Solid-State and Liquid Ion-Exchange Methods for NOx Removal by NH3-SCR, ACS Omega. 4 (2019) 14699–14713.

https://doi.org/10.1021/acsomega.9b01118.

[27] S. Fan, J. Xue, T. Yu, D. Fan, T. Hao, M. Shen, W. Li, The effect of synthesis methods on Cu species and active sites over Cu/SAPO-34 for NH3-SCR reaction, Catal. Sci. Technol. 3 (2013) 2357–2364. https://doi.org/https://doi.org/10.1039/C3CY00267E.

[28] P.E. Fanning, M.A. Vannice, A DRIFTS Study of Cu–ZSM-5 Prior to and during Its Use for N2O Decomposition, J. Catal. 207 (2002) 166–182. https://doi.org/https://doi.org/10.1006/jcat.2002.3518.

[29] G.D. Lei, B.J. Adelman, J. Sárkány, W.M.H. Sachtler, Identification of copper(II) and copper(I) and their interconversion in Cu/ZSM-5 De-NOx catalysts, Appl. Catal. B Environ. 5 (1995) 245–256. https://doi.org/https://doi.org/10.1016/0926-3373(94)00043-3.

[30] Z. Qu, Y. Li, S. Huang, P. Chen, X. Ma, Clarification of copper species over Cu-SAPO-34 catalyst by DRIFTS and DFT study of CO adsorption, Sci. China Chem. 60 (2017) 912–919. https://doi.org/https://doi.org/10.1007/s11426-016-9063-2.

[31] Y. Jeanvoine, J.G. Ángyán, G. Kresse, J. Hafner, Brønsted Acid Sites in HSAPO-34 and Chabazite: An Ab Initio Structural Study, J. Phys. Chem. B. 102 (1998) 5573–5580. https://doi.org/10.1021/jp980341n.

[32] T. Zhang, F. Qiu, H. Chang, X. Li, J. Li, Identification of active sites and reaction mechanism on low-temperature SCR activity over Cu-SSZ-13 catalysts prepared by different methods, Catal. Sci. Technol. 6 (2016) 6294–6304. https://doi.org/10.1039/C6CY00737F.

[33] J. Xue, X. Wang, G. Qi, J. Wang, M. Shen, W. Li, Characterization of copper species over Cu/SAPO-34 in selective catalytic reduction of NO x with ammonia: Relationships between active Cu sites and de-NO x performance at low temperature, J. Catal. 297 (2013) 56–64. https://doi.org/https://doi.org/10.1016/j.jcat.2012.09.020.

[34] C. Torre-Abreu, M.F. Ribeiro, C. Henriques, G. Delahay, Characterisation of CuMFI catalysts by temperature programmed desorption of NO and temperature programmed reduction. Effect of the zeolite Si/Al ratio and copper loading, Appl. Catal. B Environ. 12 (1997) 249–262. https://doi.org/10.1016/S0926-3373(96)00072-0.

[35] X. Dong, J. Wang, H. Zhao, Y. Li, The promotion effect of CeOx on Cu-SAPO-34 catalyst for selective catalytic reduction of NOx with ammonia, Catal. Today. 258

(2015) 28–34. https://doi.org/10.1016/j.cattod.2015.04.015.

[36] M. Richter, M.J.G. Fait, R. Eckelt, E. Schreier, M. Schneider, M.-M. Pohl, R. Fricke, Oxidative gas phase carbonylation of methanol to dimethyl carbonate over chloride-free Cu-impregnated zeolite Y catalysts at elevated pressure, Appl. Catal. B Environ. 73 (2007) 269–281. https://doi.org/https://doi.org/10.1016/j.apcatb.2006.11.015.

[37] D. Wang, li Zhang, J. Li, K. Kamasamudram, W. Epling, NH3-SCR over Cu/SAPO-34 – Zeolite acidity and Cu structure changes as a function of Cu loading, Catal. Today. 231 (2014) 64–74. https://doi.org/10.1016/j.cattod.2013.11.040.

[38] S.G. Hegde, R. Kumar, R.N. Bhat, P. Ratnasamy, Characterization of the acidity of zeolite Beta by FTi.r. spectroscopy and t.p.d. of NH3, Zeolites. 9 (1989) 231–237. https://doi.org/https://doi.org/10.1016/0144-2449(89)90031-6.

[39] R.Q. Long, R.T. Yang, Temperature-Programmed Desorption/Surface Reaction (TPD/TPSR) Study of Fe-Exchanged ZSM-5 for Selective Catalytic Reduction of Nitric Oxide by Ammonia, J. Catal. 198 (2001) 20–28. https://doi.org/https://doi.org/10.1006/jcat.2000.3118.

[40] Y. Duan, J. Wang, T. Yu, M. Shen, J. Wang, The role and activity of various adsorbed ammonia species on Cu/SAPO-34 catalyst during passive-SCR process, RSC Adv. 5 (2015) 14103–14113. https://doi.org/10.1039/C4RA13984D.

[41] M. Urrutxua, B. Pereda-Ayo, U. De-La-Torre, J.R. González-Velasco, Evaluation of Cu/SAPO-34 Catalysts Prepared by Solid-State and Liquid Ion-Exchange Methods for NO_x Removal by NH_3-SCR, ACS Omega. 4 (2019) 14699–14713. https://doi.org/10.1021/acsomega.9b01118.

[42] A. Varzaneh, J. Towfighi, S. Sahebdelfar, H. Bahrami, Carbon nanotube templated synthesis of hierarchical SAPO-34 catalysts with different structure directing agents for catalytic conversion of methanol to light olefins, J. Anal. Appl. Pyrolysis. 121 (2016) 11–23. https://doi.org/https://doi.org/10.1016/j.jaap.2016.06.007.

[43] F. Gao, J.H. Kwak, J. Szanyi, C.H.F. Peden, Current Understanding of Cu-Exchanged Chabazite Molecular Sieves for Use as Commercial Diesel Engine DeNOx Catalysts, Top. Catal. 56 (2013) 1441–1459. https://doi.org/10.1007/s11244-013-0145-8.

[44] T.V.W. Janssens, H. Falsig, L.F. Lundegaard, P.N.R. Vennestrøm, S.B. Rasmussen, P.G. Moses, F. Giordanino, E. Borfecchia, K.A. Lomachenko, C. Lamberti, S. Bordiga,

A. Godiksen, S. Mossin, P. Beato, A Consistent Reaction Scheme for the Selective Catalytic Reduction of Nitrogen Oxides with Ammonia, ACS Catal. 5 (2015) 2832–2845. https://doi.org/10.1021/cs501673g.

[45] D.W. Fickel, E. D'Addio, J.A. Lauterbach, R.F. Lobo, The ammonia selective catalytic reduction activity of copper-exchanged small-pore zeolites, Appl. Catal. B Environ. 102 (2011) 441–448. https://doi.org/10.1016/j.apcatb.2010.12.022.

[46] C. Yan, H. Cheng, Z. Yuan, S. Wang, The role of isolated Cu $^{2+}$ location in structural stability of Cu-modified SAPO-34 in NH $_3$ -SCR of NO, Environ. Technol. 36 (2015) 169–177. https://doi.org/10.1080/09593330.2014.941017.

Chapter V

CHAPTER V: First steps towards the development of novel all-zeolite core-shell materials.

As discussed in *Chapter I*, one of the goals of this project is to develop a multifunctional core-shell catalyst, where both, the core and the shell materials are made of advanced zeolite catalysts. These materials aim to be applied for vehicle exhaust NO_x abatement by the Selective Catalytic Reduction with NH_3 over a wide range of reaction temperatures.

As previously described, Cu/CHA-based catalysts (mainly Cu/SSZ-13 and Cu/SAPO-34) exhibit excellent features for such reaction, including their high catalytic activity at low reaction temperatures (mainly due to the copper ionic species placed in exchange positions of the CHA zeolite, as discussed in *Chapter IV*), and their high hydrothermal stability, on account of the small-pore size of the CHA zeolites [1]. As a matter of fact, the discovery of these materials was such a significant milestone [2], that the research related to Fe-exchanged small-pore zeolites became less significant for the same application, mainly ascribed to their poor low-temperature SCR performance. In this sense, the first article describing Fe/SSZ-13 and Fe/SAPO-34 SCR catalysts was published in 2012 by Ye et al. [3]. Since then, important discoveries about small-pore Fe/CHA NH_3-SCR catalysts have been made, as recently summarized in a review article by Gao [4]. Regardless the inferior low temperature activity of these materials compared to their Cu counterparts, they exhibit excellent features, such as higher SCR activity at temperatures over 400 ^oC, together with much lower selectivity towards the undesired N_2O. N_2O is known to have a global-warming impact ~300 times higher than CO_2 on a per mass basis. In addition, it is known to react with atomic oxygen to form nitric oxide (NO) in the stratosphere, thereby contributing to ozone layer depletion [5]. Therefore, the development of efficient Fe-exchanged small-pore zeolites seems an appropriate approach for the reduction of NO_x by the NH_3-SCR catalytic process with negligible emissions of N_2O.

Hence, considering the respective advantages of these catalysts, it seems evident that the combination of both, Fe- and Cu-exchanged small-pore zeolites might provide a synergy between the best characteristics of such materials. In other words, novel arrangements of Cu-Fe/CHA materials could potentially allow to develop a more efficient catalyst for NH_3-SCR over a broader temperature window, with a much lower selectivity towards N_2O. In that regard, several works have been published in the last decade [6–11]. In most of these studies (based on SSZ-13 as a CHA support), the metallic species were introduced in the zeolite framework either

by simultaneous (one-pot) ionic exchange, or rather by wet-impregnation of Fe-based precursors over a Cu/CHA zeolite. Hence, a general synergy between both, Fe and Cu species was found, with an enhanced activity and selectivity for the NH_3-SCR reaction.

In this project, a drastically new approach is pursued, where both Cu/CHA and Fe/CHA-based materials will be merged through a core-shell architecture. In this sense, as discussed in *Chapter I*, many approaches were published dealing with the development of zeolites covered by a mesoporous shell (mainly silica-based) [12,13]. These materials generally exhibit a hierarchical structure, enhancing the diffusion of reactant species through the mesopores of the silica-based shell to the microporous zeolite core. However, these materials do not show any significant advantage compared to the zeolite material alone in terms of selectivity, since the silica by itself exhibits a generally poor activity for most catalytic processes considered. In this sense, recently, novel core-shell materials have been developed for the NH_3-SCR reaction [14–19]. In most of those studies [15–19], medium and large pore Fe-and Cu-based zeolites (mainly ZSM-5) were coated with mesoporous ceria-based shells. The ceria shell not only favors the diffusion, but also favors the oxidation of NO into NO_2, further enhancing the catalytic performance through the so-called fast-SCR reaction ($NO + NO_2 + 2\ NH_3 \rightarrow 2\ N_2 + 3\ H_2O$).

Here, a new approach is proposed, where both the core and the shell materials are CHA-based materials. The development of core-shell catalysts where both materials are zeolites has been recently summarized in an excellent review article by Masoumifard et al. [20] for a wide variety of applications. However, none of these catalysts were applied for the NH_3-SCR reaction.

The idea herein is to develop a core-shell catalyst where the core is made of the hierarchical Cu/SAPO-34 catalyst (so-called *Cu-0.15/fresh*) developed in our previous study (*Chapter IV*). This material exhibited an excellent activity at low temperatures (likely attributed to the enhanced diffusion of reactants through their mesoporous-microporous framework) and high hydrothermal stability. The shell, on the other hand, will be constituted by a Fe/SAPO-34 catalyst, where iron species will be exchanged in the framework of a microporous SAPO-34 zeolite. The microporous support chosen for this purpose is the so-called *micro* material (Chapter II). This material was prepared using TEOS as a Si precursor, and exhibits a slightly bigger pore size compared to a similar material using fumed silica as a Si precursor (*Micro (Fumed silica), Chapter II)*, as previously shown in Chapter III (supporting information, Figure III.S1). This feature will enhance the diffusion of reactants through the Fe/SAPO-34 shell catalyst. Hence, the targeted core-shell assembly (Figure V.1), together with a higher catalytic

activity in the NH_3-SCR process in a wider temperature range, is expected to exhibit the following advantages compared to the above described studies: i) the hierarchical core *Cu-0.15/fresh* catalyst, with slightly lower hydrothermal stability compared with the microporous SAPO-34 zeolite (*Chapter IV*), will be protected by the Fe/SAPO-34 microporous catalyst (with a more robust framework on account of its micropores), ii) the N_2O produced at the hierarchical core *Cu-0.15/fresh* catalyst can be further transformed in the Fe/SAPO-34 microporous catalyst, decreasing the overall N_2O emissions. In this sense, previous studies have proved [5] that Fe-exchanged small-pore zeolites (e.g. SSZ-13) exhibit high performance towards the N_2O decomposition reaction ($N_2O \rightarrow N_2 + ½\ O_2$).

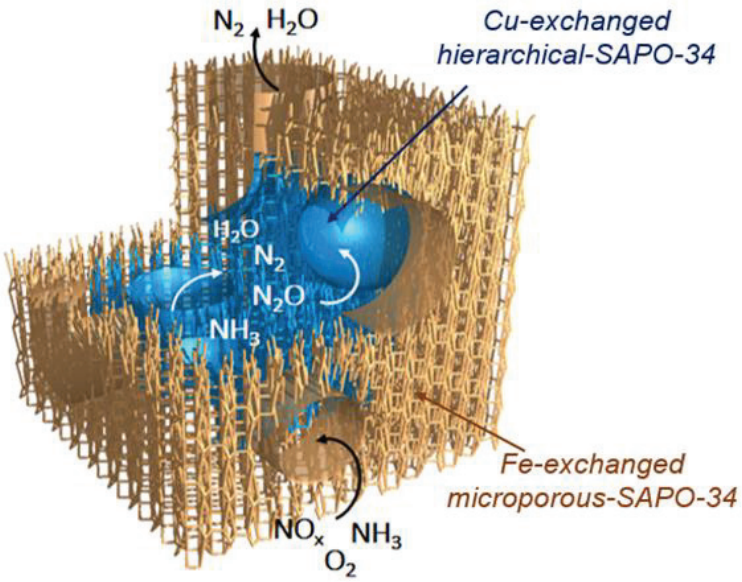

Figure V. 1. Scheme of the novel core-shell architecture proposed in this study for the reduction of NO_x through the NH_3-SCR catalytic process.

To the best of the authors knowledge, to this date, limited reports have been published regarding the development of core-shell catalysts where both phases are SAPO-type materials [21], since the formation of such assembly is usually more difficult than for other aluminosilicate-based zeolites (such as ZSM-5). Hence, in this chapter, as a first step for the development of the above described core-shell architecture, different strategies were studied dealing with the assembly of the core *Cu-0.15/fresh* catalyst, with a bare microporous SAPO-34 zeolite shell (so-called *micro* in *Chapter III*). The target core-shell material will be denominated *Cu-0.15/fresh@micro.* The different strategies will be described in the following sections, where the obtained materials were characterized mainly by high-resolution Environmental Transmission Electronic Microscopy (E-TEM, described in *Chapter II*).

1. Strategy 1: In-situ overgrowth.

One of the simplest methods for the development of core-shell materials is the *in-situ overgrowth* [20]. Generally, in a first step, the core material (which could be pretreated or not) is immersed in a gel with the precursors for the synthesis of the shell material, followed by a hydrothermal crystallization step. This approach is commonly referred to as *epitaxial growth method* [21], where the shell grows on the surface of the core. This method has been broadly used for the development of all-zeolite core-shell materials for a wide variety of applications, as recently summarized by Masoumifard et al. [20]. In this section, for the first time, an attempt will be made for the synthesis of a *Cu/0.15-fresh@micro* core-shell material by *in-situ overgrowth*.

According to previous studies, in the development of all-zeolite core-shell materials, small nano/microcrystals of the shell zeolite grow on the surface of the core zeolite [21–23]. Hence, two nucleation centers exist and compete for the growth of the shell zeolite crystals: one is in the synthesis gel (undesired, since it provides isolated crystals), and the other is on the surface of the core zeolite. In order to enable the latter, the hydrothermal crystallization step should preferably provide small zeolite crystals. Considering that in this study, both core and shell are made from zeolites of a similar nature (SAPO-34), if the gel precursor solution (for the synthesis of the *micro* shell) is prepared following the same procedure (see *Chapter II*) than the one used for the development of the materials used in *Chapters III and IV*, a similar crystal size could be expected for both, the hierarchical Cu/SAPO-34 catalyst (*Cu/0.15-fresh,* core) and the microporous SAPO-34 zeolite *(micro,* shell). Hence, in order to decrease the crystal size distribution of the latter material, a preliminary test was performed, consisting on slightly modifying the synthesis of microporous SAPO-34.

The idea was to use a gel with the same molar composition as described in *Chapter II* for the material called *micro* (i.e., the microporous SAPO-34 zeolite with TEOS as a Si precursor). However, different amounts of this gel were introduced in the autoclave (with a total volume of 25 ml) for the hydrothermal crystallization: 16 ml (i.e., ~2/3 of the total volume of the autoclave), 8 ml (i.e., ~1/3 of the total volume of the autoclave), and 5 ml (i.e., 1/5 of the total volume of the autoclave). The former corresponds to the volume used for the synthesis of the materials used in *Chapters III and IV*, and therefore will be used as a reference. After calcination (see *Chapter II*), the materials were first characterized by X-Ray Diffraction, Figure V. 2 (a).

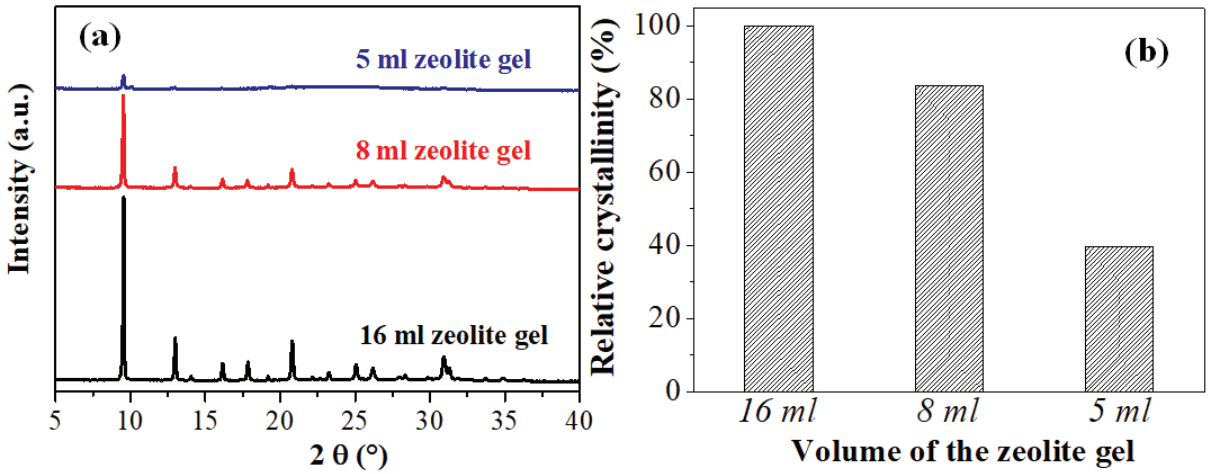

Figure V. 2. (a) XRD patterns, and (b) Relative crystallinity of the materials obtained by the crystallization of different volumes (5 mL, 8 mL and 16 mL) of microporous zeolite gel precursor. Relative crystallinity was calculated using the *16 ml zeolite gel* sample as a reference.

In this figure it can be observed that the *5 ml zeolite gel* material exhibits a rather amorphous phase, while the *8 mL zeolite gel* and the *16 ml zeolite gel* samples exhibit XRD characteristic peaks of conventional SAPO-34 CHA-based zeolite, with their main peak located at 2θ = 9.5º [24,25]. In addition, as shown in Figure V. 2 (b), the *8 ml zeolite gel* material displays a minor decrease of its crystallinity compared to the reference *16 ml zeolite gel*, giving rise to a relative crystallinity of the former ~84 % (respect to the *16 ml zeolite gel* material). The amorphous material *(5 ml zeolite gel)*, as expected, shows a relative crystallinity lower than 40 %.

These results seem to indicate that the volume of the zeolite gel solution plays a significant role on the formation of the desired SAPO-34 material. This volume is closely related to the autogenous pressure generated in the autoclave during the hydrothermal crystallization step: increasing the zeolite gel volume gives rise to a decrease of the available gas volume, resulting in an increased pressure. Hence, in order to verify whether the formation of the zeolite crystalline phase is limited by the volume of the sample introduced in the autoclave, or rather the volume of the gel (zeolite precursor solution), a series of 8 ml samples were prepared, where different gel volumes were compensated with water, followed by the same crystallization procedure as before. The obtained materials were also characterized by XRD, Figure V. 3 (a). In this figure, the formation of the SAPO-34 zeolite can be observed for all the prepared materials. In addition, according to Figure V. 3 (b), the samples with the highest amount of gel solution exhibit a similar crystallinity value (relative to the reference *16 mL*

zeolite gel), while the sample with the lowest amount of gel led to a decreased crystallinity (~76 %).

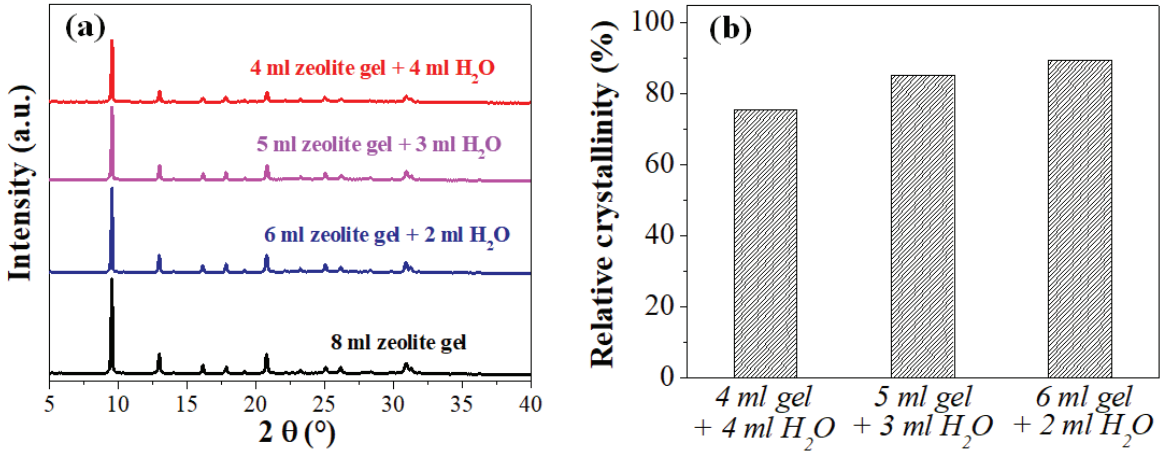

Figure V. 3. (a) XRD patterns, and (b) Relative crystallinity of the materials obtained after the crystallization of 8 mL samples with different proportion of microporous zeolite gel precursor. Relative crystallinity was calculated using the *16 ml zeolite gel* sample as a reference.

It is worth comparing the *5 mL zeolite gel+3 mL H_2O* sample with the *5 mL zeolite gel* sample previously shown in Figure V. 2 (a). Even though both samples contained the same amount of zeolite gel precursor, they gave rise to drastically different materials, where only the former led to the production of the desired zeolite phase with significant crystallinity.

The results obtained in Figures V. 2 and 3 demonstrate that the autogenous pressure generated in the autoclave is a parameter of paramount importance for the development of the SAPO-34 zeolite. In this sense, in a recent review article published by Askari et al. [26], the influence of a wide variety of parameters on the crystallization process for SAPO-34-based materials was studied, including the crystallization time, temperature, gel composition, etc. Increasing the temperature leads to a faster and more efficient crystallization of the zeolite [27]. One can relate the temperature increase with an increase of the autogenous pressure generated in the reactor, in good agreement with the results obtained herein. In addition, according to ref. [28], it seems that the crystallization process cannot become complete at high concentration of water, which explains the lower relative crystallinity obtained for the material with the highest amount of water, Figure V. 3 (b).

The morphologies of the *8 mL zeolite gel* and the reference *16 mL zeolite gel* materials were analysed by Transmission Electronic Microscopy (TEM, Figure V. 4 (a) and (b),

respectively). For comparison, Figure V. 4 (c) shows the TEM image of the hierarchical zeolite support *Aged-Meso-0.15*, prepared as described in *Chapter II* (and thoroughly characterized in *Chapter III*), also by using a gel volume of 16 ml. This material is the support of the *Cu/0.15-fresh* hierarchical catalyst (*Chapter IV*), which will function as *core* of the pursued core-shell material.

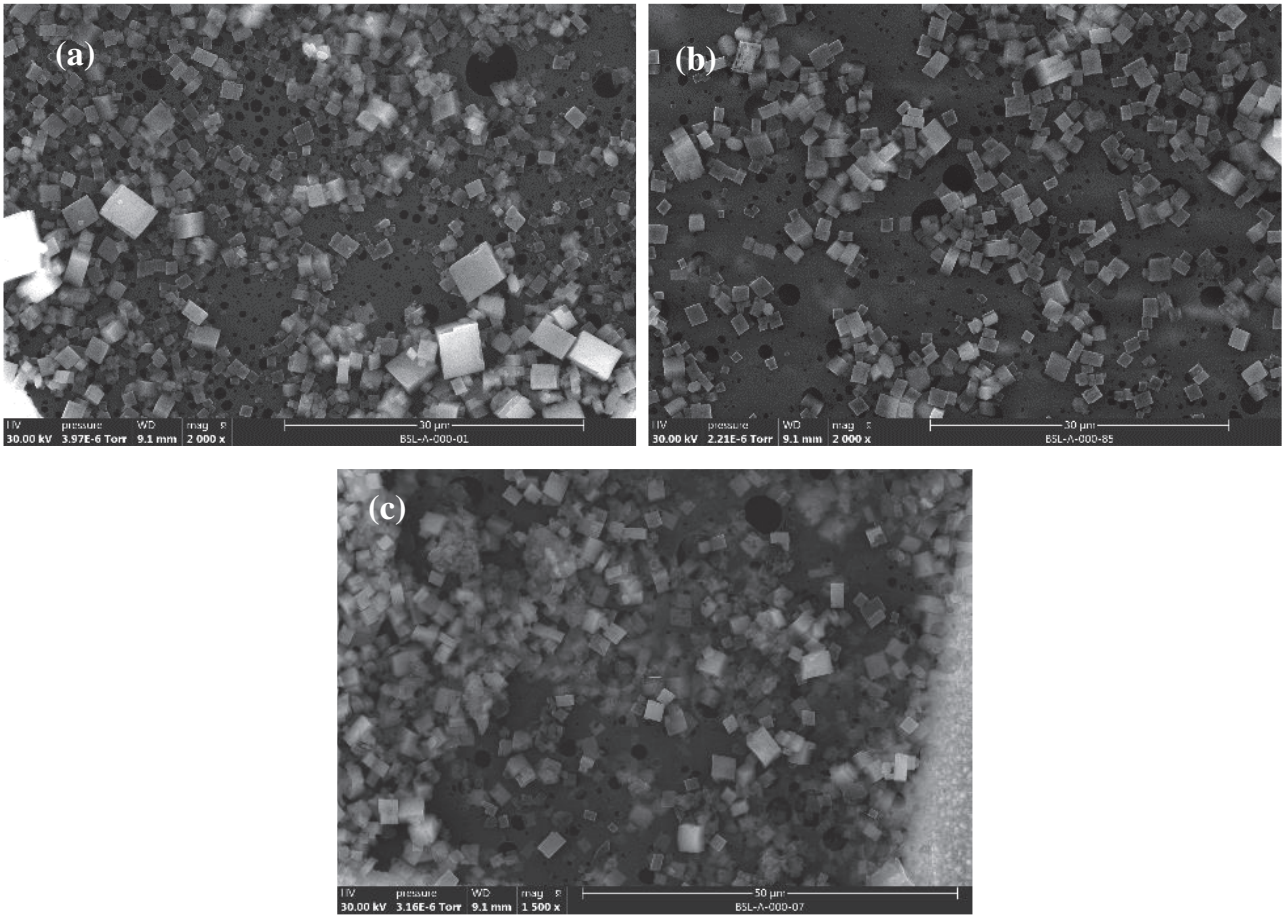

Figure V. 4. TEM images of the *8 mL zeolite gel* (a) and *16 mL zeolite gel* (b) samples (microporous SAPO-34), and the *Aged-Meso-0.15* (c) (hierarchical SAPO-34).

According to these figures, all materials exhibit micrometric crystals with a typical cubical morphology with flat and smooth external faces. However, their crystal size distribution seemed to be different. Hence, the particle size distribution was calculated by measuring more than 400 particles. In Figure V. 5 it could be observed that the *8 mL zeolite gel* material displays a majority of particles <1.5 μm, while the *16 mL zeolite gel* material exhibits a larger particle size distribution, with a more significant proportion of bigger particles (> 1.5 μm).

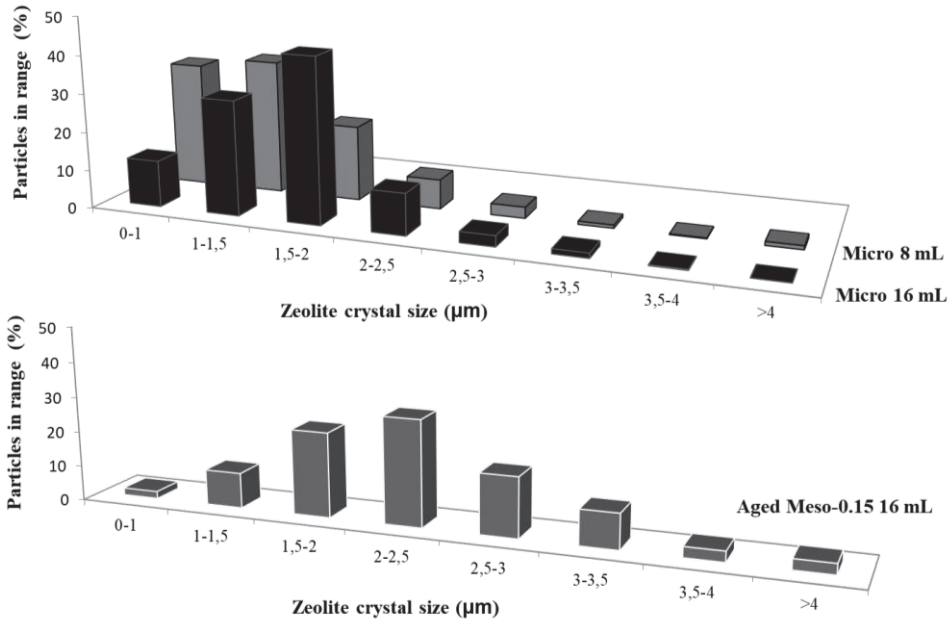

Figure V. 5. Zeolite crystal size distribution (according to the TEM images of Figure V.4) of the following samples: *8 mL zeolite gel* and *16 mL zeolite gel* (microporous SAPO-34), and *Aged-Meso-0.15* (hierarchical SAPO-34).

These results suggest, in good agreement with the XRD analysis, that the lower autogenous pressure generated for the *8 mL zeolite gel* material compared with the reference material led to a slower crystallization development, limiting the growing process, and leading therefore to smaller SAPO-34 microcrystals, which was the purpose of these preliminary tests. In addition, the hierarchical material clearly exhibits even larger crystals (the crystal size distribution shows a significant share over 2 µm). This is indeed a detail of paramount importance for the development of the desired core-shell structures, since the average particle size of the shell materials (i.e., the microporous SAPO-34 prepared from an 8 ml zeolite gel) is much smaller than the core material (i.e., the hierarchical Cu/SAPO-34 catalyst prepared with the *Aged-Meso-0.15* support). It is expected that these features will ease the development of the core-shell assemblies.

Thus, the *in-situ overgrowth* method was used as a first approach to develop a core-shell *Cu/0.15-fresh@micro* material. The experimental procedure is summarized in Figure V.6.

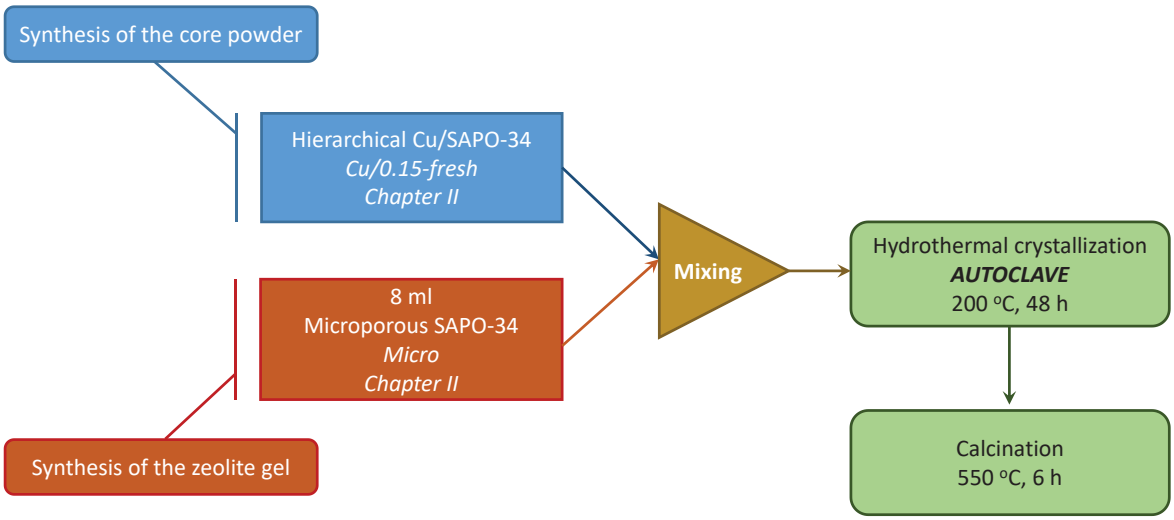

Figure V. 6. Scheme of the experimental procedure used for the development of the core-shell *Cu/0.15-fresh@micro* material by the *in-situ overgrowth* method.

The core powder, i.e. the hierarchical Cu/SAPO-34 catalyst (*Cu/0.15-fresh*) was prepared following the protocol described in *Chapter II*. On the other hand, according to the previous experiments above described, 8 mL of the zeolite gel for the shell (*microporous SAPO-34 material*) were prepared following the procedure described in *Chapter II* for the material called *micro*. Then, 0.8 g of the core material were immersed in the zeolite gel, and the mixture was directly introduced in a Teflon-lined stainless-steel autoclave, which is placed in a furnace at 200 ºC for 48 h. Ideally, the hydrothermal crystallization procedure would lead to the growing of small microporous SAPO-34 microcrystallites (epitaxial growth) on the surface of bigger crystals of the hierarchical Cu/SAPO-34 catalyst. After the crystallization, the materials were centrifuged, washed and dried at 110 °C overnight. Finally, the synthesized powders were calcined at 550 °C for 6 h in synthetic air (total flow rate = 4.5 L · h^{-1}) to remove the microporous TEAOH template.

Figure V. 7 shows the high resolution Environmental Transmission Electronic Microscopy (E-TEM) images of the obtained materials. They exhibit micrometric crystals with a wide particle size distribution, mainly with a cubical morphology and flat and smooth external faces. However, no significant interaction between those crystals was observed. These results seem to indicate that the desired core-shell structure was not obtained by the *in-situ overgrowth* method.

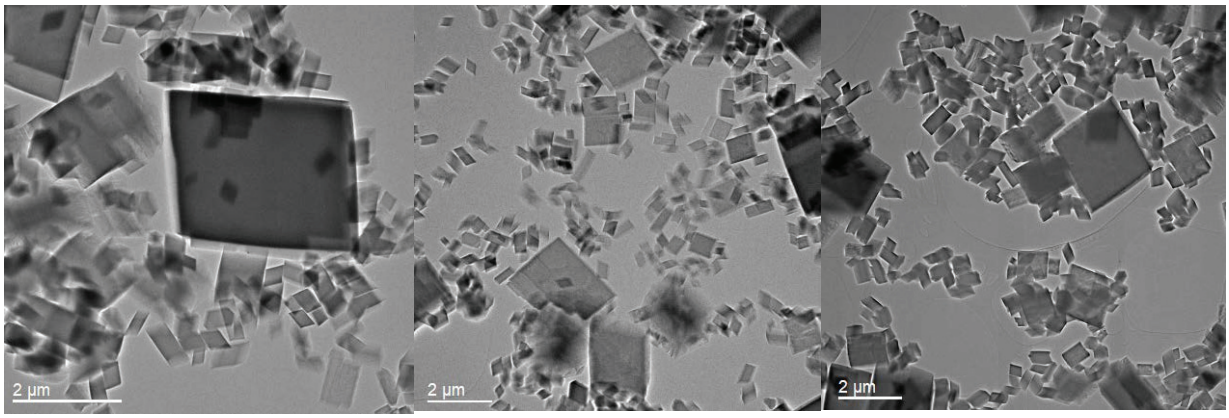

Figure V. 7. E-TEM images of the materials obtained by the *in-situ overgrowth* method described in Figure V. 6.

According to literature, this method might provide satisfactory results, especially when there is structural similarities and chemical compatibilities between the zeolites, since it favours the epitaxial growth of the shell zeolite on the core [20,21,29]. However, two important factors play a key role in the epitaxial growth [20]: i) the chemical compatibility of the core in the crystallization conditions of the shell, and ii) the competition between the nucleation centers, i.e., in the bulk gel or on the core surface. The first factor could be neglected in this case, since the core hierarchical Cu/SAPO-34 catalyst was primarily synthesized under similar crystallization conditions. In addition, no signals of partial dissolution or crystal etching were observed in the E-TEM images (Figure V. 7). However, it seems that the competition between the nucleation centers might prevent the direct growing of the microporous SAPO-34 zeolite on such core catalyst. In addition, it can be assumed that the surface charges of both, the hierarchical Cu/SAPO-34 catalyst and the SAPO-34 zeolite produced upon the crystallization procedure above described, are similar, due to the analogous nature of both materials. Hence, once the nucleation in the bulk gel starts, the microporous SAPO-34 material would be repelled from the surface of the hierarchical catalyst, impeding the formation of core-shell structures.

All in all, the results obtained in this section suggest that the *in-situ overgrowth* method is not appropriate for the development of the desired core-shell structure *Cu/0.15-fresh@micro.*

1. **Strategy 2: Seeded growth method assisted by CTAB.**

The purpose of the *seeded growth method* is to integrate a thin layer (*seed*) of previously synthesized shell material (in this case, the microporous SAPO-34 zeolite, *micro*) over the core material (in this case, the hierarchical Cu/SAPO-34 catalyst, *Cu/0.15-fresh*). Then, the seeds located on the external surface of the core induce a faster shell formation.

Zeolites have generally negatively charged surfaces [30]. In order to enhance the electrostatic interaction between the zeolite core and the seed, the surface of one of them should be conditioned to enhance the adsorption of the seed crystals. In this sense, cationic polyelectrolytes, commonly used in previous core-shell studies [20], will be used to invert the surface charge of one of the zeolites, since the cationic surfactant micelles could interact with the zeolite by electrostatic adsorption. In this section, CTAB (Cetyltrimethylammonium bromide) will be used as a surface modifier.

The surface charge of the zeolites will be controlled through the zeta-potential, which is influenced, among other factors, by the pH of the colloidal solution, as described in *Chapter II*. Prior to the core-shell synthesis by the *seeding growth method*, the zeta-potential of both, the core and the shell zeolites will be studied by impregnating the powder materials with different amounts of CTAB. To do that, different volumes of a solution 0.1 M of CTAB (in ethanol) were impregnated over them in a rotate evaporator at a temperature of 50 ºC. The samples were called *+10x CTAB* and *+40x CTAB,* meaning that the total volume of the CTAB solution used for the impregnation was, respectively, 10 or 40 times that of the pore volume of each of the materials.

Figure V. 8 shows the variation of the zeta-potential at pH 9 for the as-prepared core (hierarchical Cu/SAPO-34 catalyst) and shell (microporous SAPO-34 zeolite, prepared following the same procedure as in the previous section, for an 8 mL zeolite gel) materials, together with that for the materials impregnated with the two different CTAB amounts. The pH 9 was chosen in order to provide a similar environment to that of the microporous zeolite gel. First of all, as expected, the zeta-potential for both as-prepared zeolites was very similar, exhibiting negative values. This indicates that these materials have negatively charged surfaces, as is the case for most zeolites [30]. However, the impregnation with increasing amounts of CTAB leads to the increase of the zeta-potential for both materials at this pH. It suggests that the CTAB cationic surfactant micelles interact with both zeolites by electrostatic adsorption, inverting the surface charge from negative to more positive values.

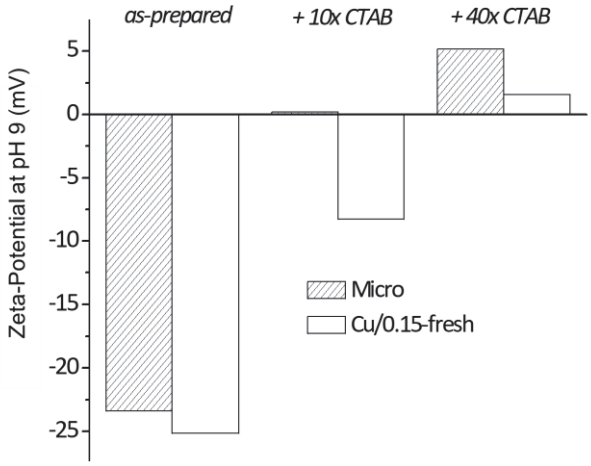

Figure V. 8. Variation of the zeta-potential of the *micro* and *Cu/0.15-fresh* materials upon impregnation with different amounts of CTAB.

Taking into account these results, a new approach for the synthesis of a *Cu/0.15-fresh@micro* core-shell material by the *seeded growth method* was attempted by the procedure described in Figure V. 9.

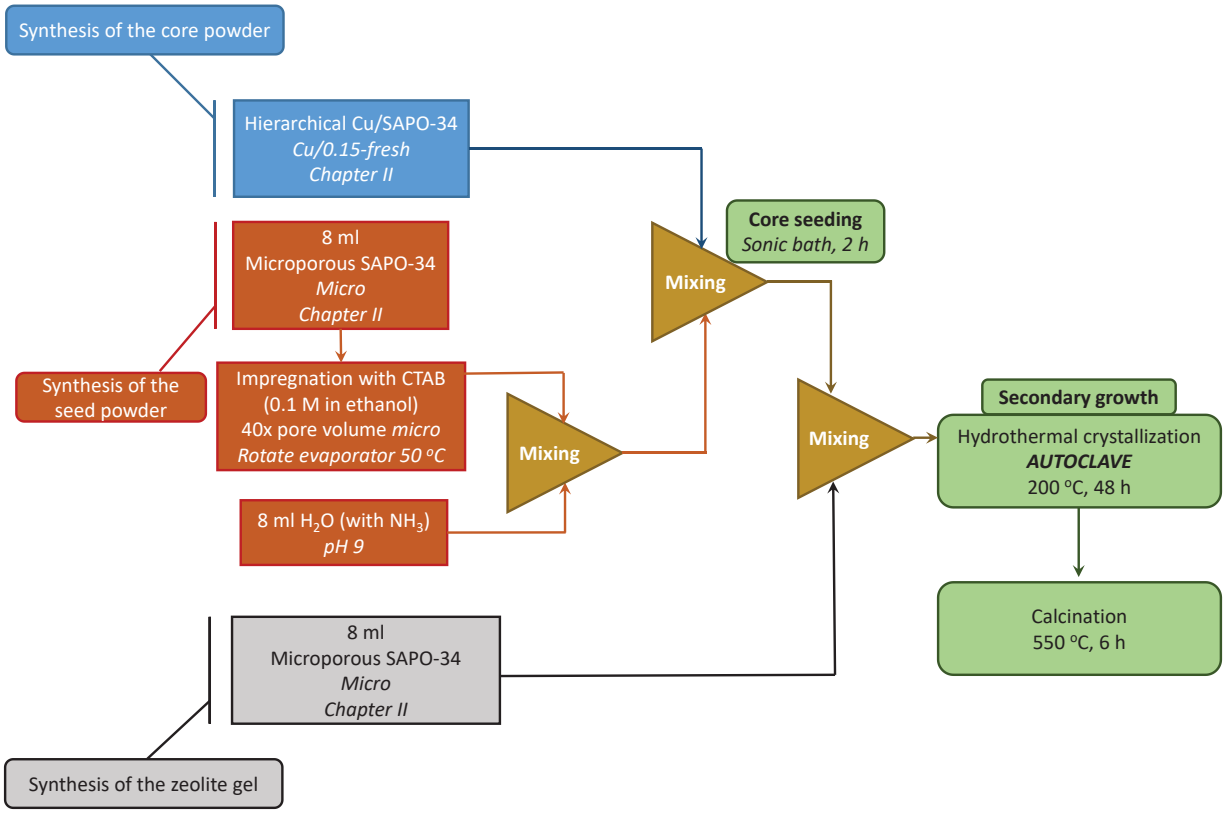

Figure V.9. Scheme of the experimental procedure used for the development of the core-shell *Cu/0.15-fresh@micro* material by the *seeded growth* method, using CTAB as a polyelectrolyte (cationic surfactant).

First, both *Cu/0.15-fresh* (core) and *micro* (8 mL) were synthesized as previously explained. Then, the *seed* was produced by impregnating the *micro* material with a 40xCTAB solution, following the same procedure as explained for Figure V. 8. Then, the seed was introduced in an 8 mL water solution with pH 9. The next step was the core seeding, where the core is immersed in this solution, which is further introduced in a sonic bath for 2 hours (to enhance the contact between both materials). At pH 9, the zeta-potential difference between the seed (*micro + 40 x CTAB,* positive zeta-potential) and the core *(Cu/0.15-fresh,* negative zeta-potential) is significant, favoring (in theory) the seeding process. After the seeding process, the secondary growth is the last step, which consists of a hydrothermal method similar to the one explained in the previous section. Here, the core seeded solution is introduced in an autoclave with 8 mL zeolite gel (precursor of the microporous SAPO-34 shell, *micro*), followed by a hydrothermal treatment at 200 ºC for 2 hours. Finally, the obtained material was treated and calcined as in the previous section.

Figure V. 10 shows the high-resolution E-TEM (and STEM, Scanning transmission electron microscopy) images of the obtained materials. In this figure, first of all, it can be observed the presence of zeolite micrometric crystals with a cubical morphology, but their external faces were not as flat and smooth as the materials in the previous section. In other words, the crystallization process seemed to be inhibited. In addition, no significant interaction between the different zeolite-based materials was observed.

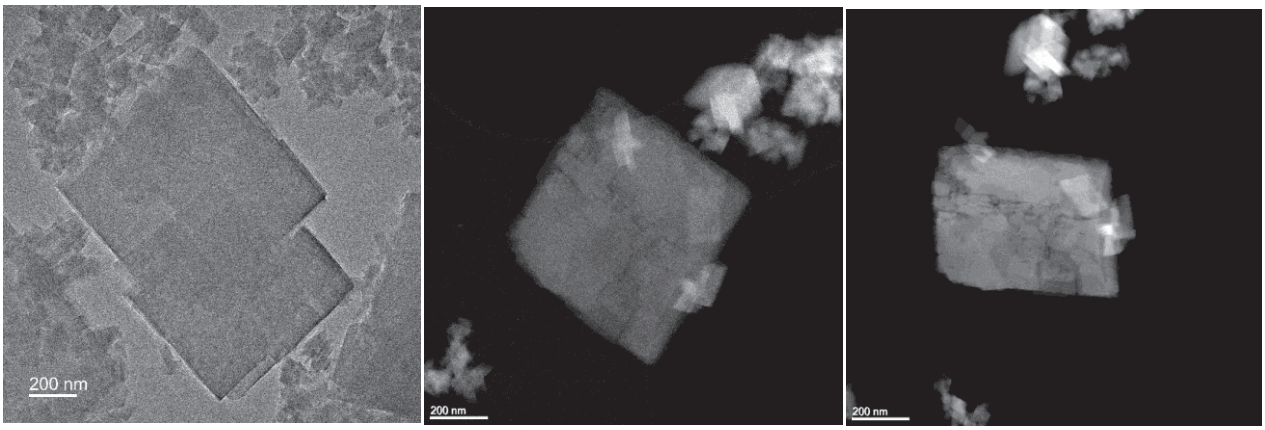

Figure V.10. E-TEM (left) and STEM (middle and right) images of the materials obtained by the *seeded growth* method (using CTAB as a polyelectrolyte) described in Figure V. 9.

These results suggest that the CTAB surfactant added before the core seeding was released and dissolved in the gel during the secondary growth step in the autoclave. As explained in *Chapters III and IV*, the CTAB also behaves as a crystal growth inhibitor [31].

Also, if CTAB is released to the solution, the core-seed interaction might dramatically decrease, limiting the secondary growth of the shell on the surface of the core. Therefore, by increasing the interaction between the seed and the core by avoiding the release of CTAB into the secondary growth gel, the desired core-shell structure might be developed. In this sense, many studies dealing with the development of core-shell structures perform a thermal treatment after the core-seeding step (usually a high temperature calcination procedure), to ensure adherence of the seeds to the surface of the core material [32–35]. Thus, in the next approach, the synthesis procedure was slightly varied (Figure V. 11). Herein, after the core seeding step, the resulting suspension was subjected to a soft thermal treatment, by drying it at 50 ºC overnight.

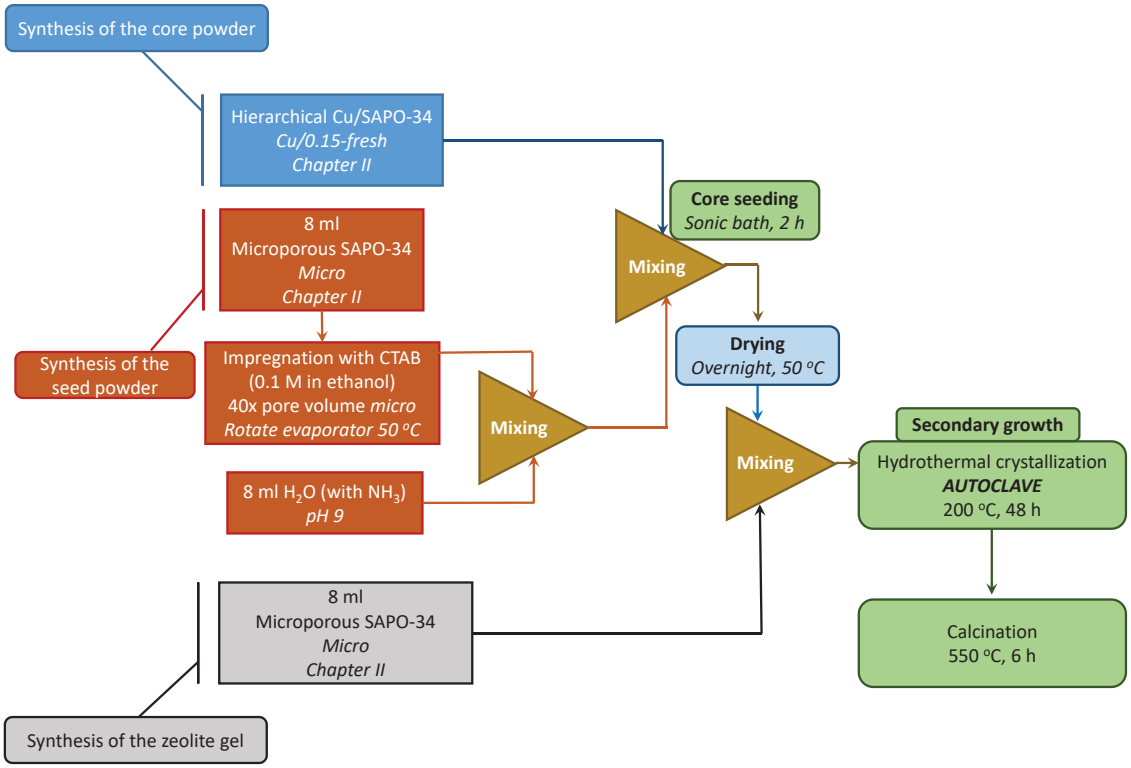

Figure V. 11. Scheme of the experimental procedure used for the development of the core-shell *Cu/0.15-fresh@micro* material by the *seeded growth* method, using CTAB as a polyelectrolyte (cationic surfactant). The procedure described in Figure V.9 was modified introducing a drying stage after the core seeding step.

Figure V. 12 shows the high resolution TEM of the materials obtained by this approach. Assuming that the smaller crystals belong to the microporous SAPO-34 zeolite (*micro*), contrary to the previous approach, a soft interaction was observed in this case with the hierarchical Cu/SAPO-34 catalyst (*Cu/0.15-fresh*, core). This experiment confirms therefore that a thermal treatment is necessary to enhance the connection between the core and the seeds.

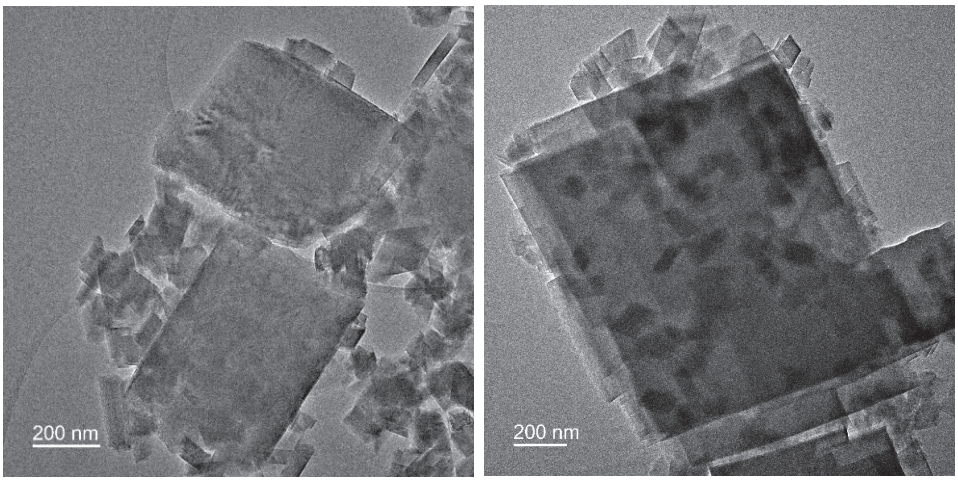

Figure V. 12. E-TEM images of the materials obtained by the *seeded growth* method with CTAB (modified by introducing a drying stage after the core seeding step, Figure V. 11).

In the aforementioned publications [32–35] (among others) a harder thermal treatment was carried out after the seeding process, by a high temperature calcination. In addition, instead of reverting the surface charge of the seed material (as we did in the approaches described in Figures V. 9 and V. 11), the charge of the core material was inverted by the use of cationic polyelectrolytes. In view of this, a last approach of this section is described in Figure V. 13.

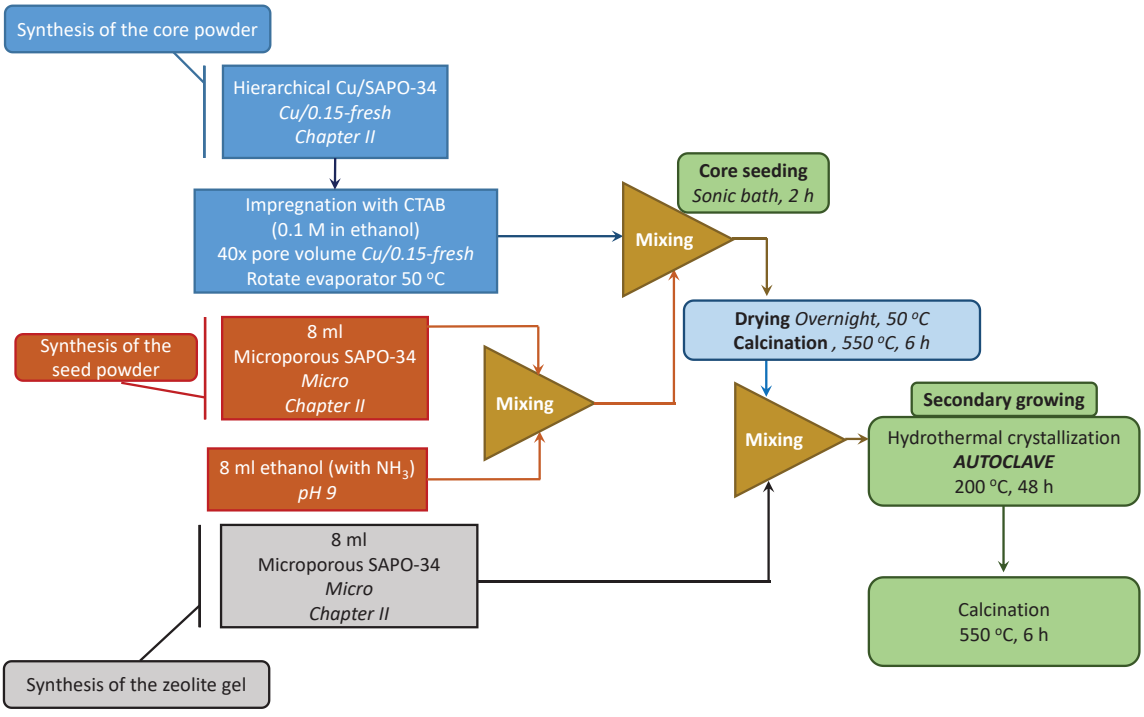

Figure V. 13. Scheme of the experimental procedure used for the development of the core-shell *Cu/0.15-fresh@micro* material by the *seeded growth* method with CTAB. The procedure described in Figure V.11 was modified: i) by modifying the charge of the core, ii) by introducing a drying + calcination stage after the core seeding step.

Herein, the charge of the core (*Cu/0.15-fresh*) was first inverted with CTAB. By doing that, as previously shown in Figure V. 8, at pH 9, the zeta-potential difference between the seed (*micro,* negative zeta-potential) and the core *(Cu/0.15-fresh + 40x CTAB,* positive zeta-potential) becomes very significant, favoring the seeding process. The materials obtained after the drying step (following the core-seeding), were calcined at 550 ºC for 6 hours. It is worth noting that this calcination procedure is similar to that of the isolated core and zeolite seed materials (as described in *Chapter II*). Therefore, it will not damage (in theory) their structure.

Figure V. 14 shows the E-TEM pictures for the materials obtained following this synthesis approach. As before, assuming that the smaller crystals are made of microporous SAPO-34 zeolite (*micro, shell*), a much more significant interaction was observed with the hierarchical Cu-based catalyst (*Cu/0.15-fresh, core*). According to these images, the materials obtained by this procedure are the closest so far in this work to the desired core-shell *Cu/0.15-fresh@micro*. It seems that modifying the surface charge of the core material has a positive effect to favor the heterogeneous nucleation of the shell material on the surface of the core. This effect appeared to be similar to the effect found in previous studies, where it was reported that the presence of defects on the surface of the core become the anchor points for the shell precursor species [21,36].

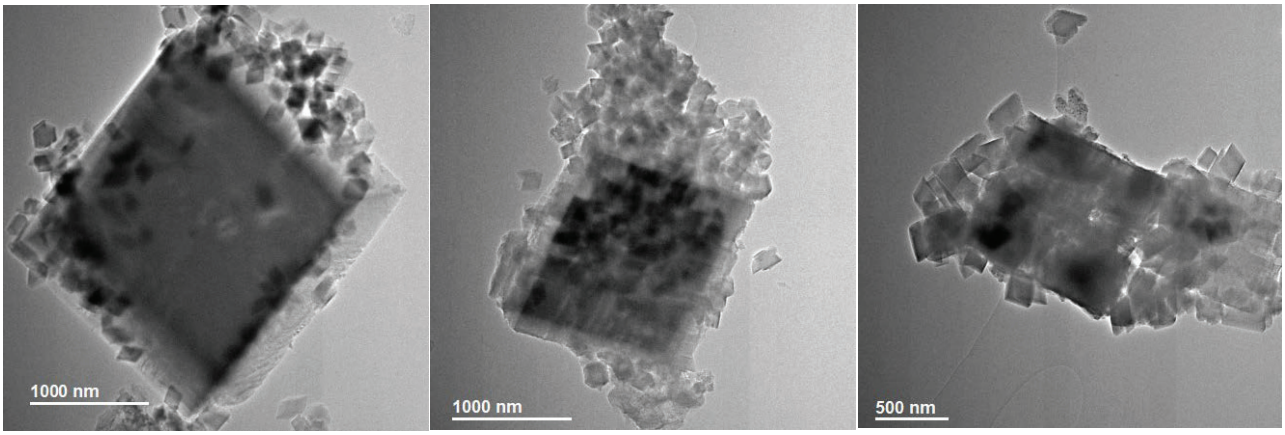

Figure V. 14. E-TEM images of the materials obtained by the *seeded growth* method with CTAB (modified by inverting the surface charge of the *Cu/0.15-fresh*, and introducing a drying + calcination stage after the core seeding step, Figure V. 13).

Hence, inverting the surface charge of the core, and calcining the core-seeded material, drastically enhanced the efficiency of the core seeding step, giving rise to significant benefits towards the production of the desired materials. In the next section, a different polyelectrolyte (cationic surfactant) was studied.

3. Strategy 3: Seeded growth method assisted by TEAOH.

The *seeded growth method* has shown great potential in the previous section for the development of the desired core-shell structure, compared with the direct *in-situ overgrowth*. In that approach, it was proven that the zeta-potential should be carefully adjusted in order to provide the required attraction between the core and the seed components. In this sense, a wide variety of polyelectrolytes were used in previous studies as cationic surfactants to modify the surface charge of the core [20]. Taking into account the strongest features of the previously described approaches, in this section, the modification of the surface charge of the core with a different polyelectrolyte (TEAOH, Tetraethylammonium hydroxide), will be studied.

First of all, the zeta-potential of the *Cu/0.15-fresh* (core) at pH 9 was studied after being impregnated with TEAOH. An aqueous TEAOH solution (1.5% wt) was used for the impregnation of the core material, followed by drying at 80 °C for 10 h. The zeta-potential obtained for this material was -18.6. It seems, as expected, that this surfactant is able to modify the charge of the raw *Cu/0.15-fresh* material (-25.2) towards more positive values [20]. However, TEAOH seemed to have a weaker effect as a surface modifier compared with CTAB (zeta-potential at pH 9 = 1.6, Figure V. 8). Nevertheless, this positive surfactant was used in previous studies dealing with the synthesis of all-zeolite core-shell structures ($Y(Na^+)$@β [37]), while other surfactants with a similar structure (TPAOH, tetrapropylammonium hydroxide) were used for the synthesis of other core-shell materials, such as Pt/Al_2O_3@silicate-1 [38,39] by the *seeded growth method*. In this section, for the first time, the TEAOH polyelectrolyte will be used to attempt to develop an all-zeolite *Cu/0.15-fresh@micro* material.

It is worth noting that, as previously explained, TEAOH participates in the synthesis of the microporous SAPO-34 zeolite (*Chapter II*) as a template. According to ref. [40] (which studied in detail the crystallization mechanism for a wide variety of zeolites, such as silicate-1, with TPAOH and TEAOH templates), the cations produced by this kind of surfactants (TPA^+, TEA^+) interact with the silicate species in the gel, and organize them into structures that are ultimately incorporated into the channel intersections of the zeolite product.

Hence, in this strategy, the idea is to take advantage of the properties of TEAOH as: i) polyelectrolyte for the modification of the surface charge of the core hierarchical Cu/SAPO-34 catalyst (*Cu/0.15-fresh*), enhancing the core seeding step and ii) template for the direct overgrowth of microporous SAPO-34 shell on the surface of the core. Since the surfactant will be covering the surface of the core, ideally, some areas will be satisfactory covered by the

negatively charged zeolite seed (microporous SAPO-34, *micro*), leading to a shell formation by the secondary growth. However, those areas of the core covered by TEA^+ species, but uncovered with the seed, might promote the in-situ growing of the *micro* shell, acting as a template for this process. The synthetic procedure studied with this polyelectrolyte is summarized in Figure V. 15.

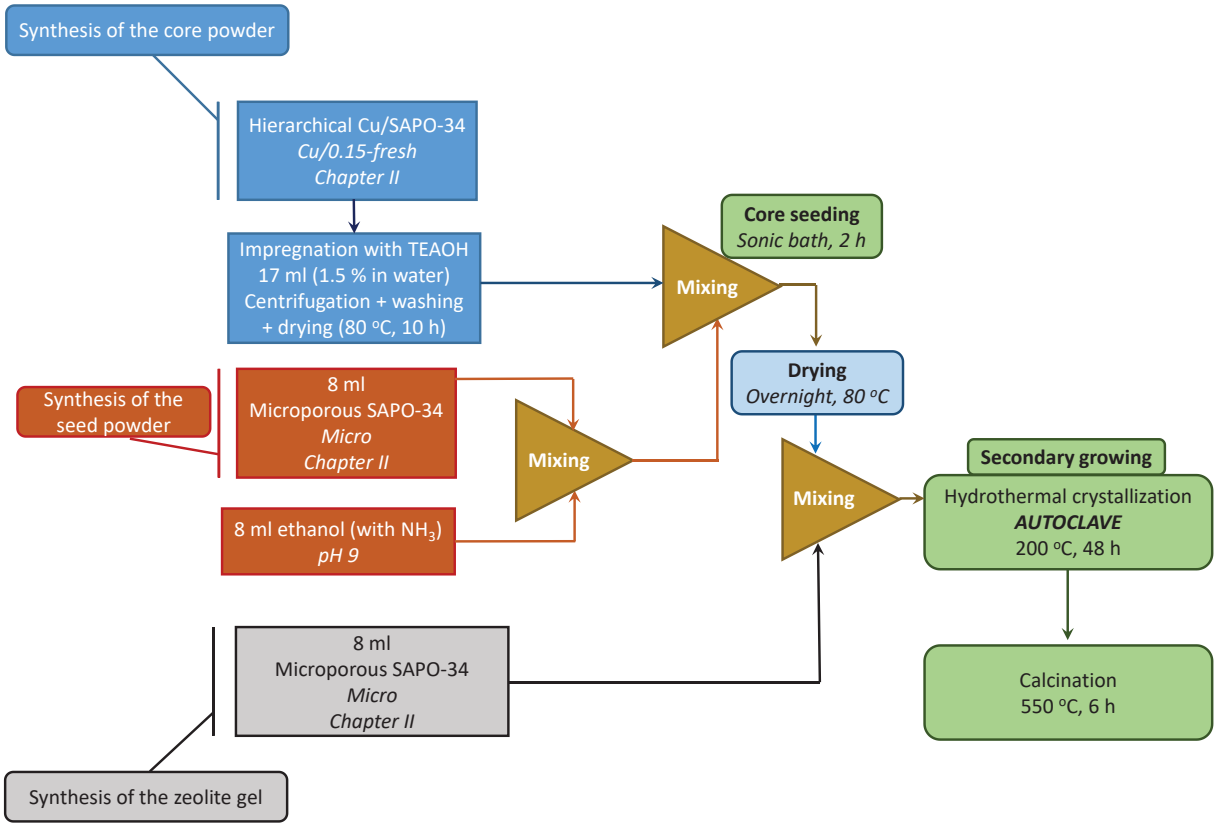

Figure V. 15. Scheme of the experimental procedure used for the development of the core-shell *Cu/0.15-fresh@micro* material by the *seeded growth* method with TEAOH.

In this approach, the core seeding process was very similar to the last approach described in the previous section (Figure V. 13). However, the core *Cu/0.15-fresh* catalyst was first impregnated with an aqueous solution (17 ml) of TEOH (1.5% wt) at 80 °C for 10 h (in a similar way than in ref. [21]). In this case, the material was not calcined after the core seeding, but it was dried at a temperature of 80 ºC overnight, in order to provide adherence of the seeds to the surface of the core material.

Figure V. 16 shows the E-TEM images of the materials obtained by this approach. Herein, well crystallized zeolites with cubic shape were obtained. Assuming the small crystals belong to the microporous SAPO-34 material, they exhibit a weak (but not negligible) interaction with the bigger crystals (presumably the hierarchical catalyst Cu/0.15-fresh).

However, such interaction seemed to be weaker than that for the approaches with CTAB as a surfactant, as observed in Figures V. 12 and V. 14. The difference observed in the performance of the two different polyelectrolyte surfactants could be attributed to the smaller charge inversion effect of TEAOH compared with CTAB, according to the zeta-potential.

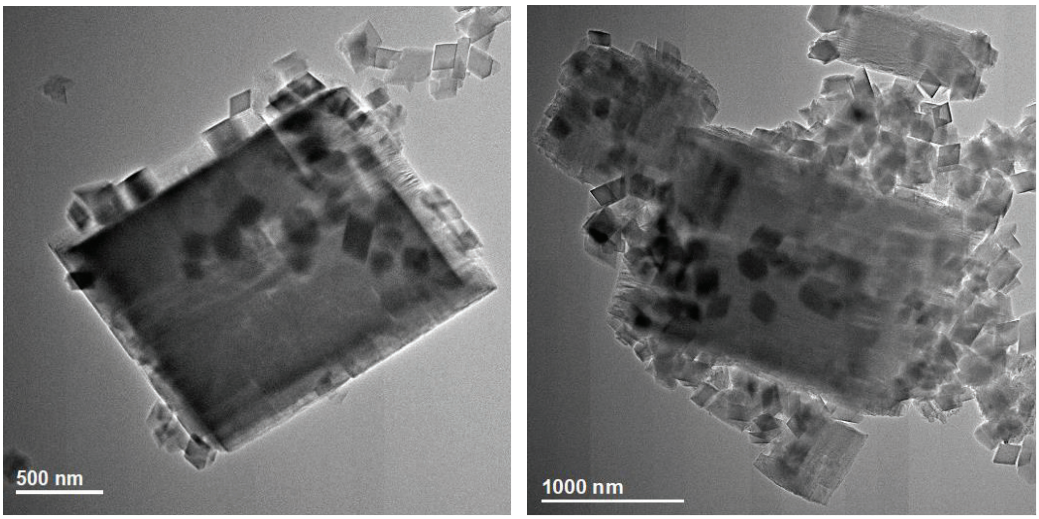

Figure V. 16. E-TEM images of the materials obtained by the *seeded growth* method with TEAOH described in Figure V. 15.

Hence, it seems that the TEAOH as a surfactant could favor the interaction between the seed and the core materials. However, further studies should be carried out to evaluate the potential of this method and to optimize the synthesis procedure in order to develop the desired *Cu/0.15-fresh@micro* core-shell material.

4. Discussion and Conclusions.

The aim of this study was to stablish, for the first time, the first steps for the development of a core-shell material with the following configuration: *Cu/0.15-fresh@micro*, where the core is made of a hierarchical Cu/SAPO-34 catalyst, chosen according to its excellent features (as studied in *Chapter IV*), and the shell is made of a microporous SAPO-34 zeolite. Different strategies were studied, and the following conclusions were obtained:

- The *in-situ overgrowth* method was not efficient to develop the desired material, most likely due to the competition between the nucleation centers in the bulk of the zeolite gel precursor, and those on the surface of the core material. In addition, both core and shell exhibit similar surface charge, which might lead to a significant repulsion between both materials.

- The *seeded growth* method was clearly more efficient than the previous one. Among all the approaches studied, it seems that modifying the surface charge of the core (*Cu/0.15-fresh*) with a CTAB surfactant, and calcining the material obtained after the core seeding, allowed to enhance the adherence between the core and the seed (*micro*). After the whole procedure, the material obtained showed a significant interaction between the core and the shell.

Nevertheless, a perfect core-shell architecture was not obtained, and further studies should be performed in this direction to improve and optimize the synthesis procedure. For instance, repeating the core-seeding process several times after the calcination (before the secondary growth) might enhance the adherence of the seed to the core. Also, the calcination procedure of the core-seeded should be optimized.

All in all, this study shows the first steps into a right direction towards the development of advanced all-zeolite core-shell materials for the catalytic NH_3-SCR process for the reduction of NO_x.

References

[1] S.J. Schmieg, S.H. Oh, C.H. Kim, D.B. Brown, J.H. Lee, C.H.F. Peden, D.H. Kim, Thermal durability of Cu-CHA NH3-SCR catalysts for diesel NOx reduction, Catal. Today. 184 (2012) 252–261. https://doi.org/10.1016/j.cattod.2011.10.034.

[2] W.M. Bull, W.-M. Xue, P. Burk, R.S. Boorse, I. Jaglowski, G.S. Koermer, A. Moini, J.A. Patchett, J.C. Dettling, M.T. Caudle, Copper CHA Zeolinte Catalysts, U.S. Patent 0,226,545, 2008., 2009. https://patents.google.com/patent/US20080226545.

[3] Q. Ye, L. Wang, R.T. Yang, Activity, propene poisoning resistance and hydrothermal stability of copper exchanged chabazite-like zeolite catalysts for SCR of NO with ammonia in comparison to Cu/ZSM-5, Appl. Catal. A Gen. 427–428 (2012) 24–34. https://doi.org/https://doi.org/10.1016/j.apcata.2012.03.026.

[4] F. Gao, Fe-Exchanged Small-Pore Zeolites as Ammonia Selective Catalytic Reduction (NH3-SCR) Catalysts, Catalysts. 10 (2020). https://doi.org/10.3390/catal10111324.

[5] A. Wang, Y. Wang, E.D. Walter, R.K. Kukkadapu, Y. Guo, G. Lu, R.S. Weber, Y. Wang, C.H.F. Peden, F. Gao, Catalytic N2O decomposition and reduction by NH3 over Fe/Beta and Fe/SSZ-13 catalysts, J. Catal. 358 (2018) 199–210. https://doi.org/https://doi.org/10.1016/j.jcat.2017.12.011.

[6] X. Wang, Y. Sun, F. Han, Y. Zhao, Effect of Fe addition on the structure and SCR reactivity of one-pot synthesized Cu-SSZ-13, J. Environ. Chem. Eng. 10 (2022) 107888. https://doi.org/https://doi.org/10.1016/j.jece.2022.107888.

[7] A. Wang, Y. Wang, E.D. Walter, N.M. Washton, Y. Guo, G. Lu, C.H.F. Peden, F. Gao, NH3-SCR on Cu, Fe and Cu+Fe exchanged beta and SSZ-13 catalysts: Hydrothermal aging and propylene poisoning effects, Catal. Today. 320 (2019) 91–99. https://doi.org/https://doi.org/10.1016/j.cattod.2017.09.061.

[8] Y. Wang, L. Xie, F. Liu, W. Ruan, Effect of preparation methods on the performance of CuFe-SSZ-13 catalysts for selective catalytic reduction of NOx with NH3, J. Environ. Sci. 81 (2019) 195–204. https://doi.org/https://doi.org/10.1016/j.jes.2019.01.013.

[9] T. Zhang, J. Li, J. Liu, D. Wang, Z. Zhao, K. Cheng, J. Li, High activity and wide temperature window of Fe-Cu-SSZ-13 in the selective catalytic reduction of NO with ammonia, AIChE J. 61 (2015) 3825–3837. https://doi.org/10.1002/aic.14923.

[10] C. Yin, P. Cheng, X. Li, R.T. Yang, Selective catalytic reduction of nitric oxide with ammonia over high-activity Fe/SSZ-13 and Fe/one-pot-synthesized Cu-SSZ-13 catalysts, Catal. Sci. Technol. 6 (2016) 7561–7568. https://doi.org/10.1039/C6CY01027J.

[11] R. Zhang, Y. Li, T. Zhen, Ammonia selective catalytic reduction of NO over Fe/Cu-SSZ-13, RSC Adv. 4 (2014) 52130–52139. https://doi.org/10.1039/C4RA09290B.

[12] A. Guerrero-Martínez, J. Pérez-Juste, L.M. Liz-Marzán, Silica-Coated Nanomaterials: Recent Progress on Silica Coating of Nanoparticles and Related Nanomaterials (Adv. Mater. 11/2010), Adv. Mater. 22 (2010). https://doi.org/https://doi.org/10.1002/adma.201090031.

[13] M. Enterría, F. Suárez-García, A. Martínez-Alonso, J.M.D. Tascón, Preparation of hierarchical micro-mesoporous aluminosilicate composites by simple Y zeolite/MCM-48 silica assembly, J. Alloys Compd. 583 (2014) 60–69. https://doi.org/https://doi.org/10.1016/j.jallcom.2013.08.137.

[14] T. Zhang, F. Qiu, J. Li, Design and synthesis of core-shell structured meso-Cu-SSZ-13@mesoporous aluminosilicate catalyst for SCR of NO with NH3: Enhancement of activity, hydrothermal stability and propene poisoning resistance, Appl. Catal. B Environ. 195 (2016) 48–58. https://doi.org/10.1016/j.apcatb.2016.04.058.

[15] L. Zhang, T. Du, H. Qu, B. Chi, Q. Zhong, Synthesis of Fe-ZSM-5@Ce/mesoporous-silica and its enhanced activity by sequential reaction process for NH3-SCR, Chem. Eng. J. 313 (2017) 702–710. https://doi.org/10.1016/j.cej.2016.12.108.

[16] J. Liu, Y. Du, J. Liu, Z. Zhao, K. Cheng, Y. Chen, Y. Wei, W. Song, X. Zhang, Design of MoFe/Beta@CeO2 catalysts with a core−shell structure and their catalytic performances for the selective catalytic reduction of NO with NH3, Appl. Catal. B Environ. 203 (2017) 704–714. https://doi.org/10.1016/j.apcatb.2016.10.039.

[17] J. Liu, J. Liu, Z. Zhao, Y. Wei, W. Song, Fe-Beta@CeO_2 core-shell catalyst with tunable shell thickness for selective catalytic reduction of NO_x with NH_3, AIChE J. 63 (2017) 4430–4441. https://doi.org/10.1002/aic.15743.

[18] L. Chen, X. Wang, Q. Cong, H. Ma, S. Li, W. Li, Design of a hierarchical Fe-ZSM-5@CeO2 catalyst and the enhanced performances for the selective catalytic reduction of NO with NH3, Chem. Eng. J. 369 (2019) 957–967.

https://doi.org/https://doi.org/10.1016/j.cej.2019.03.055.

[19] Z. Di, H. Wang, R. Zhang, H. Chen, Y. Wei, J. Jia, ZSM-5 core–shell structured catalyst for enhancing low-temperature NH3-SCR efficiency and poisoning resistance, Appl. Catal. A Gen. 630 (2022) 118438. https://doi.org/https://doi.org/10.1016/j.apcata.2021.118438.

[20] N. Masoumifard, R. Guillet-Nicolas, F. Kleitz, Synthesis of Engineered Zeolitic Materials: From Classical Zeolites to Hierarchical Core–Shell Materials, Adv. Mater. 30 (2018) 1704439. https://doi.org/10.1002/adma.201704439.

[21] Z. Xu, J. Li, W. Qian, H. Ma, H. Zhang, W. Ying, Synthesis of core–shell SAPO-34@SAPO-18 composites by the epitaxial growth method and their catalytic properties for the MTO reaction, RSC Adv. 7 (2017) 54866–54875. https://doi.org/10.1039/C7RA11395A.

[22] X. Li, F. Rezaei, D.K. Ludlow, A.A. Rownaghi, Synthesis of SAPO-34@ZSM-5 and SAPO-34@Silicalite-1 Core–Shell Zeolite Composites for Ethanol Dehydration, Ind. Eng. Chem. Res. 57 (2018) 1446–1453. https://doi.org/10.1021/acs.iecr.7b05075.

[23] L. Zhang, Z.-X. Jiang, Y. Yu, C.-S. Sun, Y.-J. Wang, H.-Y. Wang, Synthesis of core–shell ZSM-5@meso-SAPO-34 composite and its application in methanol to aromatics, RSC Adv. 5 (2015) 55825–55831. https://doi.org/10.1039/C5RA10296K.

[24] L. Kong, Z. Jiang, J. Zhao, J. Liu, B. Shen, The Synthesis of Hierarchical SAPO-34 and its Enhanced Catalytic Performance in Chloromethane Conversion to Light Olefins, Catal. Letters. 144 (2014) 1609–1616. https://doi.org/10.1007/s10562-014-1296-3.

[25] B.R.S. De Araujo, J.A. Onrubia-Calvo, I. Stambouli, G. Pétaud, J. Hidalgo-Carrillo, A. Nieto-Marquéz, B. Pereda-Ayo, J.R. González-Velasco, A. Caravaca, S. Gil, Towards the development of advanced hierarchical chabazite materials: Novel micro-mesoporous silicoaluminophosphate SAPO-34 zeolites, Mater. Today Commun. 31 (2022) 103580. https://doi.org/10.1016/j.mtcomm.2022.103580.

[26] S. Askari, A. Bashardoust Siahmard, R. Halladj, S. Miar Alipour, Different techniques and their effective parameters in nano SAPO-34 synthesis: A review, Powder Technol. 301 (2016) 268–287. https://doi.org/https://doi.org/10.1016/j.powtec.2016.06.018.

[27] H. van Heyden, S. Mintova, T. Bein, Nanosized SAPO-34 Synthesized from Colloidal

Solutions, Chem. Mater. 20 (2008) 2956–2963. https://doi.org/10.1021/cm703541w.

[28] M. Dargahi, H. Kazemian, M. Soltanieh, M. Hosseinpour, S. Rohani, High temperature synthesis of SAPO-34: Applying an L9 Taguchi orthogonal design to investigate the effects of experimental parameters, Powder Technol. 217 (2012) 223–230. https://doi.org/https://doi.org/10.1016/j.powtec.2011.10.030.

[29] G.R. Millward, S. Ramdas, J.M. Thomas, M.T. Barlow, Evidence for semi-regularly ordered sequences of mirror and inversion symmetry planes in ZSM-5/ZSM-11 shape-selective zeolitic catalysts, J. Chem. Soc. Faraday Trans. 2 Mol. Chem. Phys. 79 (1983) 1075–1082. https://doi.org/10.1039/F29837901075.

[30] X. Luo, J. Guo, P. Chang, H. Qian, F. Pei, W. Wang, K. Miao, S. Guo, G. Feng, ZSM-5@MCM-41 composite porous materials with a core-shell structure: Adjustment of mesoporous orientation basing on interfacial electrostatic interactions and their application in selective aromatics transport, Sep. Purif. Technol. 239 (2020) 116516. https://doi.org/https://doi.org/10.1016/j.seppur.2020.116516.

[31] S. ul H. Bakhtiar, X. Wang, S. Ali, F. Yuan, Z. Li, Y. Zhu, CTAB-assisted size controlled synthesis of SAPO-34 and its contribution toward MTO performance, Dalt. Trans. 47 (2018) 9861–9870. https://doi.org/10.1039/C8DT01811A.

[32] Z. Zheng, D. Yang, T. Li, X. Yin, S. Wang, X. Wu, X. An, X. Xie, A novel BEA-type zeolite core–shell multiple catalyst for hydrogen-rich gas production from ethanol steam reforming, Catal. Sci. Technol. 6 (2016) 5427–5439. https://doi.org/10.1039/C6CY00119J.

[33] N. Masoumifard, K. Kim, S. Kaliaguine, P.M. Arnal, F. Kleitz, Synthesis of microporous/mesoporous core–shell materials with crystalline zeolitic shell and supported metal oxide silica core, CrystEngComm. 18 (2016) 4452–4464. https://doi.org/10.1039/C6CE00286B.

[34] G.D. Pirngruber, C. Laroche, M. Maricar-Pichon, L. Rouleau, Y. Bouizi, V. Valtchev, Core–shell zeolite composite with enhanced selectivity for the separation of branched paraffin isomers, Microporous Mesoporous Mater. 169 (2013) 212–217. https://doi.org/https://doi.org/10.1016/j.micromeso.2012.11.016.

[35] Y. Bouizi, L. Rouleau, V.P. Valtchev, Factors Controlling the Formation of Core−Shell Zeolite−Zeolite Composites, Chem. Mater. 18 (2006) 4959–4966.

https://doi.org/10.1021/cm0611744.

[36] J. Zheng, G. Wang, M. Pan, D. Guo, Q. Zhao, B. Li, R. Li, Hierarchical core–shell zeolite composite ZSM-5@SAPO-34 fabricated by using ZSM-5 as the nutrients for the growth of SAPO-34, Microporous Mesoporous Mater. 206 (2015) 114–120. https://doi.org/10.1016/j.micromeso.2014.12.011.

[37] J. Zheng, X. Zhang, Y. Wang, Y. Bai, W. Sun, R. Li, Synthesis and catalytic performance of a bi-phase core-shell zeolite composite, J. Porous Mater. 16 (2008) 731. https://doi.org/10.1007/s10934-008-9255-2.

[38] Y. Wu, Y. Chai, J. Li, H. Guo, L. Wen, C. Liu, Preparation of silicalite-1@Pt/alumina core–shell catalyst for shape-selective hydrogenation of xylene isomers, Catal. Commun. 64 (2015) 110–113. https://doi.org/https://doi.org/10.1016/j.catcom.2015.02.004.

[39] Y. Wu, J. Li, Y. Chai, H. Guo, C. Liu, Synergetic effect of H-ZSM-5/Silicalite-1@Pt/Al2O3 core–shell catalyst to enhance the selective hydrogenation of p-xylene, J. Memb. Sci. 496 (2015) 70–77. https://doi.org/https://doi.org/10.1016/j.memsci.2015.08.048.

[40] D.P. Serrano, R. van Grieken, Heterogenous events in the crystallization of zeolites, J. Mater. Chem. 11 (2001) 2391–2407. https://doi.org/10.1039/b100818h.

Chapter VI

CHAPTER VI: General conclusions & perspectives.

1. General Conclusions.

Nitrogen oxides (NO_x), mainly emitted in combustion processes by stationary and mobile sources, are responsible of alarming environmental issues, such as the acid rain and the photochemical smog. One of the most efficient technologies for the removal of NO_x is the Selective Catalytic Reduction with NH_3 (NH_3-SCR). This process is efficiently catalysed, in internal combustion engines, by Cu/CHAbazite-based materials. These materials exhibit an excellent hydrothermal stability on account of the nanometric small pores of the CHA zeolite. However, such small pores lead to significant diffusion limitations, which in the end hinders the low temperature activity of such materials. This present PhD (ANR JCJC CHARO) targets the development of advanced materials to overcome such limitations.

Thus, the first objective was to introduce the mesoporosity in the otherwise solely microporous CHA-based catalysts, to form hierarchical structures (*Chapter III*). Conventional microporous and hierarchical SAPO-34 zeolites were synthetized by hydrothermal crystallization method. With that purpose, through the so-called One-pot method, cetyltrimethylammonium bromide (CTAB) mesoporous template was directly introduced into the conventional gel containing a microporous template (tetraethylammonium hydroxide, TEAOH), before starting the zeolite crystallization. The presence of both templates in the initial gel solution resulted in a microporous zeolite embedded in a physical mixture containing a mesoporous phase. To solve this issue, a defined aging period was implemented through the so-called Aging method, before the incorporation of CTAB to the microporous gel solution. The results obtained demonstrated that the mesoporosity into the microporous SAPO-34 was successfully introduced by both, One-pot and Aging methods. However, only in the latter case, the crystallinity, BET specific surface area and microporosity were conserved after the creation of mesopores. In order to get more insights into this original material, a series of hierarchical zeolites was prepared by the same method, varying the amount of CTAB, and a strong influence of this parameter was observed on their physicochemical properties. The formation of mesopores was achieved for all of them. Indeed, as the CTAB amount increased, the volume of mesopores increased. However, the volume of micropores, relative crystallinity and acidity seemed to follow an unexpected inverted-volcano trend. Hence, the materials with the best

physicochemical features were the hierarchical SAPO-34 zeolites so-called Aged Meso-0.15 and Aged Meso-0.66 (with CTAB/Al molar ratios of 0.15 and 0.66, respectively)

The hierarchical zeolites above mentioned were used as a support for the development of hierarchical Cu/SAPO-34 catalysts (*Chapter IV*). Cu-hierarchical SAPO-34 catalysts were optimized and characterized by several techniques. These hierarchical catalysts were targeted to allow an efficient gas diffusion through mesopores, improving the NO_x-removal efficiency at low reaction temperatures. However, a downside of mesopores is that they could eventually reduce hydrothermal stability, which is a feature of paramount importance in view of its further practical implementation. To demonstrate the potential of these novel catalytic systems, the NH_3-SCR catalytic activity of fresh and hydrothermally treated hierarchical catalysts was evaluated and compared with that of a Cu-microporous catalyst. As expected, the activity of the Cu-based hierarchical catalysts hydrothermally treated did not surpass that of the microporous catalyst at high temperatures, which could be attributed to their lower concentration of acid sites and specific surface area. However, very interestingly, their activity at low temperatures overcame that of the microporous catalyst, which could be assigned to both, the increase of the isolated Cu^{2+} active sites after the hydrothermal treatment, and the (likely) enhanced diffusion of reactants through the mesopores. All in all, the material so-called *Cu/0.15-fresh* exhibited an enhanced low temperature NH_3-SCR catalytic activity for an efficient reduction of NO_x, which is a critical feature in view of its further practical implementation.

Aiming to advance one step further, novel all-zeolite core-shell materials were targeted in *Chapter V*. The core was made of the hierarchical Cu/SAPO-34 catalyst (so-called *Cu-0.15/fresh*) developed in our previous study (*Chapter IV*). As above mentioned, this material exhibited an excellent activity at low temperatures (likely attributed to the enhanced diffusion of reactants through their mesoporous-microporous framework) and high hydrothermal stability. The shell, on the other hand, will be constituted by a Fe/SAPO-34 catalyst, where iron species will be exchanged in the framework of a microporous SAPO-34 zeolite (with slightly bigger pores than conventional CHA materials). The latter will serve to: i) protect the core material, with slightly lower hydrothermal stability due to the creation of mesopores, ii) to enhance the catalytic activity for the NH_3-SCR reaction at higher temperatures, where the Cu-based materials are not sufficiently active, and ii) to further transform the N_2O eventually produced in the NH_3-SCR reaction on the hierarchical Cu/SAPO-34 core catalyst. Hence, in the last section of this work, the first steps towards the development of such core-shell architecture

were carried out, aiming to develop a *hierarchical Cu/SAPO-34@microporous SAPO-34* (*core@shell*) material. Several approaches were carried out for this purpose, which pointed out that the use of positive surfactants (such as CTAB, to surface charge modification of the core) and the calcination of intermediate synthesis materials, among other factors, seemed to enhance the interaction between core and shell. This latter study allowed therefore to identify the main direction to follow towards the development of the desired core-shell materials, which are expected to open a uniquely large temperature window of efficient activity and selectivity for the efficient abatement of NO_x and N_2O.

- Publications associated to this PhD :

1. Towards the development of advanced hierarchical chabazite materials: novel micro-mesoporous silicoaluminophosphate SAPO-34 zeolites, B.R.S. De Araujo, J. Ander Onrubia, I. Stambouli, G. Pétaud, A. Nieto-Marquéz, B. Pereda-Ayo, J.R. González Velasco, A. Caravaca, S. Gil, ***Mater. Today Commun***. 31 (2022)103580.

2. Cu-hierarchical-SAPO-34 catalysts with enhanced low-temperature NOx removal and high hydrothermal stability, B.R.S. De Araujo, J. Ander Onrubia, G. Pétaud, A. Nieto-Marquéz, B. Pereda-Ayo, J.R. González Velasco, A. Caravaca, S. Gil, submitted to ***ChemCatChem*** August 2022.

- Congress communications associated to this PhD:

1. Hydrothermal stability enhancement of novel hierarchical-CHA catalysts, B.R.S. De Araujo, P. Rocher, G. Pétaud, A. Caravaca, S. Gil, Gecat 2021, Visio-conference (vidéo de présentation de poster) 31 mai-4 juin 2021.

2. Hierarchical CHAbazite core-shell catalysts for Reduction of NO_x and N_2O, B.R.S. De Araujo, A. Caravaca, S. Gil. Webinaire « *Jeunes de la section Ile-de-France* », 18 novembre 2021.

3. Cu-hierarchical-SAPO-34 catalysts with enhanced low-temperature NOx removal and high hydrothermal stability, B.R.S. De Araujo, J.A. Onrubia-Calvo, A. Nieto-Marquez, B. Pareda-Ayo, J.R. Gonzalez Velasco, A. Caravaca, S. Gil, (oral presentation) FCCAT 2022, Ronce-les-Bains, France, 30 May-3 June 2022.

4. Hydrothermal stability studies of novel hierarchical-CHA catalysts, B.R.S. De Araujo, P. Rocher, G. Pétaud, J.A. Onrubia-Calvo, A. Nieto-Marquez, B. Pareda-Ayo, J.R. Gonzalez Velasco, A. Caravaca, S. Gil (poster) CAPOC 2022, Brussels, Belgium, 29-31 August 2022.

2. Perspectives

Considering the conclusions described for this PhD project regarding the development of advanced hierarchical and core-shell structures, further investigations would eventually allow to better understand the kinetics and the reaction mechanism of the developed catalysts, and to continue with the development of advanced core-shell materials. Therefore, the following perspectives are suggested for further studies:

- In terms of diffusion limitations: our developed Cu-loaded hierarchical catalysts demonstrated to have an enhanced low-temperature activity, which was attributed to the reduction of diffusional limitations by the incorporation of mesopores into the zeolite framework. However, a deeper study of "enhanced diffusion" is required to clearly corroborate this point. ZLC (Zero Length Column) and TAP (Temporal Analysis of Product) over a model molecule could be carried out for this purpose.

- Some NH_3 and CO-DRIFTS measurements were performed, and reported in this manuscript, in order to evaluate the acid sites and Cu species location of the developed hierarchical catalysts. Nevertheless, a deep study by *in-situ* adsorption/desorption or co-adsorption (e.g. NH_3 or NO/O_2), and NH_3-SCR reaction at different temperatures, both followed by DRIFTS, need to be considered to characterize and confirm the NO_x species adsorbed over the novel catalysts, together with the reaction intermediates (e.g. nitrite/nitrate intermediate species, as previously mentioned in *Chapter IV*).

- Concerning the core-shell development, as previously mentioned in *Chapter V*, further studies should be performed to improve and optimize the synthesis procedure. For instance, regarding the seeded growth strategy with TEAOH as polyelectrolyte, a further calcination of the core-seeded might enhance the adherence of the seed material to the core, leading in the end to a more robust core-shell material. For both, CTAB and TEAOH surfactants, repeating the core-seeding process several times after the intermediate calcination (before the secondary growth) could better ensure an effective and uniform coverage of the core surface. Also, the calcination procedure of the core-seeded should be optimized. Moreover, the last step (secondary hydrothermal shell growth) could also be repeated several times to guarantee a continuous shell coverage and integrity. In addition, other polyelectrolytes commonly used in previous core-shell studies could be evaluated, such as Poly(diallyldimethylammonium chloride) (PDDA) .

- To minimize the above mentioned additional steps, the secondary growth of seeds can also be performed under rotation, maximising the uniformity and integrity of the resulting zeolite shell. For this purpose, a heating oven equipped with a rotary frame (30 rpm) should be used, which is indeed available at IRCELYON (Dr. Alain Tuel's team).

- Once the desired *Cu/0.15-freh@micro* core-shell architecture has been properly optimized, the incorporation of iron cations on the microporous shell zeolite should be performed. However, Fe^{2+} oxidation to Fe^{3+} must be avoided because of the penetration hindrance for Fe^{3+}, with high kinetic diameter than Fe^{2+}, into the zeolite frameworks (that is associated to the formation of bulky compounds). This risk should be avoided by using a protective N_2 atmosphere during the ion exchange. To determine the location of the iron active sites, complementary information will be sought via, for example, Mössbauer spectroscopy.

- The composition, structural features and acidic and redox properties of the final core-shell catalytic systems should be also characterized by a combination of the techniques described in the thesis manuscript.

- Proof-of-concept: Finally, we suggest to evaluate the activity of the novel catalysts developed through the assessment of the NH_3-SCR catalytic performance, notably the core-shell structures and the individual Cu- and Fe-loaded hierarchical and microporous catalysts, respectively. The performance of these materials should be compared with more traditional Cu-/Fe-bimetallic catalysts and Cu-hierarchical/Fe-microporous CHA-based catalysts physically mixed (or in a dual catalytic bed).